

**A Thesis Submitted for the Degree of PhD at the University of Warwick**

**Permanent WRAP URL:**

<http://wrap.warwick.ac.uk/99346>

**Copyright and reuse:**

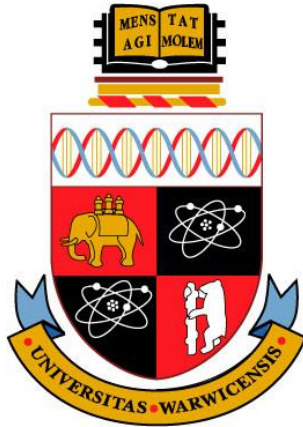
This thesis is made available online and is protected by original copyright.

Please scroll down to view the document itself.

Please refer to the repository record for this item for information to help you to cite it.

Our policy information is available from the repository home page.

For more information, please contact the WRAP Team at: [wrap@warwick.ac.uk](mailto:wrap@warwick.ac.uk)



An Investigation into the

# **Wear and Thermal-mechanical Performance of Polyacetal Gears**

by

**Zedong Hu**

A thesis submitted to the University of Warwick in partial fulfilment of the  
requirements for admission to the degree of

**Doctor of Philosophy**

**School of Engineering, University of Warwick**

October 2017

# Table of Contents

<b>Table of Contents</b> .....	<b>i</b>
<b>List of Figures</b> .....	<b>vii</b>
<b>List of Tables</b> .....	<b>xviii</b>
<b>Declaration</b> .....	<b>xx</b>
<b>Publications</b> .....	<b>xxi</b>
<b>Acknowledgments</b> .....	<b>xxii</b>
<b>Abstract</b> .....	<b>xxiv</b>
<b>Chapter 1 Introduction</b> .....	<b>1</b>
1.1 Overview and challenges.....	1
1.2 Objectives and strategies.....	8
1.3 Thesis structure .....	10
<b>Chapter 2 Literature Review</b> .....	<b>13</b>
2.1 Designs for non-metallic gears .....	13
2.2 Wear mechanism .....	14
2.2.1 Categories of principal wear mechanism.....	15
2.2.2 Wear curves .....	17
2.3 Failure modes of polymeric gears.....	18
2.4 Thermal-mechanical behaviour.....	20
2.4.1 Heat sources .....	23
2.4.2 Heat dissipation.....	28
2.4.3 Temperature prediction .....	29
2.4.4 Performance improvement .....	38

2.4.5	Thermal-wear performance .....	43
2.5	Gear mesh misalignment .....	51
2.6	Wear debris .....	53
<b>Chapter 3</b>	<b>Experimental Methods.....</b>	<b>55</b>
3.1	Design of the new non-metallic gear test rig .....	56
3.1.1	Structure of the gear test rig .....	56
3.1.2	Test gears .....	59
3.1.3	Working principle.....	60
3.1.4	Misalignment definition and adjustment .....	63
3.2	Design of the wear measurement system.....	67
3.3	Design for airflow temperature measurement .....	76
3.4	Bulk temperature measurement.....	78
3.5	Airflow velocity measurement .....	78
3.6	Vibration measurement.....	79
3.7	Examinations of worn tooth and wear debris .....	81
<b>Chapter 4</b>	<b>Aligned-Configuration Tests.....</b>	<b>82</b>
4.1	Introduction .....	82
4.2	Short-period wear tests.....	84
4.2.1	Test results and discussions .....	85
4.2.2	Topography of worn teeth .....	91
4.2.3	Regime of wear debris .....	105



4.2.4	Conclusions.....	110
4.3	Endurance test results and discussions.....	113
4.3.1	Methodology for endurance tests .....	114
4.3.2	Test at a load of 5 N·m.....	116
4.3.3	Tests at a load of 7 N·m .....	120
4.3.4	Test at a load of 8 N·m.....	125
4.3.5	Test at a load of 8.5 N·m.....	127
4.3.6	Test at a load of 9.0 N·m.....	129
4.3.7	Test at a load of 9.5 N·m.....	131
4.3.8	Test at a load of 10.1 N·m.....	134
4.3.9	Test at a load of 12.1 N·m.....	135
4.3.10	Test at a load of 14.1 N·m.....	136
4.3.11	Overall discussions .....	138
4.4	Step-load test results and discussions.....	139
4.4.1	Incremental load tests at a speed of 1000 rpm .....	141
4.4.2	Incremental load tests at various speeds .....	142
4.5	Graphite lubricated test results and discussions .....	145
4.5.1	Tests at light loads .....	147
4.5.2	Tests at medium loads .....	149
4.5.3	Tests at heavy loads .....	150

4.5.4	Discussions on lubricated test results .....	152
4.6	Conclusions .....	153
<b>Chapter 5</b>	<b>Misaligned-Configuration Tests .....</b>	<b>156</b>
5.1	Nominally aligned test.....	157
5.2	Test results and discussions for axially misaligned gears.....	158
5.2.1	Wear curve and wear rate .....	159
5.2.2	Topography of worn tooth surfaces .....	163
5.2.3	Regime of wear debris .....	168
5.2.4	Conclusions.....	172
5.3	Test results and discussions for radially misaligned gears .....	173
5.3.1	Wear curve and wear rate .....	174
5.3.2	Topography of worn tooth surfaces .....	177
5.3.3	Regime of wear debris .....	183
5.3.4	Conclusions.....	186
5.4	Test results and discussions for yaw misaligned gears .....	187
5.4.1	Wear curve and wear rate .....	188
5.4.2	Topography of worn tooth surfaces .....	190
5.4.3	Regime of wear debris .....	192
5.4.4	Conclusions.....	193
5.5	Test results and discussions for pitch misaligned gears .....	194
5.5.1	Wear curve and wear rate .....	195

5.5.2	Topography of worn tooth surfaces .....	197
5.5.3	Regime of wear debris .....	200
5.5.4	Conclusions.....	202
<b>Chapter 6</b>	<b>Thermal Tests.....</b>	<b>204</b>
6.1	Introduction .....	204
6.2	Airflow temperature measurement.....	205
6.3	Bulk temperature measurement.....	208
6.4	Thermal test results and discussions .....	210
6.4.1	Typical test results at low loads.....	211
6.4.2	Typical test results at moderate loads .....	215
6.4.3	Typical test results at high loads .....	223
6.4.4	Temperature results of step-load tests .....	231
6.4.5	General discussions and conclusions .....	232
6.5	Aerodynamic characteristics surrounding gears .....	240
6.6	Durability improvement .....	252
<b>Chapter 7</b>	<b>Conclusions and Further Work.....</b>	<b>257</b>
7.1	Conclusions .....	257
7.1.1	Design of additional measurement systems.....	257
7.1.2	Experimental investigations.....	258
7.2	Further work.....	265
	<b>References.....</b>	<b>268</b>
	<b>Appendix A Data of Test Gears .....</b>	<b>277</b>

**Appendix B Test Procedure .....279**

# List of Figures

Figure 1.1 The pyramid of polymer performance (after [5]) .....	3
Figure 2.1 Wear curves of non-metallic gears.....	18
Figure 2.2 Pitting: (a) Pitting form of plastic gears (after [26]), (b) Photographs of pitting on iron gear teeth (after [2]) .....	18
Figure 2.3 Fracture forms of plastic gears (after [26]) .....	19
Figure 2.4 Photograph of a case carburised metal gear with Me-DLC coating following scuffing (after [27]) .....	19
Figure 2.5 Modelling of heat generated by friction and hysteresis for plastic(acetal) gears (after [59]) .....	24
Figure 2.6 Pressure measured at the bottom space of tooth at various speeds (after [66]) .....	26
Figure 2.7 Velocity measured along axial position in gear tooth bottom space (tooth face width 100 mm) (after [66]) .....	27
Figure 2.8 Modelling power loss due to air trapping (spur and helical gears) (after [65]) .....	27
Figure 2.9 Flash temperature comparisons between Mao and Blok (after [7]).....	33
Figure 2.10 Air flow between engaging gears (after [50]) .....	36
Figure 2.11 Schematic tooth geometry parameters for bending strength calculation (after [84]) .....	40
Figure 2.12 Model of unmodified and modified gear tooth profiles (after [85]) .....	41
Figure 2.13 Examples of tooth profile modification (after [87]).....	42
Figure 2.14 Examples of increasing forced air convections of operating gears (after [87]) .....	42
Figure 2.15 An example of drilling holes for increasing heat dissipation (after [90])	43

Figure 2.16 Estimation models of heat generation and distribution on plastic tooth (after [29]).	46
Figure 2.17 Test results at elevated ambient temperatures (after [7])	47
Figure 2.18 An example of tooth profiles scanned before and after tests (after [97])	48
Figure 2.19 The wear and flank temperatures of benchmark geometry gears of RFL 4036 at different loads and a speed of 1000 rev/min) (after [18])	49
Figure 2.20 The relationship between wear rate and operational Yong's modulus for gears of RFL 4036 operating under 'sustainable' operating conditions (after [18])	49
Figure 2.21 Coefficient of friction versus temperature for various polymers (after [98])	50
Figure 2.22 Coefficient of friction versus sliding speed for various polymers (after [98])	51
Figure 3.1 CAD model of the new non-metallic test rig	57
Figure 3.2 Schematic diagram of the current polymer gear test rig	58
Figure 3.3 Schematic diagram of wear measurement and rotating angle	61
Figure 3.4 Schematic diagram of a gear pair mesh alignment.	64
Figure 3.5 Schematic diagram of a gear pair misaligned mesh	64
Figure 3.6 Examples of mesh misalignment of a gear pair corresponding to Figure 3.5	65
Figure 3.7 Structure schematic diagram of wear measurement system	68
Figure 3.8 Output voltage against magnetic flux density at a supply voltage $V_s$ .	69
Figure 3.9 Block diagram of Hall Effect sensor	69
Figure 3.10 Transfer characteristics of Hall Effect sensor at $V_s=5VDC$	69
Figure 3.11 Maximum supply voltage against ambient temperature.	70
Figure 3.12 Geometries of cylindrical magnetic and axial distance from the North Pole face	71

Figure 3.13 Circuit diagram of Hall Effect transducer .....	72
Figure 3.14 Assembly of the non-contact Hall-Effect displacement transducer .....	72
Figure 3.15 Displacement versus Hall output plots .....	73
Figure 3.16 Data logging programme flowchart .....	75
Figure 3.17 Velocity of airflow encircling a rotating gear .....	77
Figure 3.18 Structure diagram of airflow temperature measurement transducer ....	77
Figure 3.19 Thermocouple bracket .....	77
Figure 3.20 An example of airflow temperature measuring points .....	78
Figure 3.21 The location of the accelerometer on gear test rig .....	80
Figure 3.22 The diagram of vibration signal acquisition .....	81
Figure 4.1 Wear at varying loads and a speed of 1000 rpm .....	86
Figure 4.2 Average wear rates at varying loads and a speed of 1000 rpm .....	87
Figure 4.3 Relative incremental ratio of parameters due to variation in load .....	90
Figure 4.4 Sliding and rolling directions of driving and driven gears .....	92
Figure 4.5 SEM micrograph of full view of worn teeth (7.5 N·m $5.4 \times 10^5$ cycles) .....	93
Figure 4.6 Schematic diagram of worn tooth topology and major wear debris distribution .....	94
Figure 4.7 Topology of worn tooth flanks (scanned by ContourGT 3D optical profiler) .....	94
Figure 4.8 SEM micrograph of 'sand wave' and 'ploughing' wear marks on driver gear .....	95
Figure 4.9 SEM micrograph of quantity of pitting on driver tooth .....	95
Figure 4.10 SEM micrograph of wear debris and 'sand wave' .....	96
Figure 4.11 SEM micrograph of wear particles near pitch line zone at a load 7.2 N·m .....	97
Figure 4.12 SEM micrograph of adhesive wear (load 8.4 N·m duration $1.17 \times 10^5$ cycles) .....	98

## List of Figures

Figure 4.13 SEM micrograph of thread wear debris (load 8.4 N·m duration $1.17 \times 10^5$ cycles) .....	99
Figure 4.14 SEM micrograph of wear debris (load 8.4 N·m duration $1.17 \times 10^5$ cycles) .....	99
Figure 4.15 Schematic diagram of prospective material melting region on tooth surfaces.....	100
Figure 4.16 SEM micrographs, at different magnifications of the same area of worn tooth surface of driving gear (9.7 N·m, $3.16 \times 10^4$ cycles) .....	101
Figure 4.17 SEM micrographs, at different magnifications of the same area of worn tip surface of driven tooth (9.7 N·m, $3.16 \times 10^4$ cycles) .....	102
Figure 4.18 SEM micrographs of worn tooth surfaces of driver gear .....	103
Figure 4.19 SEM micrographs of 'fish scale' debris in the driver root vicinity of pitch line.....	104
Figure 4.20 SEM micrographs of elongated roll wear debris of driver gear .....	104
Figure 4.21 OM micrographs of wear debris generated at low load .....	106
Figure 4.22 OM micrographs of granular wear debris at low loads.....	107
Figure 4.23 OM micrographs of primary wear debris yielded before steady wear phase.....	108
Figure 4.24 OM micrographs of 'snowflake' wear debris .....	108
Figure 4.25 OM micrograph of wear debris yielded at high load tests .....	109
Figure 4.26 OM micrographs of bulk slice wear debris present at a load of 14.1 N·m. ....	110
Figure 4.27 OM micrographs of elongated roll wear debris .....	110
Figure 4.28 Schematic plot of wear versus duration.....	114
Figure 4.29 Schematic plot of four individual sections of signal.....	114
Figure 4.30 Schematic plots of stitching wear data .....	116
Figure 4.31 Wear against duration at a load of 5 N·m.....	117



Figure 4.32 Concatenating wear curve at a load of 5 N·m .....	119
Figure 4.33 Wear and duration before steady wear phase at a load of 5 N·m.....	119
Figure 4.34 Wear rate at a load of 5 N·m.....	119
Figure 4.35 Wear against duration at a load of 7 N·m.....	121
Figure 4.36 Concatenating wear curves at a load of 7 N·m.....	121
Figure 4.37 Wear and duration before steady wear phase at a load of 7 N·m.....	122
Figure 4.38 Wear rate at a load of 7 N·m.....	122
Figure 4.39 Wear versus duration at a load of 7 N·m.....	124
Figure 4.40 Concatenating wear curves at a load of 7 N·m.....	124
Figure 4.41 Average wear rate of second test result at a load of 7 N·m .....	125
Figure 4.42 Steady wear rate of second test result at a load of 7 N·m .....	125
Figure 4.43 Wear versus duration at a load of 8 N·m.....	126
Figure 4.44 Wear rates in various wear phases at a load of 8 N·m .....	127
Figure 4.45 Photographs of worn tooth at a load of 8 N·m ( $3.797 \times 10^5$ cycles) .....	127
Figure 4.46 Profiles of worn driver and driven teeth .....	127
Figure 4.47 Wear versus duration at a load of 8.5 N·m.....	128
Figure 4.48 Wear rates in three wear phases at a load of 8.5 N·m .....	128
Figure 4.49 Wear versus duration at a load of 9 N·m.....	129
Figure 4.50 Wear rates in various wear phases at a load of 9 N·m .....	129
Figure 4.51 Photograph of worn tooth at a load of 9 N·m ( $1.725 \times 10^5$ cycles).....	130
Figure 4.52 Photograph of worn tooth surfaces at a load of 9 N·m .....	130
Figure 4.53 Wear versus duration at a load of 9.5 N·m.....	132
Figure 4.54 Wear rates in two wear phases at a load of 9.5 N·m .....	132
Figure 4.55 Photograph of worn gear pair (load 9.5 N·m) .....	133
Figure 4.56 Schematic diagram of tooth flank topologies of a worn gear pair (load 9.5 N·m) .....	133
Figure 4.57 Wear versus duration at a load of 10.1 N·m.....	134

Figure 4.58 Photograph of melt wear marks on worn tooth surfaces at a load of 10.1 N·m.....	135
Figure 4.59 Wear versus duration at a load of 12.1 N·m.....	136
Figure 4.60 Wear versus duration at a load of 14.1 N·m.....	137
Figure 4.61 Worn tooth profiles of a gear pair at a load of 14.1 N·m .....	138
Figure 4.62 Incremental load-wear and its concatenated wear versus duration ...	141
Figure 4.63 Wear rate versus loads at a speed of 1000 rpm and a duration of 30000 cycles each load .....	142
Figure 4.64 Wear versus duration at respective speed of 500, 1000, 1500 and 2000 rpm .....	144
Figure 4.65 Concatenating step-load wear versus duration at various speed.....	144
Figure 4.66 Wear rate versus step loads at various speeds.....	145
Figure 4.67 Photographs of graphite paste applied on gears .....	146
Figure 4.68 Wear versus duration at a load of 5 N·m.....	148
Figure 4.69 Wear versus duration at a load of 6 N·m.....	148
Figure 4.70 Photograph of a pair of lubricated gears at a load of 5 N·m after testing .....	149
Figure 4.71 Wear versus duration at a load of 9 N·m.....	150
Figure 4.72 Photograph of a pair of lubricated gears at a load of 9 N·m after test	150
Figure 4.73 Wear versus duration at a load of 10.1 N·m .....	151
Figure 4.74 Worn graphite lubricated gears at a load of 10.1 N·m after $4.18 \times 10^5$ cycles .....	151
Figure 4.75 Dry and lubricated wear versus duration at various loads .....	152
Figure 4.76 Wear rate versus duration at various loads .....	153
Figure 5.1 SEM micrographs of worn tooth surfaces (load 7.2 N·m) .....	158
Figure 5.2 Wear versus duration in axially misaligned tests (7.2 N·m, 1000 rpm)	159
Figure 5.3 Wear rates versus axial gap.....	160

Figure 5.4 Relative variation ratio in gear and its wear versus radial gap.....	161
Figure 5.5 Schematic interaction of bulk mass wear debris and meshing tooth surfaces.....	163
Figure 5.6 SEM micrographs of worn tooth surfaces (axial gap 1.42 mm).....	164
Figure 5.7 SEM micrographs of pitting on worn worn tooth surfaces.....	164
Figure 5.8 SEM micrographs of 'fish scale' on both sides of pitch point of a driving tooth .....	166
Figure 5.9 SEM micrographs of 'fish scale' on top of pitch point of a driven tooth	166
Figure 5.10 SEM micrographs of debris and 'sand waves' wear marks (axial gap 1.42 mm) .....	167
Figure 5.11 Schematic diagram of edge wall forming due to axial deviation.....	169
Figure 5.12 OM micrographs of translucently lamellate wear debris .....	170
Figure 5.13 OM micrographs of small snowflake-like wear debris (axial gap 1.42 mm) .....	170
Figure 5.14 OM micrographs of wood shavings-like wear debris (axial gap 1.42 mm) .....	171
Figure 5.15 OM micrographs of wood shavings-like wear debris (axial gap 2.48 mm) .....	172
Figure 5.16 Wear versus duration in radial misalignment tests .....	174
Figure 5.17 Wear rates versus radial deviation .....	175
Figure 5.18 Predict parameter variation ratios versus radial deviations.....	177
Figure 5.19 Actual variation ratio in wear rate versus radial deviation: note the scale of initial wear rate (left bar graph) is significant. ....	177
Figure 5.20 SEM micrographs of worn tooth surfaces (radial deviation -0.25 mm) .....	178
Figure 5.21 SEM micrograph comparisons of tooth tips and roots (radial deviation - 0.25 mm) .....	179

Figure 5.22 SEM micrographs of adhesive wear and pitting on polyacetal gear surfaces.....	180
Figure 5.23 SEM micrographs of 'sand wave' wear marks and 'plate' wear debris .....	182
Figure 5.24 SEM micrographs of 'plate' and 'roll/string' wear debris .....	182
Figure 5.25 'Belt' wear debris close to the bottom of driven tooth root .....	183
Figure 5.26 OM micrographs of translucent slice wear debris (radial deviation of - 0.25 mm) .....	184
Figure 5.27 OM micrographs of 'cotton-wool' wear debris (radial deviation of -0.25 mm) .....	184
Figure 5.28 OM micrographs of wear debris (radial deviation of -0.3 mm) .....	185
Figure 5.29 Schematic diagram of ellipse contact area .....	187
Figure 5.30 Wear versus duration of yaw misalignment tests .....	188
Figure 5.31 Wear rates versus yaw angles .....	189
Figure 5.32 Relative variation ratio in actual wear rate versus yaw angles.....	190
Figure 5.33 SEM micrographs of worn tooth surfaces (yaw angle of $0.35^{\circ}$ ) .....	190
Figure 5.34 SEM micrographs of wear marks near pitch point (yaw angle of $0.35^{\circ}$ ) .....	191
Figure 5.35 SEM micrographs of worn driver root surfaces.....	191
Figure 5.36 Abrasive wear and 'hole' on worn driven tooth .....	192
Figure 5.37 OM micrograph of wear debris (yaw angle of $0.35^{\circ}$ ).....	193
Figure 5.38 SEM micrographs of 'needle/roll' wear debris (yaw angle of $0.35^{\circ}$ ) ...	193
Figure 5.39 Schematic diagram of load distribution change due to pitch misalignment .....	195
Figure 5.40 Wear versus duration in pitch misalignment tests.....	196
Figure 5.41 Wear rates versus pitch angles .....	196
Figure 5.42 Relative variation ratios in actual wear rate versus pitch angles.....	197

Figure 5.43 SEM micrograph of wear patterns over worn tooth surfaces (pitch angle of $0.42^\circ$ ).....	198
Figure 5.44 SEM micrographs of ‘pip’ and pitting on a worn driver tooth.....	199
Figure 5.45 SEM micrographs of ‘pitting’ and ‘pip’ on a worn driven tooth .....	199
Figure 5.46 SEM micrographs of micro-cracks near pitch points.....	200
Figure 5.47 SEM micrographs of micro-cracks near tooth roots.....	200
Figure 5.48 OM micrograph of transparent lamellate wear debris (pitch angle of $0.42^\circ$ ).....	201
Figure 5.49 OM micrographs of wear debris (pitch angle of $0.60^\circ$ ).....	201
Figure 5.50 OM micrograph of ‘cotton-wool-like’ wear debris (pitch angle of $0.42^\circ$ ) .....	202
Figure 5.51 OM micrograph of ‘cotton-wool-like’ wear debris (pitch angle of $0.86^\circ$ ) .....	202
Figure 6.1 Plots of airflow temperature surrounding gears at a load of 6 N·m .....	206
Figure 6.2 Measuring points’ distribution of airflow temperature.....	206
Figure 6.3 Measuring locations of bulk temperature on a gear pair .....	209
Figure 6.4 Infrared images of operating gears at speed of 1000 rpm .....	209
Figure 6.5 Infrared images taken after stop running gears (1000 rpm).....	210
Figure 6.6 Test results of wear, bulk and airflow temperature (7 N·m, 1000 rpm) .....	211
Figure 6.7 Wear, wear rate and bulk temperature in steady state (7 N·m, 1000 rpm) .....	213
Figure 6.8 Wear, wear rate and bulk temperature versus duration (4.9 N·m, 1000 rpm) .....	214
Figure 6.9 Three open windows around test gears .....	215
Figure 6.10 Test results of wear, bulk and airflow temperature versus duration (8 N·m) .....	216

Figure 6.11 Wear, wear rate and bulk temperature versus duration (8.0 N·m, 1000 rpm).....	217
Figure 6.12 Test results of wear, bulk and airflow temperature versus duration (8.5 N·m) .....	218
Figure 6.13 Wear, wear rate and bulk temperature versus duration (8.5 N·m, 1000 rpm).....	219
Figure 6.14 Test results of wear, bulk and airflow temperature versus duration (9 N·m) .....	220
Figure 6.15 Wear, wear rate and bulk temperature versus duration (9.0 N·m, 1000 rpm).....	221
Figure 6.16 Test results of wear, bulk and airflow temperature (9 N·m, lubricated) .....	222
Figure 6.17 Wear, wear rate and bulk temperature versus duration (9.0 N·m, lubricated).....	223
Figure 6.18 Test results of wear, bulk and airflow temperature (10.1 N·m, 1000 rpm) .....	224
Figure 6.19 Wear, wear rate and bulk temperature versus duration (10.1 N·m) ...	225
Figure 6.20 Test results of wear, bulk and airflow temperature (10.1 N·m, lubricated) .....	226
Figure 6.21 Wear, wear rate and bulk temperature versus duration (10.1 N·m, lubricated).....	226
Figure 6.22 Test results of wear, bulk and airflow temperature (12.1 N·m, 1000 rpm) .....	227
Figure 6.23 Test results of wear, bulk and airflow temperature (14.1 N·m, 1000 rpm) .....	228
Figure 6.24 Wear, wear rate and bulk temperature (12.1 N·m) .....	229
Figure 6.25 Wear, wear rate and bulk temperature (14.1 N·m) .....	230

Figure 6.26 Schematic of range of wear rate and bulk temperature (broadly representative of polyacetal gears running at 1000 rpm with loads below 8 N·m).	236
Figure 6.27 Coefficient of friction against temperature and sliding speed (after [98])	237
Figure 6.28 Schematic probability density function of operating temperature and wear rate	237
Figure 6.29 Typical DSC of test polyacetal	239
Figure 6.30 Airflow temperature changes during operation and after stopping	242
Figure 6.31 Airflow temperature comparisons between measurement positions	244
Figure 6.32 Natural air convection after test stopped	244
Figure 6.33 The airflow measurement at measurement positions of operating gears	245
Figure 6.34 Bulk and airflow temperatures (4.2 N·m, 1000 rpm)	247
Figure 6.35 Airflow velocity and temperature surrounding and against gears	248
Figure 6.36 Air vortex within gear tooth pockets	250
Figure 6.37 Aerodynamic features of a meshing gear pair	250
Figure 6.38 Schematic diagram of hot air recycling between the trapping of gear teeth	254
Figure 6.39 Testing gears with thermal dissipation structures	255
Figure 6.40 The weight loss of testing gears with various thermal dissipation structures	256
Figure A.1 Nominal dimensions of test gears	277

# List of Tables

Table 1.1 Examples of material properties of polymers and metals [9-11] .....	5
Table 3.1 Specifications of the non-metallic test rig .....	59
Table 3.2 Specifications of test polyacetal gears .....	59
Table 3.3 Specifications of Hall Effect sensor SS495A ( $V_s=5.0V$ , $T_a=-40$ to $+125^{\circ}C$ ) .....	70
Table 3.4 Exponential fit coefficient .....	74
Table 3.5 Specifications of a Brüel & Kjær accelerometer.....	80
Table 4.1 Load range value for three load categories .....	85
Table 4.2 Predicated stresses at pitch point and actual wear rate due to variations in load.....	90
Table 4.3 Time intervals between successive test-stages (load 5 N·m) .....	117
Table 4.4 Time intervals between successive tests (load 7 N·m) .....	120
Table 4.5 Life statistics for polyacetal gears (1000 rpm) .....	139
Table 4.6 Cases of step-load tests.....	140
Table 4.7 Weight of graphite grease added to test gears .....	147
Table 5.1 Predicted contact and bending stresses, actual wear rates subjected to axial gap .....	161
Table 5.2 Predicted variation in parameters and actual wear rates due to axial deviations .....	176
Table 5.3 Variation in actual wear rates due to pitch misalignment .....	197
Table 6.1 Step load tests: wear rate, bulk and airflow temperature at speed of 500 rpm .....	231
Table 6.2 Step load tests: wear rate, bulk and airflow temperature at speed of 1000 rpm .....	231



Table 6.3 Step load tests: wear rate, bulk and airflow temperature at speed of 1500 rpm .....	232
Table 6.4 Step load tests: wear rate, bulk and airflow temperature at speed of 2000 rpm .....	232
Table 6.5 Stable wear rate and corresponding bulk and airflow temperatures .....	234
Table 6.6 Unstable wear rate and corresponding bulk and airflow temperatures..	235
Table 6.7 Variations of mechanical properties of acetal due to temperature rise (BS 6168 [13]) .....	239
Table 6.8 Thermal properties of test polyacetal gears [9] .....	239
Table 6.9 Air flow temperature and velocity measurements at locations close and vertical to the meshed tooth of gears as in Figure 6.33 .....	245
Table 6.10 Air flow temperature and velocity measurements at locations close and parallel to the tangential velocity of rotating gears as in Figure 6.33 .....	246
Table 6.11 Air flow temperature and velocity measurements at locations close and parallel to the tangential velocity of rotating gears as in Figure 6.33 .....	246
Table 6.12 Air flow temperature and velocity measurements at locations close and parallel to the tangential velocity of rotating gears as in Figure 6.33 .....	246
Table 6.13 Air flow temperature and velocity measurements locations close and vertical to the gear blank (same direction as thoes in Table 6.9 ) as in Figure 6.33 .....	246
Table A.1 Material properties of test polyacetal gear samples [9] .....	278

# Declaration

I declare that this thesis is my own work, under the supervision of Dr. Ken Mao and Professor Derek G. Chetwynd in the School of Engineering, University of Warwick between the dates of Oct. 2013 and Oct. 2017.

Information derived from the published or unpublished work of others has been acknowledged in the text and a list of references is given.

This thesis has not been submitted in any form for another degree or diploma at any university or other institution of tertiary education.

## Publications

Z. Hu; K. Mao; An investigation of misalignment effects on the performance of acetal gears, Tribology International, vol.116, pp. 394-402, 2017.

K. Mao, P. Langlois, Z. Hu, K. Alharbi, X. Xu, M. Milson, W. Li, C.J. Hooke, D. Chetwynd; The wear and thermal mechanical contact behaviour of machine cut polymer gears, Wear, Article|Proceedings Paper vol.332, pp.822-826, May-Jun 2015.

# Acknowledgments

First of all, I would like to thank my supervisors, Dr. Ken Mao and Professor Derek G. Chetwynd for many valuable and stimulating scientific discussions, their strong support and patience during the work conducted for this thesis and their guidance through the British university system.

I would like to express my deepest gratitude to Professor Andre van Vee, Dr. Xianping Liu, and Professor Critoph Bob for counselling my research activities in their limited spare time and encouragement through studies and livings in the last four years.

I would like to express my sincere appreciation to Professor David Towers, Professor Tim Ashley and Kerrie Hatton, who have supported and encouraged me to concentrate on research work and to be in good spirits.

The following people deserve my sincere thanks for their expertise and assistance in performing experimental equipment and analysis: Mr. Martin Davis, Mr. Martin Milson, Mr. Roger Thorpe, Mr. Graham canham, Mr. Huw Edwards, Mr. William Higgins, Mr. Lee Davis, Mr. Adrian Seymour, Mr. Ian Griffith and all the technicians who have ever helped me.

I also would like to thank my friends and colleague: Mr. Hua Kong, Miss. Yuxin Xing, Dr. Ehsan Torabi, Dr. Oluyemi Jeged, Dr. Bashir Jimoh, Dr. Mohammad Salami, Mr. Joseph Lacey, Dr. Zhongnan Wang, Dr. Hui Niu, Dr. Xinyao Zhu, Mr. Ye Zhang, Mr. Yulin Zhou, and many more for their warm hearted assistance, advice and care.

## Acknowledgments

Last, but not least, I would like to express my heartfelt gratitude to my family (mother, sisters and brother) for their constant love, patience and reassurance during all my life and especially in the last years.

# Abstract

Numerous concepts, national and commercial design standards developed and proved for metallic gears, now are being migrated over to polymer gears. However, it is uncertain whether the same procedures should apply and there is only limited data available to attempt a validation. Since wide mechanical and thermal properties' discrepancies exist between metals and polymers, it is essential to develop and establish their individual investigation methods and science of design.

The work presented in this thesis endeavours to bridge this gap between practical application and theory, through exploring advances in fundamental experimental investigation approaches and providing effective test data. New studies on wear and failure mechanisms, in addition to adopting the prevailing methods (i.e. SEM examining worn tooth surfaces), and inspecting wear debris are proposed and employed. Schemes are proposed for measuring the temperatures and velocities in the airflow surrounding the operating gears and gear bulk temperatures. Their use adds to the work for predicting surface temperatures of polymer gears. Deliberate misalignment is introduced to investigate.

Wear and failure mechanisms of polyacetal gears at various loads and a speed of 1000 rpm are studied. Various regimes of wear debris and topographies of worn tooth surfaces are presented. The dynamic evolutions of wear, wear rate and the temperatures of airflow and the tooth body (bulk) are presented. It is found that transition temperatures are more reliable for assessing the gear wear compared to transition torques.

Gross misalignment effects on the performance of polyacetal gears are investigated. Strikingly distinct topographies of worn tooth surfaces and regimes of wear debris are presented. It is indicated that polyacetal gears are most sensitive to pitch misalignment. Micro-cracks are noted near pitch points and tooth roots.

Aerodynamic characteristics of operating gears are studied and an improved model is proposed. On the basis of it, methods for improving the durability of polyacetal gears are proposed.

Further investigations on aerodynamics, thermal-mechanism and misalignment are recommended to gain a better temperature and wear prediction, and understanding of misalignment.

# Chapter 1

## Introduction

### 1.1 Overview and challenges

In various transmission systems, flat belts and timing belts have efficiencies typically in range from 50% to upper 90%, v belts have efficiencies that may dip much lower, but gears have a reasonably high efficiency, with merely approximately 1% to 2% power loss in a pair of meshed gears [1]. Geared systems (gear trains) can change the torque, speed and direction of a power input. Other significant mechanical advantages of gears in transmission are that they can work in a compact volume, offer high motion accuracy, high power output and no slippage (slippage happens in belt and pulley transmission systems). These advantages over systems including chains and pulleys, make gears being indispensable elements in power transmission systems.

The development of gears has a long history [2, 3]. For example, in China, the earliest gear applications can date from the 4th century BC, with (wooden) differential gears seen in south pointing chariot and geared mechanical clocks. In Europe, one of the earliest examples of a geared device is preserved in the Antikythera mechanism, which may date to between 150 BC and 100 BC, and is designed to predict astronomical positions and eclipses for calendars and so on. In 26<sup>th</sup> century BC, in Egypt

the earliest example of the geared parts is for a water-lifting device.

Since the 1850s, the art of gearing technology has blossomed, with the gear rating and lubrication theories, contact stress (Heinrich Hertz, 1882) and bending stress (Wilfred Lewis, 1893), elastohydrodynamic lubrication (EHL, 1949) pushing metallic gears to high performance and high power transmission levels [1]. So far the technology of metallic gears has now reached a level of maturity. Metallic gears, as power transmission components, are widely used in various industry areas over centuries, such as automobiles, automation, aircraft, and spacecraft and many more.

In contrast, polymer gears emerged relatively recently and were broadly used in the 1960s in small sizes and low power levels for applications, such as water, electricity and gas meter counters, toys, clocks, watches and washing machine timers. However the emergence in recent years of various new (polymer) materials, such as acetal, polyphenylene sulphide (PPS), polycarbonate (PC), PEEK, carbon or glass fibre reinforced nylon or PEEK composites, and with PTFE Graphite as a self-lubricant, has led to a rapid growth in the size and power of polymer gears. For instance, the polymer bevel gears in washing machines are now typically 381 mm or more in size, 1.5 kW in power level [4]. Figure 1.1 illustrates the complexity of various applications and performance of polymers. The ongoing quest for low cost, light weight, reduced noise and vibration levels, lubricant-free reliability and resistance to corrosion has driven the advancement of the science of plastic gear design and manufacture. The use of polymer gears has greatly increased in industries and engineering applications, especially



in home products, textiles, office equipment, food industries and automobiles.

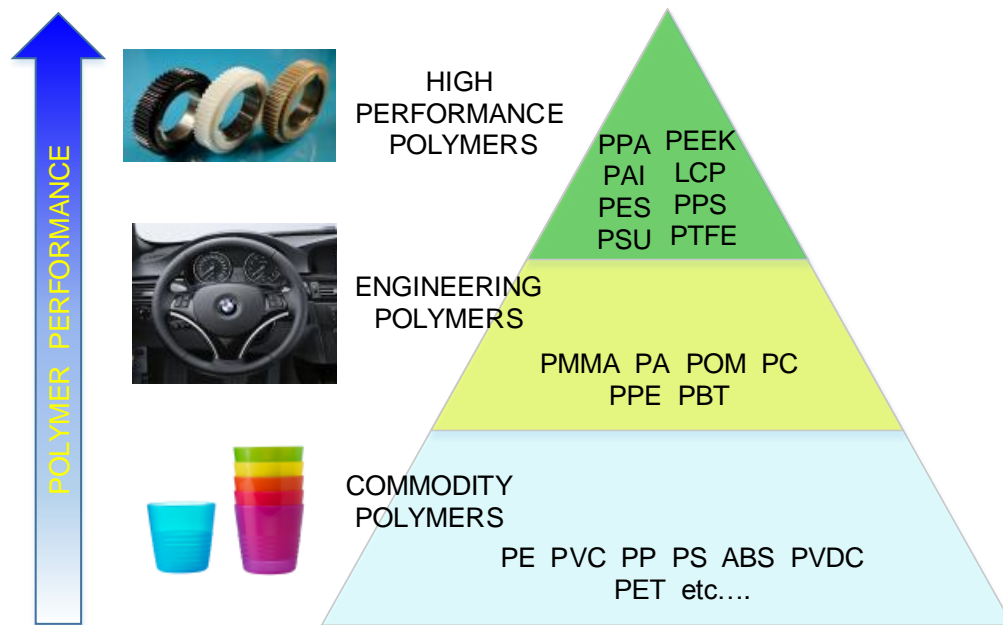


Figure 1.1 The pyramid of polymer performance (after [5])

Compared with metallic gears, polymer/composite gears have unique performance and economic advantages which the metallic ones cannot achieve [5-9]:

- Low cost, high volume manufacture of gear products by injection moulding;
- Low density leading to low weight (lighter than steel counterparts), reduced energy consumption, lower moment of inertia and improved responsiveness;
- Quiet operation and reduced vibration level;
- Low coefficient of friction and in many situations, low wear;
- Less or no need for lubrication, crucial in applications such as food processing and medical equipment;

- Corrosion resistance enhancing lifetime and service intervals;
- Chemicals and oil resistance enabling possible uses in challenging environments; etc.
- Extended complex and intricate design options, e.g. customer oriented shapes (geometry, integrated parts), colours (improving the aesthetics).

Moreover, thermoplastic gears are recyclable materials (allowing to be re-melted and reshaped) which greatly reduces the resource demands, waste and environmental pollution.

However, they are also restricted in several respects, principally,

- Lower power transmission than that of similar size of metallic gears (low tensile modulus and strength as shown in Table 1.1);
- Low allowable operating/contacting temperature (see the melting temperature and thermal conductivity in Table 1.1);
- Poorer dimensional stability due to relatively high shrinkage, thermal expansion, creep or perhaps absorbing moisture in materials, such as nylon.

In fact, the majority of mechanical properties of polymers depend highly on temperature, tending to deteriorate as temperature rises. For instance, elasticity modulus, tensile strength and stiffness tend to reduce as the temperature increases. Because of the low thermal conductivity, heat energy generated by the friction and hysteresis in engaging polymer gears is mainly accumulated on the gear tooth bodies, only marginal heat is

dissipated by thermal conduction and subsequently the operating temperature elevates rapidly. Over cyclic periods, consequently, the mechanical properties of gear tooth bodies deteriorate, or even melt and flow, due to excessive accumulated heat. This concern tends to become markedly significant when plastic gears are under conditions of high speed, high load or both.

Table 1.1 Examples of material properties of polymers and metals [9-11]

Material properties	Acetal	Nylon 46	PEEK 450G	PC	Low carbon steel	Stainless steel
Tensile modulus (GPa)	2.8	3.3	3.5	2-2.4	183-213	77-317
Tensile strength (MPa)	67	100	100	72.4	140-2400	42.4-2500
Flexural modulus (MPa)	2758	3000	4000	2410	2586	-
Flexural strength (MPa)	82.74	-	165	89.6	103	862-938
Poisson's ratio	0.38	0.37	0.4	0.37	0.25-0.3	0.27-0.3
Specific heat (kJ/kg/K)	1.5	2.1	2.2	1.2-1.3	0.45-0.486	0.2-0.62
Thermal conductivity (W/m/K)	0.23-0.31	0.3	0.25-0.32	0.19-0.22	25.3-93	2.02-34.3
Coefficient of linear thermal expansion ( $10^{-6}/K$ )	110	73	45	70.2	10.5-16	9.36-16.9
Heat deflection temperature ( $^{\circ}C$ )	110	190	152	128-138	-	-
Melting temperature ( $^{\circ}C$ )	165	295	343	225	1480-1526	1375-1450

Several authors attempted to estimate the gear surface/bulk temperature. However, the existing gear bulk temperature predictions still require to be further studied and verified by experimental data. For instance, Hachman and Strickle's equation assumed that a lubricant does not

contribute significantly to the heat transfer and ignored hysteresis losses (see Chapter 2 for detail). This is not the case when gears are continuously lubricated with oil. Garvin *et al.*'s equation are complicated and inconvenient to practically use [12]. Also Garvin's equation is limited for steel against polymer gear pairs. Mao's equation assumed that all the heat was generated by sliding friction and that it was fully transferred to ambient environment air (see Chapter 2 for detail). However, the assumption does not closely match many real situations. Various standards such as BS 6168:1987 [13] and VDI 2736:2014 [14] adopted the Hachman and Strickle's equation with some modifications. However, few studies are to be found that directly address the subject of the relationship of wear/wear rate and corresponding temperature evolutions. Therefore, it is vital to find means to accurately predict the contact/operating temperature of polymer gears and the related wear/wear rate during motion prior to design and practical application.

A degree of misalignment is inevitable for meshing gear pairs due to elastic deformation, manufacturing error, tolerances when assembling gears and shafts and many more [15]. Compared to metals, polymers have inferior mechanical properties, such as moduli of elasticity (approximately reduced by a factor of a hundred and perhaps further reduce by a rise in temperature), thermal conductivities (reduced by around 2 orders of magnitude) and softening/melting temperatures but they have a higher thermal expansion coefficient. Consequently polymer gears are more flexible than their metallic counterparts. However, almost no literature has been found on the subject of non-metallic gears meshed under misaligned conditions although in-depth studies have been performed on metallic gears.

There is only some work on transmission errors of plastic gears, investigated in simulation by Tsai [16] and Meuleman *et al.* [17]. Thus it is essential to investigate the effects of misalignment on polymer gears.

There are a few fault detection or diagnostic approaches for metallic gears, such as wear particles and vibration. However, almost no studies are to be found on this subject for non-metallic gears. However, Cropper considered the various regimes of wear debris when analysing the wear mechanism of non-metallic gears [18]. Hooke and Mao just mentioned the debris, noting what was visible by naked eye but without more detail (i.e. by means of scanning electron microscope and optical microscope) [7, 19-21]. Hence the nature of wear debris needs more attention.

There would be important impacts on automotive and aerospace engineering if polymer/composite gears could be used in high power transmission and challenging environments such as engines and satellite. But the main limitations to their application are still a very incomplete understanding of:

- Their wear and failure mechanisms;
- Their performance under relative high load and speed conditions;
- Their sliding-rolling dynamic contact;
- Their complex thermal-mechanical behaviour;
- The effects of misalignment on the wear behaviour of non-metallic gears.

## 1.2 Objectives and strategies

The long-term aim for this current work is to contribute practical insights about measurement and behaviour of polymer gears, in order to increase their range of safe applicability. To this end, its specific objectives are:

- To investigate the wear and failure mechanisms of polyacetal gears under nominally aligned and known deliberately misaligned conditions;
- To investigate the complex thermal-mechanical contact behaviour of polyacetal gears under nominally aligned conditions;
- To explore approaches to investigate the aerodynamic characteristics of polymer gears for the future work of establishing an improved forced air convection of heat dissipation model.

A current existing novel non-metallic gear test rig was exploited to investigate the research questions posed above. Nominally aligned and known misaligned configurations tests were performed on this test rig. Moreover it measures the wear of gears' contact surfaces continuously during operating. A non-contact Hall-effect displacement transducer was designed and made to measure the gear wear. A bespoke data logging software was developed to monitor and record the gear wear as a function of time. Of course, various experimental parameters and conditions were also recorded (see Chapter 3).

To understand the wear and failure mechanism, the respective mass

and profile of tooth flanks of the test gears were weighed (high precision balance, 0.1 mg) and scanned (Bruker, non-contact ContourGT 3D optical profiler) before and after testing. The worn tooth surfaces were examined (i.e. wear marks, pitting, micro cracks, fracture pattern, and melt/plastic flow) by dint of an advanced high resolution scanning electron microscope (SEM). Various features of wear debris in varying wear phases (i.e. bed-in wear phase, steady wear phase) were collected and examined by means of an optical microscope (Olympus with a x10 objective and oblique with white light illumination).

To explore the complicated thermomechanical contact behaviour, the evolutions of wear/wear rate, bulk temperature (FLIR SC660, Infrared video camera) and temperature of airflow surrounding gears (K-type thermocouples) at various loads and a speed of 1000 rpm, under nominally aligned configurations, were obtained through tests and analysed (see Chapter 6). Interpretation also considered the topographies of worn tooth surfaces and regimes of wear debris. Prospective estimation methods of the wear rate relating to bulk temperature were proposed.

Concerning the experimental investigations of polyacetal gears mesh misalignment, a set of tests will be carried out in terms of four categories of misalignment (i.e. axial, radial, yaw and pitch misalignment) at a load of approximately 7.2 N·m and a speed of 1000 rpm. Wear and wear rate, topographies of worn tooth surfaces and regimes of wear debris were compared with those obtained under aligned conditions.

With respect to the studies of aerodynamic characteristics of the

running gear pairs, two hot-wire anemometers (AIRFLOW™ TA5) were employed to measure the velocity and temperature of airflow in interesting regions around the running gears, such as where there is most exchange of heat energy through actions similar to spur gear pumps and piston effects on air trapped between teeth. Coupling the airflow measurement results by thermocouples and published computer fluid dynamics (CFD) outcomes of gear pumps (from other authors), a fundamental aerodynamic model of engaging gears was sought (see Section 6.5). This data is prospectively to be exploited for establishing improved forced air convection model and hence for heat dissipation and bulk temperature assessments. Base on the aerodynamic characteristics, ways of improved load capacity or durability of polyacetal gears were proposed.

### **1.3 Thesis structure**

After this short introduction, Chapter 2 principally review the relevant historical context and recent existing international plastic gear rating standards, wear and failure modes, theories and experiments upon heat generation and dissipation, turbulent statistics and windage power losses of external gear pumps, temperature predictions, plastic gear durability improvements, thermal-wear performance and fault detection in fashion for metallic gears.

Chapter 3 then introduces the primary experimental facilities and the designs of measurement systems which assist in fulfilling the experimental investigations of this thesis. A wear measurement system is designed to



measure the gear wear during running. Gear tooth body temperature is measured by means of an infrared camera. An airflow temperature measurement system is designed in order to measure the temperature of airflow surrounding the running gears. Two miniature anemometers (AIRFLOW™ TA5) are utilised to identify aerodynamic characteristics of running gears and possible regions of heat energy exchange. The advanced SEM (XL30ESEM) and OM (optical microscope) are exploited to examine the worn tooth surfaces and wear debris. The tooth flank profiles are assessed using a non-contact ContourGT 3D optical profiler (Bruker). A vibration measurement system is designed to use as a quick means (an auxiliary technology) to monitor the degree of wear or operating conditions (misalignment), especially for future work.

The use of these systems is reported in the next three chapters. First, in Chapter 4, the wear/failure mechanism of polyacetal gears are investigated involving short-period tests and endurance tests. The effects of wear debris on wear are studied. Graphite paste lubricant is introduced to bring away the wear debris from the meshing tooth surfaces. Incremental step-load tests are carried out respectively at speeds of 500, 1000, 1500 and 2000 rpm. Then in Chapter 5, the effects of four categories of deliberately introduced misalignment on polyacetal gears are investigated. In addition to wear rate, the wear mechanism of the misaligned gears is also examined by means of optical and scanning electron microscopes (OM and SEM). Last, in Chapter 6, the airflow temperature and bulk temperature are measured during motion to study the evolutions of wear, wear rate, airflow and bulk temperatures, and the aerodynamic characteristics of meshing gears. On the

basis of the measurements, actions for improving gear durability are proposed.

Finally conclusions and recommendations are shown in Chapter 7.

## Chapter 2

## Literature Review

### 2.1 Designs for non-metallic gears

The design standards for metallic gears are very well developed. In terms of practical applications, the design can be assessed by a few factors, such as strength (bending fatigue) calculating tooth beam tensile stress (Lewis equation), scuffing being linked to critical temperature theory (flash temperature) and durability (surface contact fatigue, such as pitting and spalling) by calculating contact stress (Hertz contact stress).

However, the designs for non-metallic gears (i.e. McKinlay: 1976, ESDU:1977, Polypenco:1985 and BS 6168:1987, VDI 2736:2014) are less developed because they are derived from those for metallic gears with some modifications [7, 13, 14, 22]. For example, they add gear body and flash temperature estimation and limits. Their designs' validation remains to be fully justified by practical experimental data. Also they only include a limited number of materials, such as acetal (POM), nylon (PA) and PET. However, there are numerous categories of plausible polymeric materials and their properties vary greatly. Of course, striking discrepancies exist between metal and polymer/polymer composite material properties, such as Young's modulus, thermal conductivity and melting point. The majority of the mechanical properties of polymeric materials depend strongly on gear

operating temperature.

## 2.2 Wear mechanism

This section generally follows the excellent treatment in the book by Straffelini (Friction and Wear) [23].

Wear is damage to a surface in contact and relative motion with another, resulting in the formation of debris (or fragments) that leave the tribological system. The consequences of wear can include reduced tolerances and poorer surface finish, with such surface damage responsible for the subsequent failure of the component (most often by fatigue) or direct failure such as fracture. The wear processes are defined by the characteristic of the relative motion between the two bodies in contact. There are various wear processes and typical ones are as follows.

Sliding wear is the resulting wear process of the bodies' sliding one over the other. Rolling wear is the resulting wear process when they roll one over the other. A rolling-sliding wear is attained if the two sorts of motion are superimposed which is the normal kinematic condition for spur gears. Fretting is the name for the specific wear process when reciprocating sliding is present with very small displacement. When one of the two bodies includes in one or more hard particles that abrade a softer surface, the wear is called abrasion (by hard, granular material). If a fluid carries such abrading particles, the wear is called erosion. Corrosive wear is the resulting wear process if there are chemical or electrochemical reactions.

### **2.2.1 Categories of principal wear mechanism**

Although there are numerous wear processes present in practice, four wear mechanisms are predominant in gear systems: adhesive wear, abrasive wear, tribo-oxidative wear and wear by contact fatigue.

- **Adhesive Wear**

Adhesive wear occurs when the adhesion forces between the contacting asperities play a leading role in the formation of wear debris (fragments). The study of adhesive wear is beneficial especially to distinguish between wear of ductile materials (i.e. the majority of metals and polymers above their glass transition temperature) and wear of brittle materials (i.e. ceramics and polymers below their glass transition temperature).

- **Abrasive wear**

Abrasive interactions can be divided into two categories: two-body and three-body abrasions. If a hard protuberance or a hard particle plastically penetrates a softer counterface and groove it, it is the two-body case. Abrasive hard particles may be embedded in the material microstructure such as in glass-reinforced composites and in grinding wheels where the particles are held together by a specific bonding system, or may come from the surrounding environment. If the hard particles trapped between two contacting surfaces are quite free to rotate/move and their action is thus limited, this is the three-body abrasion case. In any case, abrasive wear can happen only if the hardness of the hard particles is 20%

above that of the weakest surface.

- **Tribo-oxidative wear**

Tribo-oxidative wear results from the interaction of the surfaces with an environment containing oxygen. Tribo-oxidative wear is thus induced by a mixture of oxidative and mechanical actions at the contacting asperities. It is generally accompanied by the formation of a surface oxide scale.

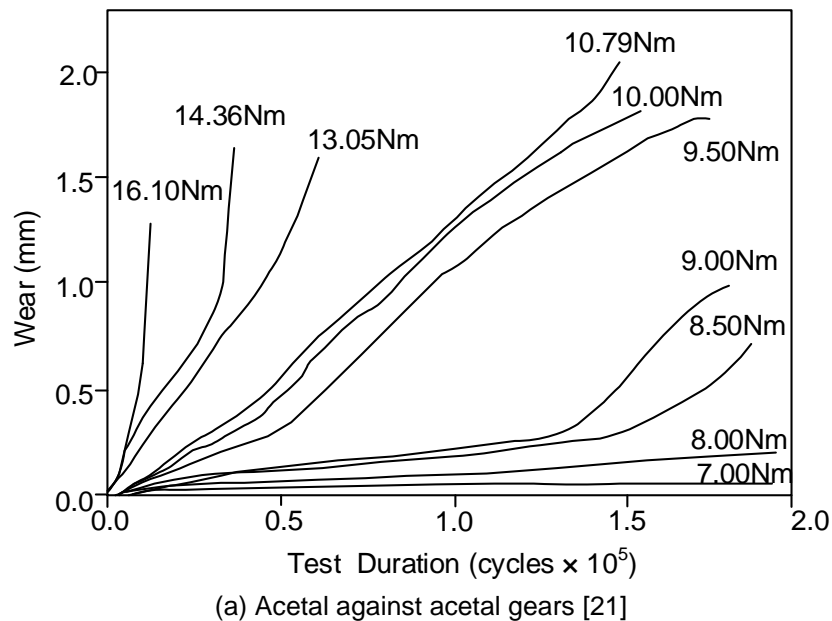
- **Wear by contact fatigue**

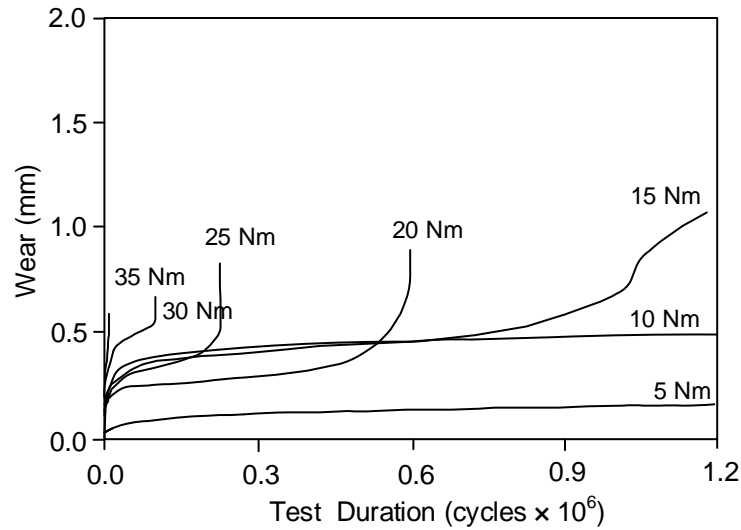
Most wear mechanisms are progressive in nature: the material removal initiates once the contact occurs and it continues fairly steadily with time. These pattern will be affected by large plastic deformations, which are common characteristics of the contact phenomena. On the other hand, wear by contact fatigue is a typical fatigue failure: under cyclic loading, a crack is nucleated and then it propagates up to the final fracture. A wear fragment is produced after some number of cycles that relates to the fatigue life of the loaded part. In the majority of events, wear by contact fatigue occurs in non-conformal contacts and in such cases this wear mechanism is also called rolling contact fatigue (RCF). Wear is induced by the cyclic contact Hertzian stresses and is influenced by many factors: contact stresses, sliding, material properties (i.e. microstructural cleanliness, mechanical strength, and fracture toughness), residual stresses and lubrication regime.

With gears, the wear process is governed by sliding-rolling motion, and the predominant wear mechanisms are contact fatigue, adhesion or tribo-oxidation in dry conditions.

### 2.2.2 Wear curves

The total wear volume increases with sliding distance during sliding between two contacting bodies. In general, there are three stages, each with the typical trends. First is the running in (run-in or break-in) stage, where the period is short for dry sliding and the wear rate is usually quite high because surfaces in contact are wearing to remove the asperity peaks. Then, it enters a steady state stage, is the main stage of the tribological process. The wear rate is usually lower than during run-in and it lasts up to the end of the useful component life. However, in some situations a wear transition may take place after some sliding distance when the wear rate may increase or decrease. This transition is led by a change in the wear mechanisms, often accompanied by a change in temperature, friction coefficient or both. Examples of wear curves are shown in Figure 2.1.





(b) Composite against Composite gears [24]  
Figure 2.1 Wear curves of non-metallic gears

## 2.3 Failure modes of polymeric gears

For polymeric gears, the failure modes are mainly wear, pitting, fracture, scuffing and plastic flow [7, 18, 25].

Pitting as shown in Figure 2.2, is a fatigue phenomenon arising in the motion that combines sliding and rolling actions. It is very common for bearing and gears. The formation mechanism of pitting is cyclic surface contact stresses that exceed the material endurance limit.

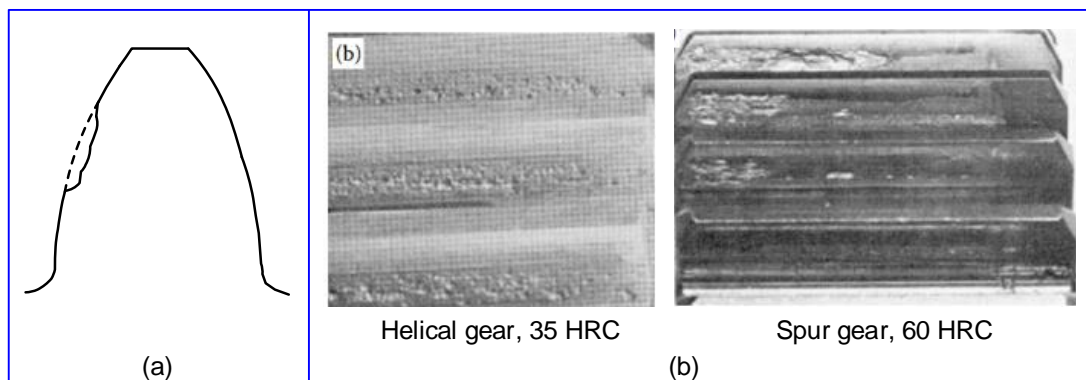


Figure 2.2 Pitting: (a) Pitting form of plastic gears (after [26]), (b) Photographs of pitting on iron gear teeth (after [2])



Fracture as shown in Figure 2.3, may take place at tooth root or pitch line due to fatigue and overload. Fracture at the tooth root or pitch line will depend on material properties, which for polymeric gears can vary quite widely and are importantly temperature dependent.

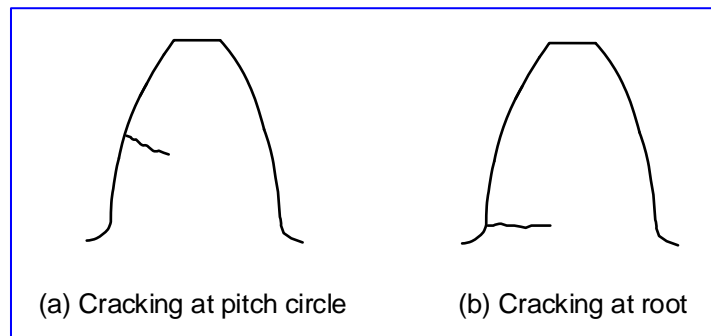


Figure 2.3 Fracture forms of plastic gears (after [26])

Scuffing is normally caused by local excessive heat, as the surface material is removed rapidly by welding and tearing. It is associated with flash temperatures. With polymer gears, high loads are likely to induce scuffing. An example of scuffing wear on metal gear tooth is shown in Figure 2.4.

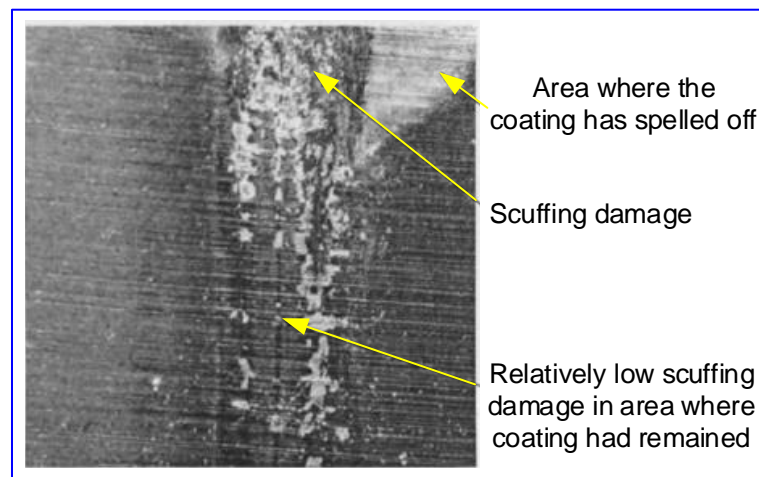


Figure 2.4 Photograph of a case carburised metal gear with Me-DLC coating following scuffing (after [27])

Plastic flow results from high contact stress and relative sliding motion, where the contact area material has been thermally softened. Peening,

rippling and ridging are also forms of plastic flow. The examples of plastic flow of polyacetal gears are described in detail in Section 4.2.2.3 (see Figure 4.17: SEM micrograph of plastic flow on polyacetal gear)

Marshek and Chan revealed that pitting and ridging are major contact surface damage for phenolic and polyacetal worm gears [28]. Terashima *et al.* found that abnormal wear frequently resulted in tooth fracture near the pitch point of (machining, Hobbed, improved) 6-nylon gear (S45C steel gear against 6-nylon pinion) [29]. Senthilvelan and Gnanamoorthy found that the failure of injection molded unreinforced, carbon reinforced and glass reinforced Nylon 66 gears was usually due to fracture near the tooth root [30]. Fracture near the tooth root also occurs to composite gears (55% nylon, 30% glass fiber and 15% PTFE) [7]. Tooth breakage under fatigue mostly arises from bending stress [31]. Pogacnik and Tavacr found that acetal (Acetal 500P, DuPont) and Nylon 6 gears failed by fatigue and sudden melting [32]. The melting failure took place within a few hours of the gear test being initiated. Mao proposed solutions to reduce gear fatigue wear through a micro-geometry modification approach, such as face-width crowning, lead correction and tip relief [33].

## 2.4 Thermal-mechanical behaviour

Surface temperature can indicate or reveal critical information on the conditions of operating gears. Thermal cycling causes microscopic changes in the internal structures of materials and the cyclic cumulative changes consequently result in cracks on gear surfaces. Many thermal-mechanical

wear behaviours of metallic gears have been investigated [34-46], in terms of the temperature of gears or their lubricant oil affect life, the quality of the lubrication film, pitting, cracking, spalling, scoring, scuffing and so on. Polymeric gears are significantly more susceptible to surface temperature than are metallic gears. Therefore, the thermal behaviour of non-metallic gears is being studied by numerous researchers via experiments and theories. For instance, Yousef and Burns built test rig and IR microscope to assess the running temperature and fatigue strength of lubricated acetal and polycarbonate gears [47]. Gauvin, Patrick and Henry used an infrared radiometer to measure the temperature distribution along the tooth contact profile of hob cut Nylon 66, acetal and UHMWPE (Ultra High Molecular Weight Polyethylene) gears and adopted statistical analysis of test results to predict the maximum operating temperature [12, 48]. Hooke, Mao, Walton Breeds and Kukureka measured the operating temperature of plastic gears (such as acetal, Nylon 66, PEEK and glass reinforced Nylon 66 composite gears) by using infrared camera video camera [7, 21, 24, 49-53]. They reported that for acetal gears there was a sharp rise in wear as transmitted torque was increased and proposed that the wear transition was effectively associated with acetal elting point. Based on the experimental results, they predicted the body and flash temperature by using a finite element method. Melick and Dijk studied the fatigue lifetime of Stanyl polyimide (Nylon 46) gears running in oil lubricant at 140°C and made correcting for tooth bending and calculating actual root stresses [54]. Terashima *et al.* measured the operating temperature of pairs of a hob improved 6-nylon gear running against a S45C steel gear by using three thermos-paints and estimated the

temperature distribution on tooth flank [29]. Karimpour, Dearn and Walton investigated into the contact behaviour of Delrin<sup>®</sup> 500 (Du Pont) gear transmissions using numerical finite element and considering the operating temperature effects on the properties of polymeric materials [55]. A rise in operating temperature results in a reduction in the mesh stiffness, which affects load sharing ratio due to tooth bending. Hoskins, Dearn, Chen and Kukureka studied the wear mechanism of poly-ether-ether-ketone (PEEK) running against itself in non-conformal, unlubricated rolling-sliding contact over a range of loads and slip-ratios by employing a twin-disc test rig [56]. Test results indicate that a rapid increase in the coefficient of friction is due to the temperature exceeding the glass transition temperature of the material, which affects the friction and wear. The test results were suggested to be in conjunction with the designs of more effective and highly loaded polymeric gear systems. Walton and Shi compared ratings of plastic gears and stressed the influence of body and surface temperatures on the properties of polymeric material [26]. Singh and Singh measured the wear and surface temperature of polymeric gears (i.e. ABS, HDPE and POM gears) running against metal (AISI 1040) gears and presented specific wear rate and surface temperature rise at various loads and speeds [57]. However no dynamic relationships between wear rate and surface temperature of polymeric gears are presented. The surface temperature prediction and the relationships between operating temperatures, wear, wear rate, load and speed still need to be explored deeply in the hope of establishing reliable and predicted design standards or references.

The developments of understanding of heat sources, heat

dissipations, temperature estimations and known achievements on thermal experimental investigations will be outlined in following sections.

### 2.4.1 Heat sources

Prior to introducing the mechanisms for heat generation and dissipation of gears, it is useful to briefly review the contact mechanism of involute spur gears.

With respect to involute profiles of gears, a pair of rigid mating teeth contact is non-conformal or counter-formal, namely with a nominal line contact [58]. With plastic gears, the non-conformal line contact may evolve, however, due to their low Young's modulus, high contact loads or high ambient temperature, into a significant area contact over the non-conformal gear teeth. The motion between non-conformal contacting teeth is a mixture of slide and roll, apart from at the pitch point where it is pure rolling (no slide). Moreover, the slip ratio (i.e. the ratio of sliding velocity to the average rolling velocity) varies throughout a meshing cycle. The sliding direction varies in terms of entering or leaving mesh for the driving and driven gears. More detailed description can be found in Section 4.2.2.

Clearly, the heat sources come mainly from the sliding and rolling contacts, bearings and shafts supporting the gears, and rapidly varying pressures in volume of air trapped between teeth.

In the 20<sup>th</sup> century, it was widely believed that for plastic gears the heat sources arose from sliding friction losses and hysteresis losses. For instance, in 1985, Koffi *et al.* [59] developed two heat generation models, an

exact one and a simplified one, to evaluate the heat for generic plastic against plastic and generic plastic against steel gears. The results, as shown in Figure 2.5, indicate that the heat generated by hysteresis is relatively small compared with that generated by friction. The solid line represents an acetal-acetal gear pair behaviour and the dotted line an acetal-steel one.

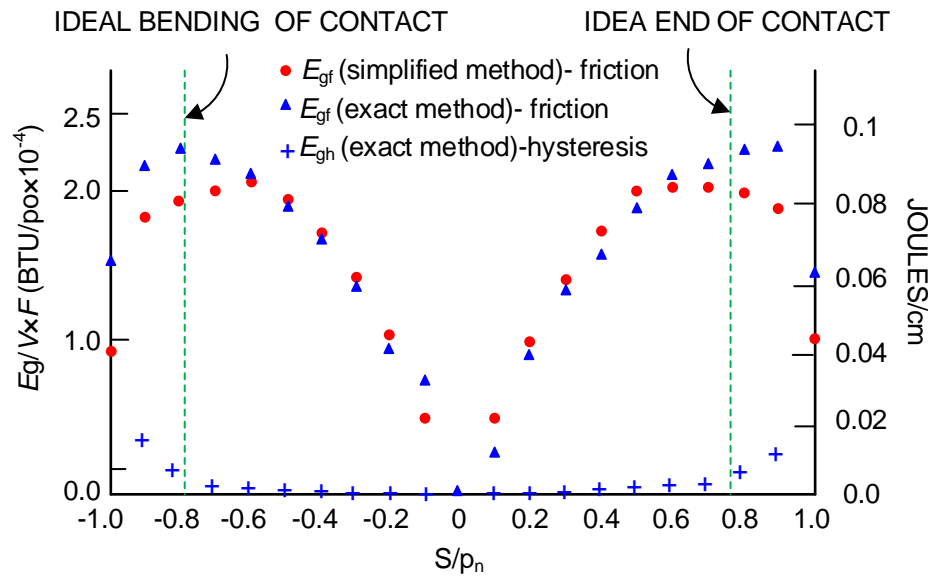


Figure 2.5 Modelling of heat generated by friction and hysteresis for plastic(acetal) gears (after [59])

In the 21<sup>st</sup> century, more heat sources have been recognized, in addition to the frictional heat and hysteresis heat. Air trapping between teeth (gears dry running) and heat conduction from the thermal behaviour of bearings also contribute to the total heat generated by plastic gears. In 2010, Letzelter *et al.* [60] identified the different aforementioned four heat sources by using a gear test bench developed by the LaMCos laboratory.

#### 2.4.1.1 Friction heat

The sliding motion generates a friction force  $F_f$  between the contacting teeth, which always opposes the local direction of sliding. The

relative sliding velocity  $V_s$  at a point P on a tooth is  $(V_1 - V_2)$ , where the suffixes represent the mating gears, such as gear and pinion. Therefore the frictional heat power is the product of  $F_f$  and  $V_s$ , namely  $F_f \times (V_1 - V_2)$ .

#### **2.4.1.2 Hysteresis heat**

Polymer gears in the cyclic rolling and sliding contact are viscoelastic materials subject to cyclic compressive, tensile and shear stresses, which results in hysteresis losses (namely, viscoelastic loss).

#### **2.4.1.3 Trapping heat**

Trapping heat is a new studies in recent work on heat generation of polymeric gears, such as the studies of nylon 6/6 cylindrical gear carried by Letzelter [60]. In one rotating cycle of gears, the meshing action of a mating teeth is very short. For instance, a pair of gears with 30 teeth and rotating at a speed of 1000 rpm, completes a meshing process (including 'approach action' and 'recess action') of a single gear tooth in about 2 ms. With more teeth or higher speed, the processes can be much shorter. In such short periods, the volume trapping between the mating teeth reduces and increases almost instantly. Therefore the almost instantaneous tooth engagement process results in the fluid (liquid or gas, i.e. oil lubricant, water or gas) trapped between the teeth suffering from compression and expansion in an extremely short time. It thus induces adiabatic heat generation. Of course, during this process, part of this heat is also brought away by the ejection of the medium between teeth.

Existing investigations on gear pump could clearly help to clarify the

above situation. For instance, Erturk *et al.* [61], Marchesse *et al.* [62], Yazdani *et al.* [63] and Al-Shibl *et al.* [64] presented the turbulent fluid characteristics of meshing gears through experiments or modelling. Diab *et al.* [65] and Houjoh *et al.* [66] provided details of variations in the velocity and pressure of the air in a tooth space during gear meshing processes, which contributes to understanding the principle of heat generation due to air trapping between teeth and the air convection process around polymer gears.

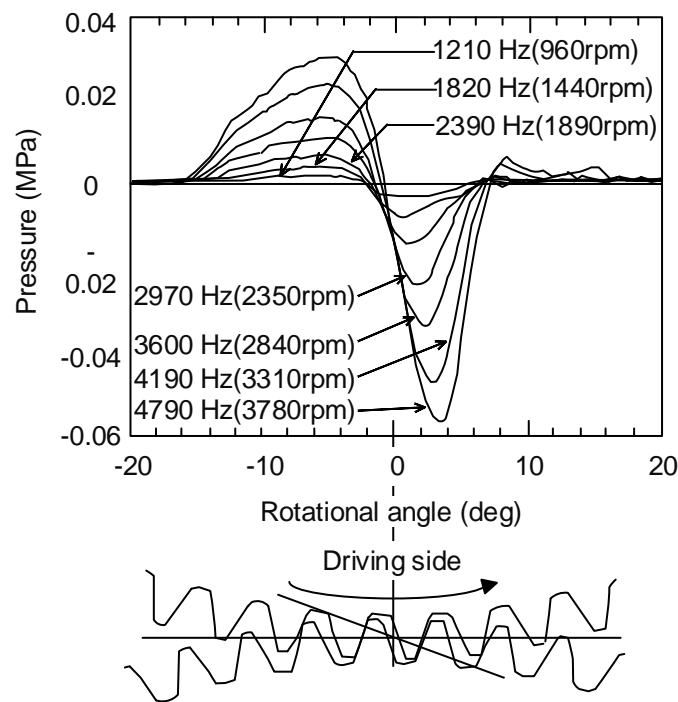


Figure 2.6 Pressure measured at the bottom space of tooth at various speeds (after [66])

Figure 2.6 shows the speed effect on the gauge pressure of air trapped between teeth in spur gear tooth bottom space. The gears' 'approach process' compresses the air resulting in high pressure, and heat will be generated during this process. The 'recess process' acts as an (air) pump due to the (measured) air pressure being much lower than ambient pressure (0 MPa). Note that the heat generated due to air trapped between



teeth will increase as rotating speed increase, as indicated in Figure 2.6. The air velocity, with air pressure, varies significantly during the meshing process as shown in Figure 2.7. Diab *et al.* [65] presented an example of the power loss due to air trapped as shown in Figure 2.8. It indicates that power loss becomes more significant at higher speeds.

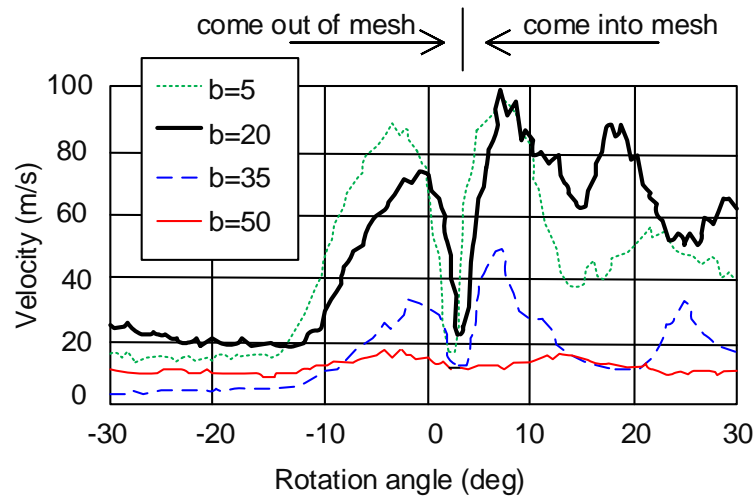


Figure 2.7 Velocity measured along axial position in gear tooth bottom space (tooth face width 100 mm) (after [66])

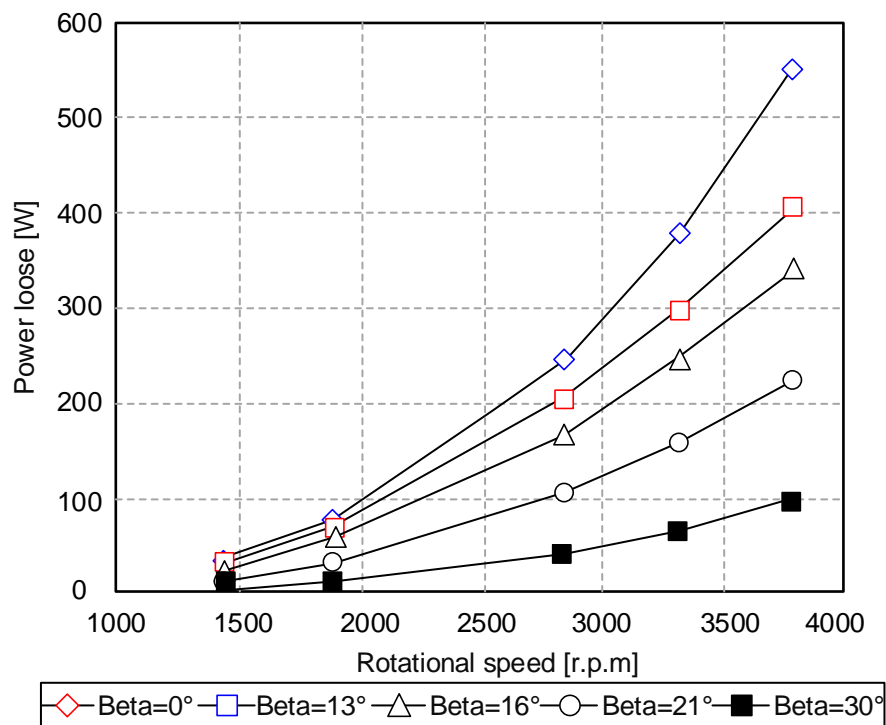


Figure 2.8 Modelling power loss due to air trapping (spur and helical gears) (after [65])

Obviously, the estimation of the heat created by trapping air and establishing an air convection model for polymer gears will become easier and time efficient if it can be based on the existing studies of gear pumps.

### **2.4.1.4 Heat conduction**

Heat energy generated in the bearings transfers through the shafts to the gear bodies [60]. This source is independent of the gear material and is regarded as a minor one in the context of the present research.

### **2.4.2 Heat dissipation**

Heat dissipation has three broad processes: thermal radiation, thermal conduction and air convection [67, 68]. Thermal conduction from the gear body to the shafts (metal shafts are common for non-metallic gears, thermal conductivity of metal is higher than polymer) [60]. The low thermal conductivity of polymers means conduction is unlikely to be a major feature in controlling temperature on tooth flanks. As with radiation: if the temperature is below 500°C, the heat dissipates mainly by radiating infrared energy; if the temperature is excessive 500°C, radiating by visible light or ultraviolet energy. Radiative energy loss (all at infra-red wavelength for body temperature below 500°C) is extremely strongly dependent on temperature. It will have a quite small effect at temperature that can be sustained on polymer gears.

Air convection includes advection (forced air convection) as meshing gears expel hot air and pump in cold air (see investigations on gear pumps

in Section 2.4.1.3), and natural convection from the diffusion of hot and cold air in gear pockets and in an envelope surrounding the gears. Air convection is likely to play the dominant role in dissipating heat from polymer gears.

### **2.4.3 Temperature prediction**

Heat accumulated on gears may result in premature failure owing to accelerated wear, scuffing, softening or plastic flow. Thus it is crucial to estimate the gear temperature preceding design and actual application. The operating/contact/maximum surface temperature of gears is governed by three components [49]:

- Ambient temperature
- Bulk /body temperature
- Flash temperature

The ambient temperature is the environmental (air) temperature, considered approximately constant. The bulk temperature is generally, fairly consistent one of a whole gear body, but for low-thermal-conductivity polymeric gears it is better take as the temperature prevailing in the bulk material of the teeth, relatively close to the contact surfaces. The flash temperature is created by frictional heat through the sliding action in the contacting region between two rubbing surfaces [69]. The flash temperature is restricted to a very thin material surface layer (5-10  $\mu\text{m}$ ) and it dissipates promptly (in a marginal fraction of a cycle) into ambient environment (i.e. air). Hence the gears' surface temperature will be approximate to gear body

temperature in the majority of each rotating cycle [49]. Studies on flash, bulk and contact/surface temperatures are reviewed in the following sections.

#### **2.4.3.1 Flash temperature**

Flash temperature is greatly significant to both metallic and non-metallic gears. For instance, flash temperature is used to assess the scuffing for metallic gears. In a nylon gear design procedure, to avoid scuffing, Housz proposed to use the flash temperature to estimate the maximum allowable load [70]. Shoji emphasized that flash temperature was used to determine working limits for polymer gears against scoring or scuffing [71].

The earliest known theoretical study on the flash temperature was performed by Blok (in 1937) [72, 73]. Jaeger [74] adopted similar study method, assuming a one-dimensional heat flow, to obtain an approximate flash temperature formula. Further studies were conducted by many authors, such as Holm [75], Bowden and Tabor [76], Archard [77] and Nakada and Hashimoto [78]. Symm [79] adopted a finite element method to study the flash temperature and partition of the heat generated between the two rubbing members. Examples of flash temperature calculation from Archard and Blok are presented briefly here:

Archard [77] calculated the temperature on the assumption that a circular contact area was considered as the source of heat that was conducted away into the bulk of the rubbing bodies. The surface temperature was derived by him in terms of heat supply rate, the size and speed of the heat source, and the material thermal properties. Concerning fast moving heat sources, the surface temperature  $\theta$  of the contact point is

$$\theta = \frac{2q\sqrt{t}}{\sqrt{\pi K \rho c}} \quad (2.1)$$

where  $q$  is the rate of heat supply per unit area and  $t$  is the time for which it has been supplied, for a fast moving contact  $q = Q_c / \pi a^2$ ,  $Q_c$  is heat supplied to body C,  $a$  is the circular radius,  $\rho$  is the density of body,  $K$  is thermal conductivity,  $c$  is the specific heat.

He also deduced the average surface temperature by considering the plastic and elastic deformation conditions, and gave the maximum attainable flash temperature (varying in terms of the speed of the heat source) under plastic deformation.

In contrast, Blok [69] derived a prevailing flash temperature  $T_{\max}$ , which could be transformed into a variety of forms in line with various contact cases, using the formula

$$T_{\max} = A \cdot \frac{q_{av}}{b} \cdot \sqrt{\frac{w}{v}} \quad (2.2)$$

where  $A$  is a form factor depending on the form of heat flux distribution,  $q_{av}$  presents the average distribution of the heat flux,  $w$  is the width of the heat source and  $v$  is its velocity,  $b$  is the square root of the product of specific heat ( $c'$ ) and the thermal conductivity ( $k$ ),  $c' = \rho \cdot c$ ,  $\rho$  denotes the density, that is  $b = \sqrt{k \cdot c'} = \sqrt{k \cdot \rho \cdot c}$ .

Regarding the maximum flash temperature  $T_{\max}$  for meshing gear teeth, he used Equation (2.2) on Hertz's theory of elastic contact to deduce that

$$T_{\max} = 1.11f \cdot W \cdot \left| \sqrt{v_1} - \sqrt{v_2} \right| / b \sqrt{w} \quad (2.3)$$

where  $f$  denotes the coefficient of friction,  $b$  is the same as that in Equation (2.2),  $W = w \cdot p_{av}$  denotes the load per unit width,  $w$  is the width of the heat source,  $p_{av}$  is the average contact pressure,  $v_1, v_2$  represent the velocity at which the conjunction area moves along the two tooth faces. Equation (2.2) holds good for the cases of engaging teeth and other non-conformal line contact such as cams, rotating-disk machines and tappets.

Clearly the assumption of Blok for calculating the flash temperature of engaging teeth is closer to the actual fact (Hertzian contact, involute gears) than that of Archard (ball contact). Note that the Blok equation has been widely adopted by various standards with modifications to assess metallic gears' scuffing.

The flash temperature and the partition of heat generated between teeth were analysed in detail by Tobe and Kato [80] and Mao [7]. Their work was conducted under the gears' typical real-life running conditions and showed that the intensity and velocity of the heat generated vary momentarily as the engaging of gears teeth proceeds. Comparisons with Blok's solution were made by Tobe and Kato which revealed that striking differences existed at a few points, such as the starting point of the mesh (values from Blok were high), but the differences got reduced as meshing point moved towards the ending mesh point. The same comparison made by Mao, as shown in Figure 2.9, reported that Bolk's results overestimated the

flash temperature by approximately 14% at the starting and ending of meshing points.

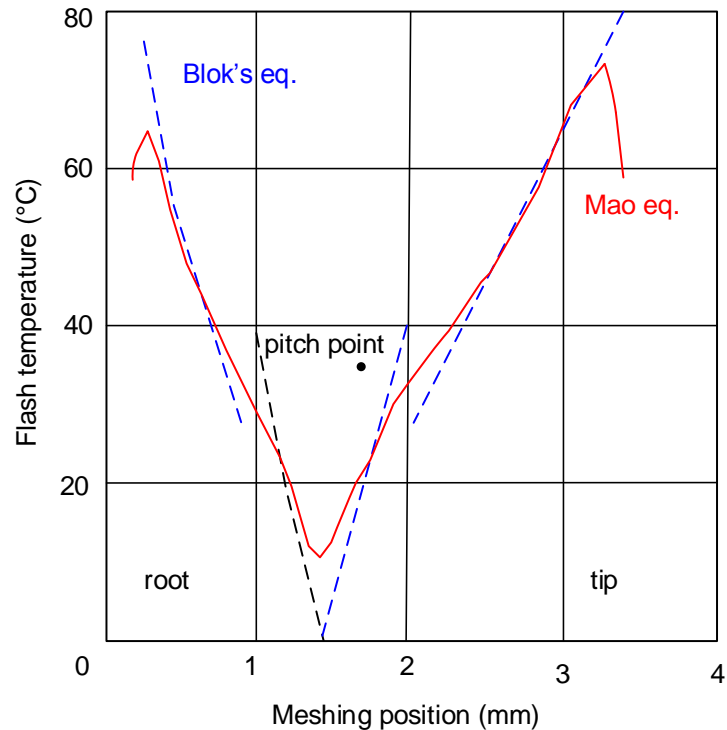


Figure 2.9 Flash temperature comparisons between Mao and Blok (after [7])

#### 2.4.3.2 Bulk temperature

Bulk temperature reflects an equilibrium between heat generation and heat dissipation during operation. The bulk temperatures are approximately constant when gears are in steady operating state. The strength and the stiffness of the gears are closely associated with the bulk temperature of teeth.

Mao [7] conveniently explores a well-known prediction of gear body and surface temperatures is predicated by Hachmann and Strickle in 1968. In their work, the heat source of nylon gears was purely frictional heat (due to sliding contact) without considering hysteresis heat. The equation is:

$$\theta_{\max 1,2} = \theta_a + P\mu \frac{i+1}{z_1 + 5i} \left[ \frac{k_2 a^{\frac{3}{4}}}{b z_{1,2} \lambda (vm)^{\frac{3}{4}}} + \frac{k_3}{A} \right] \quad (2.4)$$

where, 1 and 2 denote respectively the pinion and wheel,  $\theta_{\max 1,2}$  represents maximum surface temperature of flank or root,  $\theta_a$  is ambient temperature,  $P$  is transmitted power,  $\mu$  is coefficient of friction,  $z_1$ ,  $z_2$  is the number of driving and driven teeth,  $i = z_1/z_2$  is the gear ratio,  $b$  is the face width,  $m$  is the normal module,  $a$  is the diffusivity of the air,  $\lambda$  is the thermal conductivity of the air,  $v$  is the pitch line velocity,  $k_2$  and  $k_3$  are empirical values depending on test gears and the design of the gearbox or housing (corresponding data can be obtained from original paper),  $A$  is the area of gearbox.

Takanashi and Shoji [71] and Gauvin *et al.* [12] considered hysteresis heat and sliding friction heat and independently derived similar body temperature formulae. Gauvin's equation is

$$T_{g \max} - T_a = b_0 \cdot W_t^{b_1} \cdot V^{b_2} \cdot m^{b_3} \quad (2.5)$$

where  $(T_{g \max} - T_a)$  denotes the maximum temperature rise above ambient,  $b_0$ ,  $b_1$ ,  $b_2$  and  $b_3$  are regression coefficients calculated for each material which can be obtained from [12],  $W_t$  is tangential load per unit face width,  $V$  is the pitch line velocity,  $m$  is module. The body temperature calculated by the equation of Takanashi and Shoji and that obtained from experiments (improved 6-nylon gear running against steel gear pairs) were compared by



Terashima [29] who reported that the calculated results and experimental results agree well.

In 1977, an empirical equation for calculating the operating temperature of polymer gears under dry running condition was published by ESDU. This formula is similar to that of Gauvin, but the Lewis form factor is introduced. The ESDU equation is

$$T_b - T_a = 0.031 \cdot (W_t/Y)^{1.5} \cdot V^{2/3} \quad (2.6)$$

where  $T_b$  denotes the average temperature on the tooth surfaces,  $T_a$  means ambient temperature,  $W_t$  is tangential load per unit of face width,  $Y$  is the Lewis form factor for load applied near the middle of the tooth,  $V$  is sliding speed.

Koffi established two heat generation models: the exact one included frictional heat and hysteresis heat, while the simplified one ignored the hysteresis heat [59]. That work found that hysteresis generates marginal heat compared with the frictional heat.

The BS 6168:1987 standard supplies an operating temperature calculating equation, which is derived from the equation of Hachmann and Strickle with some modifications [13]. The operating temperature  $\theta_{1,2}$  formula from BS 6168:1987 is

$$\left. \begin{aligned} \theta_1 &= \theta_0 + \frac{136P_T\mu(1+\mu)}{z_2+5} \left[ \frac{1.71 \times 10^4 Ka}{bz_1(v\mu)^{K_M}} + \frac{7.33K_b}{A} \right] + 5.0 \\ \theta_2 &= \theta_0 + \frac{136P_T\mu(1+\mu)}{z_2+5} \left[ \frac{1.71 \times 10^4 Ka}{bz_2(v\mu)^{K_M}} + \frac{7.33K_b}{A} \right] + 5.0 \end{aligned} \right\} \quad (2.7)$$

where  $v = \pi d_i n_i / 6 \times 10^4$ ,  $i$  (1 or 2 separately) represents the pinion and wheel,  $n$  is the rotational speed,  $d$  is the reference circular diameter,  $\theta_0$  is ambient temperature,  $P_T$  is the transmission power,  $\mu$  is the coefficient of friction,  $z_{1,2}$  is the number of teeth,  $b$  is the tooth face width,  $m$  is normal module,  $A$  is the area of gear box.  $K_a, K_b, K_M, \mu$  can be obtained from BS 6168:1987.

Mao established a heat dissipation model in which gears acted effectively as a gear pump as shown in Figure 2.10 [50]. He assumed that air carried by gears was heated during each revolution and was expelled when gears come into mesh. Only a small fraction of the air stayed in gear pockets. Cold (ambient) air is sucked, or pumped into gear pockets when the gear teeth come out of mesh.

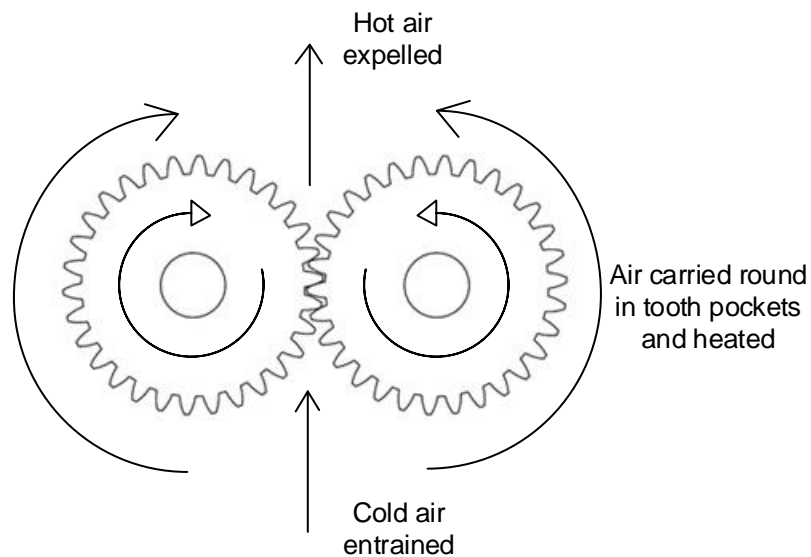


Figure 2.10 Air flow between engaging gears (after [50])

Based on this heat dissipation model, Mao made a bulk temperature prediction, ignoring thermal conduction and thermal radiation. The bulk temperature  $\theta_b$  formula is

$$\theta_b = 3.927 \mu T / c \rho N_1 b (r_a^2 - r^2) \quad (2.8)$$

where  $\mu$  is the coefficient of friction,  $T$  is transmitted torque,  $c$  is the specific heat,  $b$  is the tooth face width,  $r$  is the reference radius,  $r_a$  is the outside radius. This formula does not include the rotational speed, and it does not apply for cases running under higher speeds, such as 1500 rpm or more.

#### 2.4.3.3 Surface temperature

Many researchers working on non-metallic gears, such as Lancaster [81], Hooke [49], Mao [7] and Kono [8], reported that wear rate accelerated significantly when the contact surface temperature of acetal gear teeth got close to the melting point.

Lancaster [81] derived a formula for predicting the surface temperature of polymer plate bearings (i.e. Nylon 6.6, Polypropylene and acetal) based on two semi-infinite plate members in relative motion with the contact shape being a single asperity area of square cross section. This equation is also used for acetal gears. However Halling [82] claimed that it was not applicable for assessing gears' surface temperatures because its assumed contact model does not conform to the complex contact motion of gears, a combination of sliding and rolling actions. Mao [7] developed a gear flash temperature prediction model by means of a finite difference method. Along with the estimation of body/bulk temperature, Mao [7] derived the maximum surface temperature  $\theta_{\max}$  to be

$$\left. \begin{aligned} \theta_{\max} &= \theta_a + k_1 \cdot T + k_2 \cdot T^{3/4} \\ k_1 &= 3.927 \mu / c \rho N_1 b (r_0^2 - r^2) \\ k_2 &= 1.11 \mu \left| \sqrt{v_1} - \sqrt{v_2} \right| \cdot \sqrt[0.25]{\pi b d E' / R} / b d \sqrt{2 k \rho c} \end{aligned} \right\} \quad (2.9)$$

where  $\theta_a$  denotes the environment (ambient) temperature,  $T$  is the transmitted torque,  $\mu$  is coefficient of friction,  $c$  is the specific heat,  $\rho$  is the specific gravity,  $b$  is the tooth face width,  $r_0$  is the reference radius,  $r_a$  is the outside radius,  $v_1, v_2$  represent the sliding velocity of pinion and gear respectively,  $E'$  is the combined modulus,  $R$  is relative radius. This equation established the relationship between temperature and the contact load. It holds good for experimental temperature measurement results on spur acetal gears.

#### 2.4.4 Performance improvement

Great efforts have made by many researchers to improve load capacity and lengthen the life of polymer gears. Because plastics are temperature-sensitive materials, therefore one essential concern is to control (reduce) the operating temperature of plastic gears or, more specifically the amount of heat generation.

Basically, improvements can be achieved by three strategies. One is by adopting new materials which have better material properties. For example, adding other materials into the basic one can reduce coefficient of friction (self-lubricant, e.g. PTFE, graphite), or increase gear strength (e.g. glass/carbon fibre reinforced), or change an advanced material, etc. Another

approach is to adjust the physical design without change or modification to the material itself. For instance, there could be changes to primary design parameters such as pressure angle, specific sliding ratio, percent of recess action, backlash, root clearance, tooth profile and etc. Lastly, applying a lubricant such as oil, grease or vaseline might reduce heat generation and increase heat dissipation. The second approach is the focus here as it aims to directly optimize the performance of the gears themselves rather than change the original gears' material composition.

Tsukamoto *et al.* studied how to increase the load capacity of plastic gears (test gears were pairs of an improved 6-nylon machining hobbed gear against a steel gear), and proposed economical approaches [83]: case one, small modules (reducing relative sliding velocity between contact teeth), increasing the number of teeth and the tooth face width; case two, setting the contact ratio above two (reducing the maximum load acting on the gears); case three, increasing the plastic gear tooth width while reducing the steel one to balance the bending strengths. They proposed a new design equation for calculating the load capacity by means of bending strength at the pitch point, based on observations that the tooth failure locations of nylon gears were mainly near the pitch point and from near the inner worst point [84]. Figure 2.11 illustrates the principle of the new bending equation, where  $\tau m$  denotes the increased thickness of tooth compared with the standard thickness  $0.5\pi m$ ,  $h$  represents the arm length of the bending moment at the pitch point,  $s$  denotes the circular pitch thickness on pitch circle. The load is assumed to act on the tooth tip. The tangential force on the pitch

circle is  $P$ , its normal and horizontal components are separately  $P_n$  and  $P'$ .

The bending strength equation for plastic spur gears is then

$$P = (0.411 + 0.524\tau)mb\sigma_p \quad (2.10)$$

where  $P$  is the load capacity,  $m$  is the module,  $b$  is the tooth face width,  $\sigma_p$  is the bending stress at the weak section AA'. Equation (2.10) is applicable for plastic gears with contact ratio between one and two, and for any pressure angle.

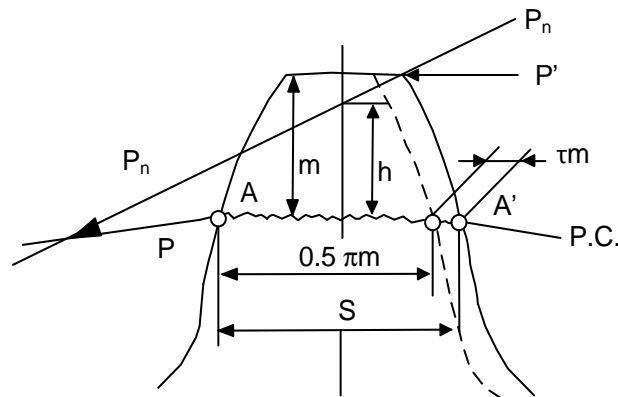


Figure 2.11 Schematic tooth geometry parameters for bending strength calculation (after [84])

Imrek [85] modified tooth profiles of Nylon 6 spur gears in the light of the load distribution characteristics along tooth profile that can be determined by the contact ratio. In most cases, the contact ratio is between one and two. The load sharing along the meshing line varies progressively that as load is shared by two pairs of teeth in contact or by a single pair of teeth in contact. Therefore to reduce the contact pressure in the meshing region where a single pair of tooth is in contact, the width of the single tooth zone within the meshing area was increased to balance it with under double tooth contact. The tooth width modification shown in Figure 2.12 results in a reduction in contact pressure and consequently a reduction in wear and

operating temperature. Experimental results confirmed that this tooth face width modification reduces the heat generation and increases the heat dissipation. Clearly, in this case, both the load capacity and life of plastic gears are improved. This method has also been applied to metallic gears [86].

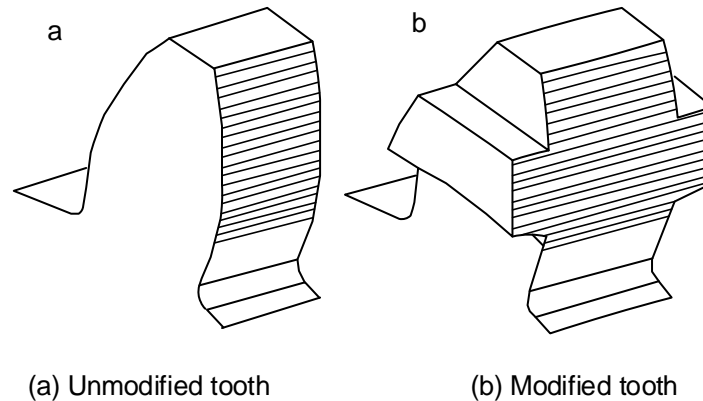


Figure 2.12 Model of unmodified and modified gear tooth profiles (after [85])

Tsukamoto and Terashima [87] attempted to prolong the life of plastic gears (an improved 6-nylon gear against a stainless steel gear) in five aspects. These involved: modifications of gear tooth profile by counter-crowning so that the centre of face width is concave, or varying the pressure angle, as shown in Figure 2.13; various changes to tooth surface roughness; various materials choices the counter (metallic) gear; introducing lubricant; increasing air convection by, e.g. drilling cooling holes in the bottom land or attaching a fin on the plastic gear shaft, as shown in Figure 2.14.

Kim [88] and Duzcukoglu *et al.* [89, 90] took similar methods, increasing air convection by drilling cooling holes on the gear teeth, as had Tsukamoto, to improve the durability. The distinction is that the locations of holes on gears are different (as shown in Figure 2.15). Also, Kim increased heat dissipation by inserting a steel pin in the internal hole of the polymer

gear tooth.

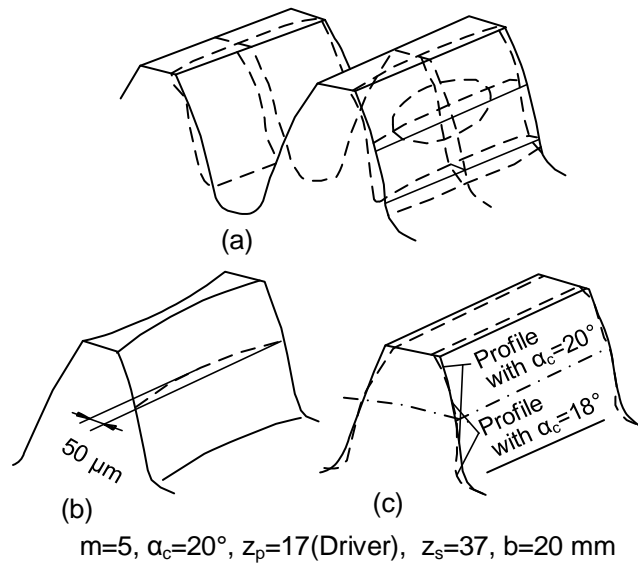


Figure 2.13 Examples of tooth profile modification (after [87])

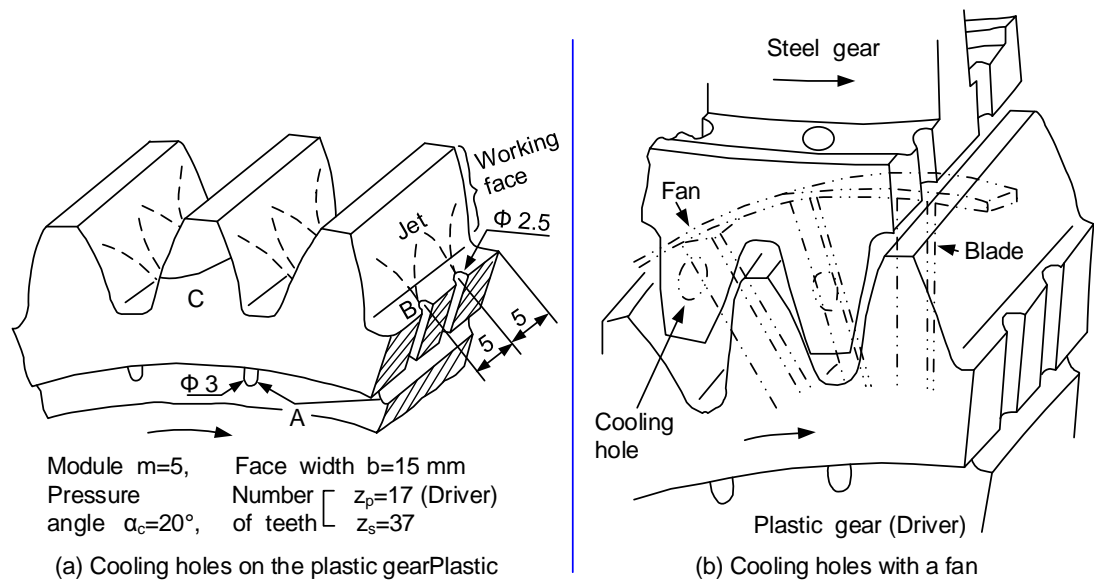


Figure 2.14 Examples of increasing forced air convections of operating gears (after [87])

Mertens and Senthilvelan [91] directed compressed air into the vicinity of gears' meshing area to aid cooling of the gear.

Nozawa *et al.* adhered Nylon 66/poly(phenylene ether) alloy sheet to the steel gear teeth and results implied that the noise reduced significantly [92]. Compared with metal gears without coating polymer, the hybrid (polymer injection moulded metal) gears exhibited superior properties in self-



lubrication, noise reduction and wear resistance [93].

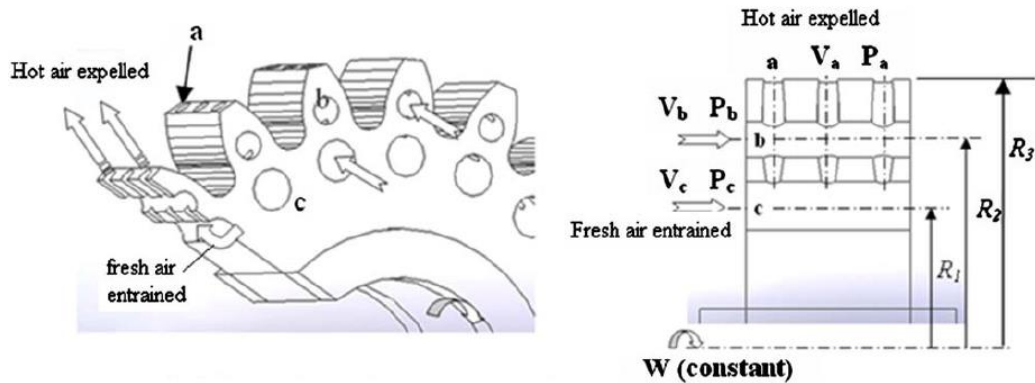


Figure 2.15 An example of drilling holes for increasing heat dissipation (after [90])

Of all the above methods, gear geometry modifications, lubricating and increasing air convection (i.e. blowing air, drilling holes) are more effective than others. However, the use of lubricant is restricted in some practical applications and adding the cooling holes or fins should incur extra power loss and extra cost. Cooling holes will also reduce the mechanical properties of plastic gears. Therefore extra careful attention needs to be paid prior to designing for particular practical applications. It is, then, important to develop a full plastic gear design theory to improve the performance polymer /composite gears.

## 2.4.5 Thermal-wear performance

### 2.4.5.1 Temperature measurement methods

The temperature measurement equipment applicable to gears is improving as the technology advances. Various gear surface and body temperature measurement methods can be exploited. The revolution in temperature measurement enables progress from conducting measurements

only after stopping tests to performing them during motion, from low accuracy to higher accuracy, from contact to non-contact sensors. Major examples of temperature measurement apparatus used in non-metallic gears' tests are listed in chronological order of their introduction: heat probe, thermocouple, infrared microscope, infrared radiometer, infrared radiation thermometers, thermo-paints, infrared video camera, non-contacting IR probes and CCD camera and so on. Of them, the infrared video camera and non-contacting IR probes are currently popular. The CCD camera is mainly used in extremely high temperature (in excess of 1000°C) and high speed conditions. Details are illustrated in the following pages.

- **Measuring after tests stopped**

Early work on gear surface temperature measurement, conducted after stopping the tests, include the use a heat probe by Hachmann and Strickle in 1966 and discussed by Mao [7], a thermocouple embedded in a cork and fitted within the tooth space (Hall and Alvord) [94], and a thermocouple touching the tooth surfaces (Tsukamoto, 1985) and reported by Mao [7].

- **Measuring during operation**

Yousef employed an infrared microscope (Barnes, model RM\_2A) to monitor the gears' temperature during running [47]. Through numerous test results, he concluded that the gear temperature decayed rapidly and the realistic running temperature could not be easily measured after tests had stopped. He also found that increases in load or deductions in diametrical pitch resulted in increases in the flank temperature.

Takanashi and Shoji measured the tooth temperature by means of two infrared radiation thermometers [71]. The test results revealed that the bulk temperature of steel gears (the driven gears) were always higher than the plastic gears. This may be due to the high thermal conductivity of steel subsequently resulting in more heat flowing to the steel one. Similar methods were adopted by Gauvin *et al.*, who used an infrared radiometer to measure the average temperature of teeth and employed thermocouples to measure gear body temperature [59]. The average temperature always increased with increases in load and speed. The effects of loads were greater than those of the rotation speeds.

Three categories of thermo-paints, thermally sensitive coating, were applied on test gear tooth surfaces to measure gear tooth temperatures separately by Takanashi and Shoji [71] and Terashima *et al.* [29]. The colour of the paints varies at 40°C, 50°C and 60°C. Obviously, this method is low accuracy, only indicating a rough temperature range. Analyses of the test results and comparisons with the temperature predictions of Takanashi and Shoji were made by Terashima *et al.*, and consequently the estimation of the temperature distribution over tooth flank were given as shown in Figure 2.16. These results confirm the intuition that that the highest temperature occurs near the pitch circle.

Tsukamoto *et al.* seeking, in 1991, to estimate the operational life of plastic gears (machining hobbed improved 6-nylon-driving gear, carbon steel-driven gear), conducted tests during running at both ordinary and elevated temperatures in a gear box [95]. The ambient air in the gear box

was raised by a heating wire heater to pre-set temperatures (80°C, 100°C and 120°C). The temperature of the plastic gear tooth was measured by a thermocouple through a slip ring. The thermocouple was embedded in a hole drilled from the side of the tooth.

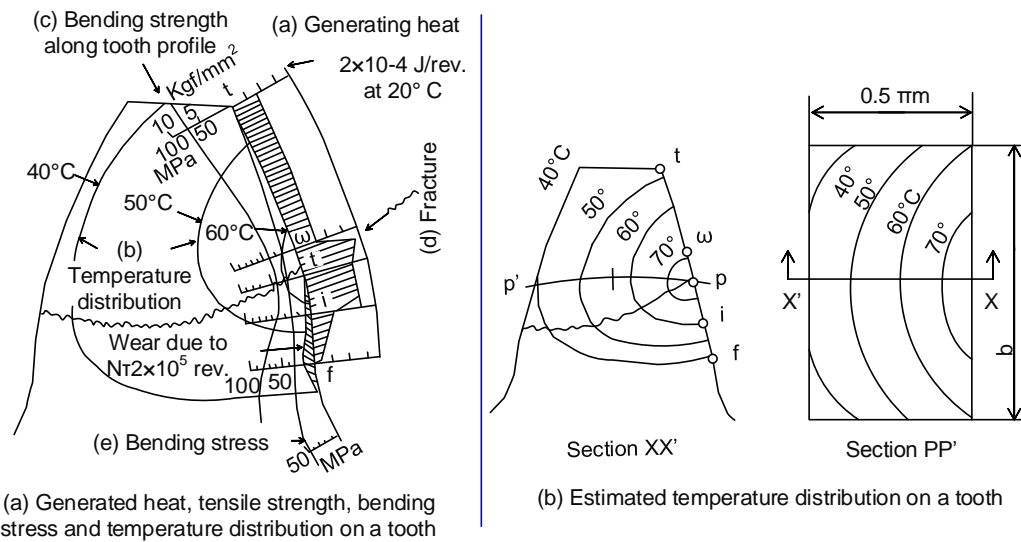


Figure 2.16 Estimation models of heat generation and distribution on plastic tooth (after [29]).

A similar method was adopted by Mao, when test acetal gears were covered by a gear box and were heated to pre-set temperatures by blowing warm air into the interior prior to running [7]. The test results show that an increase in ambient temperature results in a substantial reduction in the transition torque at which the wear rate increases significantly, as shown in Figure 2.17. He observed that the torque/temperature curve seemed to cross the zero torque line close to the melting temperature (175°C) of acetal. Tests were conducted by Mao at room temperature, with the surface temperatures measured only by an infrared video camera. The tests conducted under the high ambient air temperature conditions were measured by a thermocouple. Kono (2002) measured the surface temperature of gears by means of a non-contacting IR probes [8].

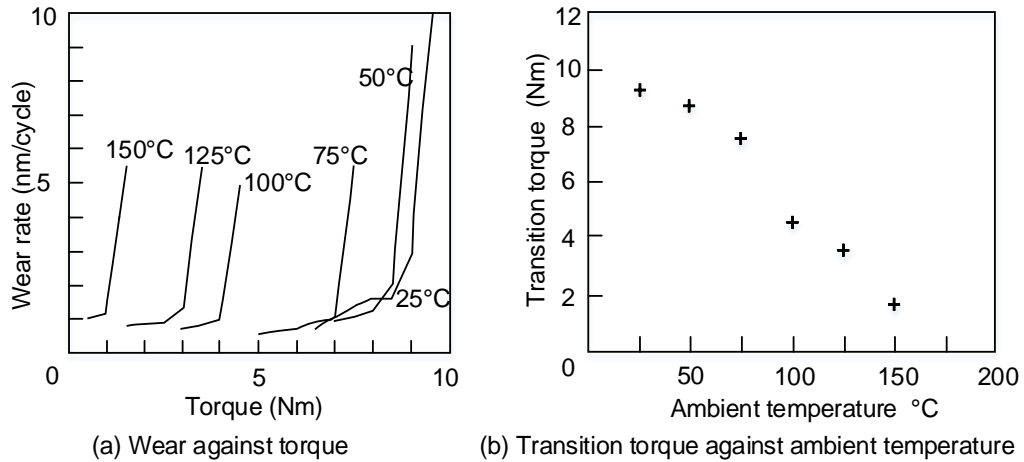


Figure 2.17 Test results at elevated ambient temperatures (after [7])

Nowadays, infrared video camera and non-contact IR/temperature sensors are popular either alone or in combination for gear tests [60, 88, 90, 91].

#### 2.4.5.2 Wear measurement methods

There are three main approaches to wear measurement. First, weighing the gears before and after tests, and so obtaining the weight loss. Second, continuously measuring indirectly through a wear measurement sensor on the test rig, such as used by Mao [7], Breeds [96] and Wright and Kukureka [97]. Third, direct measurement of the wear depth by using a (stylus or optical) profile scanner, by which the degree of tooth wear along the meshing line, the greatest wear position and the tooth permanent deformation can be clearly recorded. These have much benefited research into gears. Such scanners include a co-ordinate measurement machine used by Wright and Kukureka [97], a vertical profile optical projector (PP400TE Optomech, accuracy of 0.001 mm) employed by Mertens and Senthilvelan [91], a vertical profile optical projector (SM350, accuracy of 0.001 mm) by Duzcukoglu [90] and a projector by Kim [88]. The results from

weight loss and profile projector measurement were compared by Wright and Kukureka [97], and the values from the two methods were very close.

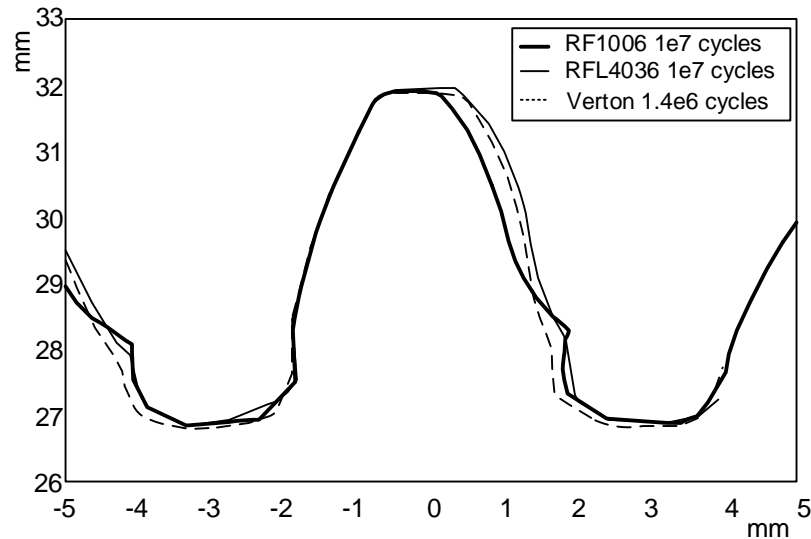


Figure 2.18 An example of tooth profiles scanned before and after tests (after [97])

#### 2.4.5.3 Existing achievements of thermal-wear behaviour

There has been limited investigation of direct links between the evolutions of the gear wear and the surface or bulk temperature, although some thermal experiments have been conducted. For instance, Mao and Hooke just presented the average wear rate at different temperatures caused by loads. There was no discussion of dynamic relationships between wear and temperature [7, 49, 50, 52]. Cropper conducted numerous thermal tests with various polymer and composite gears which involved the synchronized flank temperature and wear measurement at varying loads [8]. However, the data he attained were only for wide intervals, such as 1000 minutes per data point as shown in Figure 2.19. The detailed interactive process cannot be extracted. However his results indicate that the unsustainable wear is very likely caused by thermal softening. He also concluded that for polymer and composite gears, the sustainable wear rate

(namely, the wear rate in steady wear phase) linearly correlated with the operational Young's modulus as shown in Figure 2.20 .

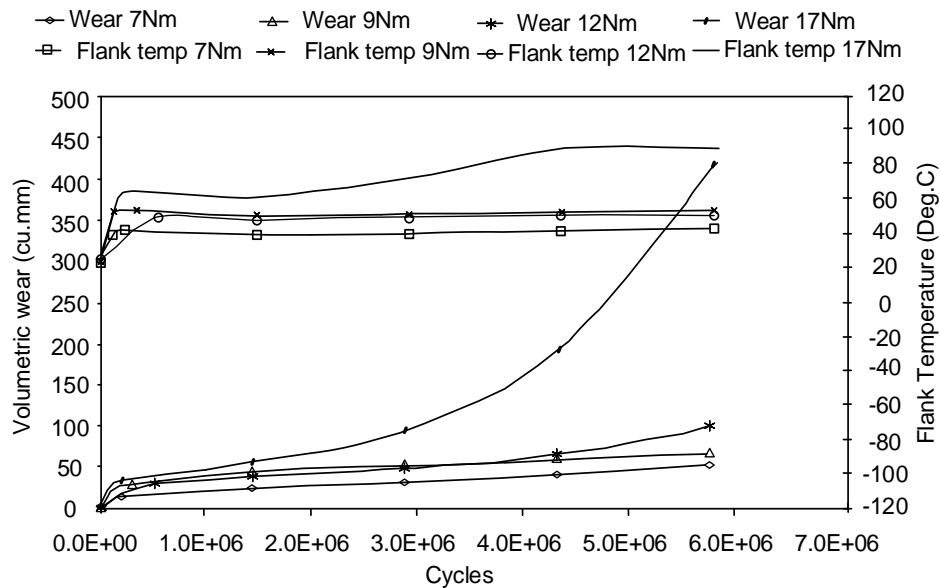


Figure 2.19 The wear and flank temperatures of benchmark geometry gears of RFL 4036 at different loads and a speed of 1000 rev/min) (after [18])

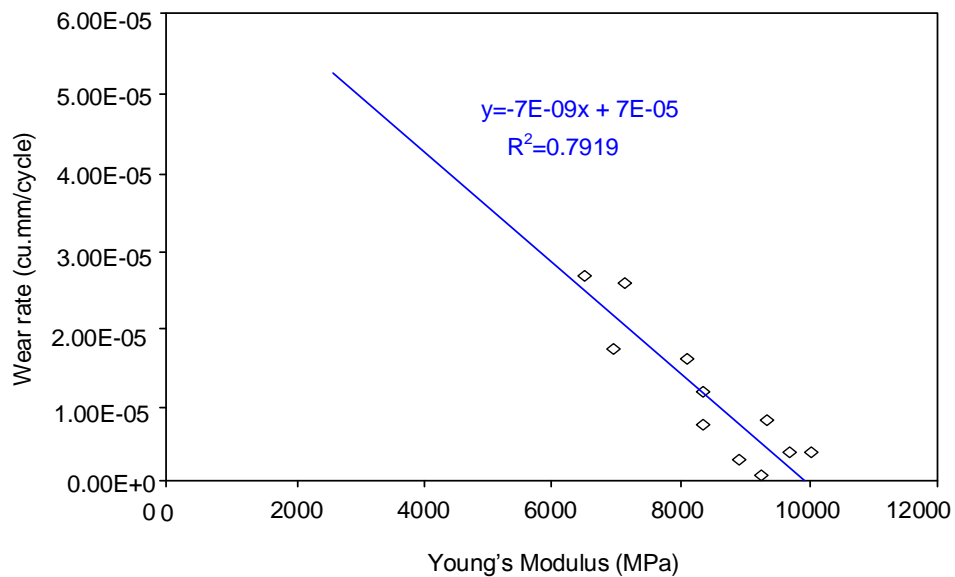


Figure 2.20 The relationship between wear rate and operational Yong's modulus for gears of RFL 4036 operating under 'sustainable' operating conditions (after [18])

Temperatures were monitored in the majority of gear durability improvement studies, but, no comparisons of total wear or wear rate values and gear temperatures were directly and simultaneously made with the number of gears' revolutions.

Wear and heat generation of polymeric gears are closely associated with the coefficient of friction. For polymers, there are existing studies on the relationships between (dynamic) coefficient of friction, load, sliding speed and temperature. Steijin [98] and Yamaguchi [99] had derived a direct relationship between surface energy and friction for polymers. It is concluded that the coefficient of adhesive friction relates with both effects of material surface energy and shear stress. The temperature and sliding speed with coefficient of friction for various materials given by Steijin are shown in Figure 2.21 and Figure 2.22 respectively. He discussed that temperature, sliding speed for coefficient of friction exhibited a maximum value which is subjected to a shift factor depending on the predominant conditions. Hooke attempted to investigate on polymer and polymer composite on the relationship of coefficient of friction, various load, slip ratio and temperature by using a twin disc machine [20]. Overall, variations in coefficient of friction with different temperatures, speeds and loads are very important for the investigations of the wear and thermal behaviour of polymer gears.

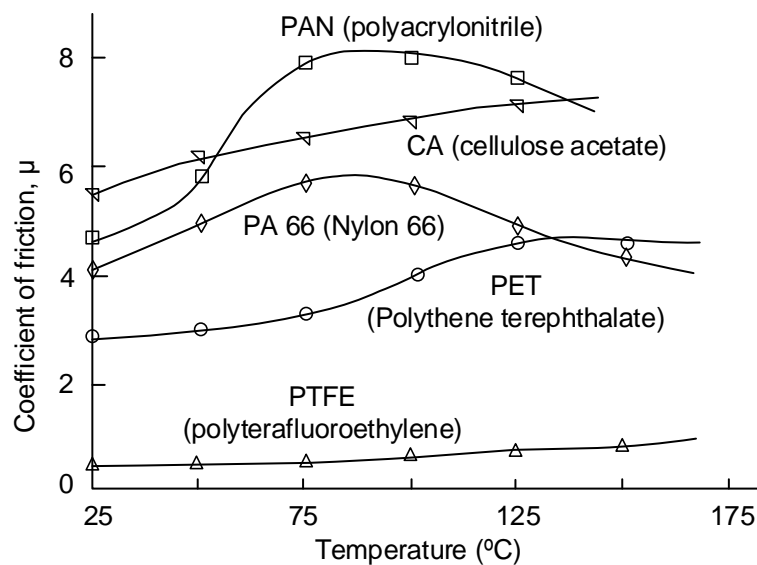


Figure 2.21 Coefficient of friction versus temperature for various polymers (after [98])



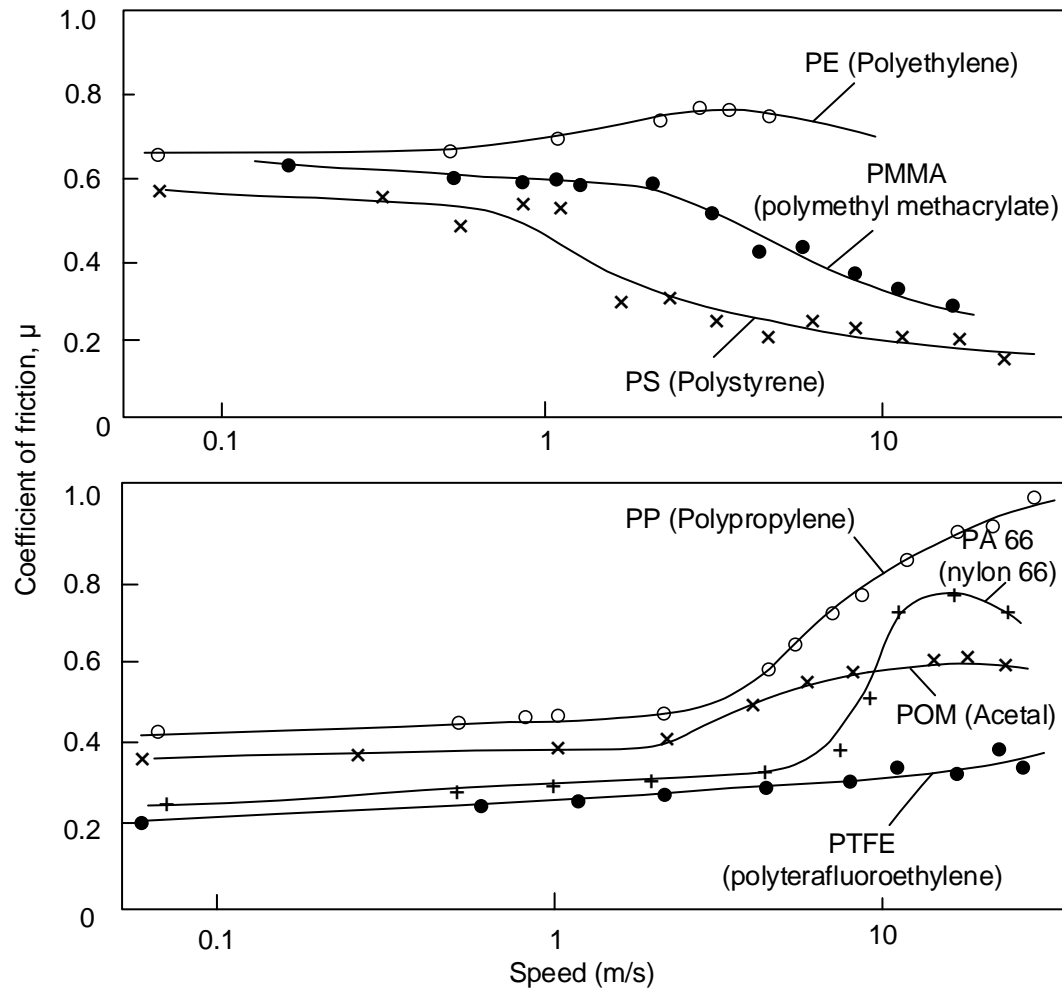


Figure 2.22 Coefficient of friction versus sliding speed for various polymers (after [98])

## 2.5 Gear mesh misalignment

The detailed concept and schematic diagram of gear mesh misalignment are given in Section 3.1.4.

Almost no literature has been found on the subject of polymer gear tooth behaviour under misaligned contact although in-depth research has been conducted on metallic gears. Houser *et al.* defined three categories of misalignment for metallic helical gears and proposed approaches such as lead crowning and end relief to reduce the detrimental effects of

misalignment [15]. Li exploited a finite element method to study the effects of shaft misalignment (in and vertical the plane of action) on tooth contact parameters of spur gear pairs, such as loading capacity, load share ratio (LSR), tooth surface contact stress (TSCS), transmission error (TE), mesh stiffness (MS), and tooth root bending stress (TRBS) [100, 101]. The results reveal that misalignment in the plane of action exerts substantial effect on TSCS and TRBS while misalignment perpendicular to plane of action has slight impact. Prabhakaran *et al.* established a numerical model to calculate the bending and contact stresses in a spur gear pair that are caused by misalignment in the plane of action [102]. Lias *et al.* analysed, by means of FEM, theoretical magnitudes for the forces that create stresses owing to axial misalignment of spur gears [103]. Ameen adopted a pattern of distributed point loads to describe the non-uniformity of load distribution caused by misalignment and determined the equivalent stresses in the contact zone and the tooth root [104]. Driot and Liaudet modelled the dynamic behaviour of spur gears subject to shaft misalignments and manufacturing errors [105]. The shaft misalignments are taken as a stochastic variables having Gaussian distribution and outcomes were obtained by Monte Carlo and Taguchi's methods. Velez and Maatar developed a comprehensive mathematical gearing system model (involving shaft misalignments, eccentricities and tooth shape deviations) to analyse gear dynamic behaviour such as dynamic load distribution, TE and ME [106]. Saxena *et al.* applied a potential energy method and considered the effect of friction force to evaluate the MS of a spur gear pair under yaw misaligned conditions [107]. Jones exploited finite element analysis (FEA) to study the

static effects of misalignments on the transmission error (TE) and load share ratio (LSR) [108]. He also used a reaction force under contact to approximate contact in a dynamic model. A similar method with computer aid was adopted by Simon. He made extensive investigations about mesh misalignment for various types of gears, such as hypoid, cylindrical worm and spiral bevel gears [109-111]. He reported that misalignments tend to degenerate conjugate actions and result in an increase in contact pressure and the TE.

Misalignment can increase the transmission error, stress concentration, non-uniform wear, vibration and noise and so on. In practice, it is inevitable that meshing gear pairs will suffer slight misalignment because of elastic deformation, manufacturing and assembling errors and so on [15]. It is unclear whether any of the data on metal gears is directly transferable to polymeric ones. Currently, solely the field of transmission errors of plastic gears seems to have been investigated by Tsai *et al.* [16] and P.K.Meuleman *et al.* [17]. No other publications are found highlighting this particular issue on non-metallic gears. It is therefore necessary and urgent to investigate into the impact of misalignment on polymer gears.

## 2.6 Wear debris

There are three major sources of information that could be used to monitor metallic geared systems in real time. These are vibration monitoring, oil debris analysis and oil temperature analysis [108]. Analysis of wear debris (particle) regime can aid understanding of the underlying wear

mechanism, tribology system diagnosis, fault diagnosis and so on [112-114]. Compared with metallic gears, the wear particles from polymeric gears can often be detected and obtained directly because most of their applications run lubricant-free. Accordingly, wear particle analysis ought to be a superior approach for polymer gears, but there is currently very little high quality and relevant data. The wear debris regime of polymer gears is associated with wear mechanisms and operating conditions such as rubbing, abrasive wear (scratching), scuffing, contact stress, local contact temperature and aligned and degree of contact misalignment. Just a few authors have given some attention to the various changes in shape of polymer wear debris [8, 19, 96, 115, 116].

## Chapter 3

### Experimental Methods

Extensive investigations on polymer/composite gears have been performed by using a traditional design for a non-metallic gear test rig [7, 8, 18, 24, 49, 50, 53, 96, 117]. The test mode for non-metallic gears is identical to the conventional test mode for metallic gears. It is intended to work with aligned gears (tests under nominally aligned condition), but (of course) it will not do so perfectly.

A novel design of polymer gear test rig has been designed and built at the University of Warwick [52, 118] with a deliberate level of controlled misalignment now being introduced. Some modifications were made to it by the author for current investigations. The test rig was developed to continuously measure the wear and the life of non-metallic gears under constant load in both aligned and misaligned modes. Linear and rotational misalignments can be introduced.

To investigate the misalignment effects on polyacetal gears and the mechanical-thermal behaviour of polyacetal gears, it is necessary to introduce systems to measure the wear of tooth contact surfaces, the temperature of airflow circling gears and bulk temperature during motion, and the velocity of airflow surrounding the running gears. Vibration monitoring is needed. The surface topography of worn teeth and the regime of wear debris then need to be examined.

Therefore this chapter has first briefly reviewed the traditional approach to designing a non-metallic gear test rig and then describe the major machine features of the new test rig design. The majority of the chapter discusses in detail the principle and practical implementation of the subsystems added to that test rig. These include the design of wear measurement system, airflow temperature measurement, vibration monitoring system and the measurement methods of bulk temperature and airflow velocity.

### **3.1 Design of the new non-metallic gear test rig**

#### **3.1.1 Structure of the gear test rig**

The CAD model of the new non-metallic gear test rig is shown in Figure 3.1 and its schematic is presented in Figure 3.2. It shows that the basic structure of the new test rig is a classical 'four square' (back to back) arrangement which consists of a pair of metallic gears in a gear box (3 in Figure 3.2) with oil lubricant and the same geometry as the test polyacetal gears (11, 12 in Figure 3.2) being located to an opposing pivot block assembly (8 in Figure 3.2). The metallic gear pair does not need to be replaced and the test polymer gears can be changed easily according to experimental requirements. These two gear pairs are joined by two drive propeller shafts (6, 7 in Figure 3.2) forming a closed loop. The drive shafts are free to move at an angle or slide axially on their double universal (cardan) joints (5 in Figure 3.2) for the four types of misalignment configuration, see

Section 3.1.4 for details. The test polymer gear pair is fixed against two bearing blocks (18, 20 in Figure 3.2) which are assembled onto a pivot block assembly (8 in Figure 3.2) that can rotate on pivot (21 in Figure 3.2). The pivot block assembly holds a moment bar (14 in Figure 3.2) with adjustable weight (13 in Figure 3.2) which can apply load to the test gear pair. The torque exerted by the 'constant weight' on moment bar is balanced by the torques on the drive shafts. The torque remains constant irrespective of tooth wear. The motor (1 in Figure 3.2) transmits its rotary motion to the gears and its power to overcome gear sliding and bearing losses in the system.

The wear of the tooth contact surfaces can be continuously, although indirectly, measured through measuring the rotation of the pivot block assembly. A non-contact displacement transducer (15 in Figure 3.2) has been designed by exploiting the Hall-Effect principle to measure the displacement induced by the rotation of the pivot block assembly. Details are given in Section 3.2. The test rig can be stopped automatically by the micro switch when gear tooth wear exceeds a pre-set maximum limit, a tooth bends excessively or tooth fracture occurs.

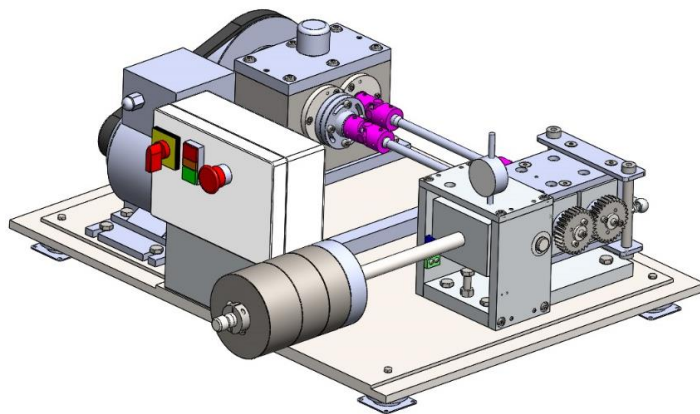
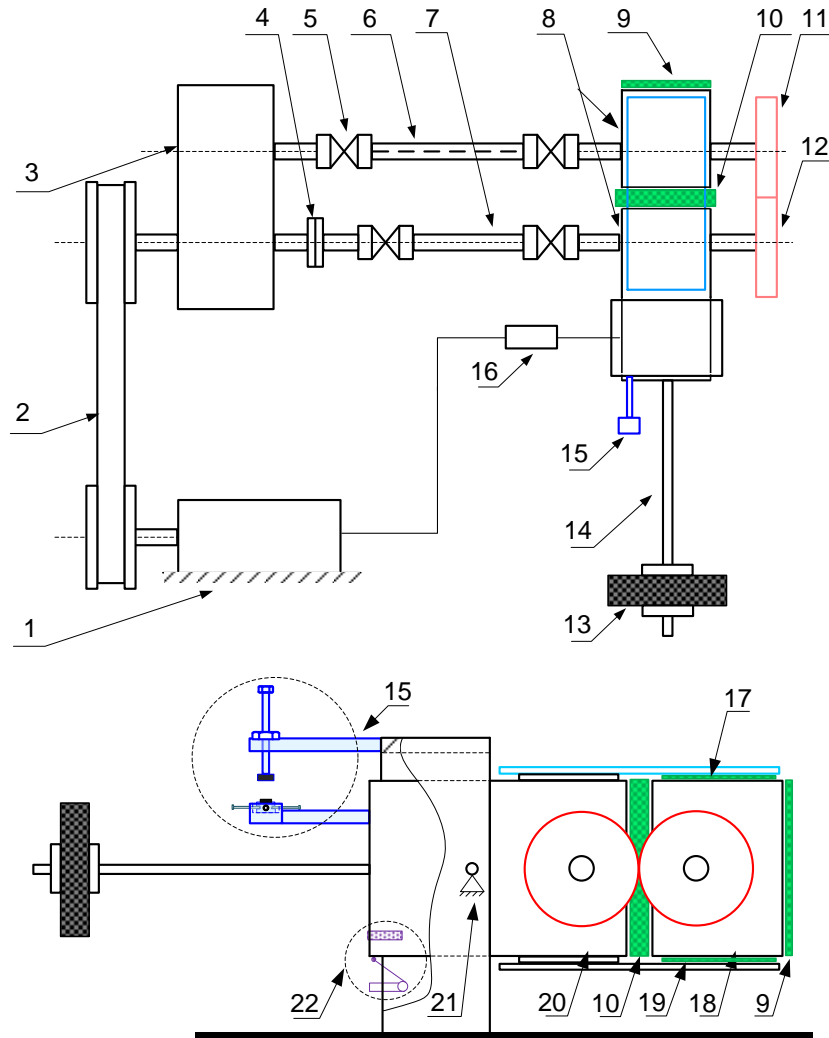


Figure 3.1 CAD model of the new non-metallic test rig



- |                            |                                |
|----------------------------|--------------------------------|
| 1. Motor                   | 12. Driving gear               |
| 2. Pulley                  | 13. Weight                     |
| 3. Gear box                | 14. Loading bar                |
| 4. Conical clutch          | 15. Displacement transducer    |
| 5. Double universal joint  | 16. Motor controller           |
| 6. Driven shaft            | 17. Top shim                   |
| 7. Driving shaft           | 18. Driven gear bearing block  |
| 8. Pivot block assembly    | 19. Bottom shim                |
| 9. Side fastener           | 20. Driving gear bearing block |
| 10. Center distance spacer | 21. Pivot                      |
| 11. Driven gear            | 22. Micro switch               |

Figure 3.2 Schematic diagram of the current polymer gear test rig

The specifications of the new non-metallic gear test rig is given respectively in Table 3.1.



Table 3.1 Specifications of the non-metallic test rig

Parameters	Value	Description
Gear ratio	1:1	The same size of driving and driven gears
Centre distance (mm)	60	Nominal centre distance of two meshing gears
Speed (revs/min)	500~2000	Adjustable rotating speed of gears
Power (W)	550	The maximum power supply of the motor
Load (N·m)	4-22	The torque applied to the test gears
Maximum wear (mm)	3.0	The maximum allowable wear of a gear pair
Temperature (°C)	17~25	Environment temperature

### 3.1.2 Test gears

All the polymeric gears used in this thesis are polyacetal (POM) involute spur gears. They are machine hobbled without any tip relief modification and manufactured by Ondrives (Precision Gears). The surface roughness of test gears were measured by 3D ContourGT optical profiler, range of 0.61  $\mu\text{m}$  to 0.88  $\mu\text{m}$ . The average outside diameter of gears measured was 63.88 mm. The specification of gear geometry is listed in Table 3.2. Detailed material properties and drawing of the test gears are given in Appendix A.

Table 3.2 Specifications of test polyacetal gears

Parameters	Value
Gear material	Polyacetal (POM )
Gear category	Spur gear
Module (mm)	2
Pressure angle (°)	20
Tooth number	30
Tooth thickness (mm)	3.14
Face width (mm)	15
Nominal pitch diameter (mm)	60
Nominal outside diameter (mm)	64
Contact ratio	1.65
Shaft diameter (mm)	16
Key size (mm)	5×5

### 3.1.3 Working principle

The working principle of current non-metallic gear test rig is the same as the conventional non-metallic gear test rig. Detailed illustrations as well as calculations and derivations were given by Mao [7]. Therefore this section briefly presents the derived relationships of weight and load as well as wear and rotating angle of the assembly pivot block.

- **Loading**

The torque  $T$  acting on each testing gears is exerted by the ‘constant weight’ through the moment bar. This relationship is given by

$$mg \times L = 2 \times T \quad (3.1)$$

then the torque  $T$  is

$$T = 0.5 \times mg \times L \quad (3.2)$$

where  $m$  is the whole equivalent mass applied to the load bar about the pivot,  $g$  is the acceleration due to Earth’s gravity and  $L$  is the horizontal distance of the weight from the pivot.

- **Wear measurement**

The assembly block (8 in Figure 3.2) is free to rotate about pivot prior to gears being fitted onto the test rig. However, the test rig is constrained from rotation by the mating teeth after a gear pair has been installed. It is set up at horizontal level as shown ① in Figure 3.3. However, the pivot block assembly will rotate a little when wear occurs in the mating teeth as ②

shown in Figure 3.3. There is a relationship between the rotation angle and wear.

Note that it is inevitable that some degree of viscoelastic deformation and thermal expansion occurs on teeth while gears are running and it is impossible to distinguish them from wear. Hence the continuous wear measurement here is the sum of wear, viscoelastic deformation and thermal expansion. However, comparison of the gear weights before and after tests allows the total wear loss to be calculated. Comparison of tooth flank profiles before and after tests allows wear profiles and viscoelastic deformation (thermal creep and flexure) to be assessed separately.

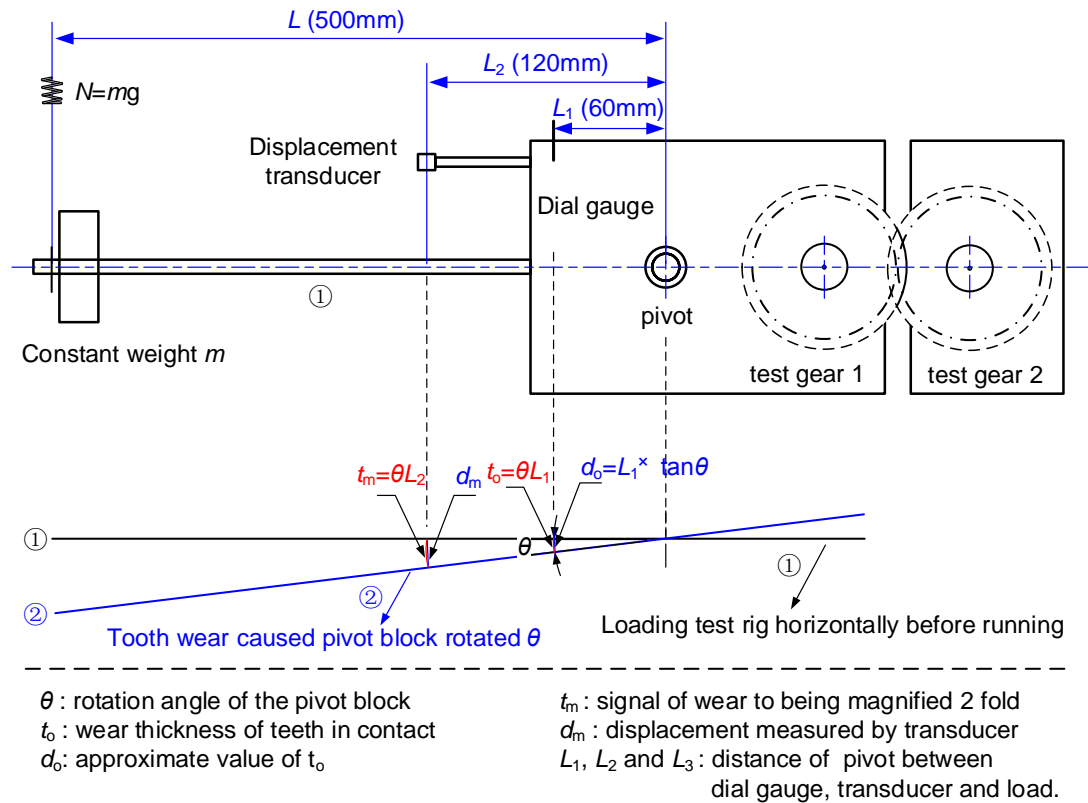


Figure 3.3 Schematic diagram of wear measurement and rotating angle

The wear values presented in this thesis are total wear, seen in continuous wear monitoring  $t_w$ . The wear of a single tooth is estimated by

simply taking half of the total wear (i.e.  $0.5 \times t_w$ ). The wear is indirectly measured through the rotation of the pivot assembly block and the rotation is indirectly measured by using a Hall-Effect displacement transducer. The expression of total wear  $t_w$  and rotation angle  $\theta$  of assembly block about pivot is

$$t_w = d_p \times \cos(\alpha) \times \theta \quad (3.3)$$

where  $d_p$  is the pitch or reference circle diameter of test gears,  $\alpha$  is the pressure angle and  $\theta$  is the rotation angle of pivot block.

In the present work the maximum wear at mating teeth is restricted (by hardware) to  $t_{\max} = 3.14$  mm. Then the maximum rotation angle is estimated from  $\theta_{\max} = t_{\max} / (d_p \times \cos(\alpha))$  and is 0.0522 radians (below 3 degree). The change of the rotation angle is so small that an extremely sensitive angle measurement transducer would be required (very expensive). Instead, measuring the displacement  $d_m$  as shown in Figure 3.3, is significantly easier and less costly. The relationship of the rotation angle  $\theta$  and the displacement  $d_m$  is

$$d_m = L_2 \times \tan \theta \quad (3.4)$$

Then  $\theta$  is derived

$$\theta = \arctan(d_m / L_2) \quad (3.5)$$

Substituting Equation (3.5) to Equation (3.3), then the total wear  $t_w$  can be given by

$$t_w = d_p \times \cos(\alpha) \times \arctan(d_m/L_2) \quad (3.6)$$

The displacement  $d_m$  is measured by a Hall-effect non-contact displacement transducer (detailed description is in Section 3.2) which was calibrated by using a dial gauge (precision 0.01 mm).

Note that in the early stages of wear (under low load and speed conditions), it can be difficult to detect marginal changes in the displacement and rotation of the pivot block because of electrical noise and vibration inevitably associated with running the test rig. A simple and effective way was adopted to magnify the wear signal relative to the rig system noise before measurement. The displacement transducer is located on an extension beam at a distance  $L_2$ , rather than  $L_1$ , beyond the pivot to form a magnifying lever. Considering the effective working distance of non-contact Hall-effect displacement transducer is approximately 8.5 mm and the maximum tooth wear which may exceed 4.0 mm when melt wear, tooth bending or fractures at high load /speed, see endurance test results beyond light loads in Section 4.3), distance  $L_2$  is set 120 mm, being double the distance  $L_1$  from the pivot.

#### 3.1.4 Misalignment definition and adjustment

In practice, some degree of misalignment is inevitable for mating gear pairs. The causes of gear mesh misalignment include many factors. The major ones are lead slope error, lead wobble, bore parallelism, bearing and housing deflections, shaft bending or torsional deflections, gear blank

deflections, wear, bearing clearance, temperature difference, assembly error and so on [20].

Polymers have elastic moduli approximately 100 times less than metals, lower thermal conductivities and softening/melting temperatures as shown in Table 1.1, which consequently increases the probability of polymer gears suffering mesh misalignment, and overheating.

The gear pair mesh alignment shown in Figure 3.4 is the ideal condition. There are four main categories of misalignment as shown in Figure 3.5 (axial misalignment, radial misalignment, yaw misalignment and pitch misalignment) for gear engagement under imperfect conditions.

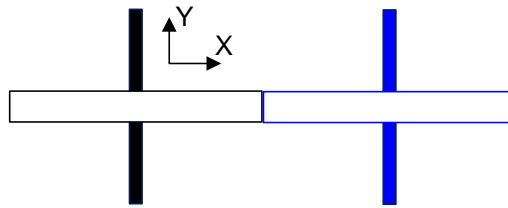


Figure 3.4 Schematic diagram of a gear pair mesh alignment

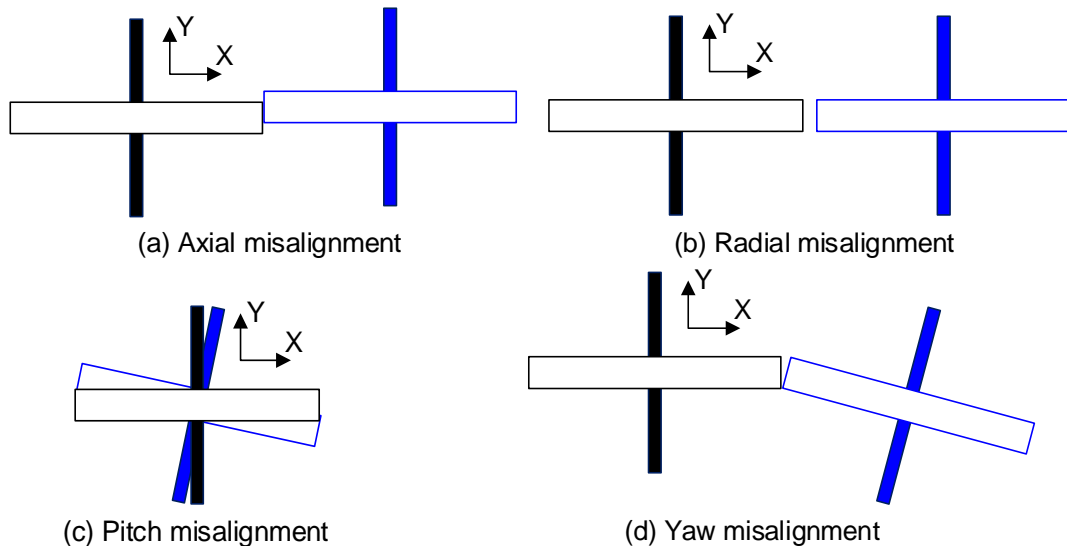


Figure 3.5 Schematic diagram of a gear pair misaligned mesh

Figure 3.6 depicts schematically causal development of four types of misalignment from an aligned mesh gear pair, where 'OXY' is on the gear

teeth's plane of action and 'OZ' is vertical to the plane of action. Axial and radial misalignment are linear effects. Axial misalignment can be simplified to be that one gear (i.e. G2) moves ' $\Delta y$ ' along axis 'OY' with respect to the other one (i.e. G1), as shown in Figure 3.6(a). Radial misalignment is equivalent to shift one gear (i.e. G2) ' $\Delta x$ ' relative to the other one (i.e. G1) along axis 'OX' as shown in Figure 3.6(b). Yaw and pitch misalignment, they are angular effects, tending to shift the load distribution over the tooth contact surfaces, resulting in non-uniform wear. Pitch misalignment is effectively rotating one gear (i.e. G2) ' $\omega$ ' around axis 'OX' as shown in Figure 3.6(c) and yaw misalignment is equivalently due to one gear (i.e. G2) rotating ' $\omega$ ' around axis 'OZ'.

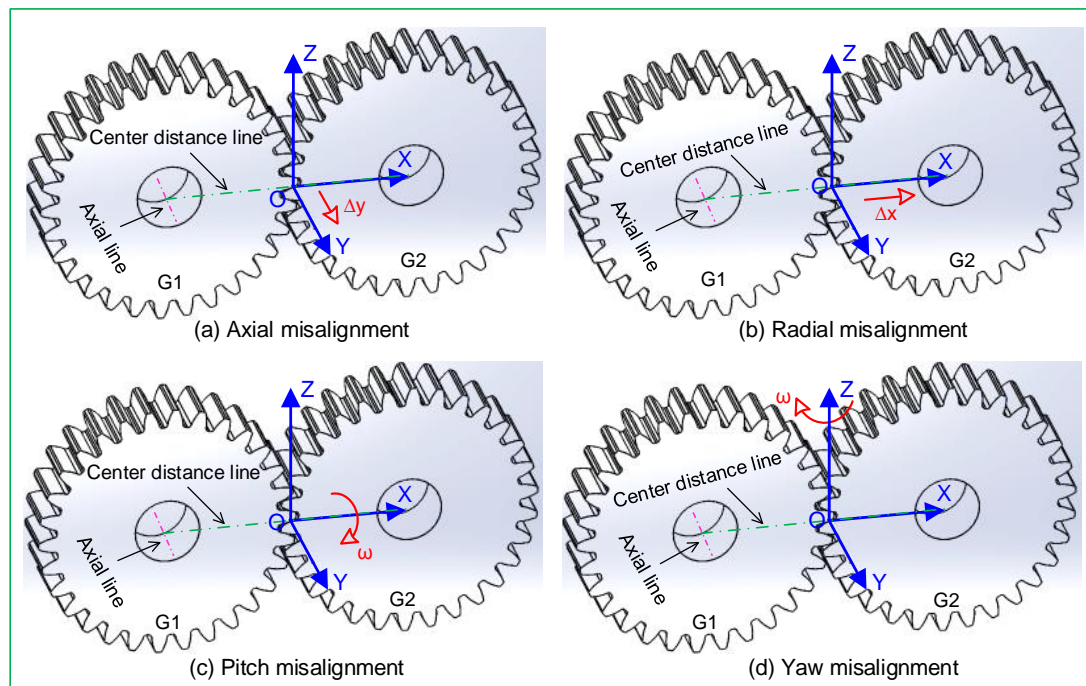


Figure 3.6 Examples of mesh misalignment of a gear pair corresponding to Figure 3.5

As for the four categories of misalignment adjustment, the pivot block assembly (8 in Figure 3.2) is fundamental to setting and making adjustments to the four types of misalignment. It was made in two halves: the driving gear

bearing block and the driven gear bearing block (18 and 20 in Figure 3.2 ). A pair of test polyacetal gears is localised separately on the driving and driven gear bearing blocks. The driven gear bearing block is able to move and rotate relative to the driving gear bearing block and is fixed into a specified orientation by using a centre-distance spacer, top shim, bottom shim, driven shaft, and side fastener. The misalignment adjustment in tests will be described in detail in the following.

Axial misalignment is due to an axial shift between shafts, causing a reduction in tooth flank active contact width/area. It consequently results in an increase in contact stress over the active area of contact on tooth flank. It is achieved by moving driven gear bearing block axially.

Radial misalignment, namely variations in position resulting from a change in centre distance between the shafts (and gear pair), which causes a slight change in the intersection of the outside diameters, and hence slightly alters the tooth profile contact ratio. The contact temperature of gear teeth tends to increase during motion, which results in gear tooth expansion, where a slight extension of the active contact area occurs: as a result the tooth profile contact ratio increases slightly. Thermal softening might lead to higher wear. The design of radial misalignment configuration incorporates spacer blocks to achieve the nominal position, so making it possible to contact or extend it relative to the nominal centre distance by using different spacers.

Yaw misalignment is a rotation in an axis (OZ), perpendicular to the plane of action ( . It is achieved by changing the geometrical shape of centre



distance spacer. A centre distance spacer having a slight trapezoidal cross-section is used instead of the nominal rectangular section. In this case the shape of the contact zone becomes skewed and the contact area is reduced. The decrease in contact area leads to a reduction of total contact ratio [15]. Edge contact and local excessive contact stress might occur and cause uneven wear.

Pitch misalignment is a rotation about an axis (OX), parallel to the plane of action, which tends to shift the load to side of the tooth by increasing the separation at the one side of the tooth and reducing the separation at the other side of the tooth [15]. This case is achieved by using top and bottom shims] having a marginal trapezoidal cross-section instead of the nominal rectangular section. Significant uneven wear, scratching or material torn off contact surfaces may take place in such situations.

### **3.2 Design of the wear measurement system**

The contact tooth surface wear is measured indirectly through the rotation of the pivot block assembly. To measure and record continuously contact teeth wear in real-time, a bespoke gear wear measurement system was designed. As shown in Figure 3.7, it is composed of a displacement transducer and a data-logging system.

The non-contact displacement transducer was designed by exploiting the basic physical principle of the Hall-Effect that generates an output (Hall) voltage in the presence of a magnetic field.

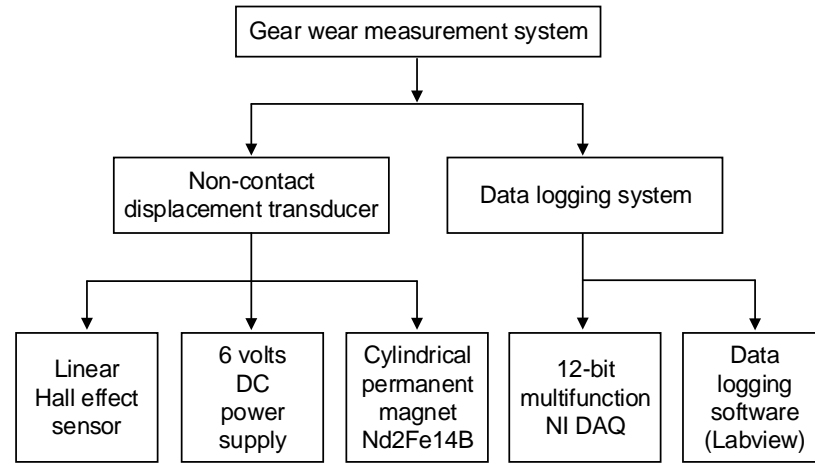


Figure 3.7 Structure schematic diagram of wear measurement system

The output voltage of Hall-Effect sensor is set by the power supply voltage and varies in proportion to the strength of magnetic field around it [119]. The Hall Effect sensor is activated by an external magnetic field from permanent magnet or electromagnet. The magnetic field has two principal characteristics, magnetic flux density ( $B$ ) and polarity (north and south poles).

As shown in Figure 3.8, the linear Hall-Effect sensor outputs a continuous Hall voltage which increases as the strength of the magnetic field increases until it begins to saturate at the limit imposed on it by the power supply voltage. The output Hall voltage prior to saturation is

$$V_H = R_H \left( \frac{I}{t} \times B \right) \quad (3.7)$$

where  $R_H$  is the Hall-Effect coefficient,  $I$  is the (constant) current flowing through the sensor,  $t$  is the sensor thickness and  $B$  is the magnetic flux density.

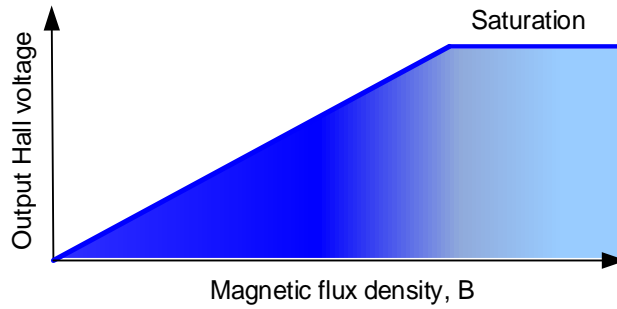


Figure 3.8 Output voltage against magnetic flux density at a supply voltage  $V_s$

A high performance linear position Hall-Effect sensor SS495A-1225627 in 3 pin TO-92 package was selected. Its structure and transfer characteristics are separately shown in Figure 3.9 and Figure 3.10. It has no magnetic flux limit, and its circuit cannot be damaged by magnetic over drive. Its performance parameters are listed in Table 3.3. To have a wide range of operating temperature, as indicated in Figure 3.11, a supply voltage of 6 V is chosen here.

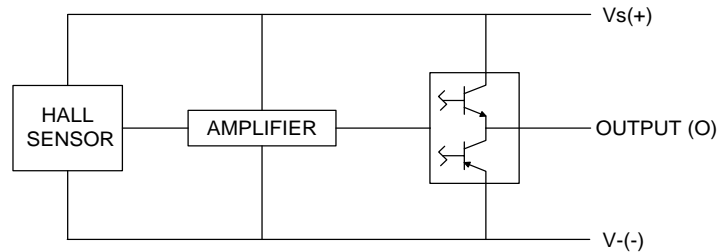


Figure 3.9 Block diagram of Hall Effect sensor

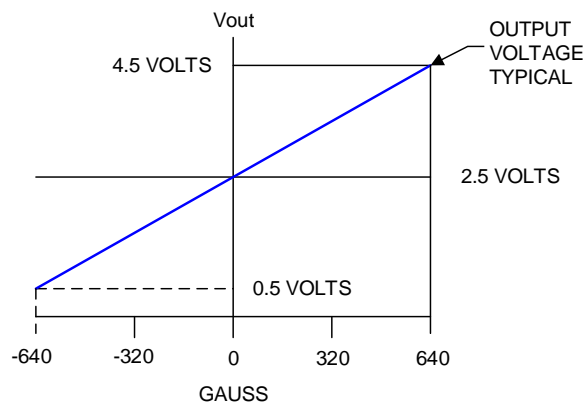


Figure 3.10 Transfer characteristics of Hall Effect sensor at  $V_s=5\text{VDC}$

Table 3.3 Specifications of Hall Effect sensor SS495A ( $V_s=5.0V$ ,  $T_a=-40$  to  $+125^\circ C$ )

Parameters	Value	Parameters	Value
Supply voltage (VDC)	4.5 to 10.5	Output voltage span (V)	0.2 to $V_s-0.2$
Current at 5VDC (mA)	7	Output current ( $\mu A$ )	600
Response time ( $\mu s$ )	3	Linearity (% of span) %	-1.0
Sensitivity (mV/G)	$3.125 \pm 0.125$	Null (Output at 0 Gauss, V)	$2.5 \pm 0.075$
Temperature null drift ( $\%/^\circ C$ )	$\pm 0.06$	Temperature sensitivity drift $<25^\circ C$ Max. ( $\%/^\circ C$ )	0.0, $+0.06$
Temperature sensitivity drift $\geq 25^\circ C$ Max. ( $\%/^\circ C$ )	-0.01, $+0.05$	Operating temperature ( $^\circ C$ )	-40 to $+150$
Weight (mg)	120	Size (in $\times$ in)	0.160 $\times$ 0.118

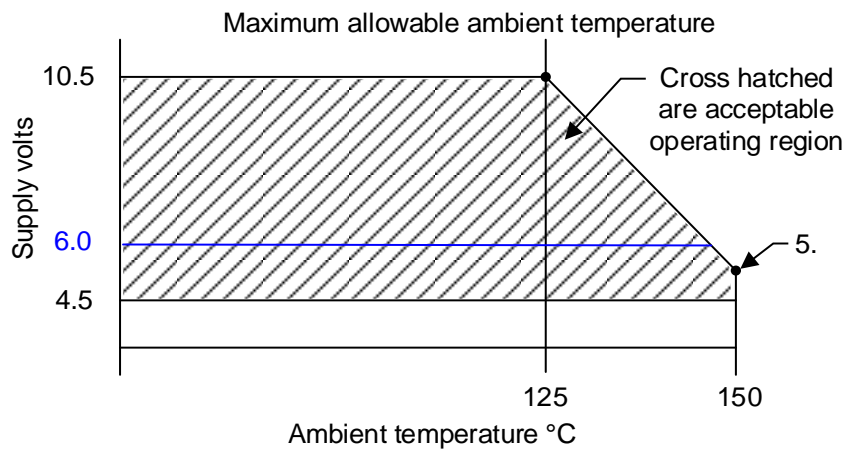


Figure 3.11 Maximum supply voltage against ambient temperature

As with the magnet component, a permanent cylindrical magnet was chosen and its magnetic flux density  $B$  in a symmetrical axial distance  $z$  from the pole face can be estimated as [120, 121]:

$$B = \frac{B_r}{2} \left( \frac{D+z}{\sqrt{R^2 + (D+z)^2}} - \frac{z}{\sqrt{R^2 + z^2}} \right) \quad (3.8)$$

where the geometry parameters above are sketched in Figure 3.12,  $B_r$  is remanence field (independent of the magnet's geometry),  $D$  is the height of the cylinder and  $R$  is the radius of the cylinder.

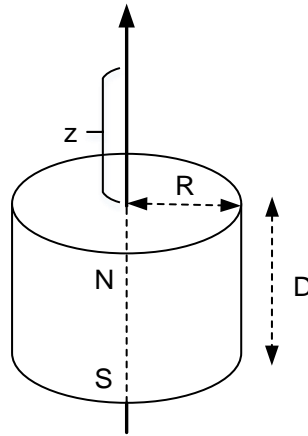


Figure 3.12 Geometries of cylindrical magnetic and axial distance from the North Pole face

The field equation shows that the axial magnetic flux density  $B$  of a cylindrical magnet decreases steadily, but non-linearly, as the distance from the pole face increases. Hence, a non-contact displacement transducer can be implemented by moving a permanent magnet axially with respect to a (fixed) Hall Effect sensor. The distance measurement range of displacement transducer should be no less than 6.29 mm on the basis of the present polymer gear test requirements (in terms of Equation (3.6), allowable tooth wear limit  $t_{\max}$  and relating parameters). Therefore a strong permanent cylindrical Neodymium magnet (Nd2Fe14B) was employed as the moving part of the transducer.

The circuit design is shown in Figure 3.13, a resistor  $R_1$  is added to the circuit of Hall Effect transducer for the purpose of limiting in conjunction with the supply characteristics the current passing through sensor, the diode LED is for indicating the presence of electricity, the other resistor  $R_2$  (7.15  $\Omega$ ) and a capacitor  $C$  (22 $\mu$ F) act to filter out high frequency noise with cut off approximately 1012 Hz.

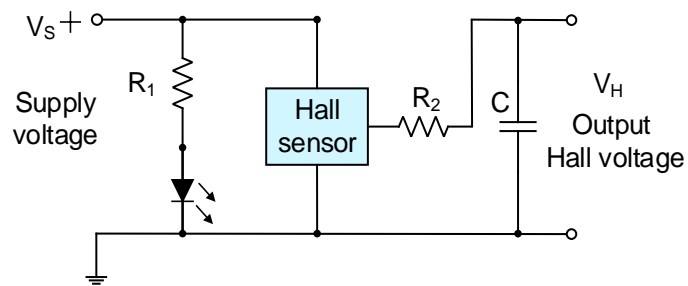


Figure 3.13 Circuit diagram of Hall Effect transducer

Clearly the performance of this transducer will be affected by the presence of ferromagnetic materials (especially the moving components) in its immediate locality, therefore an acrylic cantilever holder and four stainless steel bolts were used to locate the Hall Effect sensor. The sensor was able to be moved in horizontal level to align it to the cylindrical magnet. The cylindrical Neodymium magnet was fixed on a nylon bolt, and a stainless hexagon nut and held by an acrylic cantilever as well. Hence the magnet was able to shift in vertical direction. The distance of the Neodymium magnet from the Hall sensor could then be regulated as required. Its assembly drawing and physical picture are shown in Figure 3.14.

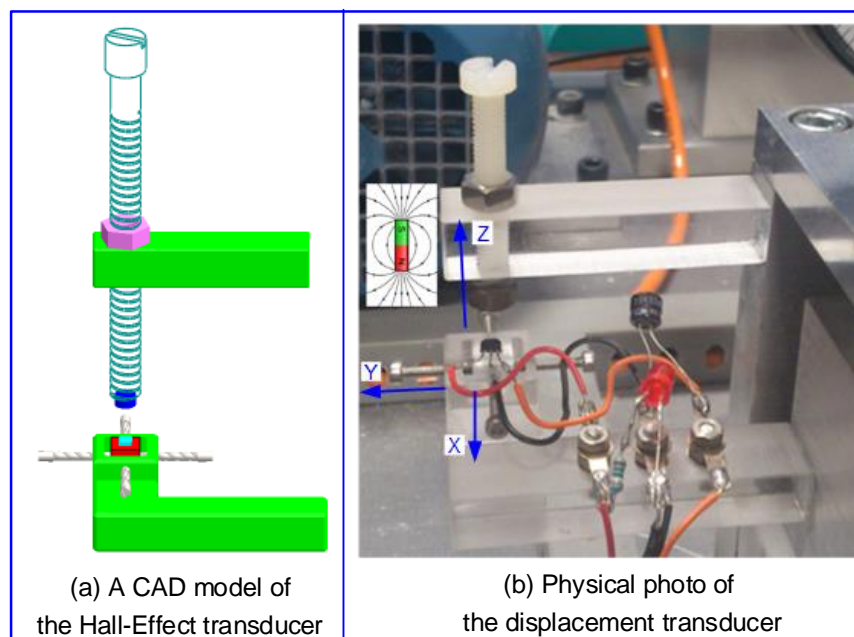


Figure 3.14 Assembly of the non-contact Hall-Effect displacement transducer

The non-contact displacement transducer was calibrated in steps of 0.05 mm over the range from 0.00 mm to 8.10 mm by using a dial gauge. Given the transducer output value  $x$ , the displacement  $y$  caused by gear wear, then the curve fit  $y(x)$  can be performed by using an exponential fit by a standard function of Matlab®. The exponential fit approximation  $y(x)$  is

$$y(x) = a \times e^{bx} + c \times e^{dx} \quad (3.9)$$

The coefficient of  $x$  in Equation (3.9) are listed in Table 3.4 (goodness of fit parameter, R-squared: 0.9989). The fitted curve is shown in Figure 3.15. The error of displacement measured by the transducer is estimated within  $\pm 0.03$  mm (after measurement data fit, calibrated by the new measurement results again by using a dial gauge). Then the displacement  $y$  value is just  $d_m$  in Equation (3.6). Hence the wear of gear  $t_w$  can be measured.

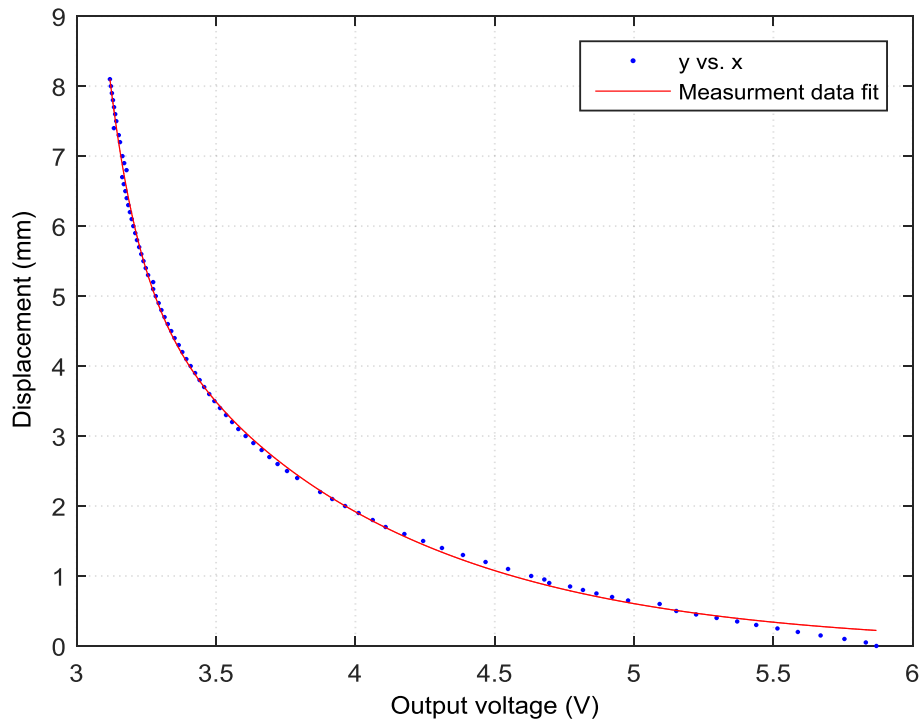


Figure 3.15 Displacement versus Hall output plots

Table 3.4 Exponential fit coefficient

Coefficient	Value
a	2.245
b	-0.9476
c	0.002493
d	-7.756

A NI-DAQ data card (National Instruments) converts the output signal (analogue signal) of the Hall-Effect transducer into a digital signal. Data logging software acquires a real-time time sequence of digital values at the sample frequency of 1000 Hz. The data logging software also records test conditions and dynamic variables, such as the test gear pair parameters (material and geometry), alignment or categories of misalignment, load, speed, wear to running time /failure, etc. Its programme flowchart is shown in Figure 3.16.



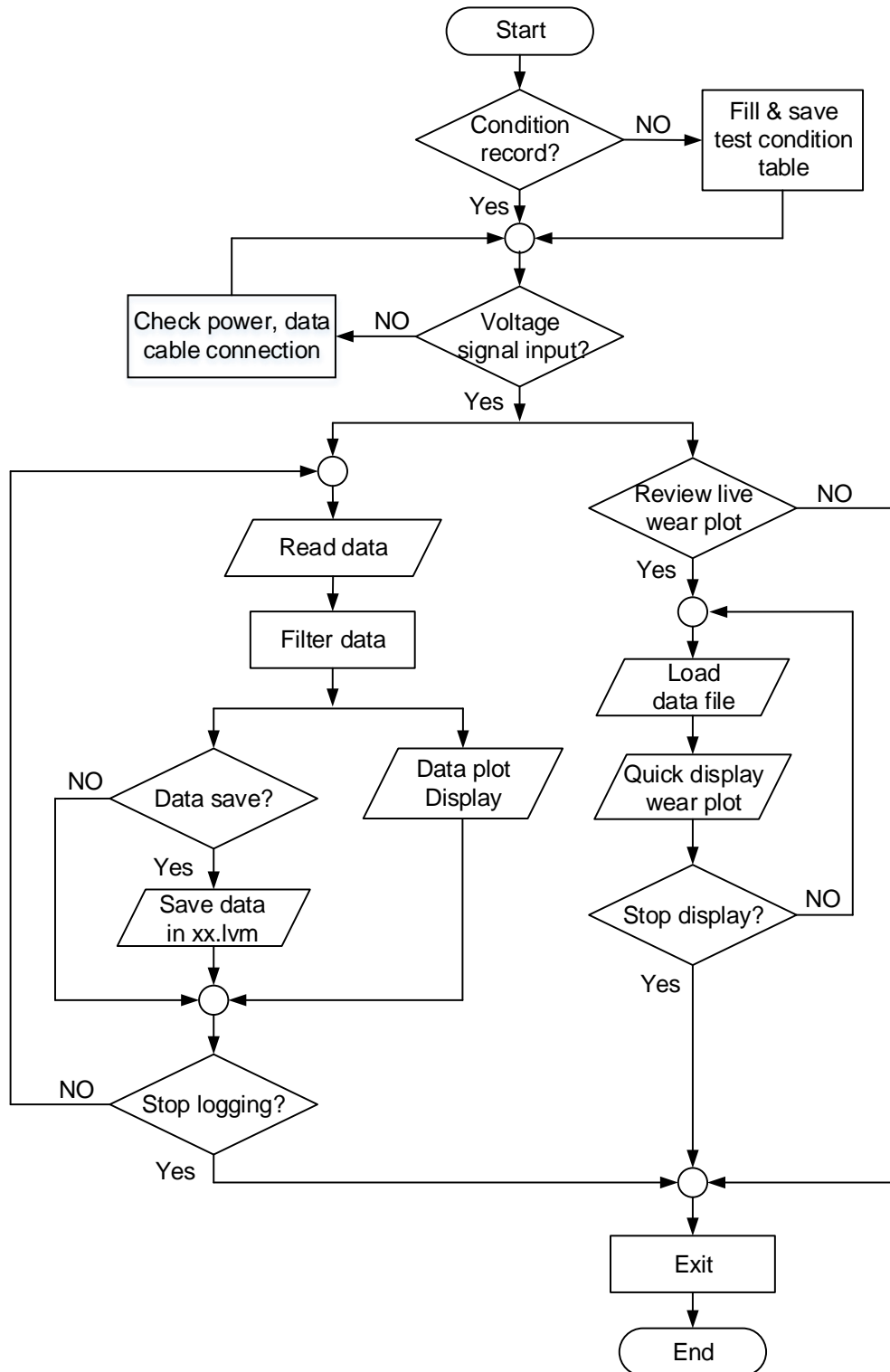


Figure 3.16 Data logging programme flowchart

### 3.3 Design for airflow temperature measurement

The airflow considered here is the air (turbulence) surrounding and close to gears. A rapid rise in airflow temperature occurs once a test initiates. It reaches thermal equilibrium as a polymer gear test reaches a steady wear phase.

Airflow (velocity) surrounding a single rotating gear was simulated as shown in Figure 3.17, by using SolidWorks®. In designing the measurement system, it was assumed that the airflow patterns around test gears would be broadly similar to that in Figure 3.17.

Figure 3.18 illustrates the overall structure of the airflow temperature measurement system. Its essential component is a set of small temperature sensors, a K-type thermocouple array. A thermocouple bracket shown in Figure 3.19 was designed and built to hold the thermocouple array at set points around the gears. The airflow temperature measurement transducer rotates synchronously with the pivot assembly block as it rotates from the wear of gears. This ensures the pre-set positions (relative to the gears) of the sensors encircling the gears would not change as the gears wear. To avoid impacting on the air vortex surrounding the running gears, the thermocouple bracket frame is always at least 29 mm away from the tooth tips. The measuring junction of each thermocouple is fairly close to tooth tip, within a 3 mm band. An Omega thermocouple data acquisition device was employed for data logging at frequency of 1 Hz or 0.05 Hz. Figure 3.20 exhibits an example of an airflow temperature measurement array. The detailed distributions of test measuring points are explained in Section 6.2.

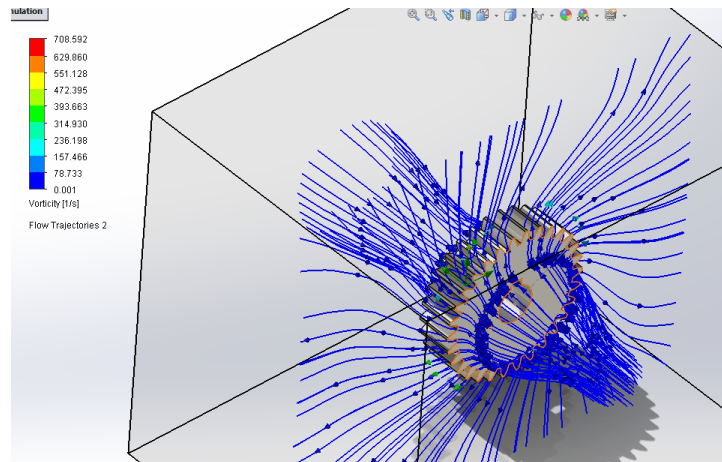


Figure 3.17 Velocity of airflow encircling a rotating gear

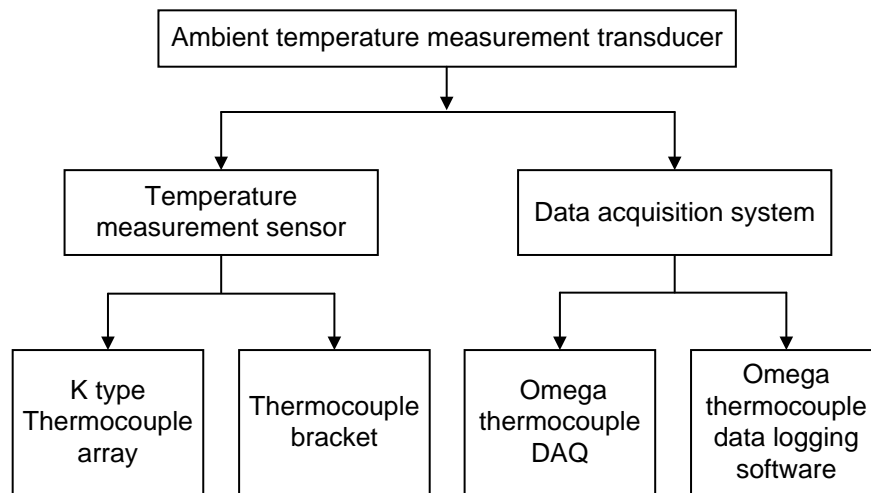


Figure 3.18 Structure diagram of airflow temperature measurement transducer

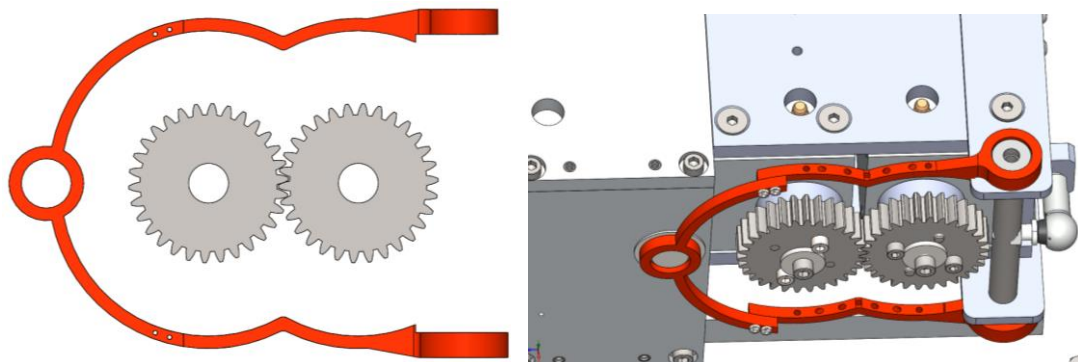


Figure 3.19 Thermocouple bracket

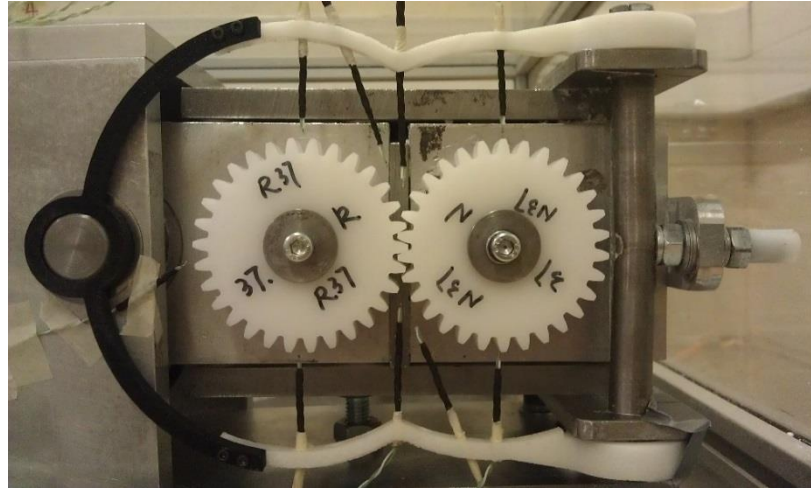


Figure 3.20 An example of airflow temperature measuring points

### 3.4 Bulk temperature measurement

Gear bulk temperature is here taken to mean the temperature of gear tooth body close to the contact surfaces. This is estimated from non-contact measurement of the temperature of the side face of the tooth. In order to avoid other thermal signals, measurement are made some distance from the contact zone. The indicated measurement area will be illustrated in detail in Section 6.3.

A FLIR SC660 infrared video camera was employed to measure the bulk temperature of running gears, set at emissivity of 0.95 and 10 or 30 seconds per data point prior to steady wear phase and 3 minutes per data point in steady phase.

### 3.5 Airflow velocity measurement

Air convection is generally supposed to be a major factor for heat

dissipation in running polymer gears. An air vortex comes into being once motion is initiated. The velocity, temperature and pressure of air in and around gear tooth pocket are closely associated with the air convection. However, since the width of bottom land of test polyacetal gears (less than 2 mm) is much smaller than the air pressure gauge (could be obtained), therefore the air pressure measurement in gear tooth pocket can only conduct for a large size of gears (i.e. involute spur gear with nominal diameter 140 mm) in the future work.

To estimate the contribution of air convection in heat dissipation, the first need is to obtain and explore a general map of the air vortex close to the meshing gears. Therefore the velocity and temperature of the airflow in the vicinity of an operating gear pair were measured by using two (handheld) miniature hot-wire anemometers (AIRFLOW™ TA5). This measurement was focused on interrogation areas as close as practicable to the gears and at positions judged likely to be important, such as the regions where gears are entering or leaving mesh. Detailed description of air velocity measurement will be presented in Section 6.5.

### **3.6 Vibration measurement**

Vibration levels associated with running gears may depend on gear bulk temperature, the degree of wear and misalignment. Therefore a high sensitivity accelerometer (Brüel & Kjær) was employed to measure vibration. The accelerometer was fixed on the top of the pivot assembly block and near the test gears as shown in Figure 3.21. The vibration measurement

device is piezoelectric charge accelerometer type 4383, the specification of which is listed in Table 3.5. Its output signal is conditioned, amplified and integrated by a measuring amplifier type 2525.

The setting of sampling frequency varies in terms of the testing gears (tooth number) and running speed (the data acquisition frequency is 16 kHz here when rotation speed is 1000 rpm). Data logging software was developed by using NI LabVIEW (National Instruments). Data were collected by a NI USB-6251 8 inputs, 16-bit and 1.25 MS/s Multifunction I/O system. Figure 3.22 sketches the vibration sensor connection diagram.

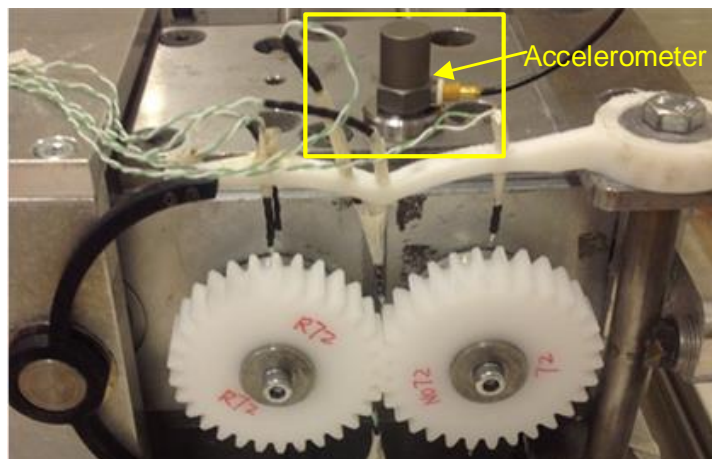


Figure 3.21 The location of the accelerometer on gear test rig

Table 3.5 Specifications of a Brüel & Kjær accelerometer

Parameter	Unit	Value
Frequency range ( $\pm 10\%$ limit)	Hz	0.1 -8400
Mounted resonance frequency	Hz	28000
Charge sensitivity at 159.2 Hz	pC/ms <sup>-2</sup>	3.191 $\pm$ 2%
Operating temperature range	°C	-74 to +250
Temperature coefficient of sensitivity	%/°C	0.05
Max. non-destructive shock ( $\pm$ peak)	ms <sup>-2</sup>	5000
Sensitivity amplified	mv/ms <sup>-2</sup>	45; 60
Weight	g	17
AO-0038	-	Low noise coaxial cable, 10-32 UNF

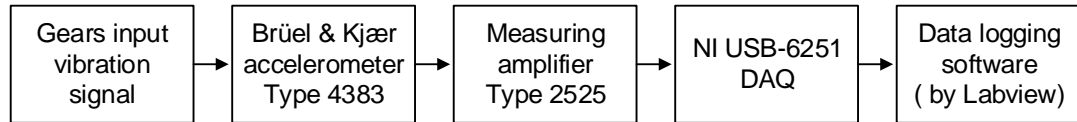


Figure 3.22 The diagram of vibration signal acquisition

### 3.7 Examinations of worn tooth and wear debris

To understand the wear mechanism of polyacetal gears, examinations were conducted after individual tests as detailed below.

The worn gears were cleaned and left in the laboratory environment for 48 hours after a test. The worn gears were then weighed and compared to their original condition to measure the wear in term of weight loss by using a high precision Westco weighing system (Western Counties Scale, accuracy 0.1 mg). The profiles of worn tooth flanks were scanned by a non-contact Bruker ContourGT optical profiler. The worn tooth contact surfaces and under various load, speed and contact (aligned/misaligned) conditions were gold coated and examined by using scanning electron microscope (SEM, XL30ESEM).

Strikingly different shapes and sizes of wear debris were examined by using an optical microscope and captured by Olympus camera using with a x10 objective and oblique with white light illumination.

## Chapter 4

# Aligned-Configuration Tests

### 4.1 Introduction

To study the wear behaviour of polyacetal spur gears, extensive experimental investigations were conducted under nominally aligned conditions through the non-metallic gear test rig.

Investigations into the wear characteristics of polyacetal gears under a wide range of loads and running at a speed of 1000 rpm were performed. The studies on wear characteristics preliminarily concentrate on four aspects:

- Features of wear curves in varying load groups, including wear phases expressed in terms of wear rate;
- The relation of wear rate and variations in loads at a constant rotating speed;
- The relationship of the gear teeth contact pattern and the topography of worn tooth surfaces;
- Regime of wear debris.

From the first two aspects, the effect of loads on wear behaviour of gears could be qualitatively investigated. Referring to the test results of Mao [7], it is predicted that an increase in load leads to an increase in wear and transition loads exist where wear rate increases dramatically. The last two



aspects are expected to improve understanding of the interrelation of non-conformal contact, sliding/rolling contact and wear tooth surface asperities, and the interaction between topographies of worn tooth surfaces and visual observations of wear debris. Through the preliminary analysis of the test results, further verification tests upon wear durability, incremental step-load at various speeds, and adding graphite paste lubricant were devised and performed.

Unavoidable practical limitations of the experimental conditions (the test rig was not available 100% of time because the laboratory was also shared with other groups of students and staff) for these studies of wear characteristics led to the majority of endurance tests on polyacetal gears at 1000 rpm being interrupted, which is not the way Mao [7] did non-stop tests until failure. It is predicted that the wear life estimated by simply joining or concatenating the interrupted data segments will be almost consistent with that from non-stop test providing that the test rig is not disturbed mechanically during the intermediate resting time. The method of exploiting the segmented test results to assess the lifetime of polyacetal gears is novel, which virtually is in line with the industry/engineering application.

As is demonstrated later, the expected pattern is for slightly higher wear at the start of each segment, followed by a rapid return to a consistent steady wear-rate, so the interrupted test provides a moderately conservative estimate. Comparing wear phases between individual segments in the complete endurance tests, it is found that there is an evident 'start up' wear (initial fast wear-in phase) when the load is within the medium range. The

steady wear seems linked closely with environmental temperature and the equilibrium of gears' operating temperature. Therefore the cooling time intervals between segmental tests in an endurance test were recorded and compared.

To provide a time-efficient inspection of the relationships of wear, load and speed, a wide range of step-load tests at four speeds were carried out. To compare the effect of rotating speed on wear of polyacetal gears, the running duration at each individual load for all the test cases was set to approximately  $2.25 \times 10^4$  cycles. There was a cooling time interval for each load increment which was expected to reduce the accumulative heat extended from the previous segment of the test, which may impact on gear wear.

This chapter has first outlined test schemes and will subsequently describe the wear characteristics tests, endurance tests, step-load tests and lubricated tests in detail before presenting the results obtained from these tests under gear aligned conditions.

### **4.2 Short-period wear tests**

The first aim of short-period experiments is to understand the effect of load on the wear of gears under certain operating environments. Based on the variation in wear rate and durability life, loads for polyacetal gears were divided roughly into three categories: low, moderate and high loads at a speed of 1000 rpm as shown in Table 4.1. Due to the restrictions of

experimental conditions (principally, limited number of new, nominally identical gears), investigations were mainly performed with regard to these three load ranges.

Table 4.1 Load range value for three load categories

Low load (N·m)	Medium load (N·m)	High load (N·m)
<8	8~9.5	>9.5
Low wear rate	Medium wear rate	High wear rate

## 4.2.1 Test results and discussions

### 4.2.1.1 Wear curves

Tests at various loads and speed of 1000 rpm were conducted and test results were obtained as shown in Figure 4.1. The wear curves in Figure 4.1 exhibit strikingly different wear trends which could be roughly divided into three groups. Group One (marked 'a' on Figure 4.1), with loads being less than 8 N·m, mainly experience three wear phases prior to final fast wear phase: initial fast wear-in ('start-up' wear), transitional wear and steady wear phases. Group Two (marked 'b' on Figure 4.1), with loads in range of 8 N·m to 9 N·m, presents four wear phases: initial fast wear-in, transitional wear, steady wear and final fast wear phases. Group Three (marked 'c' on Figure 4.1), with loads being greater than 9.5 N·m, exhibits two wear phases: initial fast wear-in and a final fast wear phase which has extremely short wear duration (less than 50000 cycles overall).

This total set of test results (Figure 4.1) reveals that an increase in load results in an increase in wear gradient, and that critical loads exist

between 7 and 8 N·m, perhaps between 9 N·m and 9.5 N·m and between 9.5 N·m and 10.1 N·m beyond which there is an extremely accelerated wear rate.

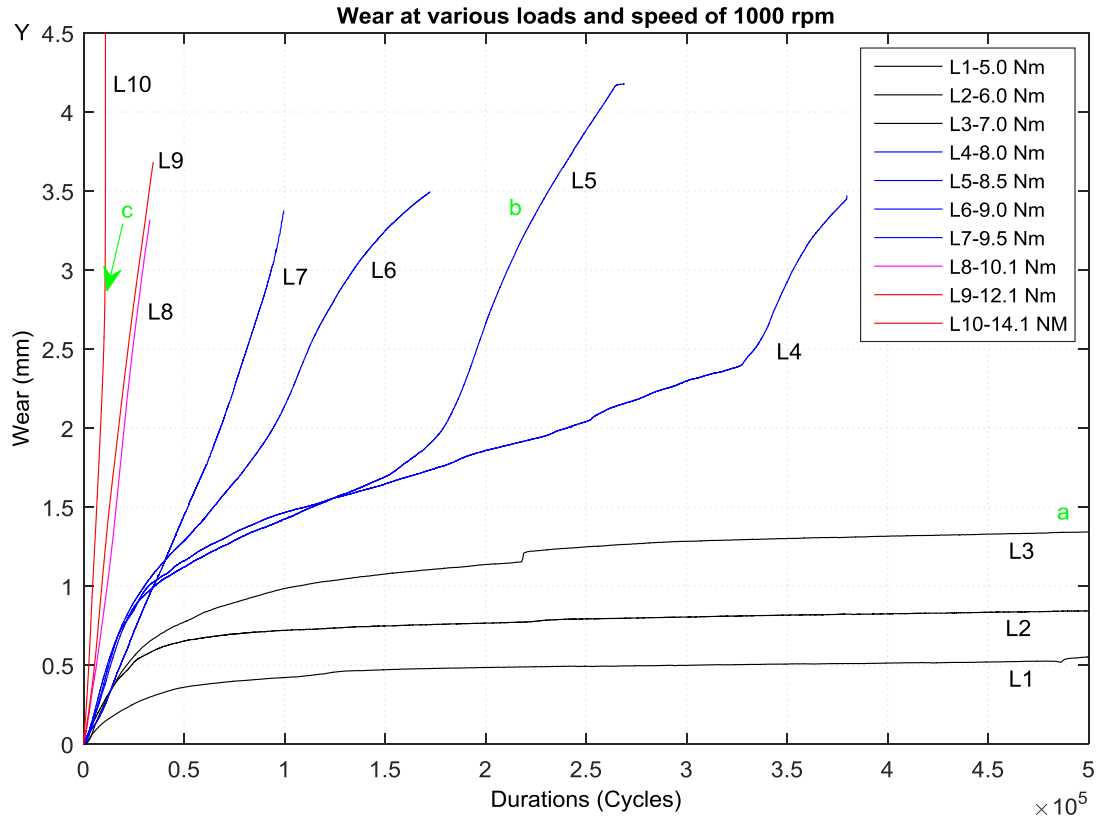


Figure 4.1 Wear at varying loads and a speed of 1000 rpm

#### 4.2.1.2 Wear rate

Wear phases (wear rate) may be greatly different at various load conditions, such as a clearly visible initial fast wear-in phase at low load, steady and fast wear phases at medium load or having solely rapid wear at high load. Therefore, comparing average wear rate of the whole wear curve was employed. The calculation method adopted here varies slightly according to the relevant load range, referring to Figure 4.1, the average wear rate for the low load range is defined as  $(Y_a - Y_0)/(X_a - X_0)$ , where  $(X_a)$  and  $(Y_a)$  are the total wear measured and duration at the end of the test and

( $X_0$ ) and ( $Y_0$ ) are the wear and duration at the start, being zero. The formal use of ( $Y_0$ ,  $X_0$ ) is to allow exactly analogous methods to be used for intermediate wear phases, where the starting values will be non-zero. For the medium load range, the duration ( $X_b$ ) is taken to be that at which the where ( $Y_b$ ) reaches approximately 3.14 mm and the average wear rate is  $(Y_b - Y_0)/(X_b - X_0)$ . Finally at extremely high loads, as case at 14.1 N·m, the gear fails prematurely (at  $Y_c = 2.84$  mm, in this example) and the expression for wear rate is  $(Y_c - Y_0)/(X_c - X_0)$ .

Adopting above calculation method, average wear rates are obtained and shown in Figure 4.2. This emphasises how substantially the wear rate is likely to increase at loads above 9.5 N·m.

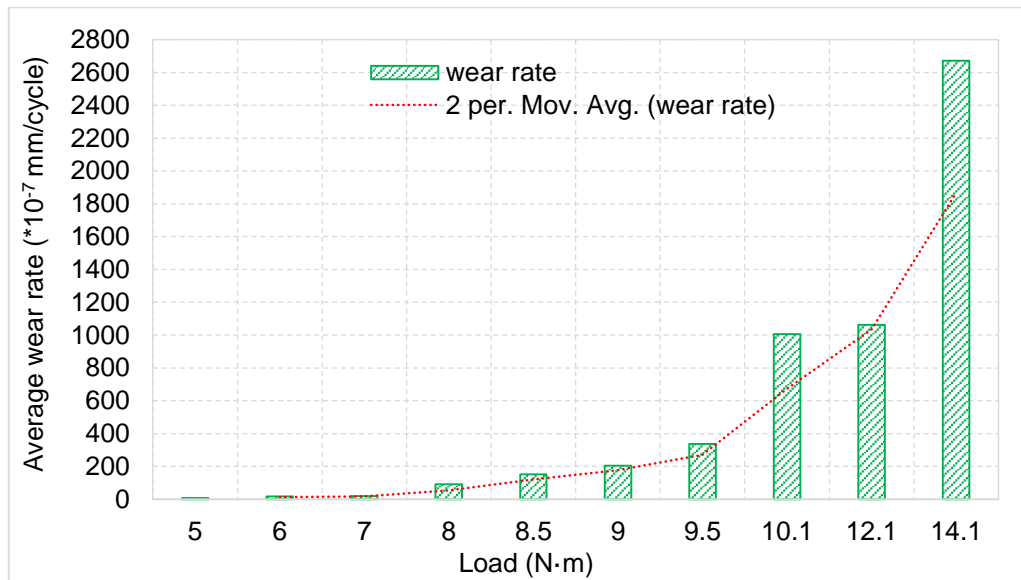


Figure 4.2 Average wear rates at varying loads and a speed of 1000 rpm

An increase in load gives rise to increases in contact stress, bending stress and wear rate. Direct viewing of their relationships to wear and load exploit a relative ratio method. That is, values at a load of 5 N·m are

designated as references, for the Hertzian contact stress, bending stress and wear rate, expressed respectively as  $\sigma_H$ ,  $\sigma_F$  and  $k_a$ . Then values of these parameters at various loads are expressed as proportions of these reference values and are tabulated in Table 4.2. The calculation formulae for Hertzian contact and bending stresses are adopted from the BS 6168 (1987) Standard [13]. The Hertzian contact stress  $\sigma_H$  is

$$\sigma_H = Z_H Z_E Z_\varepsilon \sqrt{\frac{F_t}{bd_1} \times \frac{u+1}{u} \times K_A} \quad (4.1)$$

where  $Z_H$ ,  $Z_E$  and  $Z_\varepsilon$  are obtained through Equations (4.2), (4.3) and (4.4).

$$Z_H = \sqrt{\frac{2 \cos \alpha_w}{\cos^2 \alpha \times \sin \alpha_w}} \quad (4.2)$$

$$Z_E = 1 / \sqrt{\pi \left( \frac{1 - \nu_1^2}{E_1} + \frac{1 - \nu_2^2}{E_2} \right)} \quad (4.3)$$

$$Z_\varepsilon = \sqrt{\frac{4 - \varepsilon_a}{3}} \quad (4.4)$$

where  $\alpha_w = \cos^{-1}(a \cos \alpha_t / a_w)$  is the real contact pressure angle,  $a = 0.5 \times m \times (z_1 + z_2)$  is theory centre distance,  $\alpha_t$  is the theoretical pressure angle,  $a_w$  is the real (working) centre distance,  $\nu$  is Poisson's ratio and it is 0.35 at 40°C,  $\varepsilon_a = \left( \sqrt{r_{a1}^2 - r_{b1}^2} + \sqrt{r_{a2}^2 - r_{b2}^2} - a_w \sin \alpha_w \right) / \pi m \cos \alpha_t$  is contact ratio,  $r_{a(1,2)}$  present outside radius (pinion, wheel),  $r_{b(1,2)}$  present base radius (pinion, wheel).

The bending stress  $\sigma_F$  is given by

$$\sigma_F = Y_F Y_\epsilon K_A F_t / b m_n \quad (4.5)$$

where  $F_t = 2 \times 10^3 \times T_1 / d_1$ ,  $T_1$  is transmitted torque,  $d_1$  is diametrical pitch and  $Y_\epsilon = 0.2 + (0.8 / \epsilon_\alpha)$ ,  $Y_F$  and  $K_A$  values are given in BS 6168 (1987).

The relative incremental ratios of Hertzian contact and bending stresses, load and wear rate are presented as a column graph in Figure 4.3. As all the cases are running at the same speed 1000 rpm, therefore, PV (contact pressure-velocity) mainly depends on the contact pressure values. Note that for loads of less than 8 N·m, the degree of wear rate increases less than the increase of contact and bending stresses, which indicates that low load does not greatly impact on the wear of gears. However, when loads are between 8 and 9.5 N·m, the average wear rate seems directly proportional to contact stress. When the loads are greater than 9.5 N·m, test results show that the increase in wear rate has greatly exceeded increase in contact and bending stresses. Note that an increase in load results in a rise in the tooth body/flash temperature (see temperature measurement results in Chapter 6). Then subsequently the high temperature causes an increase in Poisson ratio and a reduction in Young's Modulus. Consequently the contact stress gets reduced, and then the PV value reduces as well. In high load cases the heat does not originate dominantly from sliding friction, but also from increases in heat generation by air trapping between teeth, hysteresis and perhaps thermal conduction from the shafts. Therefore the temperature of teeth in contact is expected to be much higher than that at medium load cases. It perhaps causes the material microstructure and coefficient of friction varies greatly, and ultimately results in augmentation in

wear rate. For further more detail in dynamic temperatures and wear rates, see Chapter 6.

Table 4.2 Predicated stresses at pitch point and actual wear rate due to variations in load

Load (N·m)	Relative ratio of load	Contact stress	Bending stress	average wear rate
5	1.0	1.00* $\sigma_H$	1.0* $\sigma_F$	1.00 * $k_a$
6	1.2	1.095* $\sigma_H$	1.2* $\sigma_F$	2.0745* $k_a$
7	1.4	1.183* $\sigma_H$	1.4* $\sigma_F$	2.3517* $k_a$
8	1.6	1.265* $\sigma_H$	1.6* $\sigma_F$	11.371* $k_a$
8.5	1.7	1.304* $\sigma_H$	1.7* $\sigma_F$	18.913* $k_a$
9	1.8	1.342* $\sigma_H$	1.8* $\sigma_F$	25.446* $k_a$
9.5	1.9	1.378* $\sigma_H$	1.9* $\sigma_F$	42.223* $k_a$
10.1	2.02	1.421* $\sigma_H$	2.02* $\sigma_F$	125.83* $k_a$
12.1	2.42	1.556* $\sigma_H$	2.42* $\sigma_F$	133.02* $k_a$
14.1	2.82	1.679* $\sigma_H$	2.82* $\sigma_F$	334.35* $k_a$

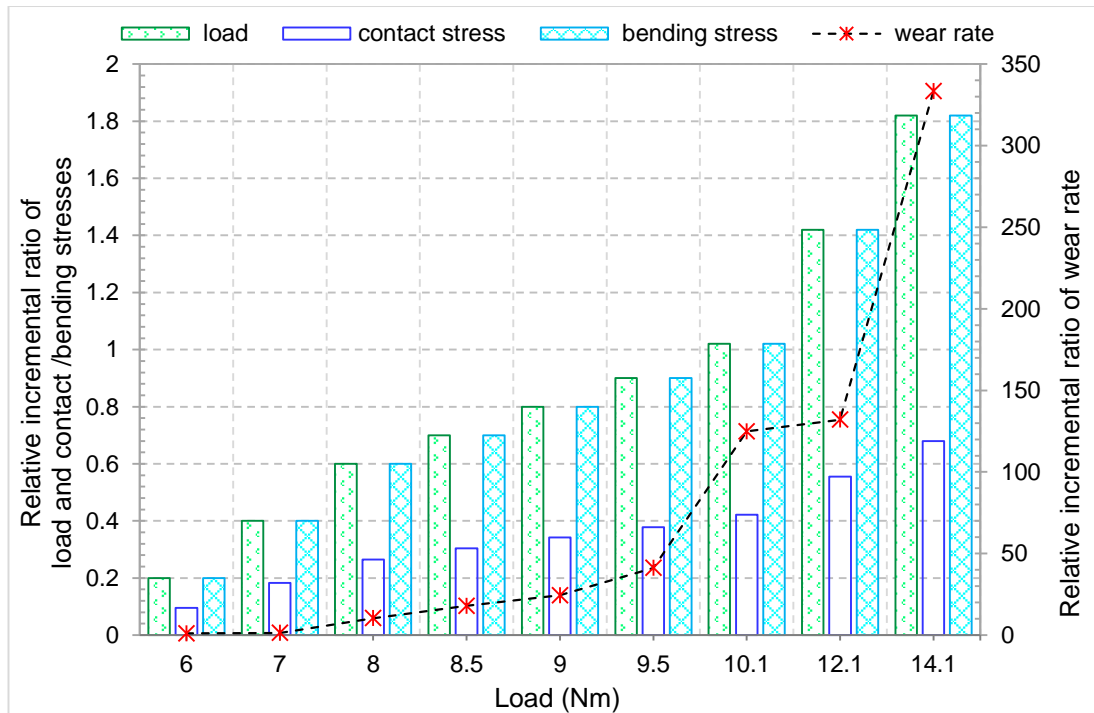


Figure 4.3 Relative incremental ratio of parameters due to variation in load

As discussed previously, many mechanical properties of polymers depend highly on temperature, a high increase in wear rate is expected to be associated with surface temperature of operating gears. Hence, to



understand and predict accurately wear behaviour of polyacetal gears, it is essential to obtain valid gear operating temperatures from tests, corresponding to thermal expansion, material creep, Young's modulus, coefficient of friction, material absorbing heat energy rate and so on.

A conclusion is drawn that to understand the wear mechanism of polymer gears, it is crucial first to estimate operating temperatures on polymer gears.

### **4.2.2 Topography of worn teeth**

The topography of worn tooth surfaces is related closely with the contact patterns of gears. When a pair of gears is in mesh, the contact form of mating teeth is line contact. However for polymer gears, a low Young's modulus, high environment temperature or high contact loads may result in a broad area instead of line contact.

A gear's motion involves a mixture of sliding and rolling contact and their directions differ between driving and driving gears. Figure 4.4 illustrates rolling and friction directions when one mating gear tooth pair enters and then leaves mesh [96]. The friction direction is the direction of the friction force generated on a tooth by the sliding contact of the counter mating tooth. The rolling direction of driving gears is from tooth root to tooth tip and of driven gears is from tooth tip towards tooth root. The friction direction of a driving gear is away from the pitch line towards both tooth root and tip. The friction direction of driven gear is conversely from tooth root and tip towards the pitch line. Pure rolling acts only at the pitch point. Such types of gear

contact may result in material flow in the sliding directions. The directions of rolling and friction mutually affect the distribution of wear debris and the location of wear over tooth contact surfaces.

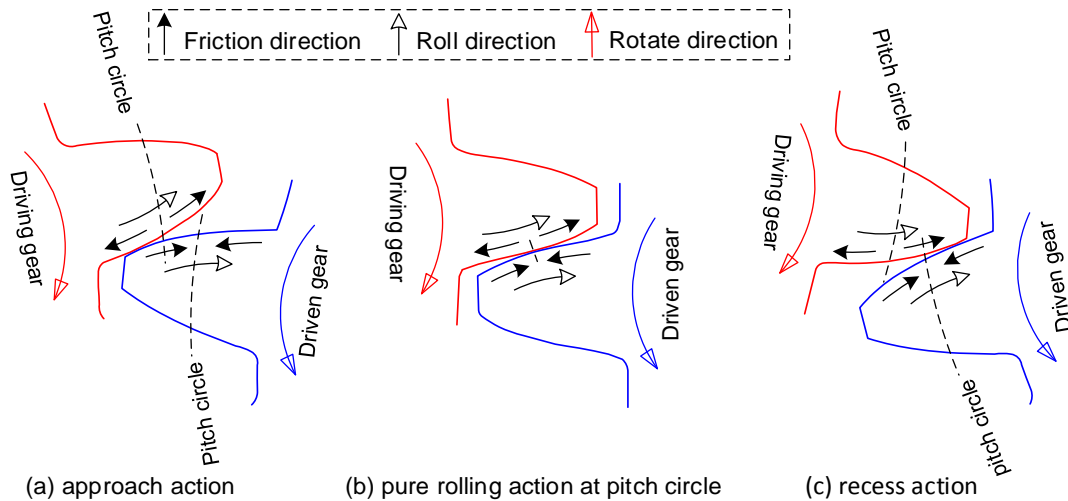


Figure 4.4 Sliding and rolling directions of driving and driven gears

Varying topographies of worn tooth surfaces and topologies of worn tooth flanks were examined through the scanning electron microscope (SEM) and Bruker ContourGT 3D optical profiler. Firstly 'groove' wear marks form in pitch line zone of drivers and 'ridge' wear marks at the region of the pitch line of driven gears, which agree with the statement of Breeds [96]. Secondly, the addendum of drivers and dedendum of driven gears are smoother than their counterparts. Thirdly, copious (flat plate-like) wear debris distributes close to and along the pitch line of the addendum side on a driver and the dedendum side on a driven gear. Fourthly, an increasing number of pits are observed while approaching the pitch line zone from the tooth tip and from its root. There were more visible over dedendum of driver and addendum of driven gears. Fifthly, visible 'sand wave' topographic patterns (wear marks) occurred over the dedendum of driver and addendum of driving gear, which

gets more evident when getting close to pitch line. It is interesting to note that there is always wear debris spreading in the vicinity of 'sand wave' wear marks. Detailed examinations through using SEM and Bruker ContourGT 3D optical profiler are described below.

When the load is less than 8 N·m, significantly visible wear characteristics were observed on worn tooth surfaces. 'Groove' and 'ridge' wear marks are presented in the vicinity of pitch line of driver and driven gears respectively as shown in Figure 4.5. Also, heavy wear debris scatters along the pitch line, close to the addendum of the driver and dedendum of the driven gear. Figure 4.6 depicts the wear characteristics mentioned above and it can only be seen on worn tooth profiles with light wear, such as a polyacetal gear pair running for  $6 \times 10^5$  cycles at a load of 7.5 N·m and a speed of 1000 rpm. For long term operation or large power transmission conditions, severe deterioration of the tooth profile develops due to abnormal wear.

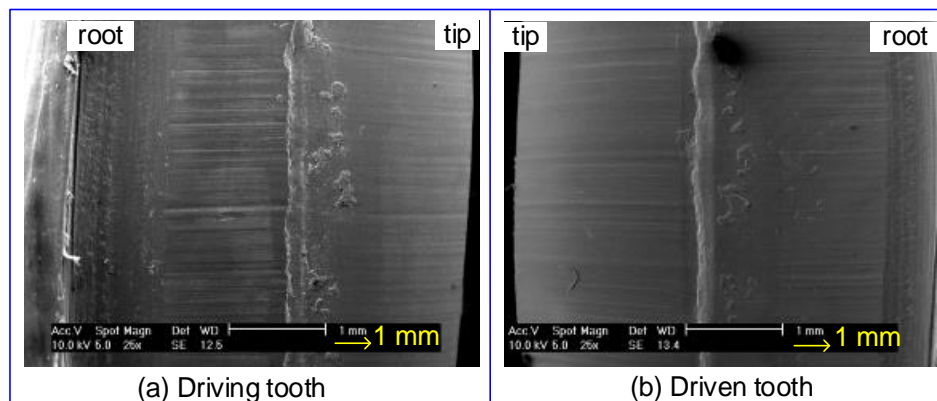


Figure 4.5 SEM micrograph of full view of worn teeth (7.5 N·m  $5.4 \times 10^5$  cycles)

The shapes of worn tooth flanks from high-load tests are distinctly different from those at low loads. The Bruker optical profiler was exploited to examine the worn tooth flank profiles. Figure 4.7 clearly demonstrates that

worn tooth flanks of a driver gear present an 'S' shape and there is a complementary shape on driven gear flanks. Note that a wear groove occurs closely along the pitch line of the driven tooth where the relative sliding velocity is approximate zero.

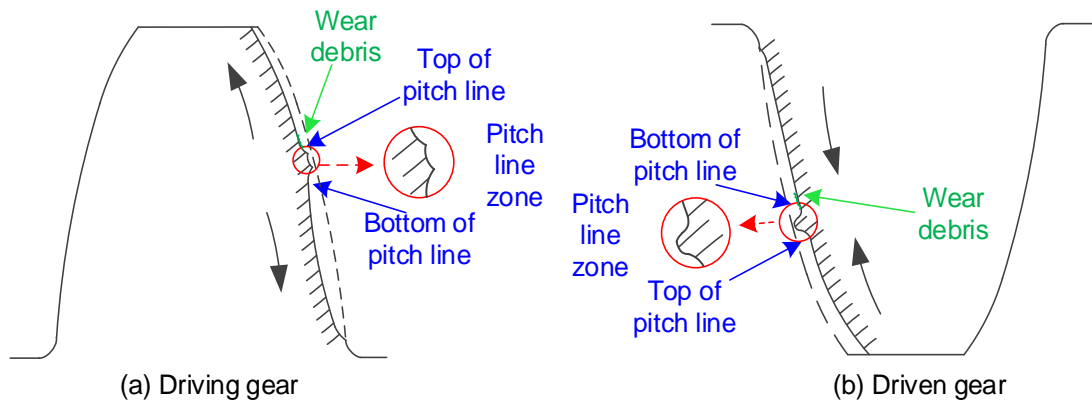


Figure 4.6 Schematic diagram of worn tooth topology and major wear debris distribution

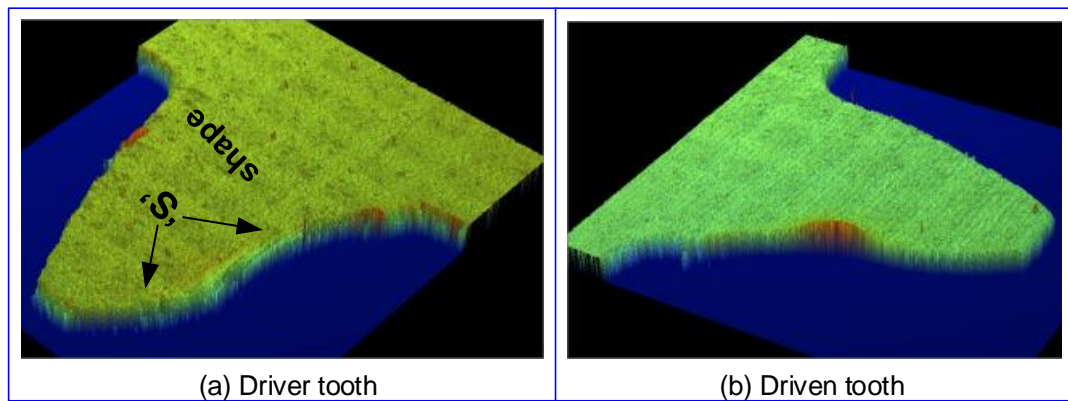


Figure 4.7 Topology of worn tooth flanks (scanned by ContourGT 3D optical profiler)  
(At a load of 9.7 N·m, a speed 1000 rpm, after duration  $3.16 \times 10^4$  cycles)

#### 4.2.2.1 Low load cases

It is perceived that more visible wear marks, pitting, and wear debris are present on the component of worn tooth surfaces which act in the 'approach action' in gear transmission as described in Figure 4.4 (a), namely the dedendum of driver and addendum of driven gears. For instance, marked 'ploughing' wear marks shown in Figure 4.8 (b) spread over the dedendum of driver and addendum of driven gears. In stark contrast, clearly

visible 'sand wave' wear marks, as shown in Figure 4.8 (a), disperse over the tooth sections which perform recess actions, namely addendum of the driver and dedendum of the driven gear (Figure 4.4 (c)).

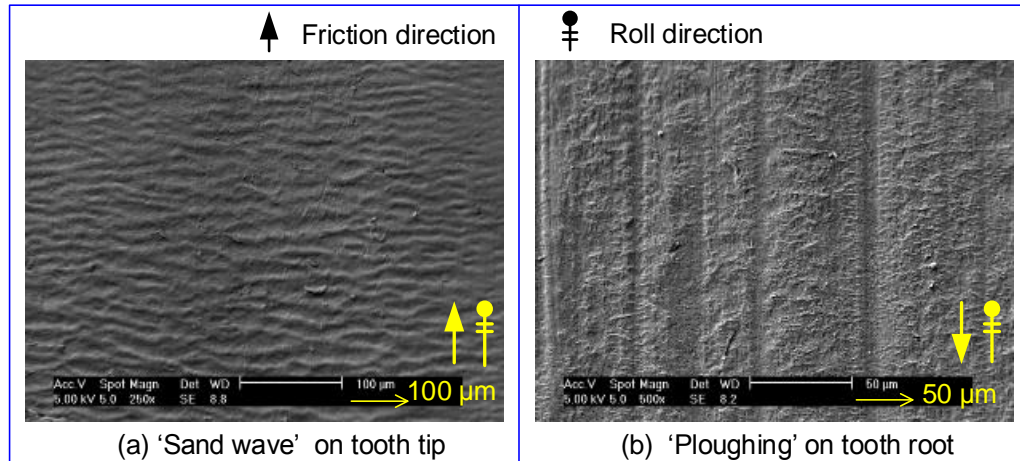


Figure 4.8 SEM micrograph of 'sand wave' and 'ploughing' wear marks on driver gear (At a load of 7.5 N·m, speed of 1000 rpm, after duration  $5.4 \times 10^4$  cycles)

A quantity of pits, as shown in Figure 4.9, scattered on worn tooth surfaces, is rather evident on the tooth parts coming into mesh. Overall, the number and size of these pits increase when getting close to the pitch point (the rolling ratio increases as well). It can be found on worn tooth surfaces across almost all the load range. Clearly pitting is one typical mode of surface wear fatigue for polymer gears as well as for metallic ones.

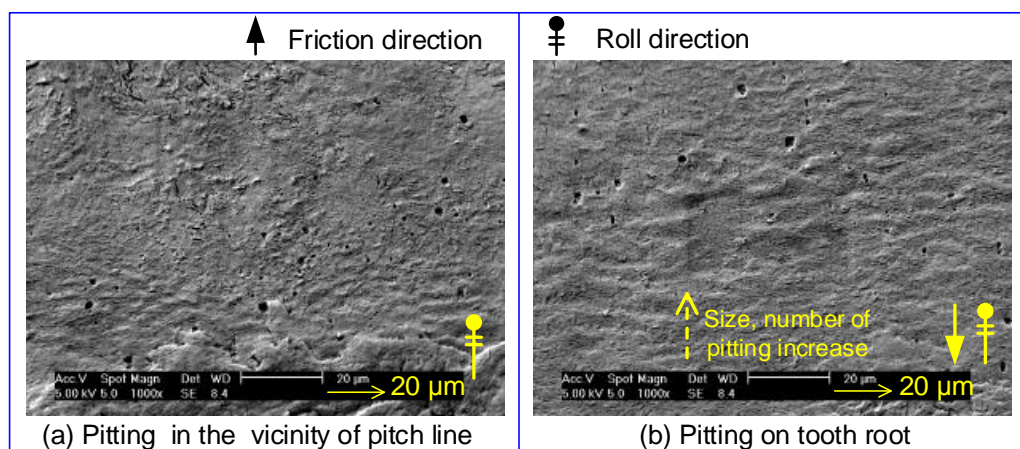


Figure 4.9 SEM micrograph of quantity of pitting on driver tooth

Through numerous SEM examinations, it is interesting to note that wear debris could always be found somewhere surrounding ‘sand wave’ wear marks. Figure 4.10 demonstrates clearly the relation of ‘sand wave’ wear marks and wear debris. Their generation and development may interact with each other. Certainly the sliding and rolling actions are also essential contributors.

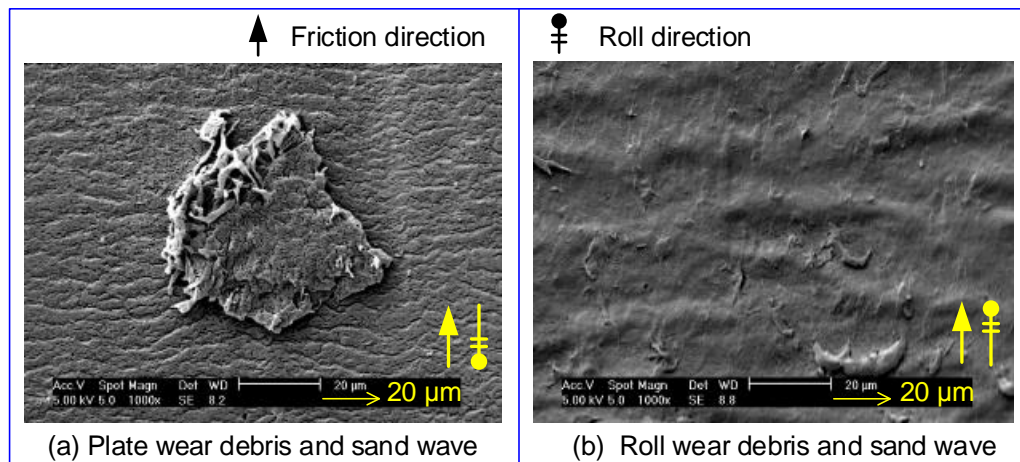


Figure 4.10 SEM micrograph of wear debris and ‘sand wave’

It is common to see fine thread, roll, rod and flat plate wear debris on wear surfaces of polyacetal gears. However, it is rare to observe small wear particles of around 7 μm as shown in Figure 4.11. In close-up view, it resembles slightly a balloon after bursting or splintered shell. Its origin is not currently clear, but it may arise from the growth of cracks, outset of delamination or early stage of spalling. Proceeding through further repetitions of mesh it may be peeled or cut off by shear forces. Consequently it is likely to be rolled into roll, rod or bulk debris under cyclic rubbing actions of the mating teeth surfaces. Understanding its formation mechanism and its prospective evolution will require further studies.



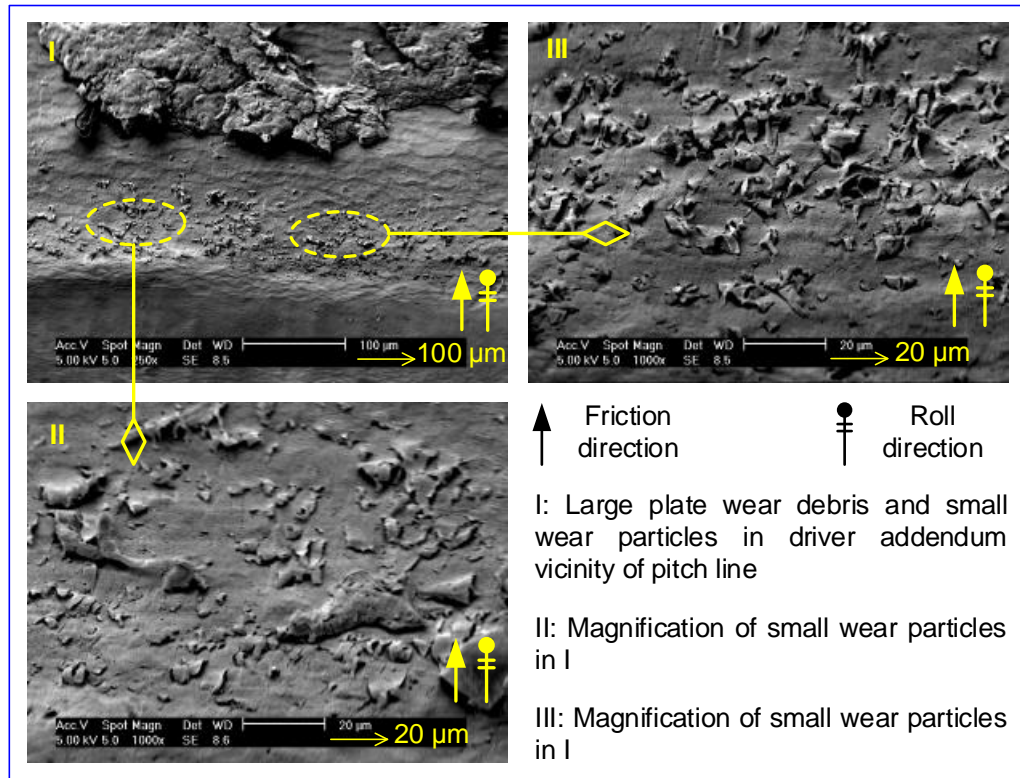


Figure 4.11 SEM micrograph of wear particles near pitch line zone at a load 7.2 N·m

#### 4.2.2.2 Moderate load cases

Compared to light load cases, more severe wear happened to polyacetal gears at medium loads. Scanning electron micrographs revealed that in addition to large sizes and amounts of wear marks and pitting, adhesive wear may occur. For instance, Figure 4.12 demonstrates adhesion at a load of 8.4 N·m, a speed of 1000 rpm, and shows that the bulk wear debris is spread around at rolling and sliding contact. In such conditions superficial material on a tooth may develop highly viscoelastic behaviour and, therefore, some wear particles are likely to grow into elongated rolls with curves, like worms. Figure 4.13 is a good example of them.

In spite of the occurrence of adhesive wear, there is still evidence of

surface peel and some debris developing into rolls or rods. Figure 4.14 confirms this view, showing the occurrence of stacks of rod/roll wear debris near pitch line region and delamination far from pitch line. In view of the dispersion of subtle thread (Figure 4.13) and roll/ rod wear particles, it is speculated that the roll/ rod wear debris possibly evolves from the former under high rolling action (especially in regions approaching pitch line). One more thing worth mentioning is that during operation noise was noted like those of taking apart two components glued together and, when demeshing the gear pair after test, it seemed that teeth in contact were virtually glued together. The higher the load, the harder it was to separate the gear pair. It denotes that scuffing surface damage occurs on engaging teeth.

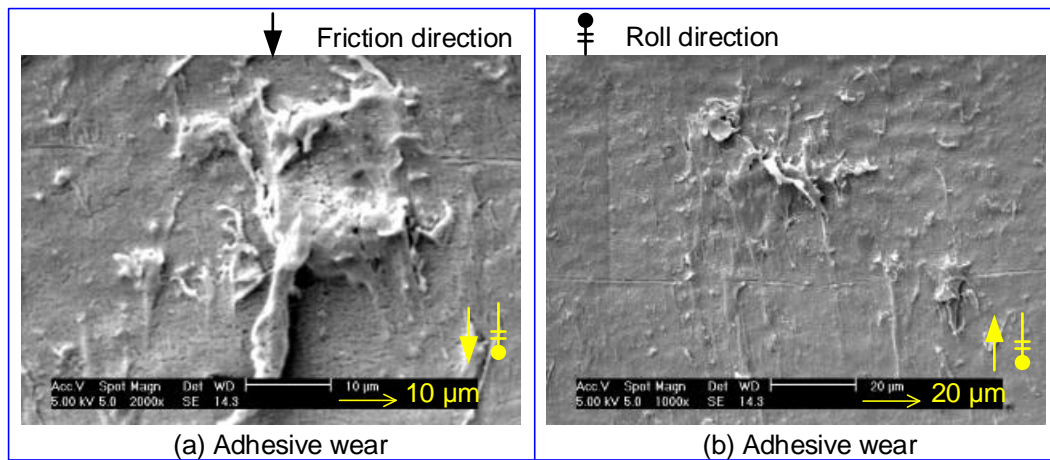
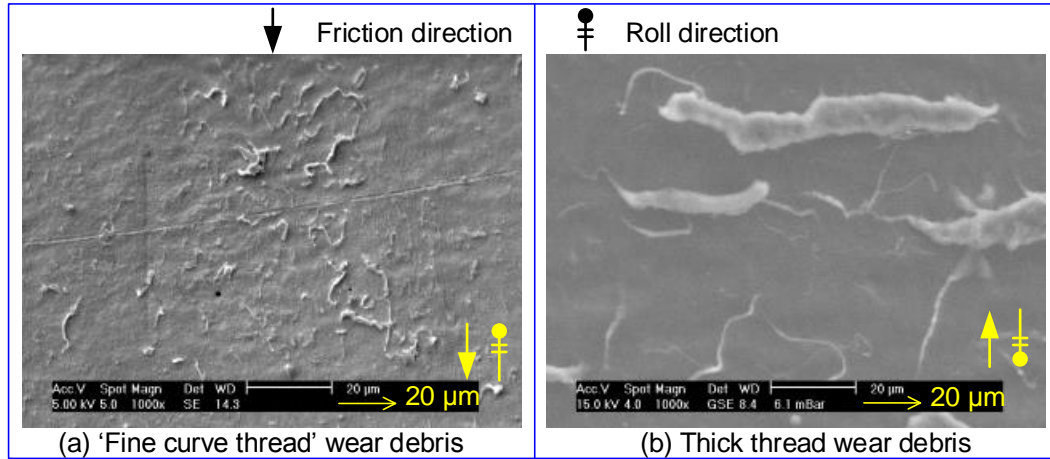
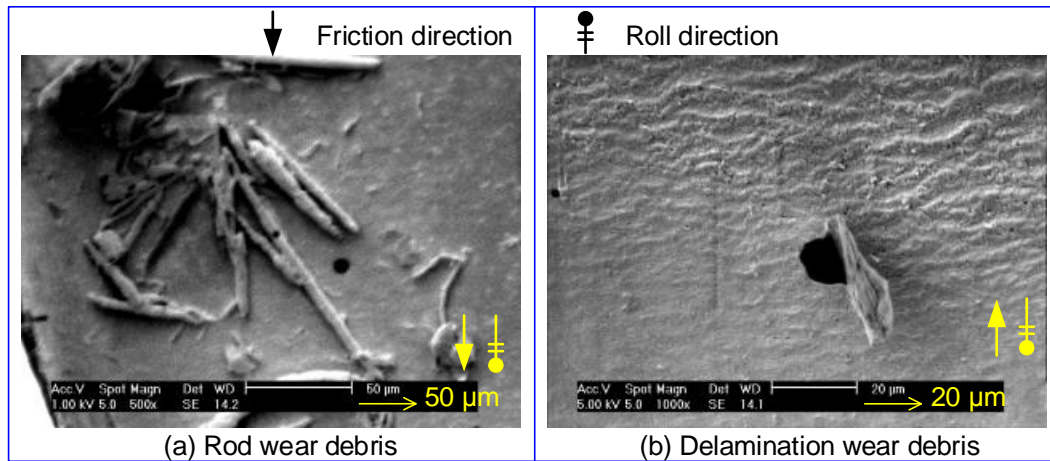


Figure 4.12 SEM micrograph of adhesive wear (load 8.4 N·m duration  $1.17 \times 10^5$  cycles)



Figure 4.13 SEM micrograph of thread wear debris (load 8.4 N·m duration  $1.17 \times 10^5$  cycles)Figure 4.14 SEM micrograph of wear debris (load 8.4 N·m duration  $1.17 \times 10^5$  cycles)

#### 4.2.2.3 High load cases

Extensive experimental investigations as previously described prove that adhesive wear is one principal wear mechanism of polyacetal gears in medium load cases. Moreover the melting point of polyacetal is rather low, 165°C. Hence heat generated in gears in relation to high load (without lubricant) contains not only the friction heat between two rubbing surfaces but also increased heat resulting from hysteretic losses, air trapping between teeth, interference fit (due to rapid expansion of teeth). Hence, wedging, material melt flowing, elongated stretching and tooth bending are expected to be primary wear mechanisms of polyacetal gears. Gears' premature

failure is likely to ensue in the form of tooth softening and bending or local melt stretching (viscoelastic deformation) within short operating period.

On the basis of previous studies on temperature distributions in nylon gears, such as Takanashi *et al.* and Terashima *et al.* [29, 71], it is predicted that the most elevated temperature region for polyacetal gears also locates in the centre of the tooth flank and close to the pitch point as depicted for pitch line zone II in Figure 4.15. Consequently, corresponding contact surfaces initially melt in region II and material flows around under the influences of rubbing between mating tooth surfaces.

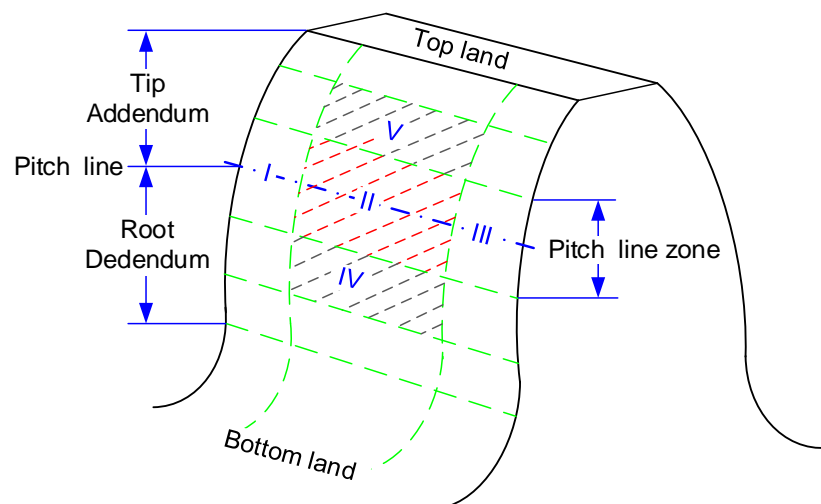


Figure 4.15 Schematic diagram of prospective material melting region on tooth surfaces

Figure 4.16 and Figure 4.17 exhibit a typical melting wear state on driving and driven teeth at a load of 9.7 N·m, a speed of 1000 rpm and duration of 31600 cycles. The most severe wear effectively takes place in the vicinity of the pitch line where the material gets melted and spread around. There are marked openings in the approximate scale of 0.8 mm x 0.3 mm and macro-cracks within pitch line zone III of driver and driven teeth. The openings and large cracks along pitch lines are expected

to grow and join together with other cracks if the test did not stop in short period which resulted in substantial weakness in tooth bending strength and consequently incurred tooth softening or excessive thermal elongated (creep) deformation near pitch lines. Of course, if loads being higher than 9.7 N·m also results in similar modes of failure. A case of tooth excessive thermal elongated (creep) deformation can be exemplified strongly by Figure 4.61 in Section 4.3.10.

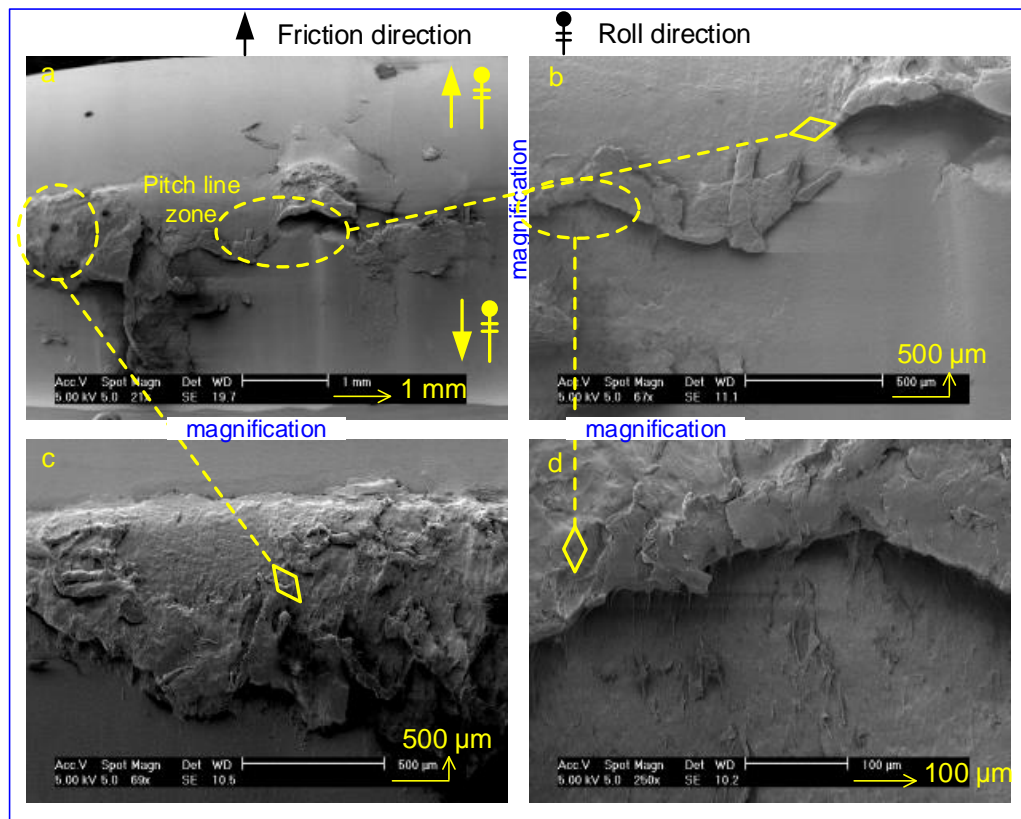


Figure 4.16 SEM micrographs, at different magnifications of the same area of worn tooth surface of driving gear (9.7 N·m,  $3.16 \times 10^4$  cycles)

Next to the melt band (zone II), the tooth components (dedendum of driver and addendum of driven gears) entering mesh are predicted to be the second highest temperature regions, where the local mechanical properties of polyacetal will become deteriorated. Broad SEM examinations reveal that

major excessive heat is accumulated in the pitch line zone II and the centre of the driver root as well as driven tooth tip as zones IV and V sketched in Figure 4.15. For instance, Figure 4.18(a) and Figure 4.19(a) illustrate material degeneration spreading on 'sand wave' patterns and a quantity of pits in regions II and IV of the driver tooth. In contrast with Figure 4.18(a), there is no degradation and pitting apart from some wear debris and slight 'sand waves' in Figure 4.18(b).

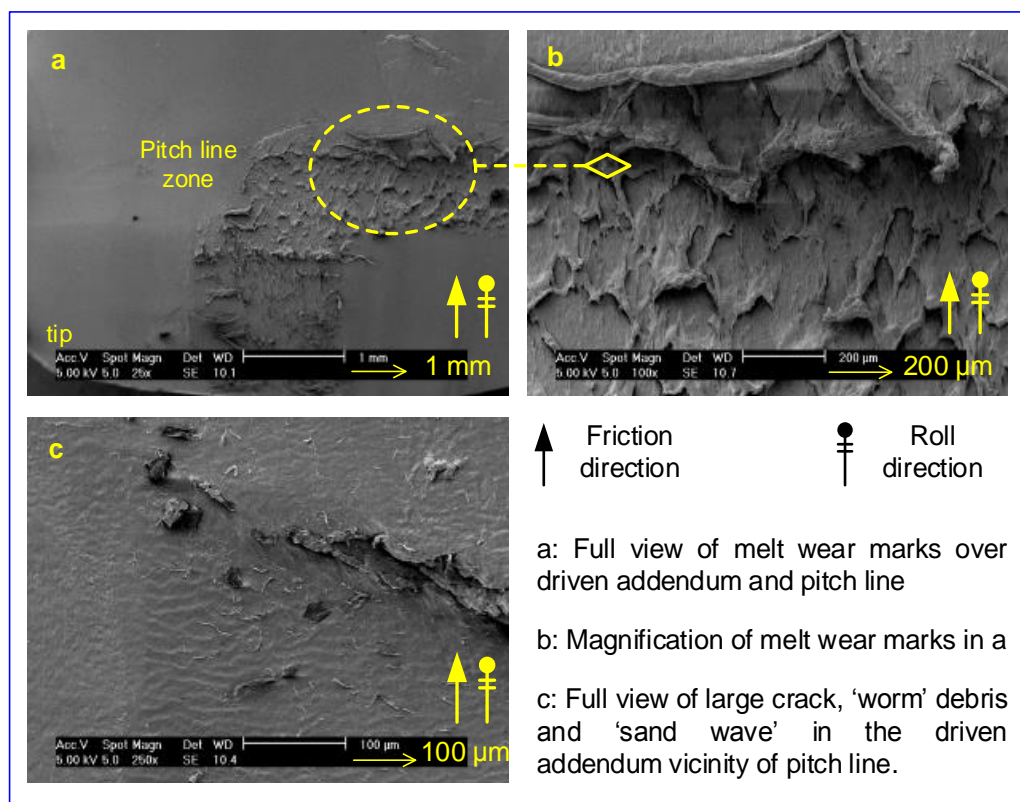


Figure 4.17 SEM micrographs, at different magnifications of the same area of worn tip surface of driven tooth (9.7 N·m,  $3.16 \times 10^4$  cycles)

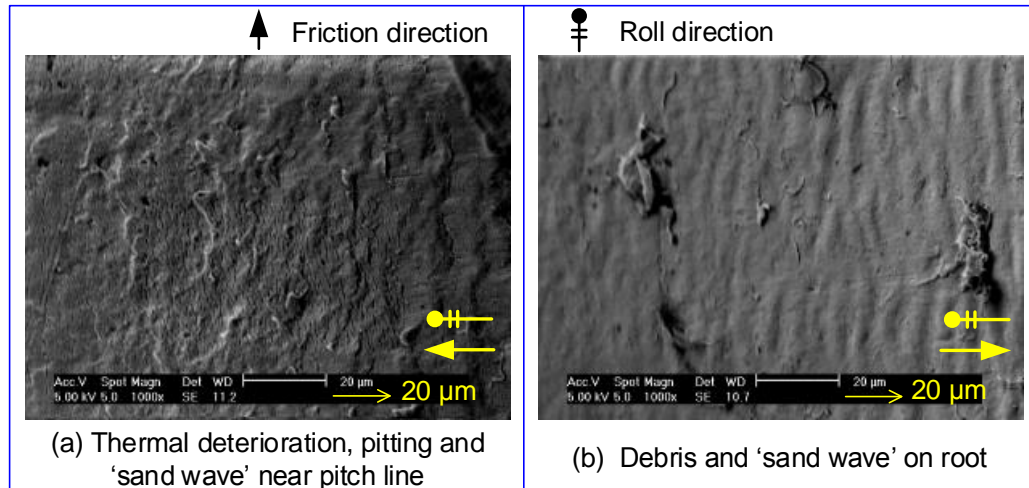


Figure 4.18 SEM micrographs of worn tooth surfaces of driver gear

In addition to the marked melting scars, bulk pieces, 'fish scale' and elongated roll wear debris are also present on the corresponding driving and driven gear tooth parts which are active in the approach process. Figure 4.19 shows that 'fish scale' wear debris (in Figure 4.19(b) may also show micro-cracks) is slightly away from the pitch line towards the driving tooth root: it closely resembles that present on the worn tooth surfaces subjected to axial misalignment discussed in Section 5.2.2. Its generation is perhaps associated with the temperature of the tooth surface, the volume of wear debris and sliding-rolling actions (cyclic tensile, compressive and shear stresses), but its origin remains to be determined by further investigations.

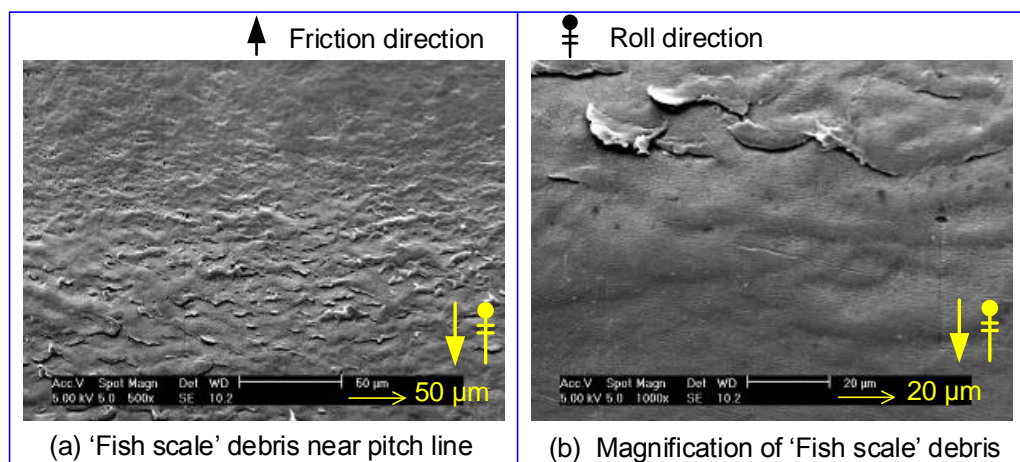




Figure 4.19 SEM micrographs of 'fish scale' debris in the driver root vicinity of pitch line

Strikingly different characteristics of 'worm' wear debris, curly roll and thread, as shown in Figure 4.20, are noted on wear tooth surfaces. Moreover, their distribution presents a certain regularity in that the dimensions (length and diameter) decrease from pitch line towards driving tooth roots and driven tooth tips respectively. However almost no 'worm' wear debris was found near the ends of driver roots and of driven tips where there were only some slight 'sand wave' wear marks and some bulk wear debris. Viewing the positions of melting and degeneration and debris on worn tooth surfaces, it is surmised that the formation mechanism of roll and elongated roll wear debris is related to temperature. It is also likely that fine thread wear debris evolves successively into roll and bulk wear debris, which implies a fundamental nature change in a gear's wear process.

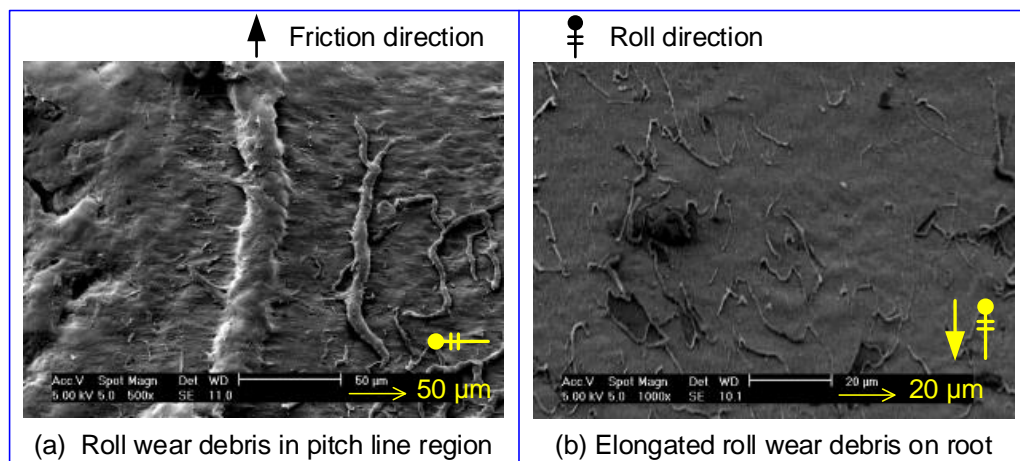


Figure 4.20 SEM micrographs of elongated roll wear debris of driver gear

Overall, extensive SEM examinations clarify that polyacetal gears bearing high power transmission are expected to suffer macro cracks, softening, melt flowing (plastic flow) and degeneration of material properties, with 'fish scale'/micro cracks and roll wear debris on not only the roots of

driver teeth but also the tips of driven teeth, but only slight wear over addendum of driving gear and dedendum of driven gear. Hence at heavy load cases, premature failure of gears is likely to be in the form of tooth bending/softening, openings (macro-cracks) and excessive thermal elongation/creep/stretching (plus sudden jump out of engagement) near the pitch line.

### **4.2.3 Regime of wear debris**

A large number of studies on wear particles has been conducted within the research of wear mechanisms and tribology systems of metallic gears' transmissions [112-114]. However, the role of wear debris has not received enough attention in the research of polymer gears [7, 19, 52, 116]. The current extensive experimental investigations reveal that wear debris have great influence on the wear behaviour of polyacetal gears. Note that cases where copious wear debris fly out from mating gears tend to correlate with a reduction in wear rate, surface temperature of operating gears and airflow temperature surrounding mating gears, discussed in Sections 4.3.3 and 6.4.1. Strikingly different regimes of wear debris are noted between varying load ranges. Various regimes of wear particles may indicate polymer gears' operating condition (load, gears' operating temperature, wear phases, aligned/misaligned mesh and so on). Therefore, the investigation of the regimes of wear debris is focused on here.

Five main categories of regime of wear debris are observed in these aligned tests: powdery, small translucent lamellate, translucent 'needle',

'snowflake/cotton' wear debris and 'belt' wear debris. In fact, some shapes and scales of debris are present solely in certain load ranges. Hence it is speculated that the origin of various forms of wear debris may relate closely with contact stresses sliding/rolling actions and surface temperatures of gears. The presence and characteristics of wear debris at the three load ranges are conspicuously different. Hence, the varying features of wear debris are elaborated below in terms of the range of test load.

#### 4.2.3.1 Low load cases

Low load tests generate mainly two classes of wear debris, which are translucent lamellate and powdery debris as shown in Figure 4.21. The size is up to around 0.2 mm x 0.2 mm. The translucent lamellate wear debris primarily occurs prior to gears' steady wear phase. Powdery wear debris dominates the steady wear phase.

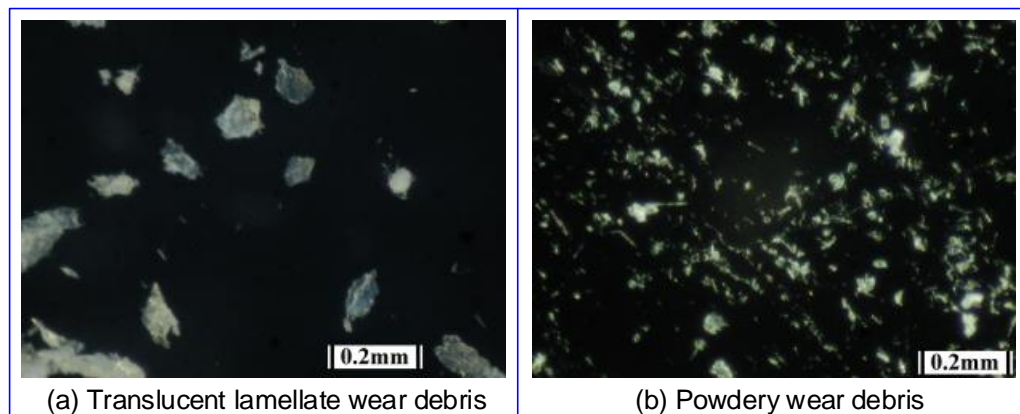


Figure 4.21 OM micrographs of wear debris generated at low load

However, there may be another type of wear debris (granular debris as shown in Figure 4.22) present in small amounts, which also presents more commonly in the tests at medium load range. In close-up view, it is also similar to that produced in tests subjected to axial misalignment. The



slight discrepancy is that the shape of granular wear debris is not as sharp as in the axial misaligned case (see Section 5.2.3). It might, then, may result from an axial gap smaller than that in the axial maligned tests. Therefore the formation of granular wear debris is most likely to be caused by the unavoidable slight residual axial misalignment (axial gap less than 0.6 mm).

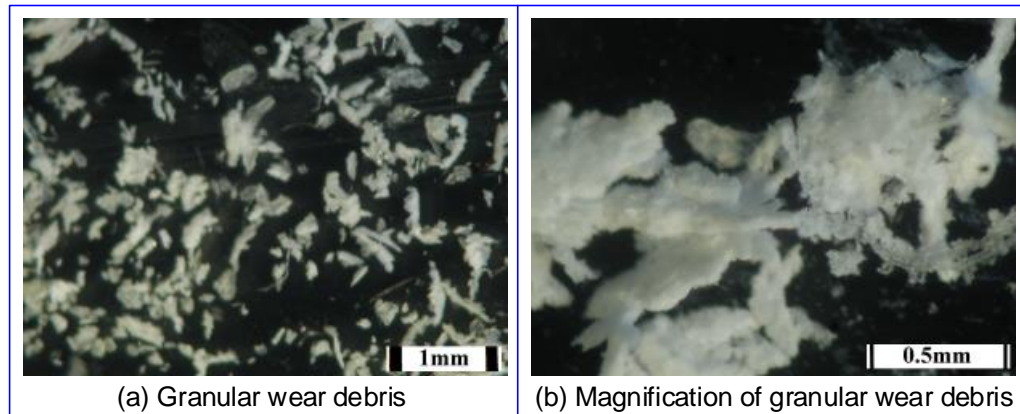


Figure 4.22 OM micrographs of granular wear debris at low loads

#### 4.2.3.2 Medium load cases

For medium load tests, three major categories of wear debris were presented, namely translucent lamellate, roll and 'snowflake/cotton-wool' wear debris. The typical sizes of wear debris are greater than in the low load tests.

Figure 4.23 shows the wear debris that appears mainly preceding the steady wear phase. Translucent lamellate wear debris as shown in Figure 4.23 (a) is similar to that in tests subjected to low load. Its formation is possibly caused by the contact surface asperity of new gears being sheared off between relative moving actions of the teeth. The amount of roll wear debris shown in Figure 4.23 (b) increases as load increases.

The primary wear debris during steady wear phase is roll wear debris, as shown in Figure 4.24 (a). The roll wear debris may be directly resulting from the narrow line-area contact cuttings or may roll from the lamellate or large pieces of wear debris into 'roll' wear debris under the tooth roll actions. Figure 4.24 (b) exhibits snowflake-like wear debris which can occur at medium load tests, but only in small amounts, not as heavy as that in pitch misaligned tests (see Chapter 5.5.3). In close-up view, it is mainly made up of a large amount of small roll wear debris.

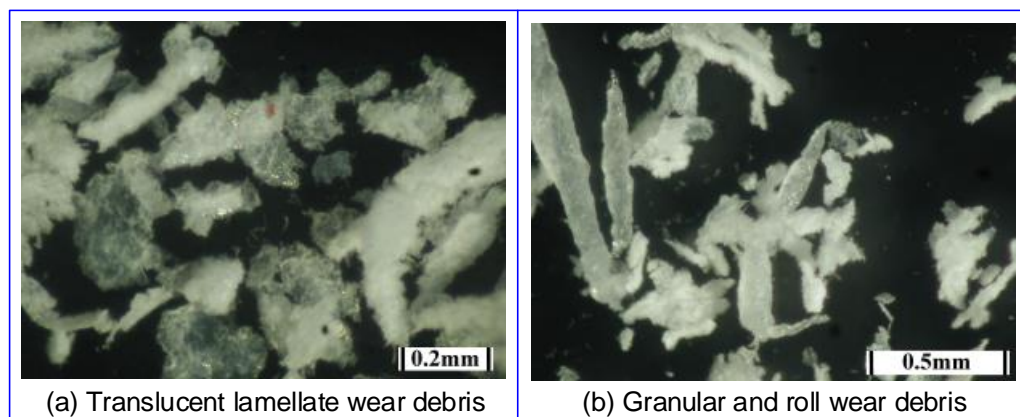


Figure 4.23 OM micrographs of primary wear debris yielded before steady wear phase

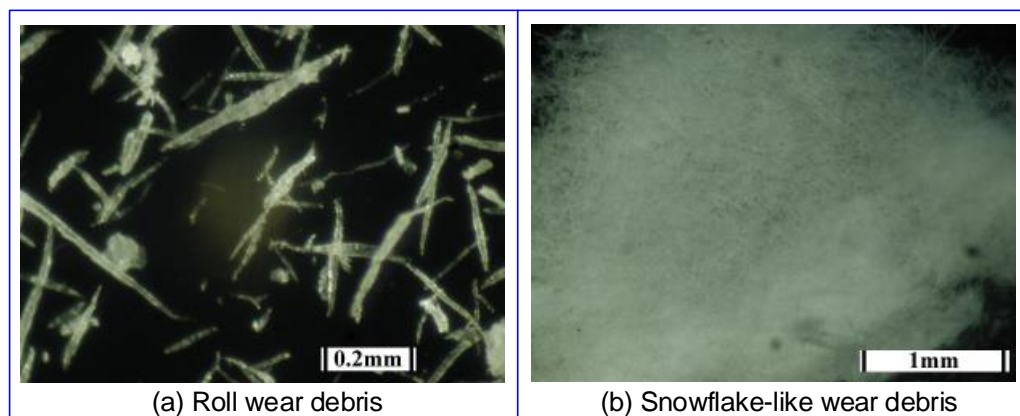


Figure 4.24 OM micrographs of 'snowflake' wear debris

#### 4.2.3.3 High load cases

For high load tests, three predominant categories of debris were observed, namely large pieces and elongated roll and transparent bulk slice

wear debris. The large pieces and elongated roll wear debris are shown in Figure 4.25. The large pieces are semi-transparent and their surfaces are quite rough. They, perhaps suffer from numerous cyclic shear cutting forces prior to currently ultimate formation. It is surmised that the generation of elongated roll wear debris may experience less number of cycles. An increase in load results in an increase in the typical sizes of wear debris.

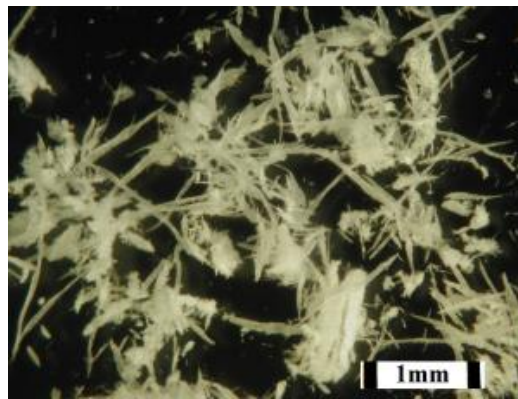


Figure 4.25 OM micrograph of wear debris yielded at high load tests

The transparent bulk slice wear debris presented almost immediately the test initiated, which suggested that the material was torn off /peeled off. The formation mechanism of the translucent bulk slice wear debris is due to significant thermal expansion caused by high friction heat, and subsequent the engaging gears becoming, in effect, an interference fit. Consequently, the material is removed once relative motion of mating teeth occurs. A classic example is shown in Figure 4.26.

Following a reduction in the quantity of translucent bulk slice wear debris as the test progressed, long roll wear debris became the primary debris. The size was much greater than that at medium load. For instance, Figure 4.27 exhibits the roll wear debris at a load of 14.1 N·m.

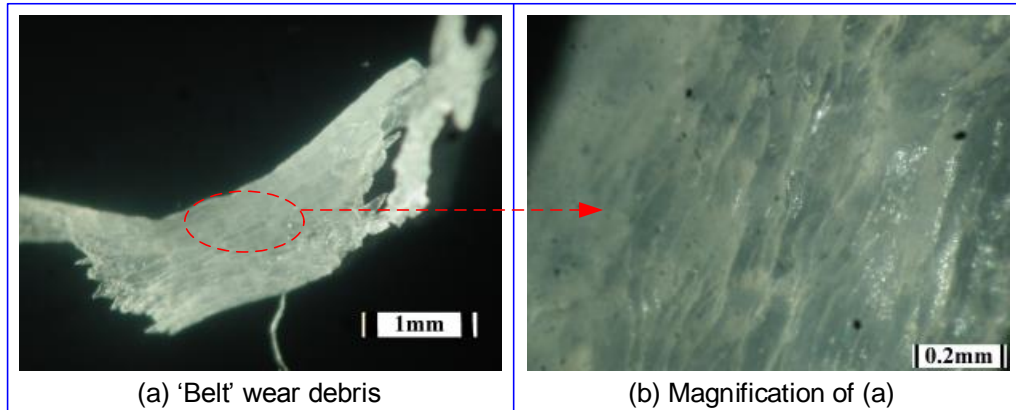


Figure 4.26 OM micrographs of bulk slice wear debris present at a load of 14.1 N·m.

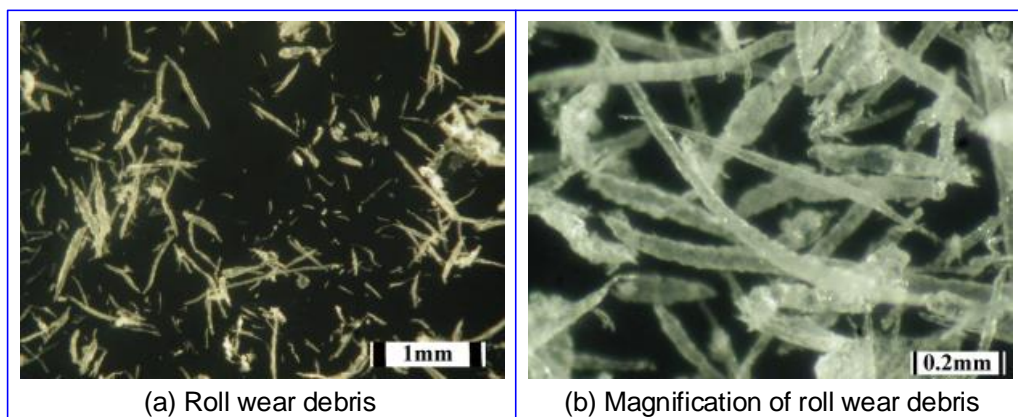


Figure 4.27 OM micrographs of elongated roll wear debris

## 4.2.4 Conclusions

### 4.2.4.1 Wear and wear rate

Consistently an increase in load results in an increase in wear rate and decrease in wear life. Test results indicate that the wear transition corresponds to the maximum surface temperatures of operating gears which degrade the mechanical properties of polyacetal.

When engaging gears are running at low load, the wear rate tends to decrease slightly with operating duration increasing. The wear rate tends to reduce if visible debris falls away from the gears. It indicates that the wear debris may be one component contributing to the generation of friction heat

or bringing heat away from the gear teeth.

At medium load, gears' wear exhibits a transition operating stage, where a sudden significant increase in steady wear rate occurs and wear rapidly reaches allowable limits.

At high load, the wear slope is extremely steep at all times from initiation virtually always fail due to driving and driven tooth binding or the driver tooth melting near the pitch line and getting elongated.

### **4.2.4.2 Topographies of worn tooth surfaces**

The profile of worn tooth flanks varies in the depth of the tooth wear. Severe wear occurs over the dedendums of driver gears and addendums of driven gears, where typical 'ploughing' wear patterns are present. Over the counterparts, 'sand wave' wear marks spread. Wear debris could always be noted somewhere around 'sand wave' wear patterns. The initiation and growth of the 'sand wave' and wear debris perhaps interact with each other. Of course, the sliding and rolling actions contribute them too. The numbers and sizes of pitting increase with getting close to the pitch line. 'Fish scale' wear debris was noted near pitch line zone. Plate-like or roll wear debris compacted on the contact surfaces tend to result in deep wear marks, such as the visible 'sand wave' and 'ploughing' wear marks. Local excessive heat build-up on tooth surfaces occurred in the cases of medium and high loads. The degradation of local contact surface material was noted. Marked plastic flow marks (resulting from melting) and macro cracks near pitch line zone II in high load cases were noted.

### 4.2.4.3 Wear debris

The investigation of various features of wear debris at varying loads and wear phases reveals that there are fundamental alterations in the process of gear wear.

The presence of translucent lamellate wear debris occurring in initial fast wear-in phases perhaps is due to tooth contact surface asperity interacting and shearing. The powdery-like wear debris in steady stage in low load cases is the most common consequence of the gear wear. The roll wear debris may develop from matching surfaces rubbing cyclically each other, and some is accumulated and finally is compacted into large pieces, such as granular and snowflake-like wear debris. However, it is surmised that the axial misalignment also contributes to the formation of the granular wear debris. If transparent bulk slice wear debris presents, it is likely that the polyacetal gears bear excessive contact load, and to fail instantaneously, such as the case load at 14.1 N·m. If the elongated long roll wear debris comes up continuously, it indicates interference fit between teeth may take place, such as the cases of tooth thermal expansion and creep. An increase in load tends to increase the dimension of roll wear debris. Long elongated roll wear debris was predominantly present in upper low load cases. Significant thermal expansion occurred when gears ran at high loads.

### 4.2.4.4 Wear /failure modes

Severe wear primarily occurs to the tooth component which acts with 'approach action' during the gears' engagement process

The wear mechanism of polyacetal gears at low load might be wear surface fatigue such as pitting; at medium load it may be surface fatigue (i.e. pitting, micro-cracks, spalling), adhesive wear, scuffing wear(welding), thermal creep, and bending fatigue; at high load it could be scuffing wear macro cracks, thermal creep/elongation, plastic flow (melt), softening and bending fatigue.

### 4.3 Endurance test results and discussions

Wear against life tests for polyacetal gear pairs were conducted with loads of 5 N m, 7 N m, 8 N m, 9 N·m, 9.5 N·m, 10 N·m, 12.1 N·m and 14.1 N m at speed of 1000 rpm. However due to unavoidable interruptions during tests (due to laboratory being shared by three groups), some long duration tests could not run continuously until the allowable wear teeth limit (3.14 mm) was reached. These tests were run to their finish in several successive stages (with no mechanical disturbance during the 'rest' periods) and so to assess the endurance of polyacetal gears at speed of 1000 rpm, a novel methodology of stitching test results was introduced. Detailed illustration of this methodology will be presented in Section 4.3.1.

It is interesting to note that the patterns of wear curves may be closely linked to environment temperature, gear bulk (body) temperature and types of wear debris observed.

### 4.3.1 Methodology for endurance tests

Imagine there is an ‘ideal’ wear signal running over the whole life as shown in Figure 4.28.

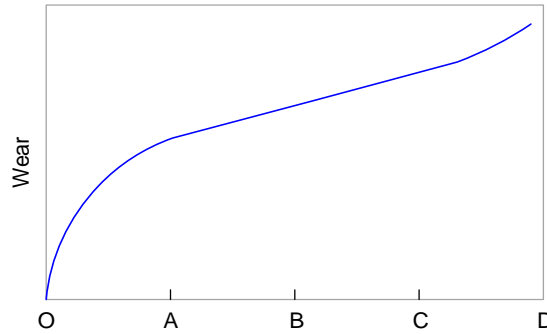


Figure 4.28 Schematic plot of wear versus duration

It can be looked upon as individual sections shown as in Figure 4.29, and it is clearly valid to re-attach these sections to reconstruct Figure 4.28.

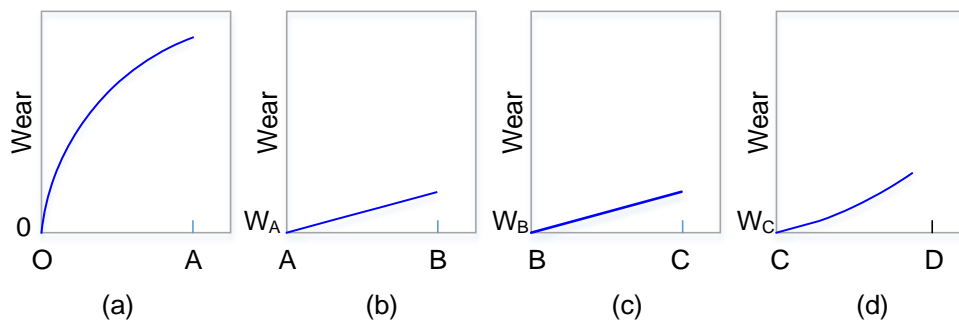


Figure 4.29 Schematic plot of four individual sections of signal

The data sets of interrupted tests here look a bit like Figure 4.29. Therefore it is reasonable under many practical conditions to ‘reconstruct’ a full wear life from the segments of an interrupted trial. However, there are some problems in interrupted gear endurance tests, which are listed as follow:

- Stopping an operating gear wear test will break the ‘steady state’ conditions;



- There will be a cooling to ambient temperature;
- It is useful to adjust the load bar to horizontal level (avoiding large cumulative load error)

Crucially, no other mechanical resetting was done beyond load bar adjustment. The effect is to expect a little extra 'start up' wear before the steady phase is re-established for each section. Figure 4.30 presents two individual test results obtaining from one gear pair wear test. There is a 'start up' wear ' $t$ ' in Figure 4.30(b), which may be not real wear, that would have been observed in a continuous test.

Therefore total 'reconstructed' wear estimate is conservative as it reports extra wear. It will not, though, be overly so (in practical terms) provided care is taken to apply reconstruction only in cases where the extra steps are small and each section rapidly recovers to a steady slope similar to that before the interruption. Taking the graph in Figure 4.32 (in Section 4.3.2) as an example, the slopes of L1 to L6 are almost the same in steady state. Note that the 'stop period' may affect the 'start up' value. When the 'stop period' is less than 40 minutes, the 'start up' step is marginal, such as L5 and L6 in Figure 4.32 (in Section 4.3.2).

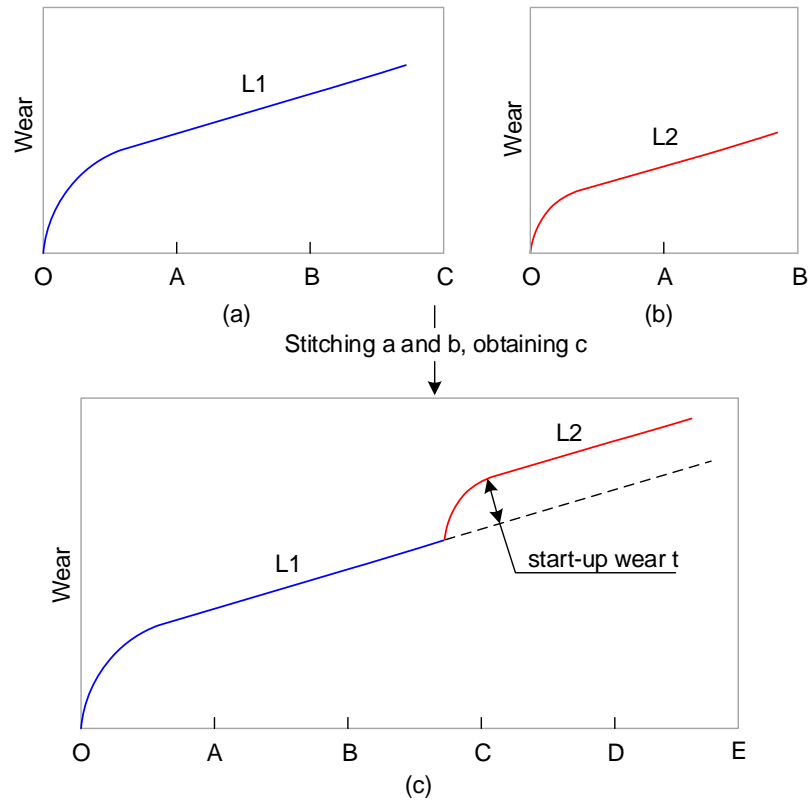


Figure 4.30 Schematic plots of stitching wear data

### 4.3.2 Test at a load of 5 N·m

Figure 4.31 shows an endurance test for polyacetal gear pair run as six separate stages at a load of 5 N·m and a speed of 1000 rpm. Environment temperature is in the range of 23°C and 26°C. The wear curves (data sets) are labelled in chronological order of the test, with L1 denoting the first conducted stage and L6 being the last one in this test sequence.

The cooling interval times (stop period) between two successive stages are listed in Table 4.3. The cooling time interval is simply the duration of a stage stop before the next stage of the test initiates. For instance, test-stage L2 starts after 160 minutes after test-stage L1 stops.

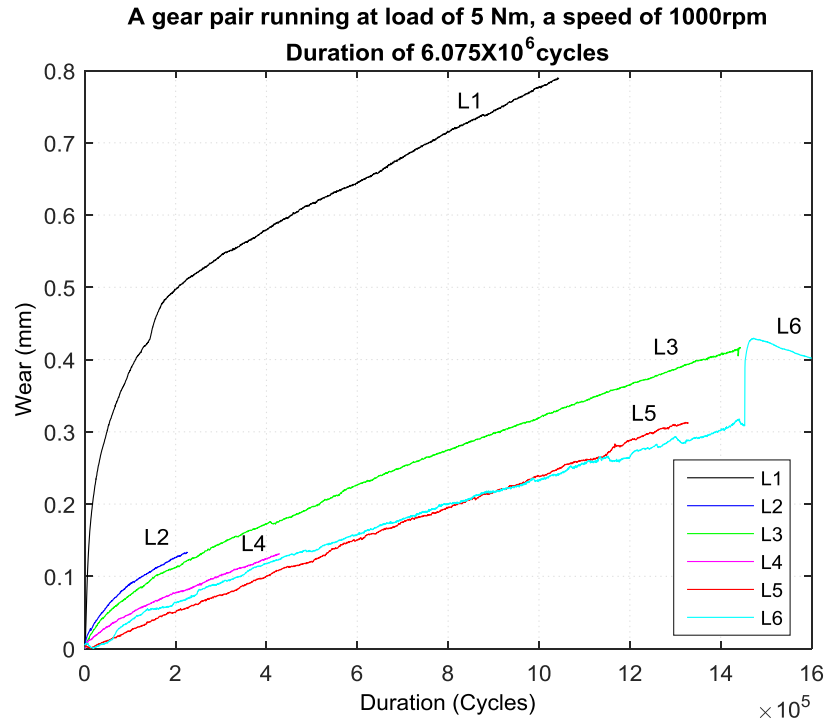


Table 4.3 Time intervals between successive test-stages (load 5 N·m)

Cooling time interval (minutes)	Stage
-	L1
60 +	L2
60 +	L3
55	L4
33	L5
10	L6

Table 4.3 illustrates that test-stages L2 and L3 had relatively long cooling periods (160 minutes and 3 days) before they started; test-stages L4 and L5 had short cooling times (33 minutes and 10 minutes) before the start of next stage. This indicates that the gear tooth bulk temperature before stages L2 and L3 are much as in stage L1 and close to the environment temperature, while the tooth body temperatures at the start of stages L5 and L6 are not significantly lower than their equilibrium of bulk temperatures during operation. However the detailed temperature gaps are unknown.

Figure 4.31 shows that L2 and L3, whose gear body temperatures started close to environment temperature, had similarly visible initial wear-in phases while the wear of stages L5 and L6 were almost all in steady wear phases without initial wear-in phases. These observations imply that the wear before the steady wear phases, may be partly dependent on gear body temperature and environment temperature, in addition to the roughness of contact tooth surfaces, load and speed.

These six test-stage results are concatenated into the test time sequence as shown in Figure 4.32, which reveals that no striking difference from the continuous (one-off) test result of Mao [7]. The restart transients and consistent slopes clearly meet the criteria discussed in Section 4.3.1.

The wear curve shown in Figure 4.32 exhibits three obvious wear phases, which is classic wear behaviour of polyacetal gear running at no greater than medium load level. The initial wear is within L1. The steady wear gradient holds fairly constant through L2 and then drops somewhat during L3 to L5, as the cumulative wear increases (see Figure 4.32, Figure 4.33 and Figure 4.34). Just prior to the final fast wear phase in L6, there is a small reduction of the steady wear rate.

The initial wear and initial wear duration of each section of the wear curve are presented in Figure 4.33 and the initial wear rate and steady wear rate are plotted in Figure 4.34. These are estimated by the method discussed in Section 4.3.1.

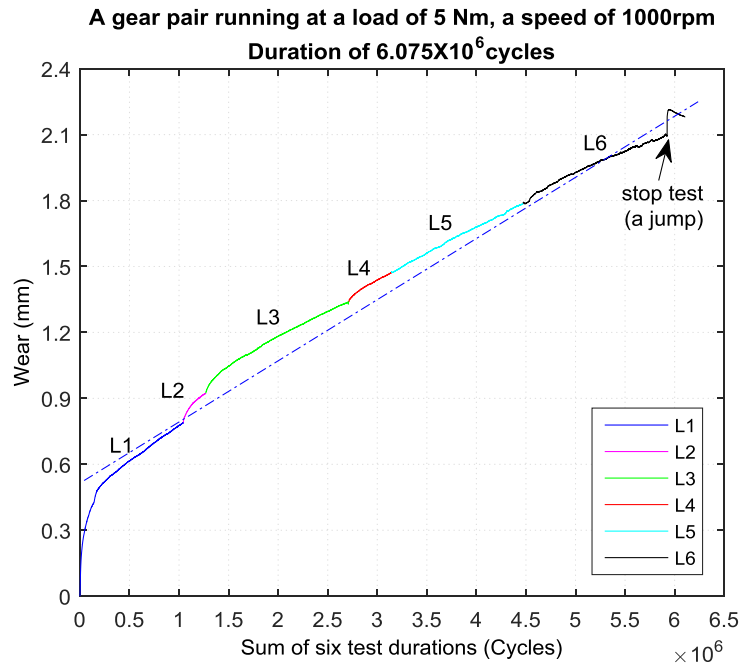


Figure 4.32 Concatenating wear curve at a load of 5 N·m

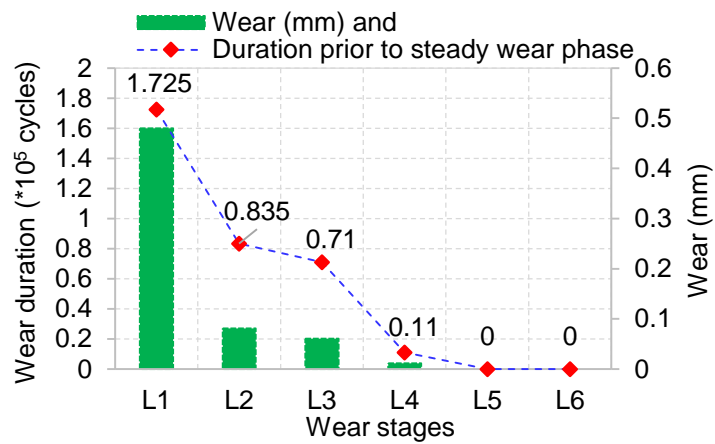


Figure 4.33 Wear and duration before steady wear phase at a load of 5 N·m

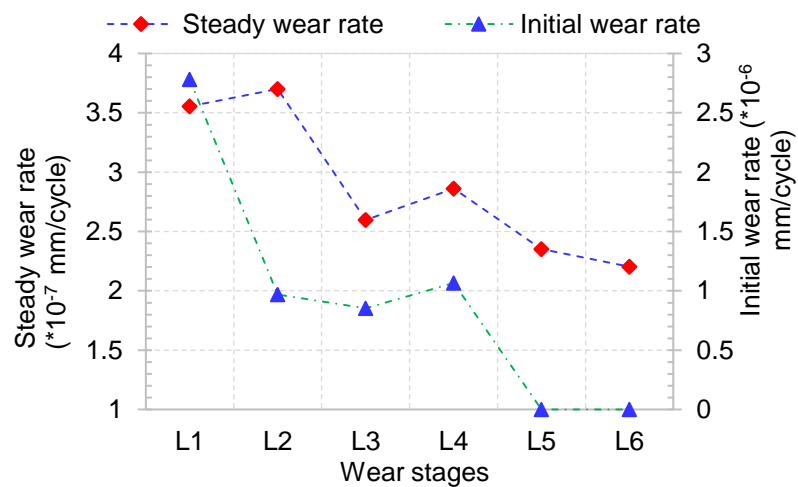


Figure 4.34 Wear rate at a load of 5 N·m

Overall the life cycle of polyacetal gears at a load of 5 N·m, it could be estimated in terms of the wear prior to steady phase in L1 and the steady wear rate of wear curves in Figure 4.32. Hence it is conservative to estimate service life at approximately  $9.6 \times 10^6$  cycles.

### 4.3.3 Tests at a load of 7 N·m

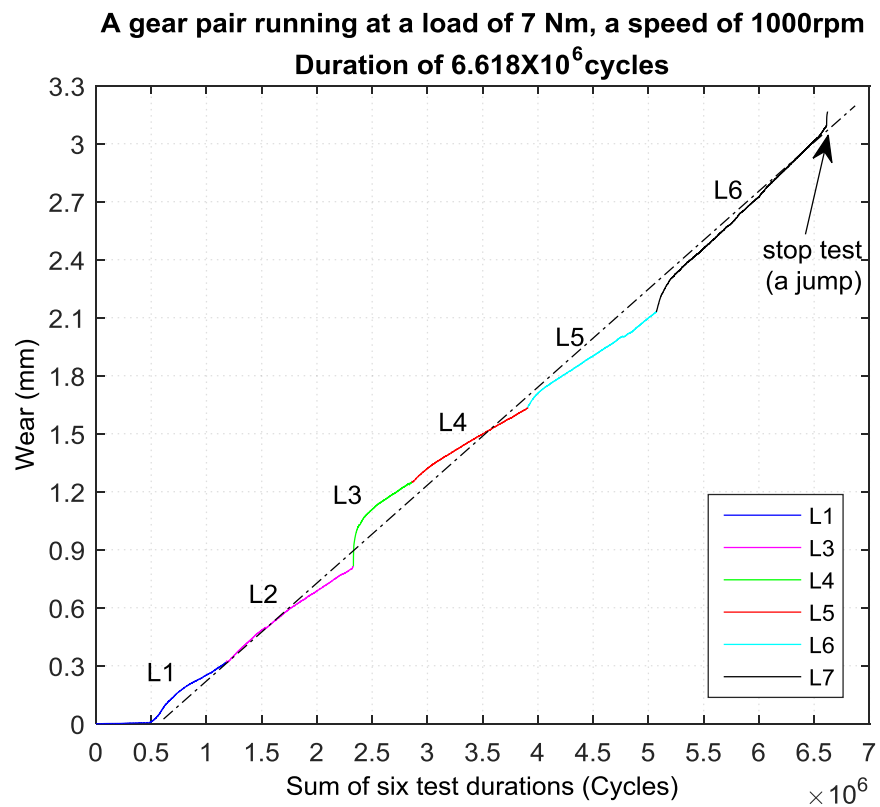
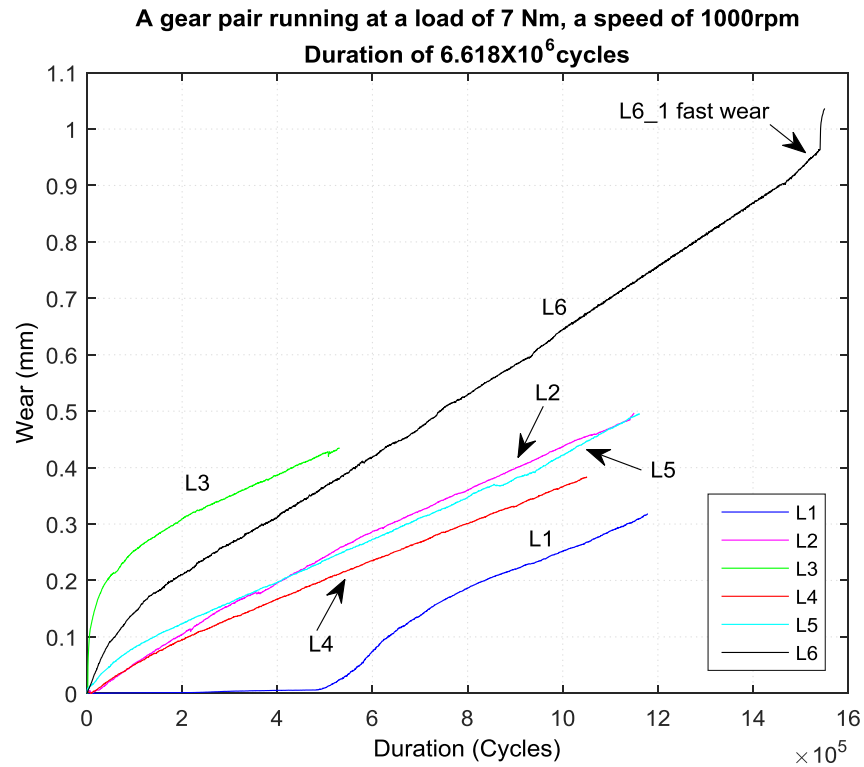
Two tests at a load of 7 N·m were conducted with six stages (five stops) in the first test and two stages (one stop) in the second. When the first test was set up, the load bar was a little above the horizontal level, which caused slight wear in the first  $5 \times 10^5$  revolutions, as L1 shows in Figure 4.35.

#### 4.3.3.1 First test

Figure 4.35 depicts the wear versus duration of a polyacetal gear pair running individual six stages at a load of 7 N·m and a speed of 1000 rpm. The six wear curves are labelled the same way as in Section 4.3.2 and are stitched in test chronological order as shown in Figure 4.36. The cooling interval time of successive tests is given in Table 4.4. The initial wear and wear duration of individual test are shown in Figure 4.37 and wear rates are shown in Figure 4.38.

Table 4.4 Time intervals between successive tests (load 7 N·m)

Cooling time interval	Test
-	L1
40 minutes	L2
242minutes	L3
100 minutes	L4
>7 hours	L5
>14 hours	L6



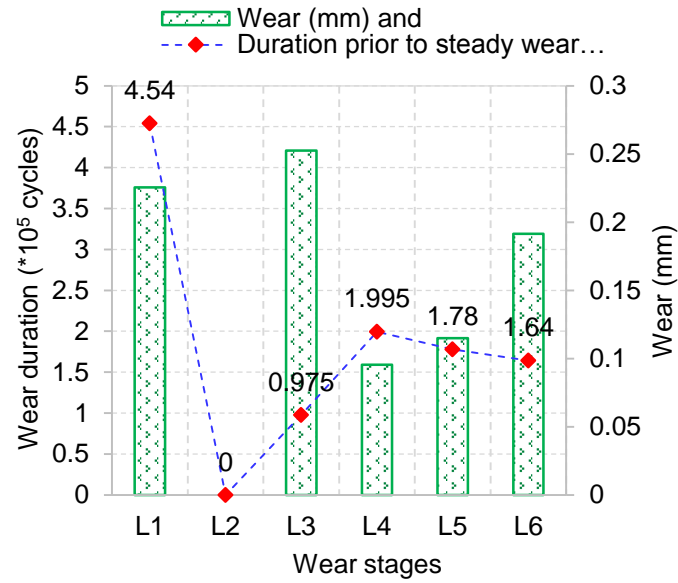


Figure 4.37 Wear and duration before steady wear phase at a load of 7 N·m

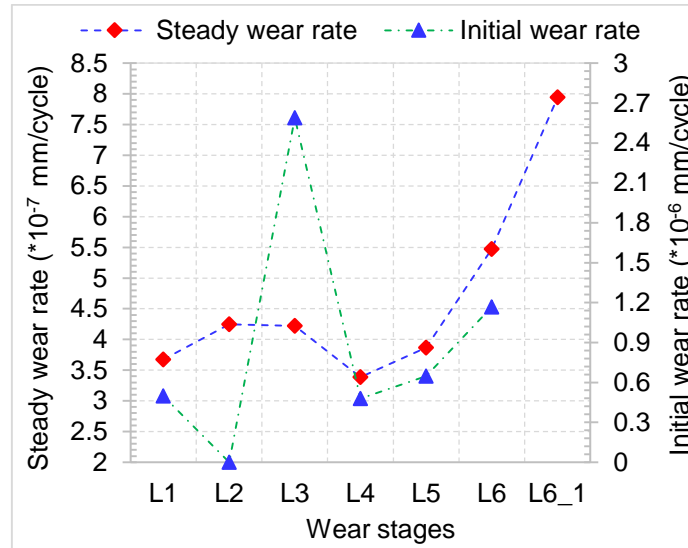


Figure 4.38 Wear rate at a load of 7 N·m

Evident differences of the wear curves are shown in Figure 4.35, such as L3 and L6 with visible initial wear-in and transitional wear phases and variations in the wear gradients. Figure 4.38 further illustrates the wear rate of the wear curve. On the whole, there is a rise in the steady –condition wear rate. For the cooling time intervals listed in Table 4.4 and the wear before steady wear phase shown in Figure 4.37, it is found that the initial wear-in phase is apparent when the cooling time is greater than 40 minutes. This



suggests that the gear body temperature prior to the test may affect the initial wear-in and transitional wear phases. The cascaded six wear curves plotted in Figure 4.36 present a complete wear progress, with an estimated service life of over  $6.6 \times 10^6$  cycles.

#### 4.3.3.2 Second test

The second test stopped once, after approximately 16 minutes, to adjust the load bar to horizontal level reducing load error. The test results are shown in Figure 4.39, where wear curve L1 goes into steady wear phase after approximately  $3.2 \times 10^5$  cycles (a wear of 1.3 mm), and L2 exhibits a marginal 'start up' wear as initial fast wear-in phase ( $7.6 \times 10^4$  cycles, a wear of 0.10 mm). There are some small but distinct jumps highlighted in circles on the curves L1 and L2, which are mainly due to high volume of wear debris dropping off gears. The two individual wear curves are stitched as shown in Figure 4.40, which demonstrates that the wear life is longer (about  $9.5 \times 10^6$  cycles) than in the first test. The wear increases but the wear rate again tends to decrease slightly as the test duration increases. The average wear rates of L1 and L2 before and after steady phases are solved in a step about  $0.5 \times 10^6$  revolutions, as shown in Figure 4.41.

If removing the average wear rate in initial wear phase of L1 (see Figure 4.41), then the steady wear rate is as shown in Figure 4.42, which decreases slightly as operating cycles increase. This finding is consistent with the statement of Yousef [94].

Comparison of first and second test results at a load of 7 N·m demonstrate that the methodology for endurance tests is right and

reasonable.

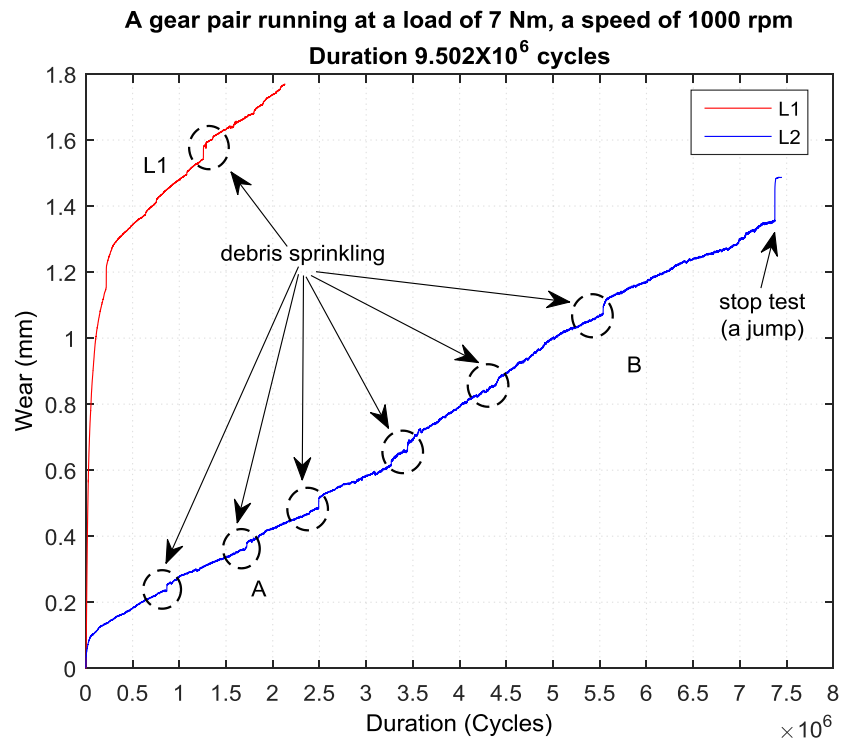


Figure 4.39 Wear versus duration at a load of 7 N·m

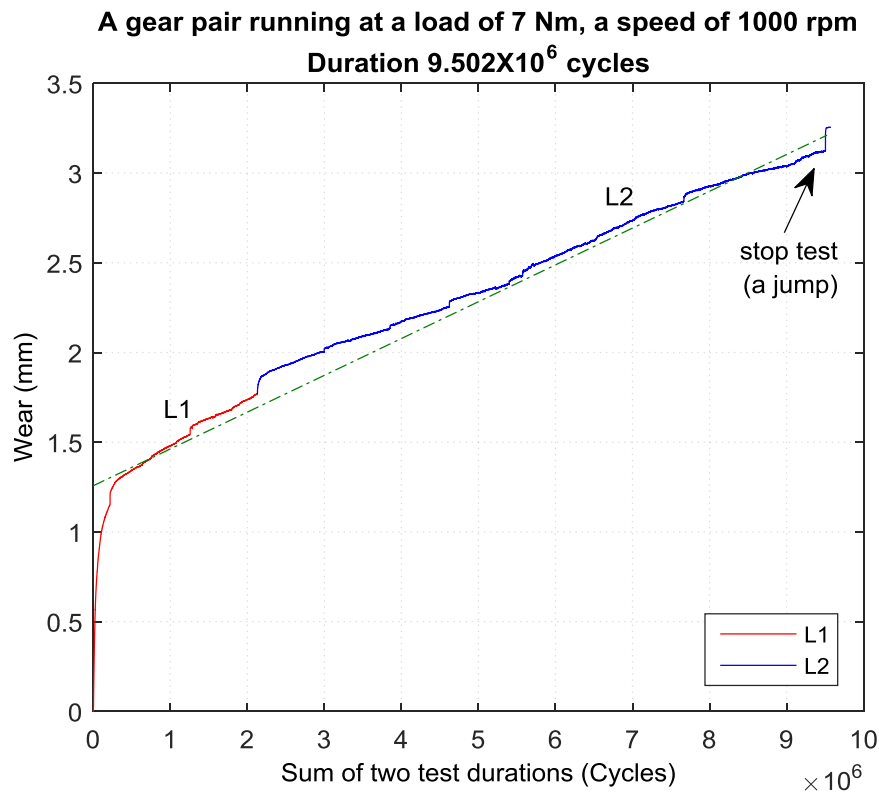


Figure 4.40 Concatenating wear curves at a load of 7 N·m

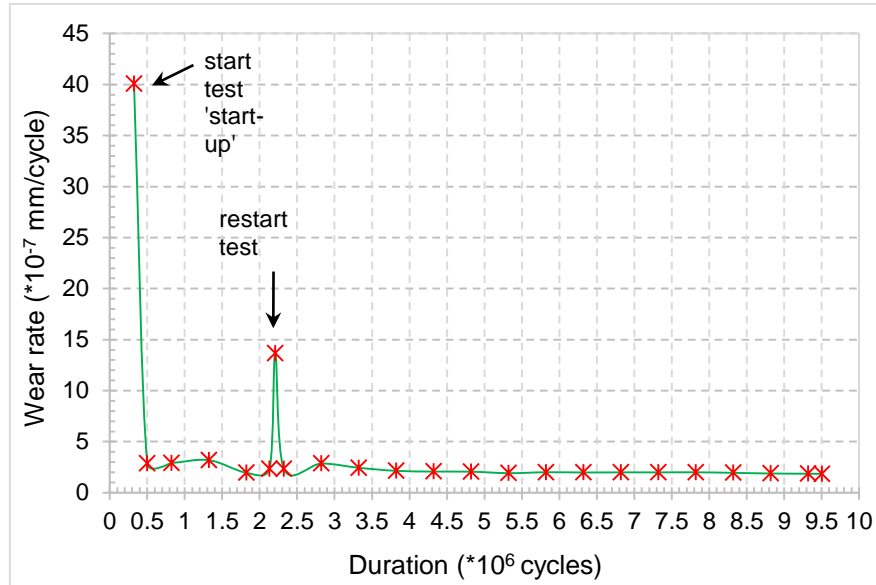


Figure 4.41 Average wear rate of second test result at a load of 7 N·m

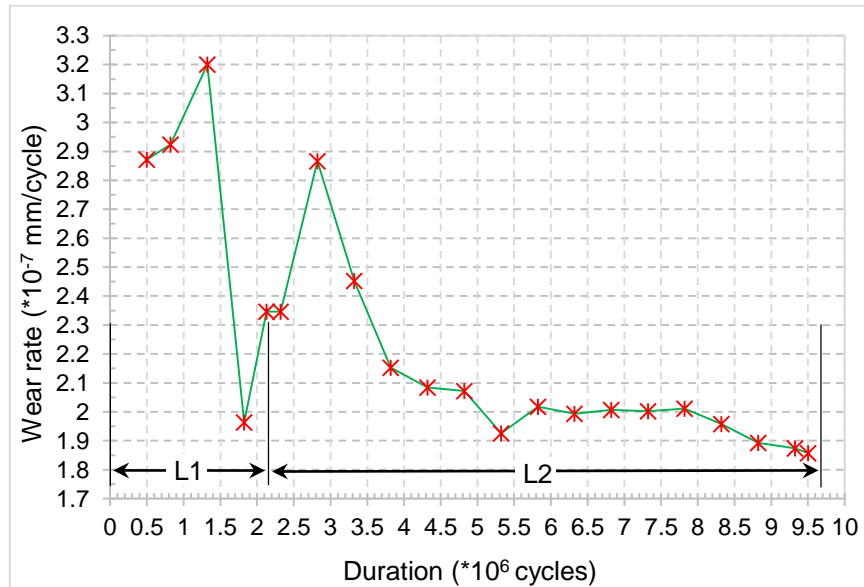


Figure 4.42 Steady wear rate of second test result at a load of 7 N·m

#### 4.3.4 Test at a load of 8 N·m

One test at a load of 8 N·m ran continuously until the allowable wear limit without any stops. The test result is shown in Figure 4.43, which exhibits four wear phases: initial fast wear-in, transitional wear, steady wear and final fast wear phases. The wear rate before the steady wear phase, within steady wear and final fast wear phases are here termed the ‘initial’, ‘steady’

and ‘fast’ wear rates respectively. The average wear rates obtained (using the method in section 4.2.1) from the test result (Figure 4.43) are shown in Figure 4.44, which demonstrates that the fast wear rate is approximately five times the steady wear rate.

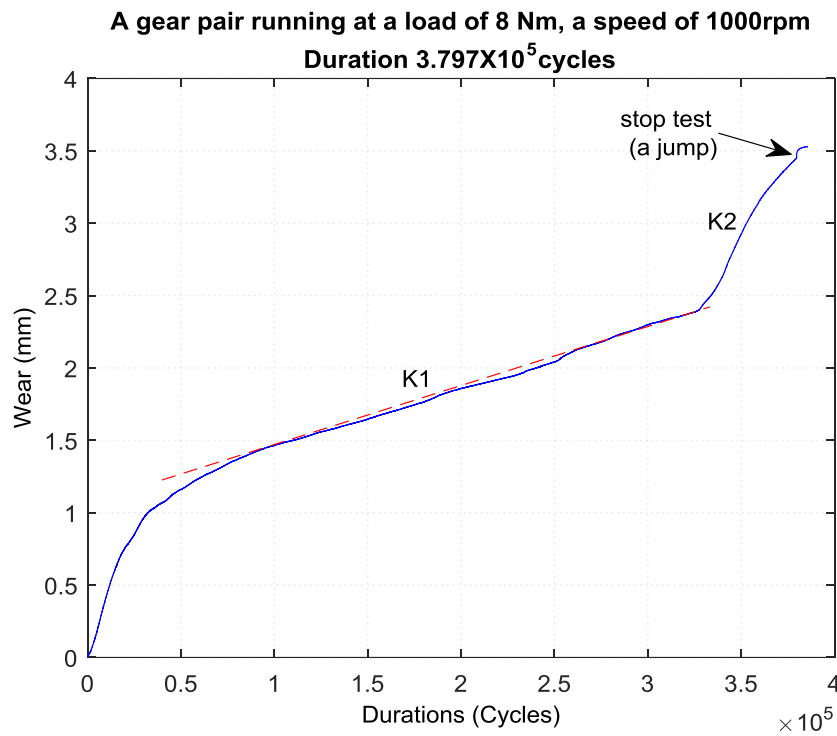


Figure 4.43 Wear versus duration at a load of 8 N·m

A photograph of worn gears is shown in Figure 4.45. The surfaces are very smooth without any softening or melting wear marks. A sketch of the worn tooth profiles (drawing from observation under a microscope) is shown for added clarity in Figure 4.46, which reveals that the driven gear was worn significantly more than the driving gear. The wear weight loss of driving and driven gears are 1.708 gram and 2.042 gram separately. The estimated service life under these running conditions is about  $3.6 \times 10^5$  cycles

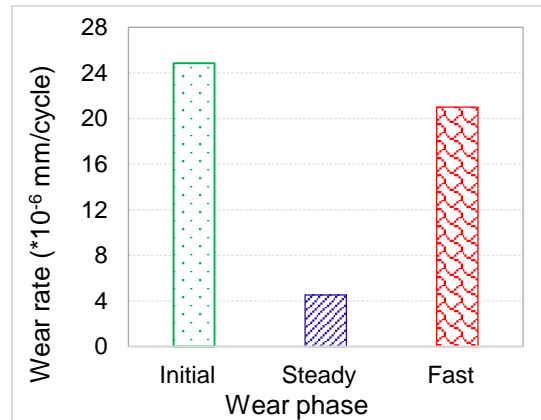


Figure 4.44 Wear rates in various wear phases at a load of 8 N·m

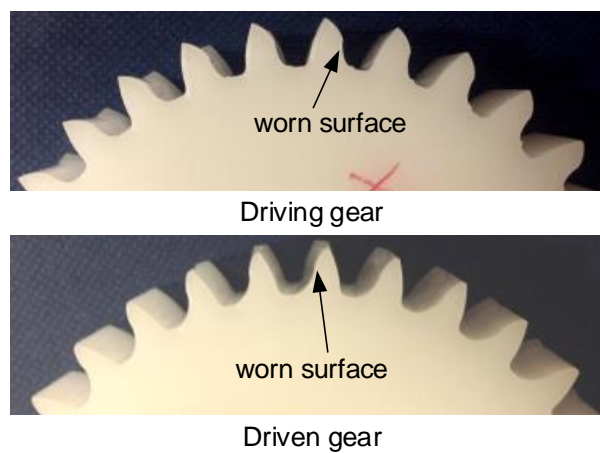


Figure 4.45 Photographs of worn tooth at a load of 8 N·m ( $3.797 \times 10^5$  cycles)

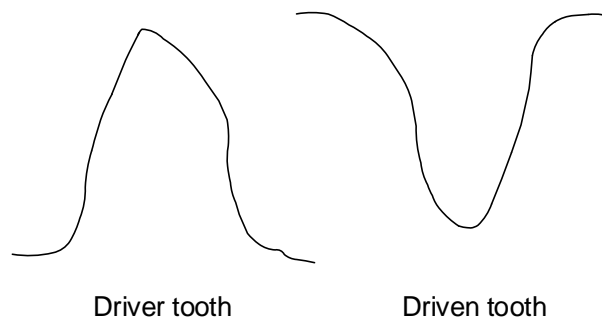


Figure 4.46 Profiles of worn driver and driven teeth

### 4.3.5 Test at a load of 8.5 N·m

The test result at a load of 8.5 N·m is shown in Figure 4.47, which shows it experiences three wear phases: initial fast wear-in (I), steady wear (II) and final fast wear (III) phases. The average wear rates (using the

method in section 4.2.1) in these three phases are presented in Figure 4.48. The wear rate in the steady wear phase is much lower than the other two. The gears finally failed by a form of severe wear on tooth tips and tooth bending. As in the test at a load of 8 N·m, wear weight loss of the driven gear, 4.600 g, is heavier than that, 3.855 g, of driving gear. The estimated service life under these running conditions is about  $2.1 \times 10^5$  cycles.

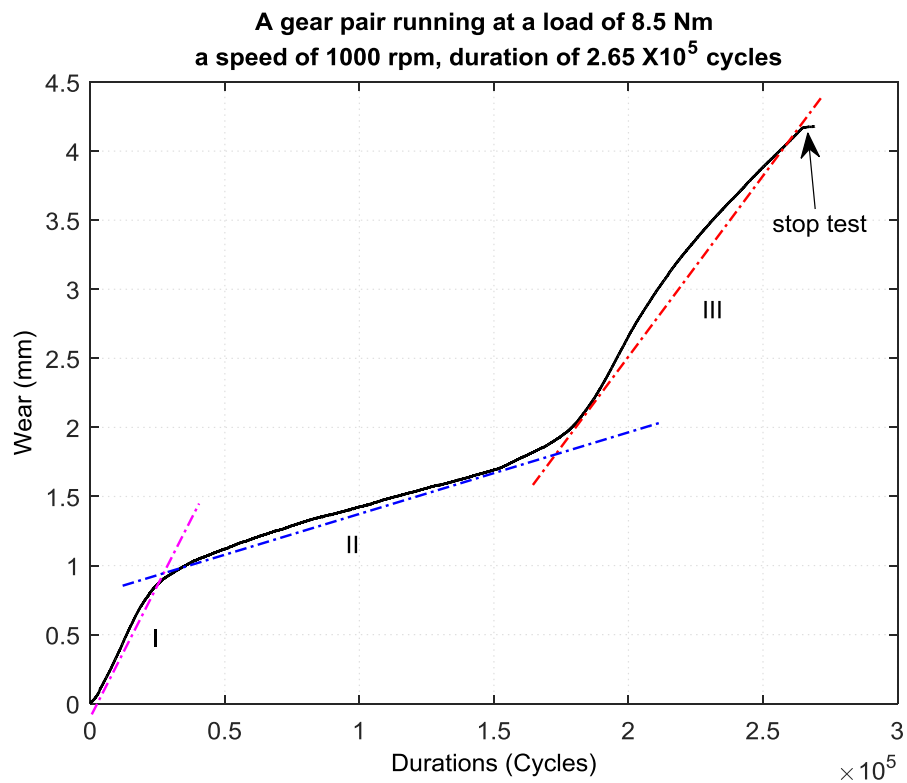


Figure 4.47 Wear versus duration at a load of 8.5 N·m

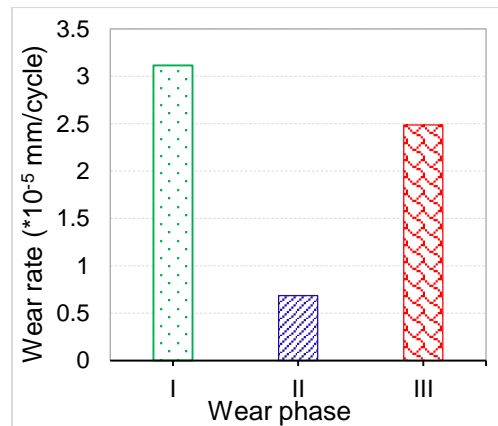


Figure 4.48 Wear rates in three wear phases at a load of 8.5 N·m

### 4.3.6 Test at a load of 9.0 N·m

The test result at a load of 9.0 N·m is presented in Figure 4.49. It does not exhibit the striking fast wear phase seen at a load of 8 N·m, but various wear gradients are visible. On roughly dividing the wear curve into three regions (0→a→b→c), corresponding wear rates are obtained as shown in Figure 4.50. The average wear rate in initial wear phase (o-a) is around twice the others. It reveals that there is a much smaller and hardly significant change of wear rate between the initial and steady wear phases.

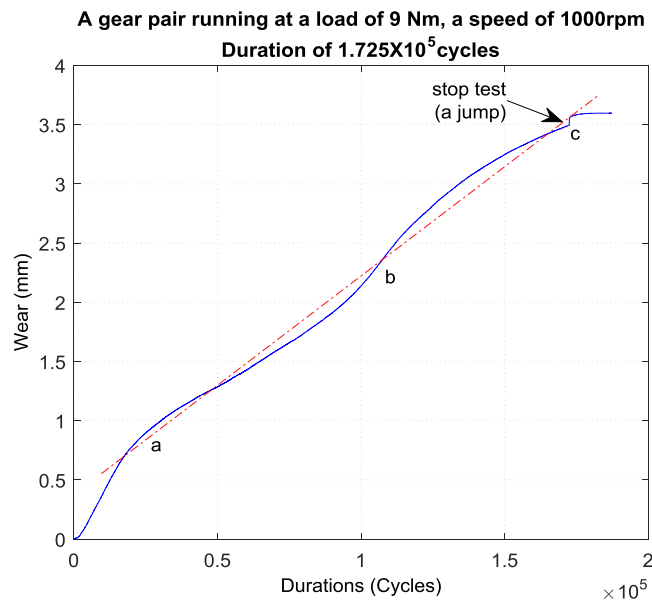


Figure 4.49 Wear versus duration at a load of 9 N·m

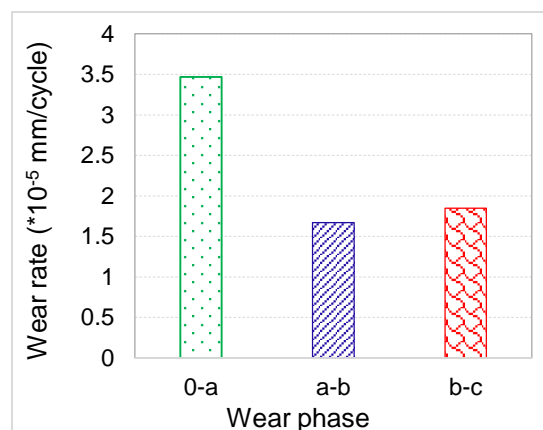


Figure 4.50 Wear rates in various wear phases at a load of 9 N·m

The photograph of worn gears' profiles shown in Figure 4.51 reveals that the driven teeth worn more than drivers and the surfaces are very smooth. However, from close-up views of worn tooth surfaces, over half the number of teeth have one instance of softening or melting wear marks: a 'groove' and 'ridge' respectively on each driver and driven worn tooth surfaces as shown in Figure 4.52. The origin of these wear marks may be closely linked with the surface temperature of the gears during operation. Detailed discussions on this will be presented in Chapter 6. The estimated service life under these running conditions is about  $1.4 \times 10^5$  cycles.

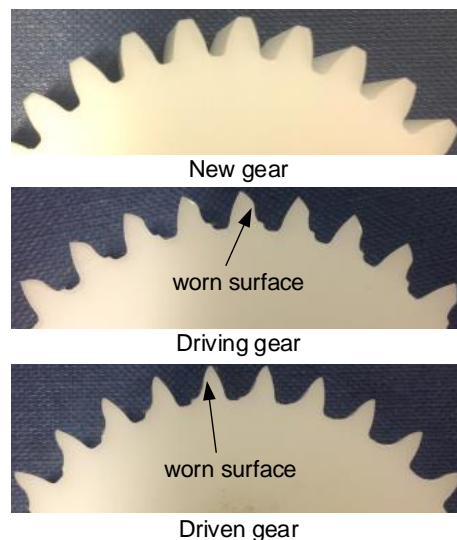


Figure 4.51 Photograph of worn tooth at a load of 9 N·m ( $1.725 \times 10^5$  cycles)

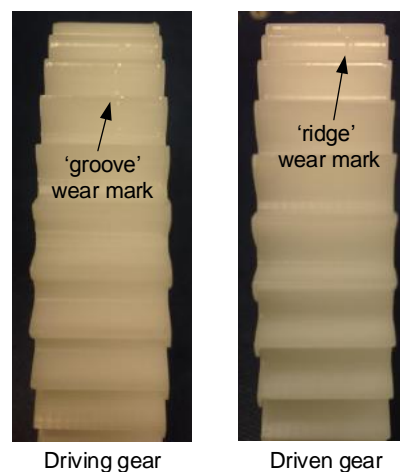


Figure 4.52 Photograph of worn tooth surfaces at a load of 9 N·m



### 4.3.7 Test at a load of 9.5 N·m

Figure 4.53 exhibits the test result of a polyacetal gear pair running at a load of 9.5 N·m and a speed of 1000 rpm. There is almost no distinction between initial wear-in and transitional wear phases. In terms of wear rate, the wear curve can be divided roughly into two ( $0 \rightarrow a$ ) and ( $a \rightarrow b$ ) wear phases. The corresponding wear rates are shown in Figure 4.54. The average wear rate in initial phase ( $0-a$ ) is reduced about one-third of that in fast wear phase ( $a-b$ ).

Photograph of worn gear and tooth contact surfaces are shown in Figure 4.55. Compared with driving gear teeth, much heavier wear occurred to the addendum area of driven gear teeth. The tooth flank topologies of the test gears are hand sketched under observation using a microscope as shown in Figure 4.56 to highlight the features in Figure 4.55. A striking feature is that 'scallops' wear deformation occurs especially towards to the central regions of the teeth for this gear pair, rather more widely on the driving tooth than the driven one. The tooth contact surfaces might melt during meshing, which suggested that the temperatures in the centre of the gear teeth were much higher than near the two sides of tooth flanks. This may be linked closely to the low conductivity of polyacetal material and the lower heat dissipation around the centre regions. The accumulative heat in the middle of teeth cannot dissipate as much as at both side of gear teeth. The 'scallops' extrude onto the tooth tip of the driver and also exist on the dedendum. For the driven gear, tooth tips are sharp, with breaks (macro cracks) near the pitch point and 'scallop' on the dedendum.

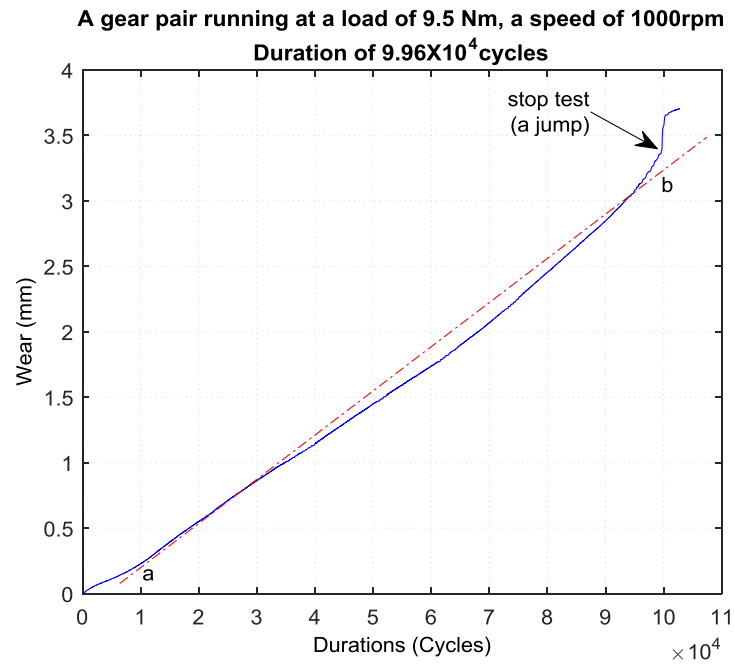


Figure 4.53 Wear versus duration at a load of 9.5 N·m

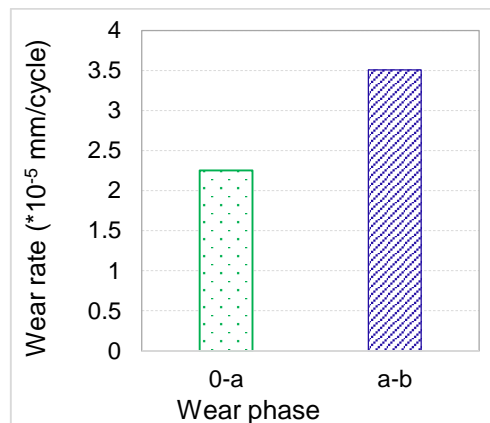


Figure 4.54 Wear rates in two wear phases at a load of 9.5 N·m

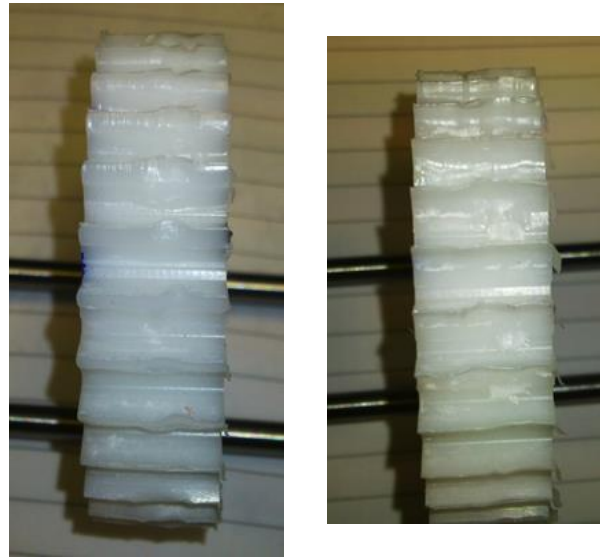


Driving gear



Driven gear

Tooth shapes of a worn gear pair



Driving gear

Driven gear

Worn tooth contact surfaces

Figure 4.55 Photograph of worn gear pair (load 9.5 N·m)

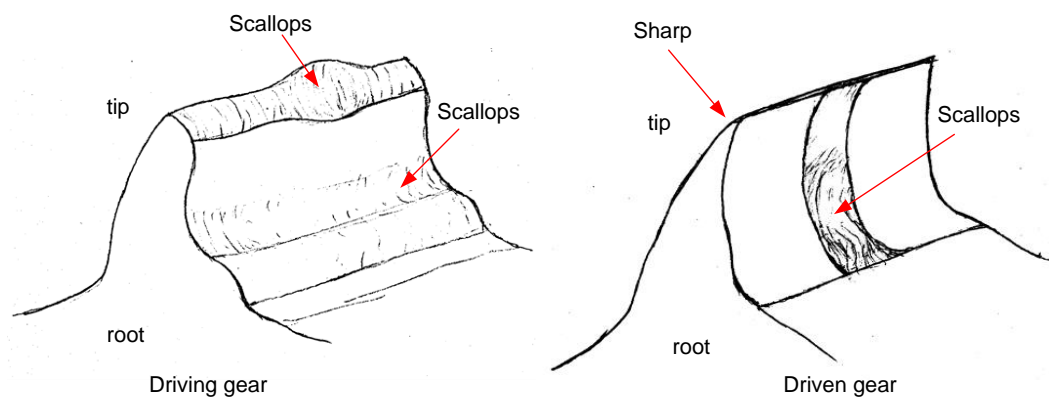


Figure 4.56 Schematic diagram of tooth flank topologies of a worn gear pair (load 9.5 N·m)

The test results imply that the failure of polyacetal gears transmission at a high load is likely to due mainly to high wear rate which is caused by excessive heat built-up on gear teeth and consequently resulting in instantaneous material softening/melting. The detailed thermal studies needed to verify this will be presented in Chapter 6. Estimated service life under these running conditions is about  $9.3 \times 10^4$  cycles.

### 4.3.8 Test at a load of 10.1 N·m

Figure 4.57 illustrates the test result at a load of 10.1 N·m, exhibiting less variation in wear gradient than that at a loads of 9-9.5 N·m. Average wear rate is approximately  $10 \times 10^{-5}$  mm/cycle, two and half fold that at a load of 9.5 N·m. Heavy wear occurred to the driven gear, weight loss 2.023 g, compared to 1.708 g for the driving gear (Westco scale, accuracy 0.1 mg).

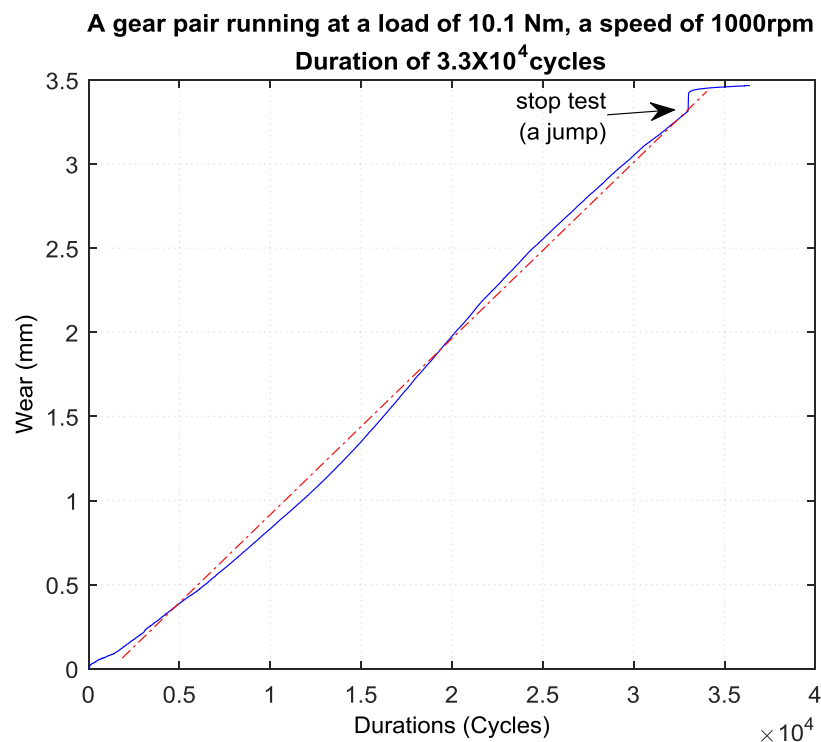


Figure 4.57 Wear versus duration at a load of 10.1 N·m

Markedly different wear topologies of driver and driven gears are shown in Figure 4.58. The worn tooth surfaces are similar to those at a load of 9.5 N·m. Evident material melt wear marks are seen in the centre of driver tooth flanks, and perhaps scuffing or melting flow wear marks are around the centre of the driven tooth flanks and along the vicinity of the pitch line. The wear marks result mainly from high operating temperature. It is surmised that the contact surface temperatures are around the melting point of 165°C.

Comparisons of temperature effects will be discussed in detail in Chapter 6. The effective practical service life is approximately  $3.0 \times 10^4$  cycles. As the running speed is 1000 rpm, denoting that only 30 minutes, the wear depth of a pair of mating teeth has reached the allowable wear limit, 3.14 mm. Cases at this load and speed suggest that polyacetal gears are not applicative for engineering power transmission above 10 N·m under the above conditions.

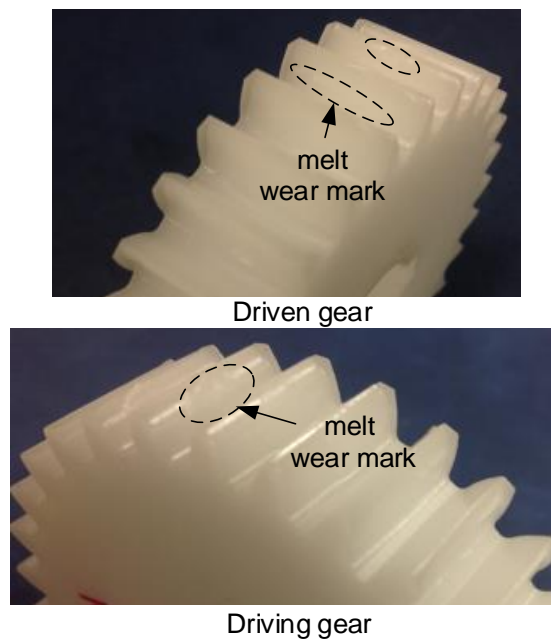


Figure 4.58 Photograph of melt wear marks on worn tooth surfaces at a load of 10.1 N·m

### 4.3.9 Test at a load of 12.1 N·m

Figure 4.59 depicts the wear curve for a test at a load of 12.1 N·m. It is close to a straight line, whose average wear rate is approximately  $1.06 \times 10^{-4}$  mm/cycle, close to that at a load of 10.1 N·m. Heavier wear occurs to the driven gear, and the wear weight loss of the driven and driving gears are respectively 2.889 gram and 1.468 gram. Estimated service life is about  $2.8 \times 10^4$  cycles, similar to that at a load of 10.1 N·m. The effective working time is about 28 minutes. This result, again, indicates that the torque range

from 10 to 12.1 N·m at these conditions is only suitable for very short (28 minutes) practical applications.

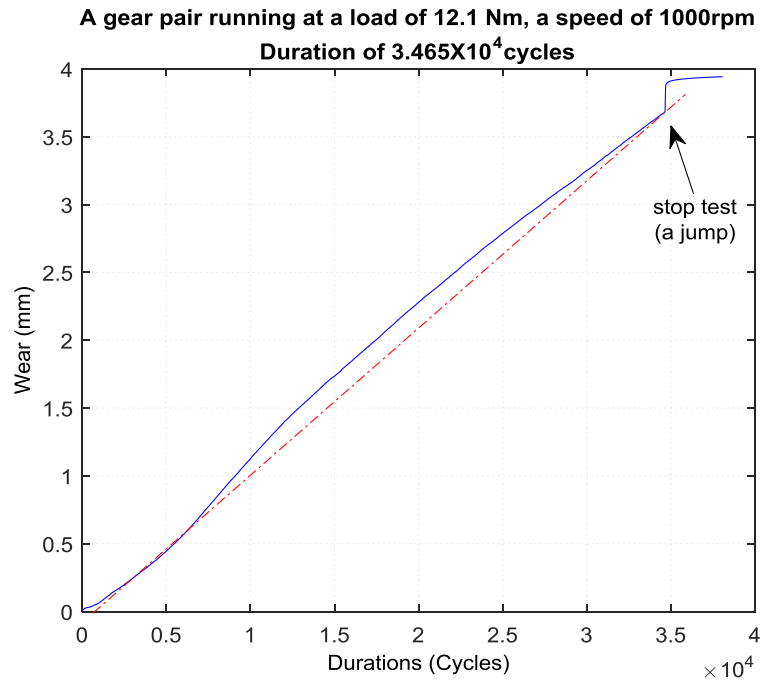


Figure 4.59 Wear versus duration at a load of 12.1 N·m

#### 4.3.10 Test at a load of 14.1 N·m

Figure 4.60 shows a test result at a load of 14.1 N·m. The wear curve approaches a straight line prior to teeth bending and the driving gear teeth becoming elongated (and consequently thinned) or melt rupture near the pitch line. The average wear rate is approximately  $2.67 \times 10^{-4}$  mm/cycle, over two and half times that at a load of 12.1 N·m. As the gear pair failed prematurely (at the wear depth about 2.75 mm) due to becoming elongated and thin near the pitch line, the effective service life was about  $1.0 \times 10^4$  cycles. This means that running duration is only ten minutes, very short, therefore it is not suggested to use at these conditions.

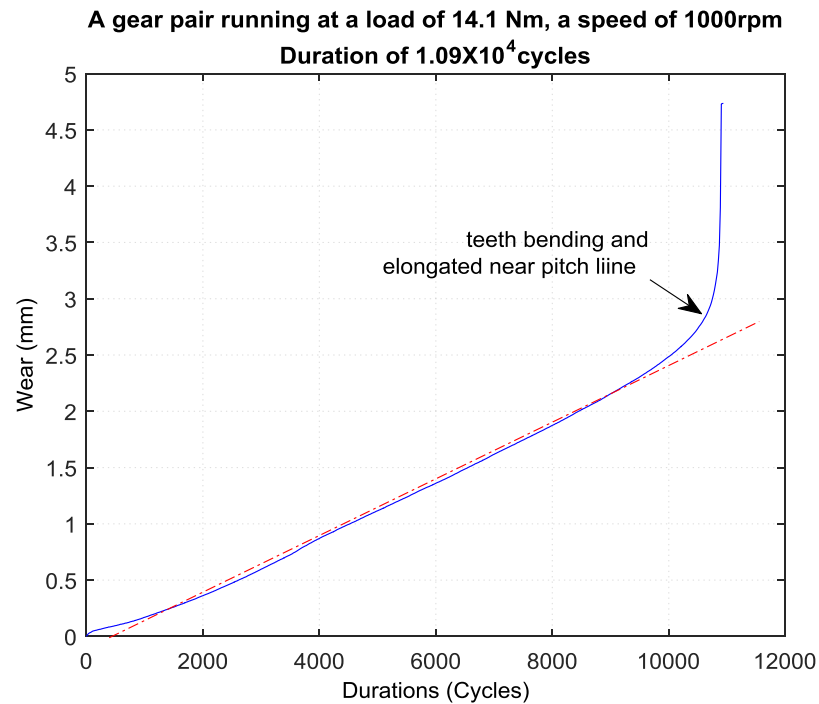


Figure 4.60 Wear versus duration at a load of 14.1 N·m

Figure 4.61 shows photograph of worn driving and driven gears. Most of driver teeth have been bent and of them seven teeth have melt and elongated thinly (thermal creep) and rupture close to their pitch points; however, a third of the teeth have been markedly bent but no elongation and melting has occurred to driven teeth. Melting wear (rupture) and bending of the driver teeth are the reason why the wear at approximately 2.75 mm (shown in Figure 4.60) suddenly rises almost vertically upward. The gear pair at a load of 14.1 N·m fails before the tooth allowable wear limit. Virtually the full-length of tooth contact surfaces' material have melted and been pushed to the tooth tip ends. On approximately four fifths of the driven teeth, the addendum material has been melted and removed. Therefore, the driven tooth tips have become very sharp and some have worn off.

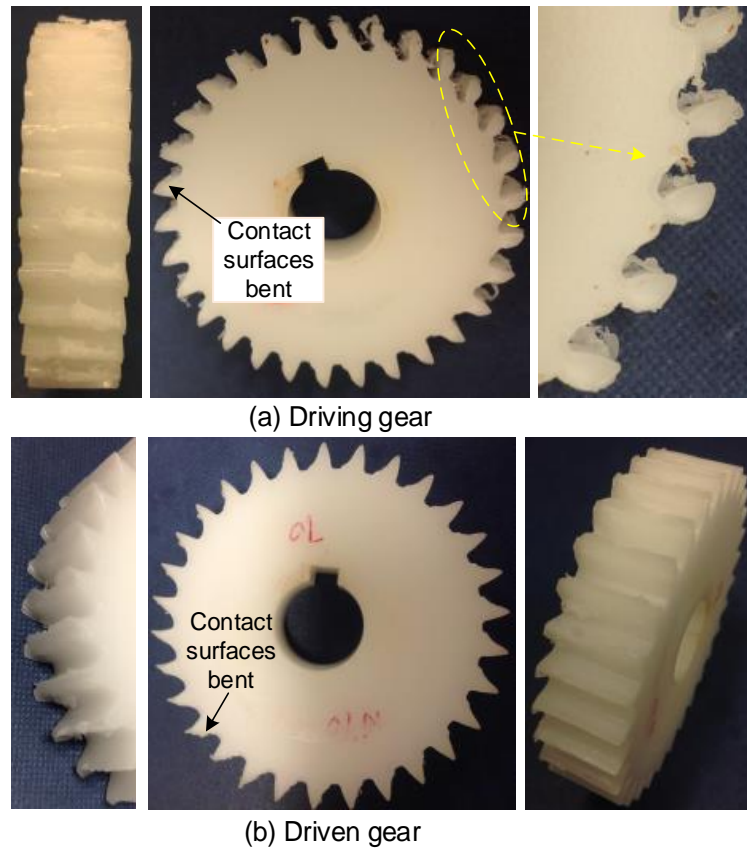


Figure 4.61 Worn tooth profiles of a gear pair at a load of 14.1 N·m

#### 4.3.11 Overall discussions

The statistic for gear wear life obtained from this set of endurance tests and from Mao [7] were compared and tabulated in Table 4.5. On the whole, except for similar results at the lowest load compared, the wear life of machine cut gears is significantly shorter than that of moulded polyacetal 100 gears. This may relate with physical differences such as that machine cut gears have no tooth tip relief and injection moulded gears have less perfect tooth profiles and more variations in degree of crystallinity at room temperature.

Table 4.5 illustrates that an increase in load (5 N·m→7.0 N·m→8 N·m→9 N·m→9.5 N·m→10.1 N·m→14.1 N·m) results in a reduction in gears'



endurance. The service life almost reduces by a factor of 10 between three load ranges. Generally, the predicted service life becomes too short for most applications at torques above, perhaps, 9.0 N·m.

Table 4.5 Life statistics for polyacetal gears (1000 rpm)

Machine cut polyacetal gears			Injection moulded acetal gears	Comparison
Torque (N·m)	Life-A (cycles)	Test stages	Life-B (cycles) in [7]	A/B
5	$>9.61 \times 10^6$	6	-	-
7	$>6.61 \times 10^6$	6	$6.00 \times 10^6$	1.101
7	$8.0645 \times 10^6$	2	$6.00 \times 10^6$	1.334
8.0	$3.6 \times 10^5$	1	$1.38 \times 10^6$	0.261
8.5	$2.162 \times 10^5$	1	$8.10 \times 10^5$	0.267
9.0	$1.424 \times 10^5$	1	$2.6 \times 10^5$	0.547
9.5	$9.63 \times 10^4$	1	$1.6 \times 10^5$	0.602
10.1	$3.099 \times 10^4$	1	$1.6 \times 10^5$ (10.0 N·m)	0.194
12.1	$2.88 \times 10^4$	1	-	-
14.1	$1.066 \times 10^4$	1	$3.6 \times 10^4$ (14.36 N·m)	0.296

#### 4.4 Step-load test results and discussions

To save on both the number of experimental samples and time, a quick experimental method, using a step-load test, was employed to roughly determine within hours the critical load and wear rate at various loads. The step-load test method involved using a single test gear pair loaded with a constant torque running for a short period (such as 30000 revolutions) and then stopping the gear test rig, adding a load increment (such as 0.5 N·m) without other mechanical disturbance to the set-up before running again for the same period. This process continues until the maximum load level required or the gears' allowable wear limit (3.14 mm) is reached. For

instance, at a speed of 1000 rpm, a gear pair loading initiated at 5 N·m for a running period 30000 revolutions, with incremental loads of 1 N·m, so the next period of 30000 cycles was at 6 N·m and so on. Compared with endurance and short period tests (several days and new gear pairs), this test is able to complete tests within hours by solely using one gear pair.

Before running at the next increment load, the gear pair in this test was first given 40 minutes cooling down to reduce accumulated heat on gears, making it similar to the interrupted endurance tests discussed previously. The test results were stitched in the order of tests. The detailed method is described in Section 4.3.1.

In this work five sets of step-load tests were conducted using speeds of 500, 1000, 1500 and 2000 rpm as presented in Table 4.6. To better study the effect of rotation speed on the wear of gears, four sets of the tests were at different speeds with closely the same operating period  $2.25 \times 10^4$  cycles.

Table 4.6 Cases of step-load tests

Test case	Speed (rpm)	Load (N·m)					Duration for each load ( $\times 10^4$ cycles)
1	1000	5	6	7	8	-	~3.0
2	500	5	6	7	8	9	~2.25
3	1000	5	6	7	8	9	~2.25
4	1500	5	6	7	8	9	~2.25
5	2000	5	6	7	8	-	~2.25

This section first introduces Case One as shown in Table 4.6: two sets of step-load tests running at speed of 1000 rpm with consistent individual duration 30000 revolutions and load increment 1N·m, but only present one set of test results due to the two sets of results were very similar;

and then comprehensive comparisons and discussions are made for Case Two to Case Five.

#### 4.4.1 Incremental load tests at a speed of 1000 rpm

Figure 4.62 presents a step-load test result at rotation speed of 1000 rpm, which initiated at 5 N·m, with a running period  $3 \times 10^4$  revolutions per load step and bearing load increments of 1 N·m, up to a load of 8 N·m. Wherein the label of the individual wear curves are labelled in time order of sequence of tests, with L1 is the first test conducted and L4 the last one.

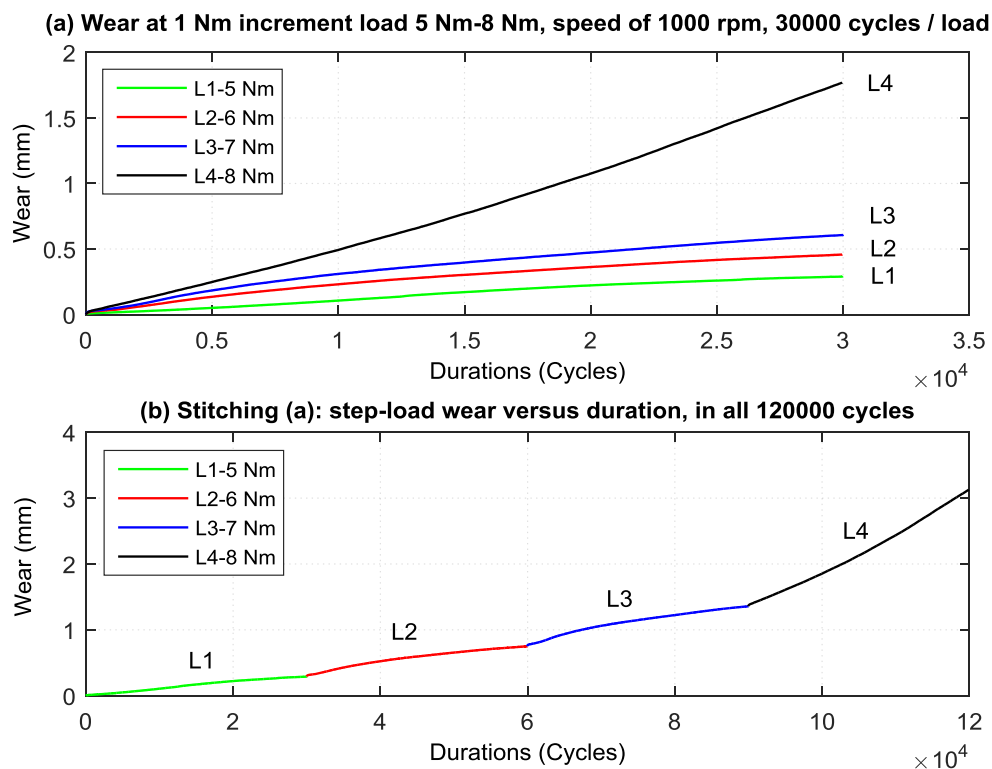


Figure 4.62 Incremental load-wear and its concatenated wear versus duration

Figure 4.62(a) shows the individual wear curves for each load step, while Figure 4.62(b) re-plots them cumulatively, using the same stitching method as applied previously in the multi-stage endurance tests. Overall, the

degree of wear increases with the increment in the loads, especially the last test stage at a load of 8 N·m (see Figure 4.62(a)) with wear loss of about 1.8 mm. The average wear rate at each load step is elevated the entire individual wear divided by its corresponding duration. The average wear rates at varying loads are shown in Figure 4.63. Clearly, at a speed of 1000 rpm there is a critical load between 7 N·m and 8 N·m where the wear rate increase dramatically.

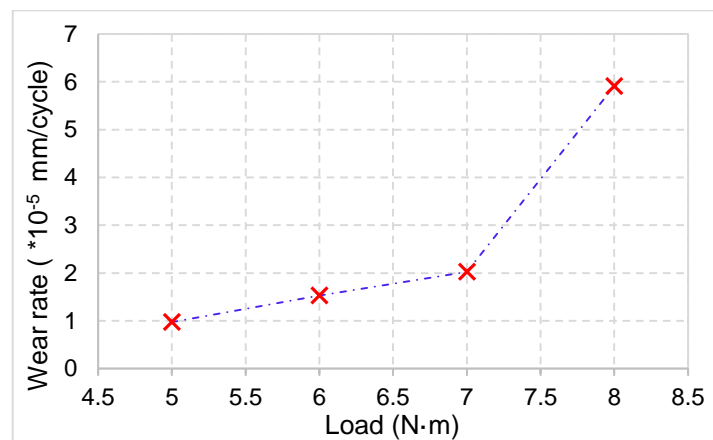


Figure 4.63 Wear rate versus loads at a speed of 1000 rpm and a duration of 30000 cycles each load

#### 4.4.2 Incremental load tests at various speeds

Step-load tests from an at outset of 5 N·m were conducted running at speeds of 500, 1000, 1500 and 2000 rpm with a duration of  $2.25 \times 10^4$  revolutions per load. If wear became close to the gears' allowable wear limit, the tests were stopped. For instance, tests were not able to be completed over  $2.25 \times 10^4$  cycles in the case of speed 1500 rpm when the load was 9 N·m. A test at 2000 rpm, 9 N·m could not be completed due to a failure of the test rig; there was no opportunity to conduct it again.

The test results are shown in Figure 4.64, which illustrates that not

only does an increase in load lead to an increase in wear but also an increase in rotation speed results in an increase in wear. Take the wear over almost the same operating durations of L3 as an example, the wear is 0.252, 0.321, 0.351 and 0.471 mm respectively at speeds of 500, 1000, 1500 and 2000 rpm. The case at a speed of 2000 rpm, the wear of a load of 8 N·m is expected to be over 1.5 mm (if compared to the same load conditions of the other three cases), however, it was about 1.0 mm, less than expected, which may be due to the duration at the stage of a load of 5 N·m was much shorter than  $2.25 \times 10^4$  cycles. Consequently it further affected the wear of the next three stages.

Of the four wear cases, wear at speed of 500 rpm exhibits a distinctly different wear feature that from 5 N·m to 9 N·m, all the wear curves experience initial fast wear-in and transitional wear phases prior to their steady wear phases. This suggest that the durations of initial fast wear-in and transitional wear phases are likely to be longer at a low speed than those at a high speed.

The wear curves at individual loads at the same speed were stitched together in test sequence as shown in Figure 4.65. The average wear rates are shown in Figure 4.66. Wear rate increases as rotary speed increases, and high differential values appear above 7 N·m compared to those at 500 rpm. It also indicates that an increase in speed results in a reduction in critical load.

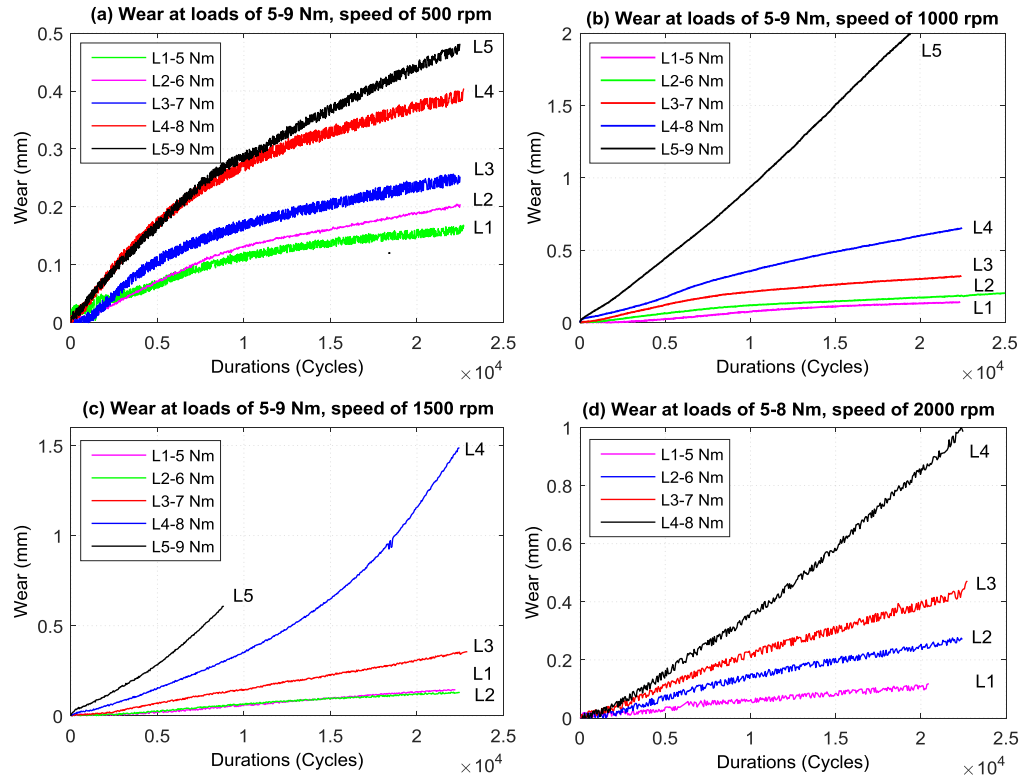


Figure 4.64 Wear versus duration at respective speed of 500, 1000, 1500 and 2000 rpm

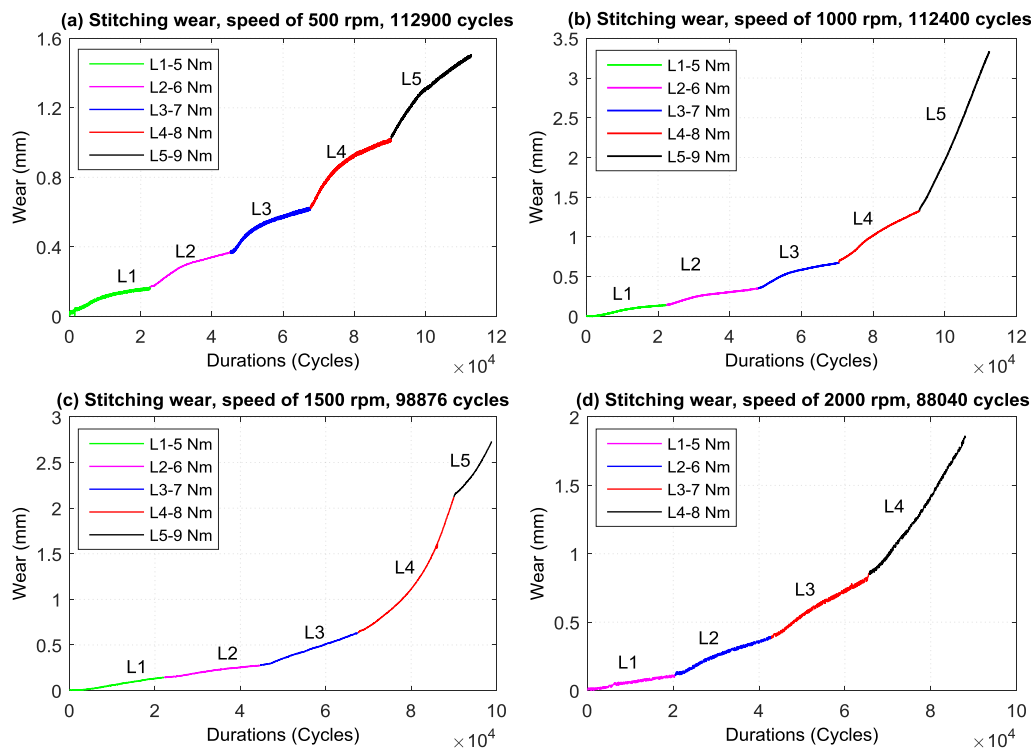


Figure 4.65 Concatenating step-load wear versus duration at various speed

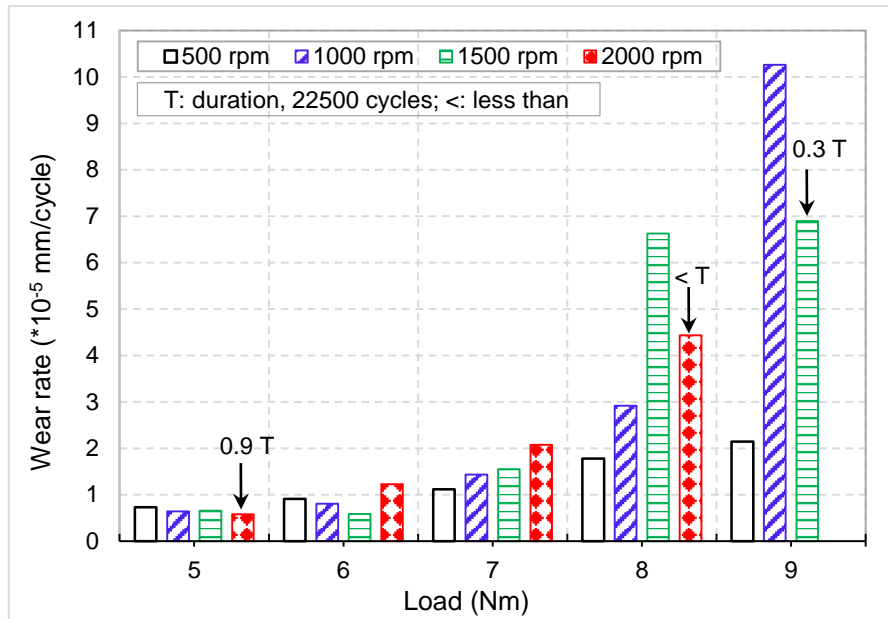


Figure 4.66 Wear rate versus step loads at various speeds

High speed brings about high relative sliding velocity between engaging teeth which consequently produce a significant level of sliding frictional heat and an increase in heat resulting from air trapping between teeth ('piston' effects, see Section 6.5). A rise in the temperature of the gears is likely to accelerate their wear rates.

Overall, increases in load and speed tend to accelerate wear; critical loads may exist between 7 N·m and 8 N·m at all four speed conditions, as well as between 8 N·m and 9 N·m when speed is equal or greater than 1000 rpm.

## 4.5 Graphite lubricated test results and discussions

Extensive studies on the wear mechanism of polyacetal gears indicate that the wear debris may also play an important role in the wear process. Therefore a test method was proposed that introduced graphite

grease to move away the wear debris from the mating teeth, and then to compare the wear to that under dry running conditions. Although lubricant also reduces the frictional coefficient of gears significantly, the effect of wear debris could still be noted slightly.

The graphite paste lubricant applied is produced by BOSTIK. INC., product number MS-MSDS-NNS-1CP. The composition of its major chemical components held in its grease base are, by weight: synthetic graphite 21.8%, nickel powder 17.9% and aluminium flake 2.7%. Its appearance is greyish-black semi-solid with a grease-like odour.

The graphite paste is smeared (painted) near the tooth roots of driving gears as shown in Figure 4.67(a). To make sure two gears have been evenly coated with lubricant prior to the formal test, the gear pair is first run at a low load such as 2 N·m for 10000 cycles and only then was the formal test started, with grease distributed as illustrated in Figure 4.67(b). For comparison, tests without lubricant were also first run for 10000 cycles at 2 N·m and then the formal test proceeded.

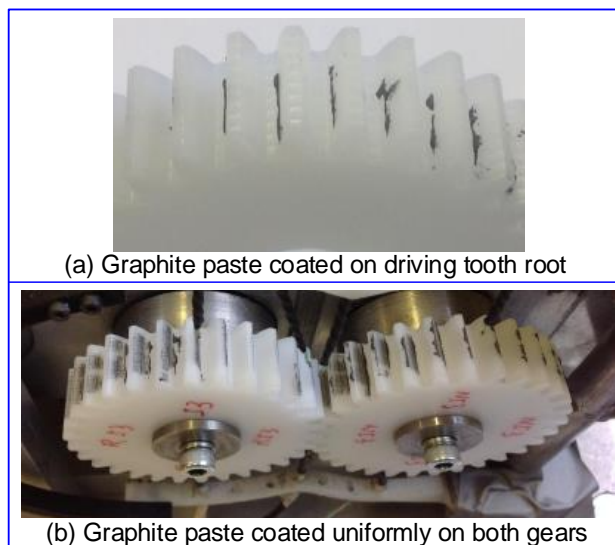


Figure 4.67 Photographs of graphite paste applied on gears



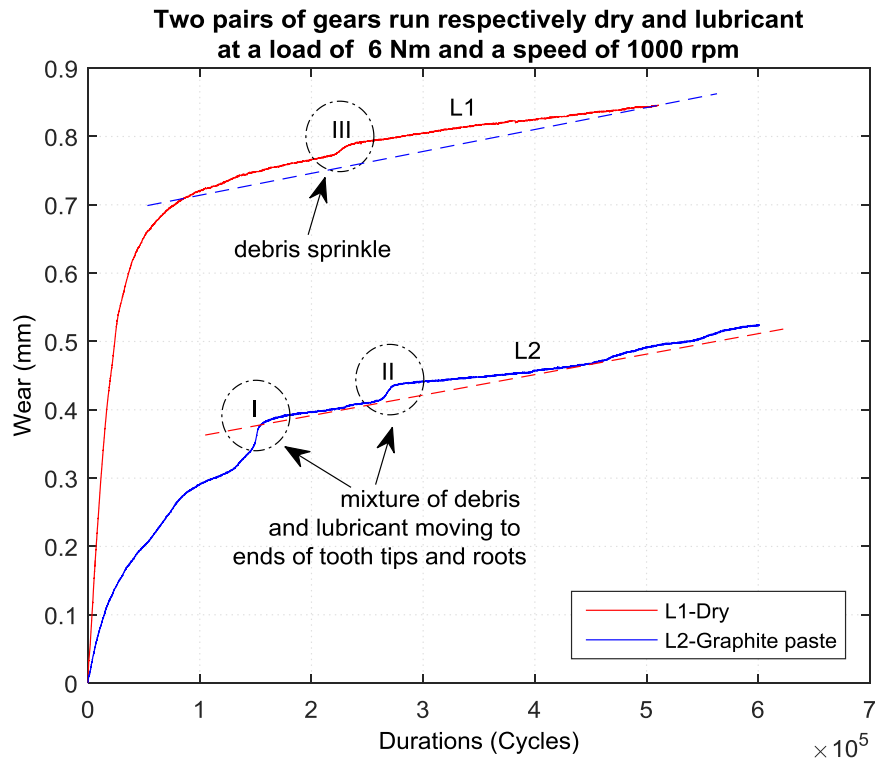
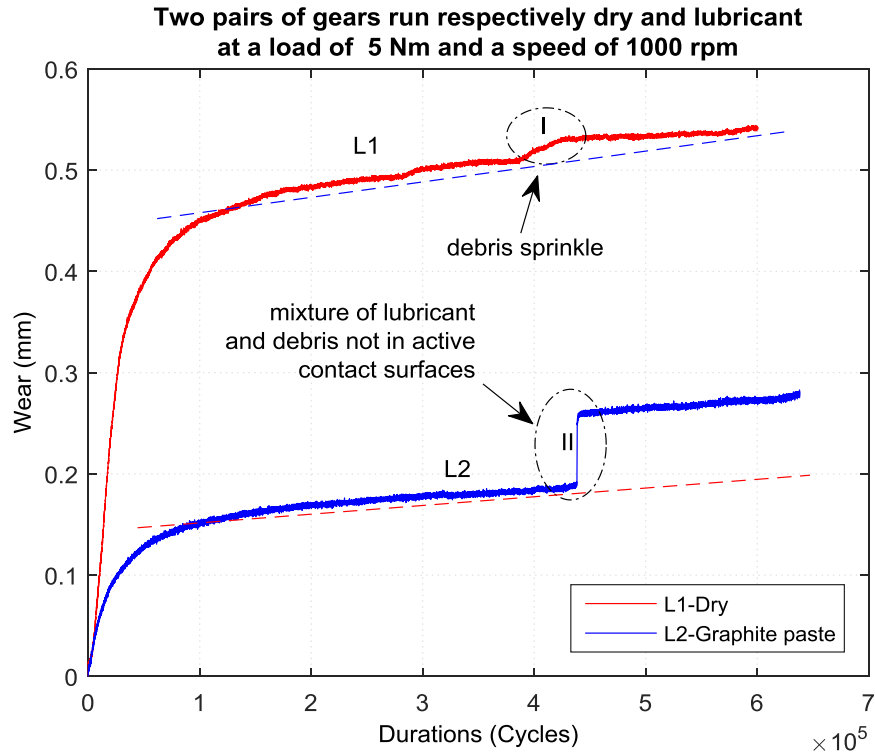
All the tests in this section ran at a speed of 1000 rpm. Again, the test results and discussions will be presented in terms of load range, namely low, medium and high loads (see Table 4.7).

Table 4.7 Weight of graphite grease added to test gears

Load range	Load (N·m)	Lubricant weight (gram)	Speed (rpm)
Low load	5	0.0707	1000
Low load	6	0.0721	1000
Moderate load	9	0.0302	1000
High load	10.1	0.0503	1000

#### 4.5.1 Tests at light loads

Test results of lubricated and dry running at loads of 5 N·m and 6 N·m are presented respectively in Figure 4.68 and Figure 4.69. A common striking (but not surprising) feature is that wear with lubricant is significantly less than the dry running ones. Note that there are a few jumps on the wear curves that were recorded. It was observed that the wear jumps compared to times when large amounts of debris were sprinkled onto the base below dry running gears or attached to the driver tooth tips for lubricated running. Note that wear rate tends to decrease slightly after the ejection of a spray of debris for dry running gears and when a mixture of graphite paste and debris being was partly pushed out from the tooth active contact surfaces for lubricated gears. The distribution of this mixture of graphite lubricant and wear debris on worn tooth surfaces can be noted in Figure 4.70. Almost no graphite paste was seen on tooth active surfaces and there was much debris and lubricant on tooth tips and roots, although, the wear rate remains steady and low.



The mix of graphite paste and wear debris on the ends of teeth (in particular on the edge of a driver tooth tip) may act as ‘brooms’ which clear

away wear debris on active tooth surfaces during gears' engagement. The observed reduction in wear under this condition then implies that the wear debris tends to increase the wear of gears.



Figure 4.70 Photograph of a pair of lubricated gears at a load of 5 N·m after testing

#### 4.5.2 Tests at medium loads

Test results at a load of 9 N·m are shown in Figure 4.71, which reveals that prior to a mixture of debris and lubricant dropping off the wear was steady and low. However shortly afterwards the wear rate increased rapidly and the wear curve exhibits much the same shape as the one without lubricant. It indicates that once lubricant has been almost completely ejected from the gear teeth (only, probably, a trace remaining), the wear tends to proceed as dry running in short period. Quick stopping the running test, it was found that almost no wear debris and graphite paste was left on the gear tooth tips and active contact surfaces as shown in Figure 4.72, which presents a striking contrast to Figure 4.70. Under such conditions, the wear rate increase significantly.

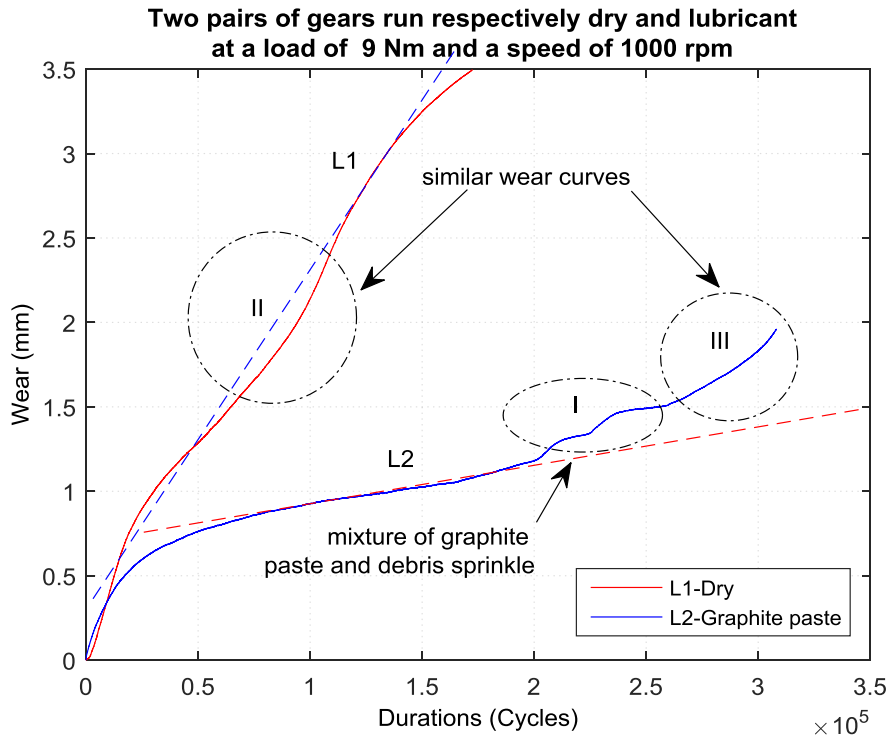


Figure 4.71 Wear versus duration at a load of 9 N·m

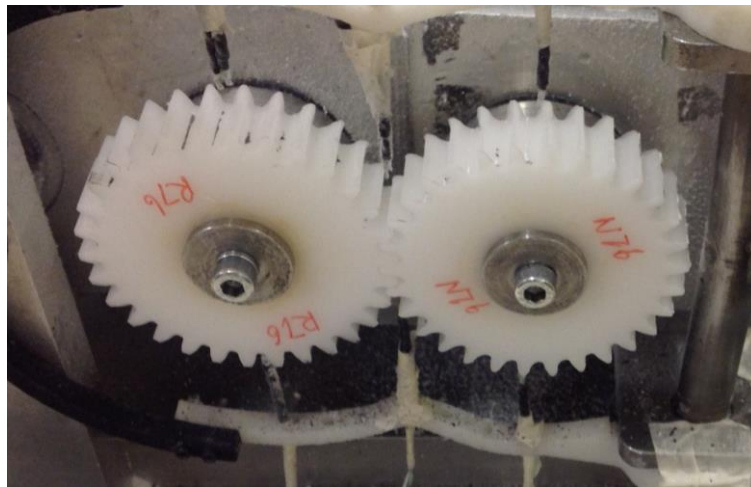


Figure 4.72 Photograph of a pair of lubricated gears at a load of 9 N·m after test

### 4.5.3 Tests at heavy loads

Figure 4.73 shows test results at a load of 10.1 N·m under both dry and lubricated conditions. It illustrates that wear rate in steady phase is as low as at light load condition, such as at a load of 7 N·m. However, a sharp increase in wear was observed instantly after a mixture of debris and

lubricant was ejected from the teeth as shown at 'I' in Figure 4.73. Then within  $0.3 \times 10^5$  revolutions driving and driven gear teeth underwent softening bending and subsequently the driving gear teeth became elongated (consequently thinner) near pitch line, which is similar to the dry condition behaviour (L1 in Figure 4.73, detail was discussed in Section 4.3.10). The worn gears are shown in Figure 4.74, from which the teeth bending and melt deformation could be noted.

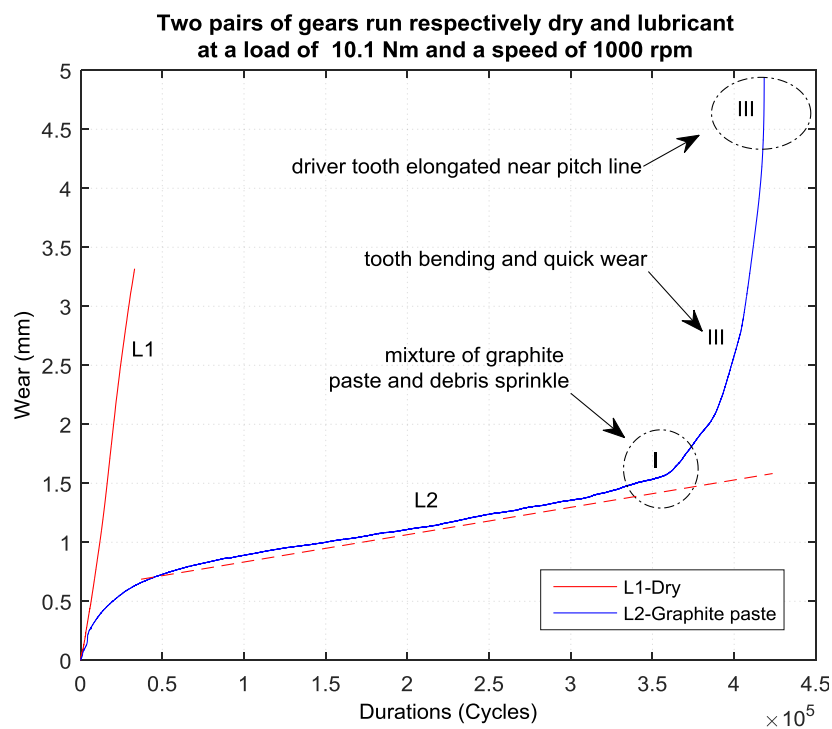


Figure 4.73 Wear versus duration at a load of 10.1 N·m

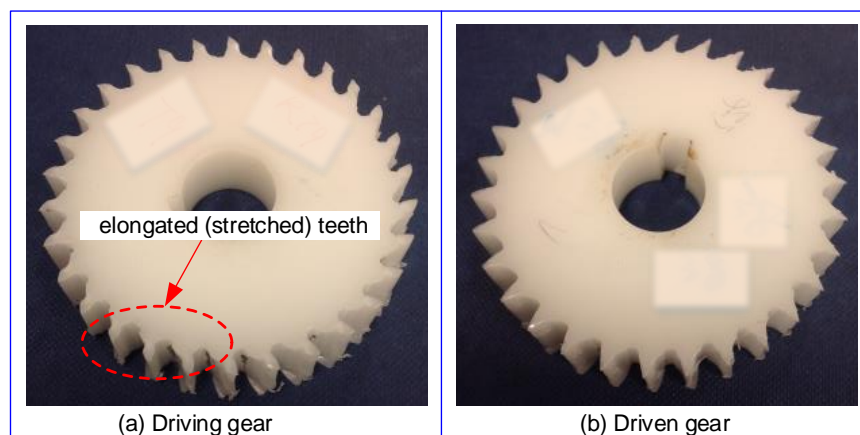


Figure 4.74 Worn graphite lubricated gears at a load of 10.1 N·m after  $4.18 \times 10^5$  cycles

#### 4.5.4 Discussions on lubricated test results

Both graphite lubricated and dry test results are plotted together on one graph in Figure 4.75. All the wear curves subjected to graphite lubricant are similar to the one run dry at loads no greater than 8 N·m, with initial fast wear-in, transitional wear, steady wear and final fast wear phases (at loads of 9 and 10.1 N·m). Before the mixture of graphite grease and wear debris was completely removed from driving tooth tips, all the wear remains steady and lower than for the dry run at 8 N·m. Averaging the wear against duration before final fast wear phase gives the wear rates presented in Figure 4.76. The wear rate at 9 N·m is somewhat greater than that at 10.1 N·m, which may be due to less lubricant being applied to gears.

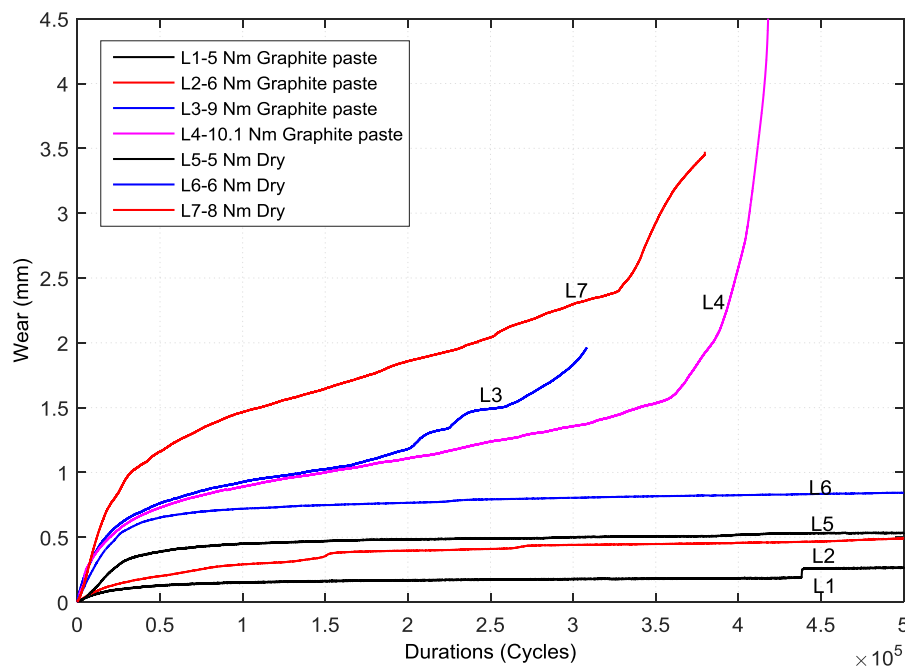


Figure 4.75 Dry and lubricated wear versus duration at various loads

Graphite paste lubricant tends to sweep away wear debris from tooth active contact surfaces during engagement and eventually the mix of lubricant and debris are pushed out to the tooth tips of driving gears and

tooth roots of driven gears during the gears' 'recess actions'. The wear rate does not increase significantly when there remains a mixture of lubricant and debris on the edges of driver tooth tips. It is likely to work as a sweeper, clearing wear debris from active contact tooth surfaces while gears are operating. When it falls completely off the tooth tips of the driving gear, the wear rate immediately increases to significantly greater than at low load conditions. This reveals that wear debris may also affect the wear processes of polymer gears. Therefore, if wear debris could be removed from engaging gears, their wear rate might be reduced slightly and their wear life might lengthen (extend). Understanding of the detailed role of the debris on gears' wear will require further study.

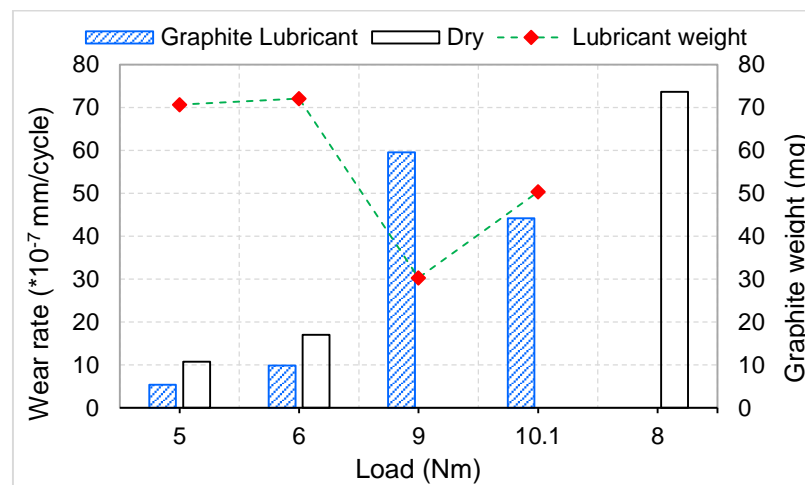


Figure 4.76 Wear rate versus duration at various loads

## 4.6 Conclusions

A wide range of experimental work was performed, from which the major wear mechanism and failure modes were noted to be surface fatigue (i.e. pitting, micro-cracks in particular at the cases of low loads), adhesive

wear, scuffing wear, softening/viscoelastic deformation, local melting, plastic flow and macro cracks (breaks). It is novel to exploit segmented test results (link to the interrupted tests in Section 4.3) to estimate the lifetime of polyacetal gears. The comparison between the interrupted test results and continuous (non-stop) test results indicate that these two ways can be used for endurance tests of polymeric gears.

When polyacetal gears run under high loads, premature failure is most likely to occur due to gears' teeth excessive softening-bending or melting elongated near the pitch line, which result from gears' elevated operating temperature. Note that nearly all tooth deformation (melting elongated/ stretching thin) in the pitch line vicinity of the dedendum takes place on the driving gears. Tooth bending transformation mainly happens on the addendum regions of mating gears. Cracks or breaks occur to the pitch line regions of driver and driven gears. Polyacetal gears at a load of 14.1 N·m, typically fail by tooth softening-bending and excessive elongated near the pitch line of the driving gear, as elaborated in Section 4.3.10.

It is essential for designs to consider the allowable contact stress and speed of polymer gears and to predict dynamic heat equilibrium that between heat energy produced by gears' engagement (friction, flexural losses, fluid trapped between teeth) and heat dissipation (air convection, thermal conduction and radiation). Test results indicates air convection take main role in thermal dynamic balance of gears which interaction with the steady state of gears' wear.

Wear debris trapping between mating teeth may increase slightly the



wear of polymer gears, and its effects were observed in lubricated tests as well. Various regimes of wear debris hold some information of operating gears' conditions. For instance, increasing sizes of wear debris indicate high loads, high speed or perhaps high temperature. Translucent bulk slice wear debris indicates that interference occur to meshing gears (i.e. high loads causing teeth great thermal expansions, reduction in centre distance and misalignment) and the gears may fail in short duration. The presence of granular wear debris may be due to unavoidable slight axial misalignment. The long roll wear debris mainly comes up in the cases at media and high loads.

An increase in running speed tends to accelerate wear rate, especially cases above low loads. Meanwhile step-load test results also demonstrate that critical loads (where wear rate increase/reduce significantly) generally reduce as a running speed increases.

## Chapter 5

### Misaligned-Configuration Tests

Many research studies of polymer gears have been conducted under aligned conditions. However, studies on the subject of polymer gears that mesh with known deliberate misalignment are hard to find. In practice, some degree of misalignment is inevitable for meshing gear pairs due to the elastic deformation, manufacturing error, assembling of gears and shafts and so on [15], but it is generally considered as an (unquantified) process uncertainty. Polymers have low elasticity moduli, low thermal conductivities and low softening and melting temperatures, compared to metals. Consequently, it is more flexible than their metallic counterparts. The occurrence of misalignment may therefore be higher for polymer gears than metallic gears. Hence it is essential to investigate the effect of misalignment on the wear behaviour of polymer gears.

Extensive tests of polyacetal gears subject to four categories of misalignment were conducted using the new non-metallic gear test rig. This chapter will describe the observed wear phenomena, presenting the preliminary aligned and misaligned experimental results which include wear, wear rate, load distribution, contact patterns, noticeable various regimes of wear debris and topographies of worn tooth contact surfaces. Some possible causal wear mechanisms and general conclusions are given.

All the tests presented in this chapter were conducted continuously

until finishing, without any interruption (different from aforementioned endurance tests subject to interrupting in Section 4.3), at a load of 7.0 N·m to 7.2 N·m, a speed of 1000 rpm and a room temperature between 19°C and 23°C. First the wear behaviour of a nominally properly aligned gear pair will be briefly described in Section 5.1. Then its results are used as a reference basis to compare with those of misalignment tests outlined in Sections 5.2 to 5.5.

### 5.1 Nominally aligned test

For alignment tests under low and medium load conditions, there are three main wear phases prior to final fast wear and failure: initial wear-in, transitional wear and steady-state wear phases.

In the alignment test, two major regimes of debris, translucent lamellate and powder wear debris, as shown in Figure 4.21 (see Section 4.2.2.1). Powdery debris dominated through all the test except when translucent lamellate debris emerged before the steady-state wear phase. Of course, small amounts of granular wear debris as shown in Figure 4.22 was present.

The worn tooth surfaces were examined by using scanning electron microscope (SEM, gold coating, 5.0 volts) as shown in Figure 5.1, which exhibits strikingly different wear features between driving gear tooth and driven gear tooth. A 'groove' forms at the pitch line on the driving tooth and a 'ridge' on the driven tooth. Many more 'ploughing' wear striations are

observed over the worn tooth dedendum area than that of the addendum of the driving tooth. For the driven tooth, many more ‘ploughing’ wear marks are over the tooth addendum than the dedendum. This implies that heavy wear occurs to the dedendum of the driving tooth and addendum of the driven tooth for a mating gear pair.

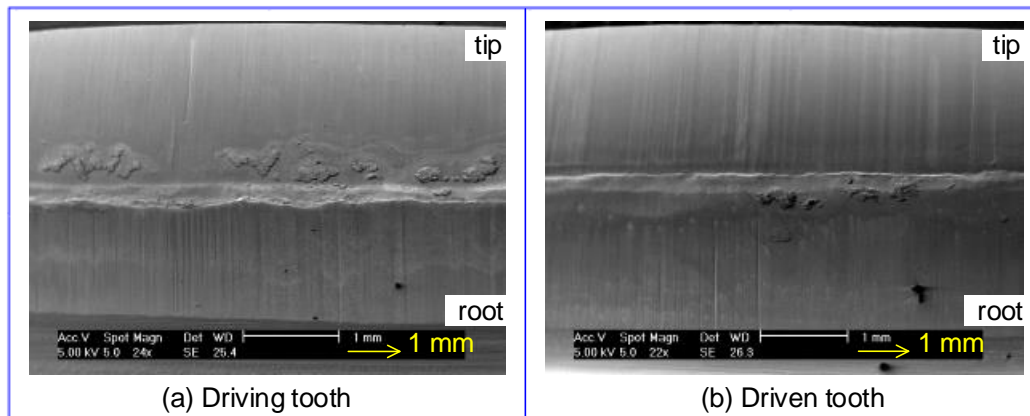


Figure 5.1 SEM micrographs of worn tooth surfaces (load 7.2 N·m)

## 5.2 Test results and discussions for axially misaligned gears

Two sets of tests subjected to axial misalignments were conducted with axial gaps of 1.42 mm and 2.48 mm respectively. These are equivalent to that the real active working tooth face widths reducing to approximately 13.58 mm and 12.52 mm separately, which results in an increase in tooth surface-contact stress and bending stress and a shift in load towards one edge of tooth. Consequently, the wear rate is predicted to increase in response to axial gap. Detailed test results with discussions are presented in Section 5.2.1 and topologies of worn tooth contact surfaces and wear debris are described separately in Sections 5.2.2 and 5.2.3. General conclusions

concerning the effects of axial misalignment are given in Section 5.2.4.

### 5.2.1 Wear curve and wear rate

Representative axial misalignment test results are presented in Figure 5.2, which exhibits similar wear curves to that of aligned tests including initial wear-in, transitional wear and steady-state wear phases.

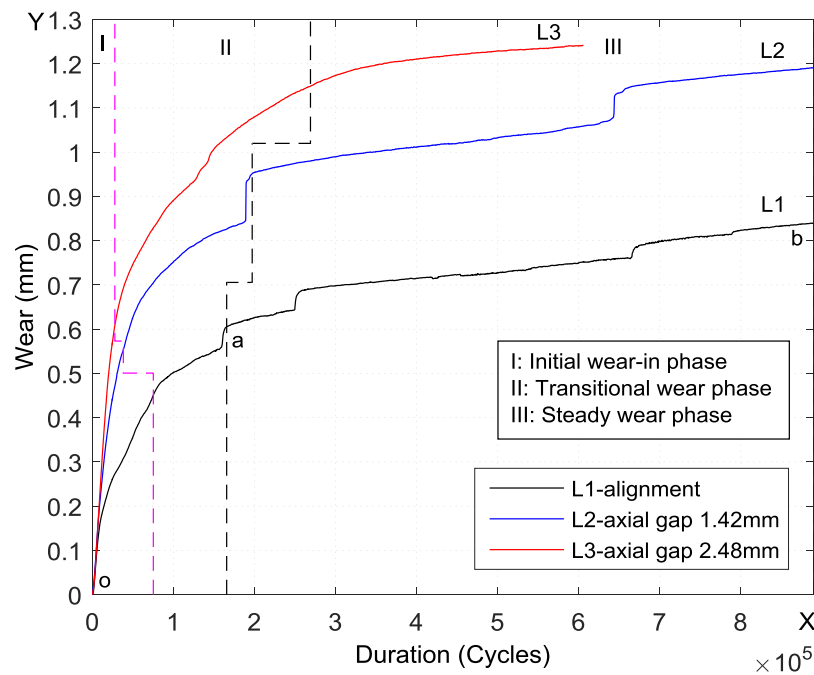


Figure 5.2 Wear versus duration in axially misaligned tests (7.2 N·m, 1000 rpm)

To investigate the effect of axial misalignment on gear wear, comparisons of initial and steady wear rates as shown in Figure 5.3 were made. Wear rate here is estimated by averaging the total wear over its corresponding operating revolutions. The wear rate calculated before steady wear phase is defined as initial wear rate ( $k_i$ ) and the one within steady phase is referred as steady-state wear rate ( $k_s$ ). Taking the results of aligned test (see Figure 5.2) as an example, the expression of initial wear rate  $k_L$  is  $(Y_a - Y_o)/(X_a - X_o)$  and the steady-state one  $k_s$  is  $(Y_b - Y_a)/(X_b - X_a)$ .

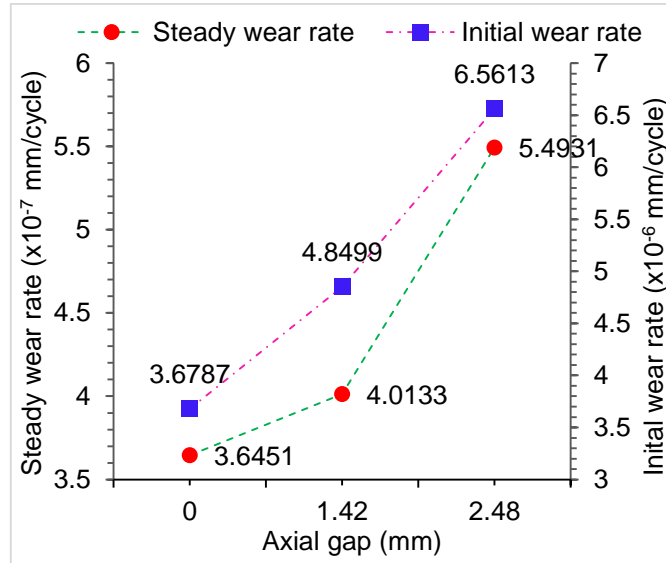


Figure 5.3 Wear rates versus axial gap

### Discussions

In axial misalignment tests, apart from deviation of the contact tooth face width, all the other gear parameters and operating conditions remained the same as the aligned tests. Thus, the variation in contact and bending stresses mainly depends on tooth contact width. Gear tooth contact and bending stresses were calculated by using Equation (4.1) and Equation (4.5) (BS 6168:1987 [13], see Section 4.2.1.2), given the Hertzian contact stress and bending stress to be  $\sigma_H$  and  $\sigma_F$  at zero axial gap (nominally aligned condition), then the approximate parameters subject to axial gaps 1.42 mm and 2.48 mm were solved and tabulated in Table 5.1. Meanwhile, for the sake of discussions, the statistics of initial and steady wear rates due to axial deviations are also listed in Table 5.1, where  $k_I$  and  $k_S$  are designated as initial wear rate and steady wear rate of the alignment test results at a load of 7.2 N·m and a speed of 1000 rpm. Then the wear rates under axial misaligned conditions can be expressed in coefficients of  $k_I$  and  $k_S$ . Figure 5.4 clearly shows that the relative variation ratio in these parameters

compared to those of aligned test results due to axial deviation. Positive and negative values indicate respectively a relative increase and reduction compared to that in the aligned condition.

Table 5.1 Predicted contact and bending stresses, actual wear rates subjected to axial gap

Axial gap (mm)	Tooth contact face width (mm)	Hertzian contact stress	Bending stress	Initial wear rate	Steady wear rate
0	15	$1.0 \cdot \sigma_H$	$1.0 \cdot \sigma_F$	$1.0 \cdot k_I$	$1.0 \cdot k_S$
1.42	13.58	$1.051 \cdot \sigma_H$	$1.105 \cdot \sigma_F$	$1.318 \cdot k_I$	$1.101 \cdot k_S$
2.48	12.52	$1.095 \cdot \sigma_H$	$1.198 \cdot \sigma_F$	$1.784 \cdot k_I$	$1.507 \cdot k_S$

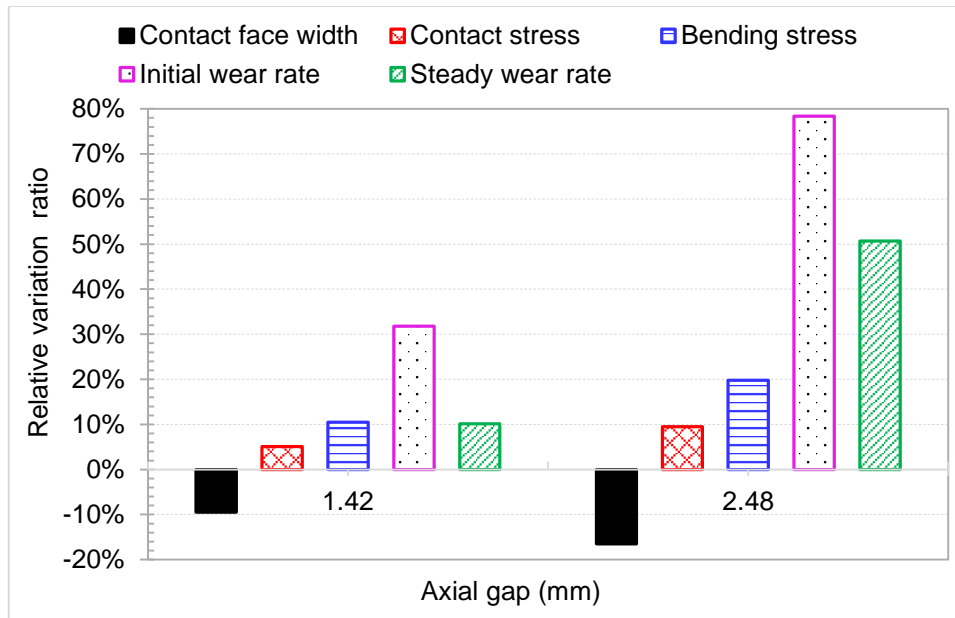


Figure 5.4 Relative variation ratio in gear and its wear versus radial gap

In contrast to the aligned test results (graph L1), the initial wear under axial misalignment as shown in Figure 5.2 is shorter and heavier but transitional wear duration is longer than for the aligned case. Figure 5.3 illustrates that the initial wear rate is a factor of 10 higher than corresponding steady-state wear rate and an increase in axial gap results in a dramatic increase in the wear rate. The deviations of wear rate due to axial

misalignment are much higher than and disproportional to the deviations of the approximate contact and bending stresses as shown in Figure 5.4. It implies that the axial misalignment gives rise to complex behaviour which results in only slight increases in gear contact and bending stresses, but also leads to a marked increase in wear rate. With respect to the disproportional increase in wear rate, one possible reason is the wear measurement and the calculation. The experimental data represents reality (to within its own reasonable uncertainties as it includes wear and viscoelastic deformation such as the tilting of the teeth and tooth bending) and so discrepancies of their magnitude must arise from factors not considered in the predicted models. One factor might be due to the disproportionately accumulative gear surface and bulk temperatures during operation. The effects of temperature on the wear behaviour of polyacetal gears, will be discussed in detail in Chapter 6. Another may be an increase in surface roughness owing to more wear debris trapped between contacting teeth than the aligned case and consequently further increasing gear wear as discussed in Section 4.3.3 and statement in [19, 96, 116]. Two possible interactions between wear debris and two engaging tooth surfaces are sketched schematically in Figure 5.5, where Figure 5.5(a) depicts a pair of teeth relatively sliding without interactions of wear debris. One is that wear debris may join the worn tooth contact surfaces which leads to an increase in the roughness of local tooth contact surfaces, and subsequently may cause local overheating or even local melting as shown in Figure 5.5(b). The other may be that the bulk mass wear debris trapping between two meshing tooth surfaces may act as a third body (particle) as shown in Figure 5.5(c) which is likely to increase sliding



wear and sliding frictional heat due to the relative sliding actions respectively between wear debris and driving tooth surface and driven tooth surface. The details of tooth wear surfaces and characteristics of wear debris due to axial misalignment will be presented and discussed in the following Sections.

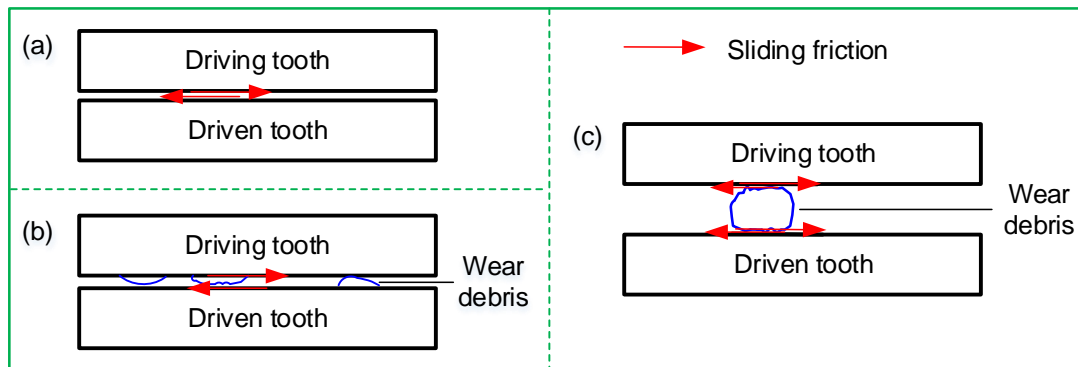


Figure 5.5 Schematic interaction of bulk mass wear debris and meshing tooth surfaces

### 5.2.2 Topography of worn tooth surfaces

- **Distribution of wear debris and ‘ploughing’ wear marks**

The non-contact regions of the tooth surfaces that arise from the axial misalignment have structures in stark contrast to the worn surfaces, as shown in Figure 5.6. It reveals that axial gear misalignment leads to edge loading, resulting in a reduction in contact tooth face width, and subsequently an increase in contact pressure. It is interesting to note that wear debris tends to distribute away from the pitch point. For the driving gear much more debris scatters to the tooth root, where it is evenly distributed, than to the tip, where it collects mostly near the middle. For driven gears, the wear debris spreads uniformly across both the bottom of the tooth root and the tooth rip, with much more of it collecting at the tip than at the root. Massive ‘ploughing’ wear marks develop on the gear tooth surfaces which

may partly result from interactions with the wear debris.

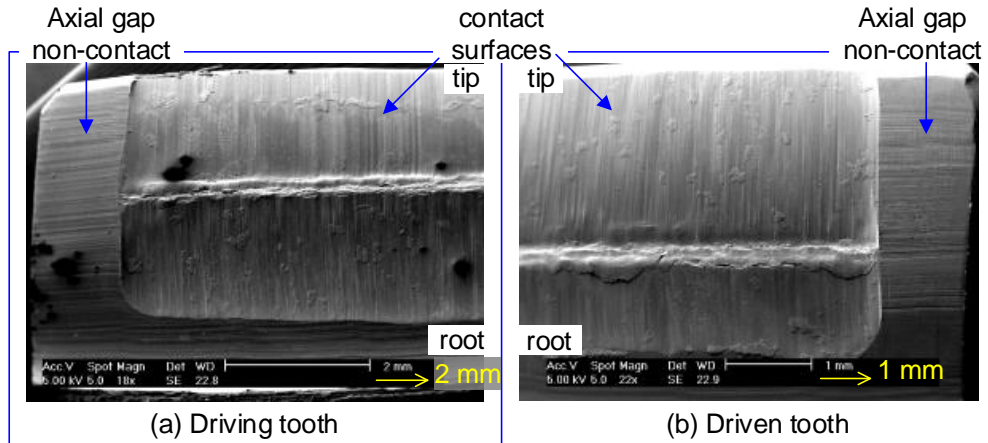


Figure 5.6 SEM micrographs of worn tooth surfaces (axial gap 1.42 mm)

- **Pitting**

Figure 5.7 exhibits many pits over the tooth contact surfaces subjected to an axial gap of 1.42 mm. The size of micro pitting is not greater than  $5\ \mu\text{m}$ . Note that the amount of micro pitting increases with approach to the region of the pitch point from both tooth tips and roots. A rise in the ratio of rolling to sliding contact (pure rolling at the pitch point) results in the generation of micro pitting. It is a classic wear characteristic of rolling contact, such as happens with cams, rollers (bearings) and metallic gears.

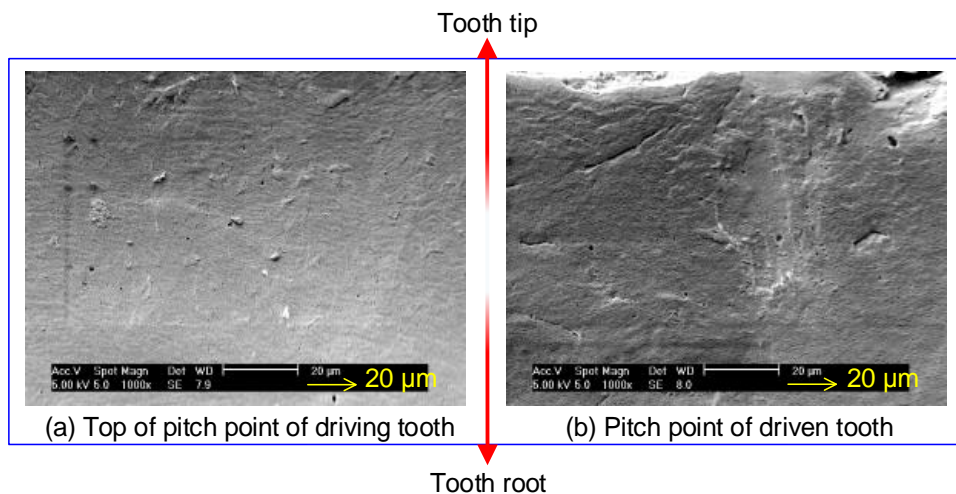


Figure 5.7 SEM micrographs of pitting on worn tooth surfaces (about  $9 \times 10^5$  cycles, axial gap of 1.42 mm)

- **‘Fish scale’ structures**

‘Fish scale’ like material structures on the worn gear tooth surfaces (axial gap 1.42 mm) were observed through using scanning electron microscope (SEM), as shown in Figure 5.8 and Figure 5.9. The ‘fish scale’ scatters in the vicinity of the pitch line of both driving and driven gear teeth. The size of the ‘fish scale’ is in the range of 5-20  $\mu\text{m}$ , which is much larger than that of micro pits (as in Figure 5.7). Moreover, micro pits and the ‘fish scale’ do not occur in the same location although they are all close to the pitch line. Therefore no causal relationship between the formations of micro pits and ‘fish scale’ is found. The ‘fish scale’ in Figure 5.9 (a) resembles the propagation of micro-cracks and perhaps is on the verge of delamination. As the ‘fish scale’ is present on both sides of the pitch line, it is hard to determine its physical processes that cause in its formation of mechanism (e.g. directions of rolling/sliding actions, local excessive stresses and surface asperity removal). The formation of ‘fish scale’ may be due to surface-defect originated contact fatigue leading to extended surface cracks, or delamination. However, establishing its origin requires further study involving different test configurations. Similar features were observed on worn gear surfaces in the aligned cases at various loads (see Section 4.2.2).

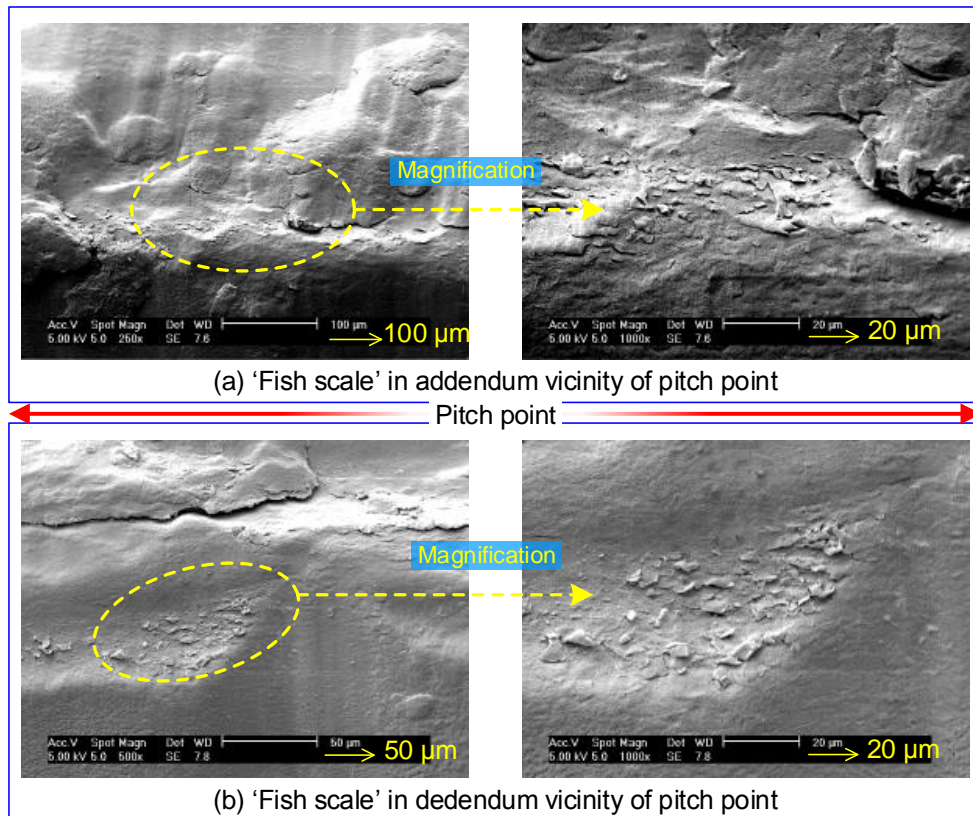


Figure 5.8 SEM micrographs of 'fish scale' on both sides of pitch point of a driving tooth (Axial gap 1.42 mm)

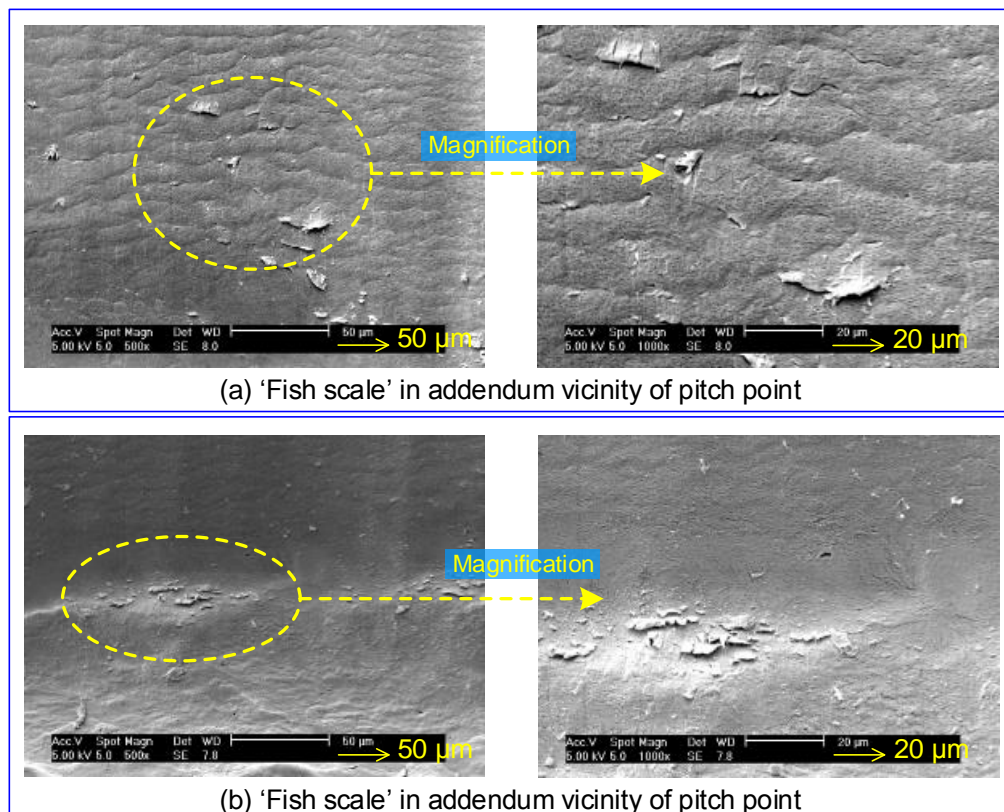


Figure 5.9 SEM micrographs of 'fish scale' on top of pitch point of a driven tooth (axial gap 1.42 mm)

- **‘Sand wave’ wear marks**

Figure 5.10 shows the plate-like wear debris and ‘sand wave’ wear marks. The fringe of plate debris indicates that roll-like wear debris is compacted into the plate debris. ‘Sand wave’ wear patterns were commonly seen in nominally aligned cases (see Section 4.2.2), observed, mainly present over the gear teeth components which act ‘recess action’. Somewhere surrounding the ‘sand wave’ wear marks wear debris mostly could always be noted, similar to the nominally aligned cases presented in Section 4.2.2. The presence of the striking ‘sand waves’ wear patterns may be due to the wear debris coupling sliding/rolling actions.

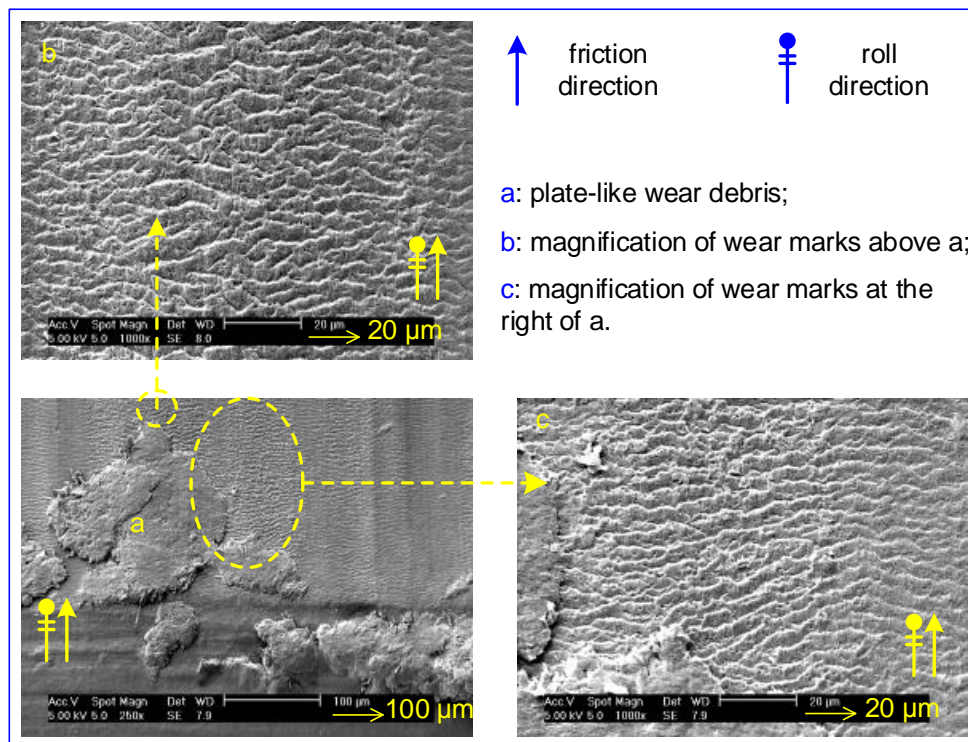


Figure 5.10 SEM micrographs of debris and ‘sand waves’ wear marks (axial gap 1.42 mm)

### 5.2.3 Regime of wear debris

- **Possible formation mechanism for large size wear debris**

Increases in volume and size of wear debris were observed on worn tooth surfaces subjected to axial misalignment compared to those in nominal alignment. In fully aligned tests, wear debris can fly from both sides of tooth flanks, the tips and the roots. However, the wear debris has little potential to escape from two sides of tooth flank in axially misaligned tests. This suggests a possible formation mechanism for copious and large piece (plate-like, over 50  $\mu\text{m}$ ) wear debris. As Figure 5.11 illustrates, the noncontact surface ends due to axial gap gradually extrude out as wear occurs to the contact surfaces. The noncontact ends develop into walls a and b, as in Figure 5.11, which tend to prevent wear debris escaping. Therefore, copious powdery wear debris is trapped between the tooth contact surfaces and is recirculated numerous cycles to become consequently compacted into large piece of wear debris. In turn, this results in an increase in the roughness of the contact surfaces and subsequently an increase in the friction (or frictional heat) which accelerates gear wear as discussed in Sections 4.3.3.2 and 4.5, agreeing with the statement in [19, 96, 116].

The wear particles were collected from axial misaligned tests and were observed by using an optical microscope (OM) using Olympus with a x10 objective and oblique with white light illumination. In addition to powdery debris, three categories of regime of wear debris were noted, which are translucently lamellate, wood shavings-like and small snow flake-like wear



debris.

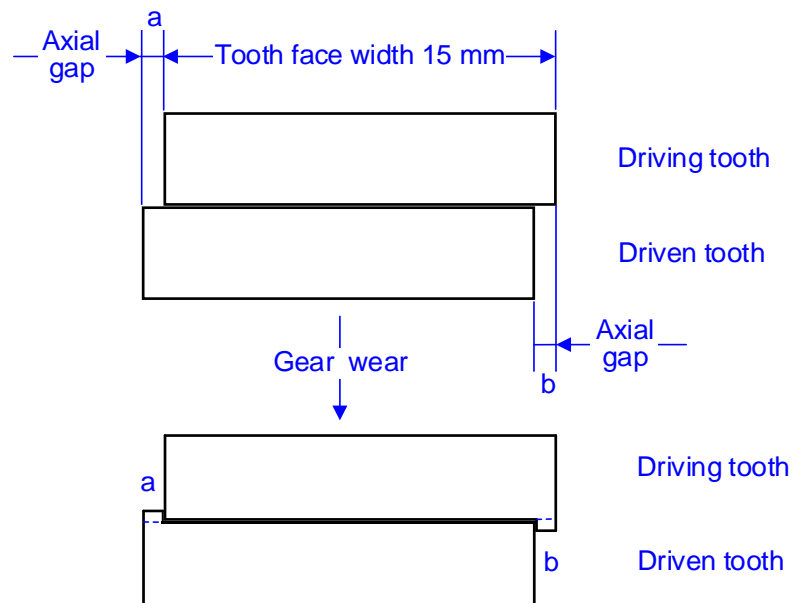


Figure 5.11 Schematic diagram of edge wall forming due to axial deviation

- **Translucently lamellate wear debris**

Figure 5.12 exhibits the translucently lamellate wear debris which was generated in fast wear-in phases. Most of semi-transparent wear particles have areas of about 0.2 mm x 0.2 mm and 0.4 mm x 0.4 mm respectively in tests with axial gaps of 1.42 mm and 2.48 mm. An increase in axial deviation consistently results in a rise in the size of the wear debris. The semi-transparent wear debris was generated in the initial fast wear-in phase and is likely to be cut off straight from gear contact surface without undergoing repeated friction events. Therefore its formation may originate from the surface roughness of new gears when surface asperities are sheared off once relative motion of gears initiates.

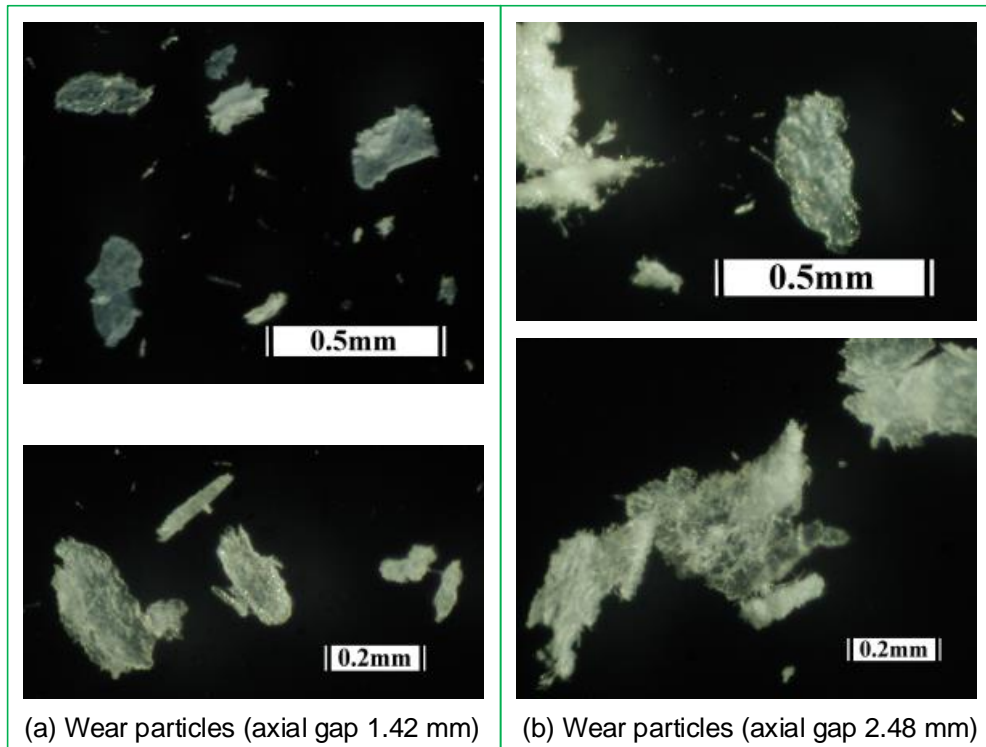


Figure 5.12 OM micrographs of translucently lamellate wear debris

- **Small snowflake-like wear debris**

Some small snowflake-like wear debris was noted in tests as which, presented in Figure 5.13, seems composed of an accumulated amount of small needle-like/roll and powdery wear debris. This type of debris is very likely a starting point for the formation of ‘wood shavings’ like debris.

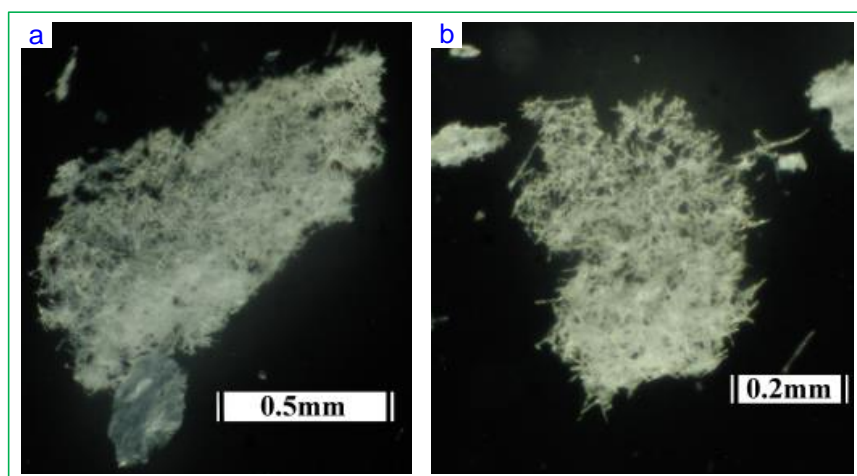


Figure 5.13 OM micrographs of small snowflake-like wear debris (axial gap 1.42 mm)



- **‘Wood shavings’ wear debris**

A strikingly different feature of wear debris developed in axially misaligned tests was the ‘wood shavings’ like wear debris shown in Figure 5.14 and Figure 5.15. For the majority of cases, the size is greater than 0.2 mm x 1.0 mm. Its formation may be due to a high volume of small ‘needle/roll’ like and powdery wear debris being compacted into this bulk size after numerous recirculated cycles. Therefore it may be a development of the small snowflake-like wear debris. The wood shavings-like appearance may be associated with the coarse ‘ploughing’ wear marks (see Figure 5.6 ) and the edge walls (see Figure 5.11). Note that the presence of granular wear debris in nominally aligned tests (described in Section 4.2.3) is also related to the edge walls due to gears not in full alignment. The distinction between the ‘wood shavings’ and the granular wear debris is speculated to be caused by the high contact stress, the high volume of the wear debris, deep ‘ploughing’ wear marks and large size of the edge walls in deliberately setting axial deviations (1.42 and 2.48 mm) tests, compared to nominally aligned tests possibly having small deviations (less than 0.6 mm).

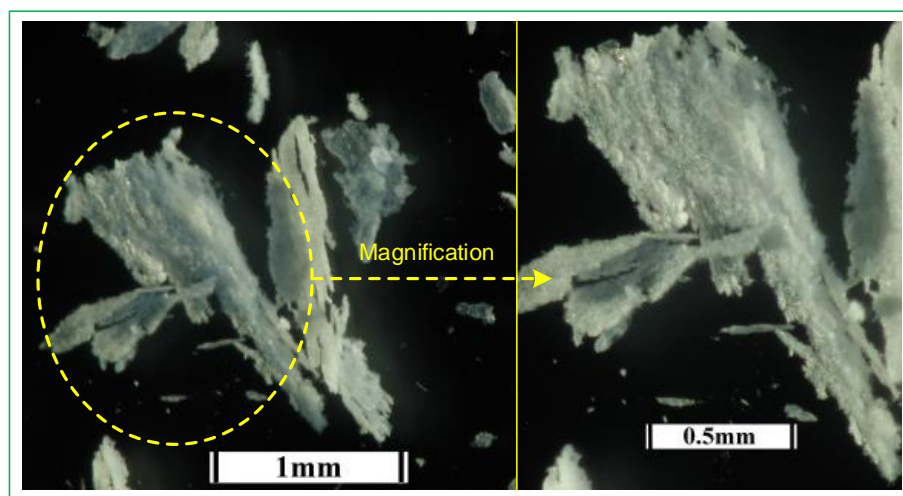


Figure 5.14 OM micrographs of wood shavings-like wear debris (axial gap 1.42 mm)

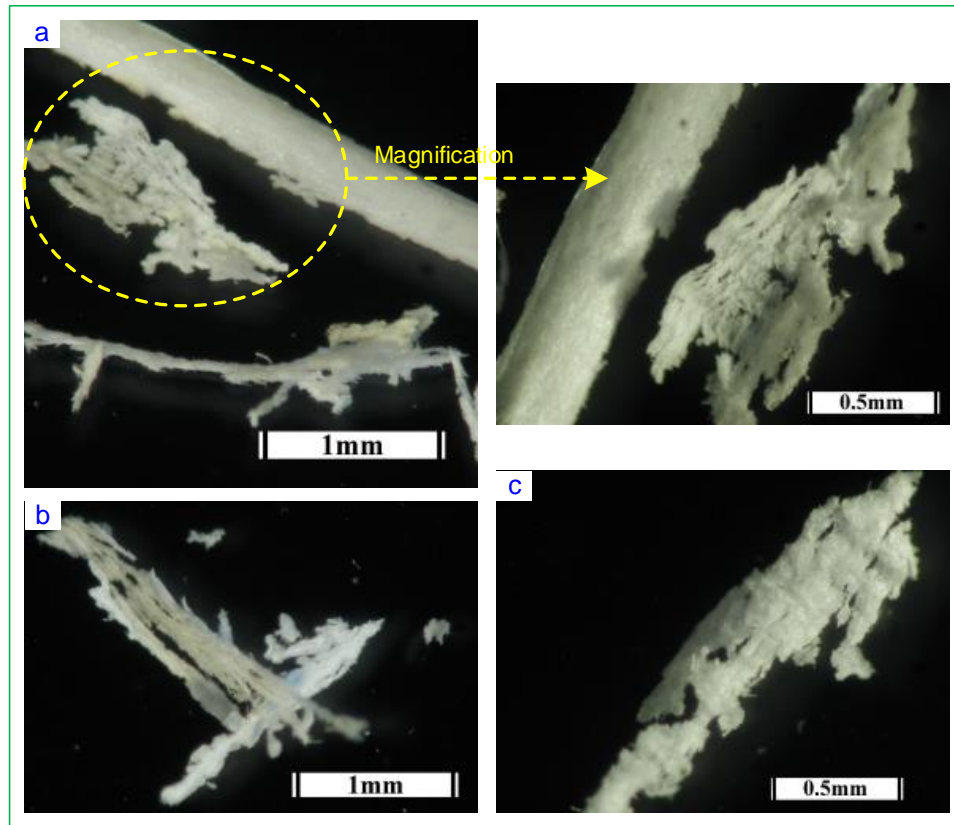


Figure 5.15 OM micrographs of wood shavings-like wear debris (axial gap 2.48 mm)

### 5.2.4 Conclusions

In order to clearly see the effect of axial misalignment on gear wear, these tests were conducted with considerably larger axial deviations than are likely to occur in real applications.

As expected, an increase in axial deviation results in an increase in the wear rate of polyacetal gears. The increase in wear gradient is greater than predicted simply from those in Hertzian contact and bending stresses.

Compared with the aligned test, many more visible ‘ploughing’ type of wear marks and large piece of wear debris were seen on worn tooth surfaces under axial misaligned conditions. A striking shape of wear debris (falling off gears), ‘wood shavings’ like debris, was generated under axial

misalignment.

Possible interactions are proposed as causes of the observed deep 'ploughing' and 'sands wave' wear marks, 'plate' like and 'wood shavings' like and wear rate are proposed. Unworn outer regions of axially misaligned gear teeth help to trap wear debris between tooth surfaces, which tends to promote the formation of 'wood shavings/plate' wear debris and deep 'ploughing' wear patterns which then further affect gear wear processes.

### **5.3 Test results and discussions for radially misaligned gears**

Radial misalignment has two cases: that the operating centre distance (OCD) is less than or greater than the nominal centre distance (NCD). Therefore two categories of tests subjected to radial misalignment were conducted and corresponding radial deviations  $d$  were set to -0.25 mm, -0.3 mm and +0.45 mm respectively. Note that OCD equals the sum of NCD and  $d$ . The radial deviation causes parameter variations including reference radius  $R_p$ , pressure angle, contact ratio, Hertzian contact stress, bending stress and so on, which induce varying gear wear. Therefore the wear rate in the initial wear-in phase is predicted to increase in correspondence with a reduction in OCD. Test results and discussions are given in Section 5.3.1 and topologies of worn tooth contact surfaces and wear debris are described in Sections 5.3.2 and 5.3.3 respectively. General conclusions regarding the effects of radial misalignment are outlined in Section 5.3.4.

### 5.3.1 Wear curve and wear rate

The radial misaligned test results are shown in Figure 5.16, which shows the wear curve (L1) for slight expansion in OCD to be similar to that of alignment (L4). However, the wear curves (L2 and L3) for slight contractions in OCD are visibly different. Comparing with L4, the wear gradients of L2 and L3 in the initial wear-in phase are much steeper, but they are gentler in the steady wear phase. The initial wear-in periods of L2 and L3 are short. The initial wear of L3 is also short but involves a total wear greater than 2 mm. The wear rates of those test results are plotted in Figure 5.17. It depicts an approximate trend that a contraction in OCD results in an increase in initial wear rate and no striking difference when there is a slight expansion in OCD. For instance, initial wear rates of L2 and L3 are over three fold and 12 fold that of nominally aligned case (L4) respectively. Radial deviation gives rise to a reduction in steady wear rate.

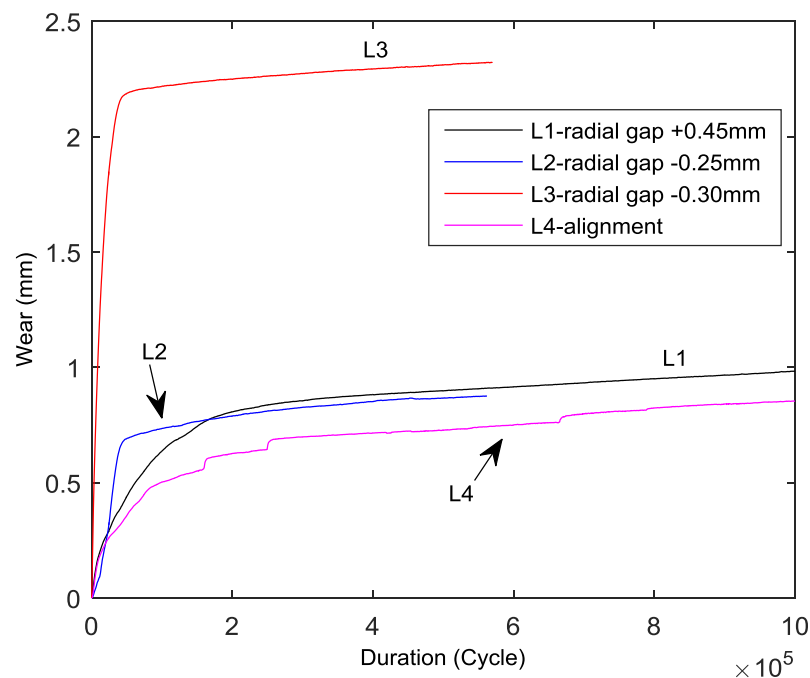


Figure 5.16 Wear versus duration in radial misalignment tests

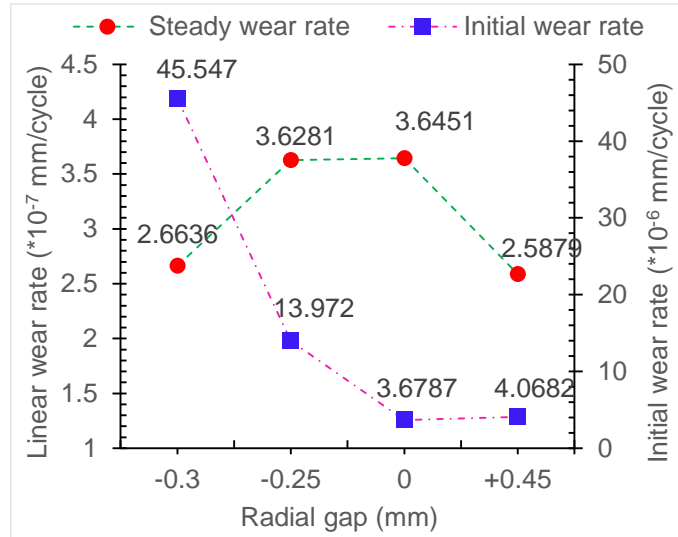


Figure 5.17 Wear rates versus radial deviation

### • Discussions

The test results confirm that radial misalignment results in notable variations in mating gears' parameters and wear performance, such as pressure angle, contact ratio, Hertzian contact and bending stresses and wear rate. Using the Equations (4.1-4.5) given in Section 4.2.1 (BS 6168:1987 [13]), the values form some parameters such as pressure angle, contact ratio, contact stress and bending stress can be obtained. If we designate the Hertzian contact stress, bending stress, initial wear rate and steady wear rate to be  $\sigma_H$ ,  $\sigma_F$ ,  $k_I$  and  $k_S$  at nominally no radial deviation, then corresponding values at radial deviation -0.3 mm, -0.25 mm and +0.45 mm can be expressed in these symbols and are tabulated in Table 5.2. For the convenience of discussion, the variation ratios for the above parameters in relative to the aligned case are depicted in Figure 5.18 and Figure 5.19, where positive and negative values denote a relative increment and a reduction based on that in aligned condition.

Table 5.2 Predicted variation in parameters and actual wear rates due to axial deviations

Radial deviation (mm)	+0.45	0	-0.25	-0.3
OCD (mm)	60.45	60.0	59.75	59.7
Reference radius $R_{p1}$ (mm)	30.225	30	29.875	29.85
Pressure angle ( $^{\circ}$ )	21.141	20.0	19.331	19.193
Contact ratio	1.4366	1.6535	1.7793	1.805
Hertzian contact stress	$1.007^* \sigma_H$	$1.0^* \sigma_H$	$0.995^* \sigma_H$	$0.994^* \sigma_H$
Bending stress	$1.099^* \sigma_F$	$1.0^* \sigma_F$	$0.954^* \sigma_F$	$0.945^* \sigma_F$
Initial wear rate	$1.106^* k_I$	$1.0^* k_I$	$3.798^* k_I$	$12.381^* k_I$
Steady wear rate	$0.710^* k_S$	$1.0^* k_S$	$0.995^* k_S$	$0.731^* k_S$

Figure 5.18 and Figure 5.19 illustrate that centre distance expansion (CDE) results in significant reductions in contact ratio and steady wear rate and visible increase in operating pressure angle, bending stress at  $R_{p1}$  as well as slight increase in Hertzian contact stress and initial wear rate; while centre distance contraction (CDC) leads to a significant increase in initial wear rate and a decrease in pressure angle, bending stress and steady wear rate and a slight reduction in contact stress. In a word, a slight CDE introduces backlash that can allow thermal expansion and moves the load towards the tooth tip; therefore it does not markedly affect gear wear. However, CDC results in an increase in the gear profile contact ratio which is likely to induce interference fit conditions between the mating gears. In this case, the stress levels grow extremely high at both the entering and leaving corners of tooth contact. For instance, in case of radial deviation of (-0.3 mm) there is a high differential wear rate between initial and steady wear phases, probably because corner contact get polished out so that the stress reduces to closely match the ambient values. The SEM micrographs of Figure 5.21 (II and III) may demonstrate this view. Hence, CDC deteriorates strikingly the wear performance of polyacetal gears. Note that the two cases do not

greatly affect Hertzian contact stress. The engagement of polymer gears will always involve some degree of thermal expansion and creep which are likely to introduce effects resembling the case of CDC.

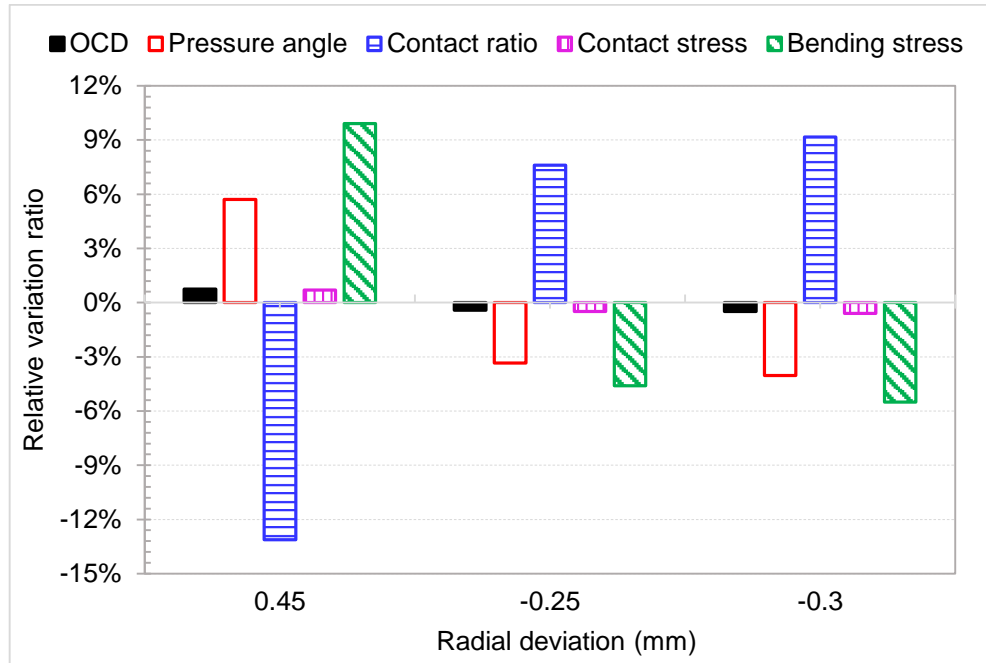


Figure 5.18 Predict parameter variation ratios versus radial deviations

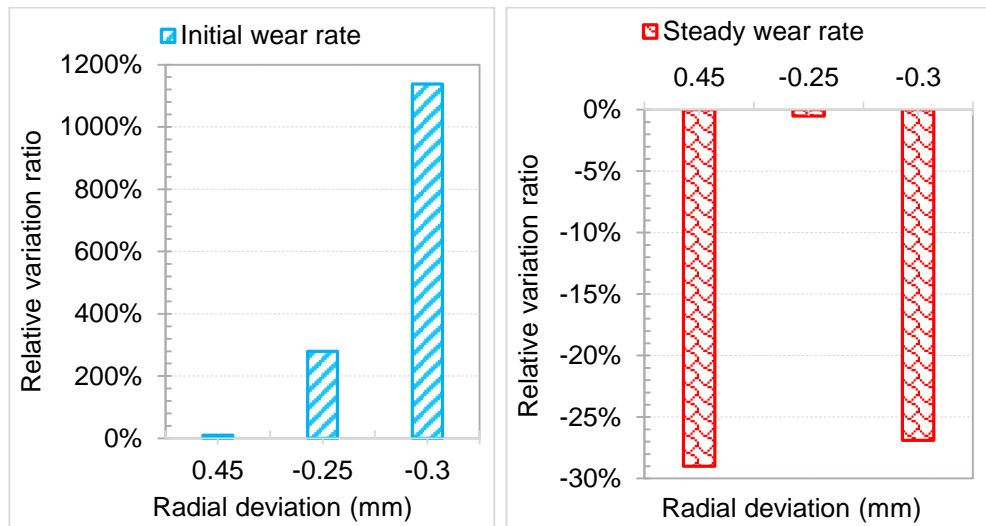


Figure 5.19 Actual variation ratio in wear rate versus radial deviation: note the scale of initial wear rate (left bar graph) is significant.

### 5.3.2 Topography of worn tooth surfaces

Scanning electron scanning (SEM) examinations of worn tooth

contact surfaces report that almost no difference was found when a gear pair experienced a slight expansion in OCD ( $CD+0.45\text{mm}$ ), however striking different features were observed when a slight contraction occurred ( $CD-0.25\text{ mm}$ ). Details are described in the following paragraphs.

- **Superimposed and dense ‘ploughing’ wear marks**

The roughness of driving tips and driven roots is much lower than their counterparts. Substantial wear occurs to the dedendum region of driving gears and addendum area of driven gears. The contact surfaces seem to have been ploughed and form superimposed deep and dense ‘ploughing’ wear patterns, as shown in Figure 5.20. It also demonstrates that an increase in the gear profile contact ratio due to centre distance contraction.

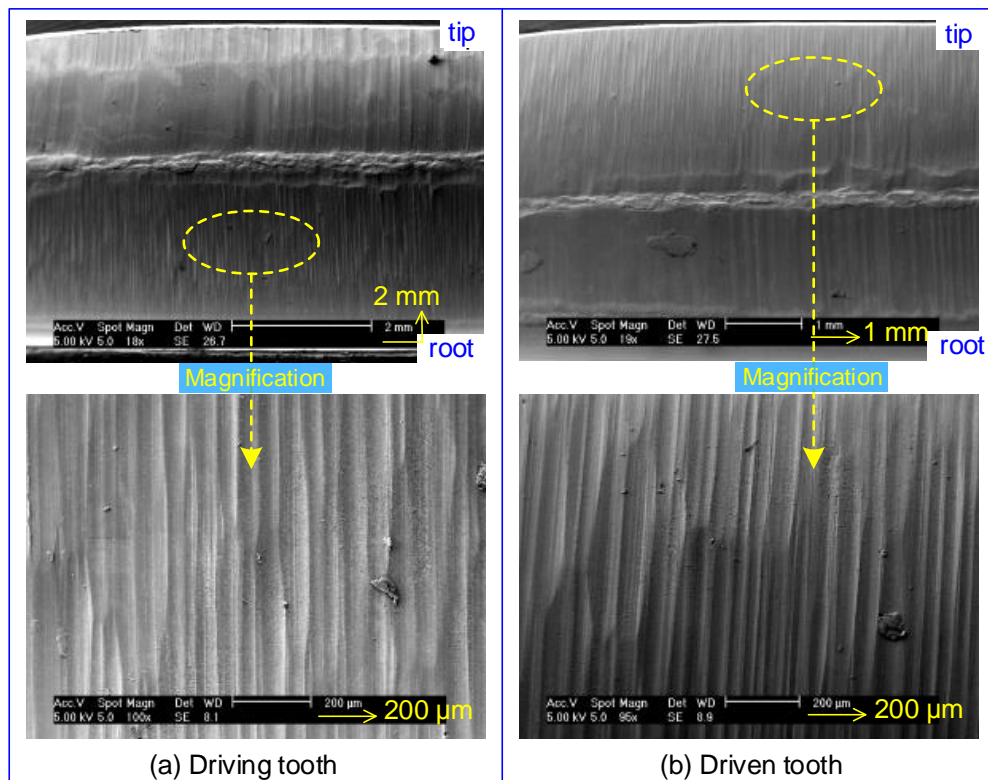


Figure 5.20 SEM micrographs of worn tooth surfaces (radial deviation  $-0.25\text{ mm}$ )



The operating centre distance contraction results in the mating teeth experiencing an interference fit which mainly takes place during a gear pair approach process; no significant effect is imposed on the tooth contact surfaces during gears recess process. Hence once the gear pair comes into mesh, the interaction of tooth contact surfaces initiates and subsequently considerable surface material is removed (by shearing off, scratching or welding, see the regimes of wear debris in Section 5.3.3). The degree of wear may also differ greatly according to the roughness and the nature of asperities on the contact surfaces. It is a possible origin for the formation of the densely imposed 'ploughing' wear marks.

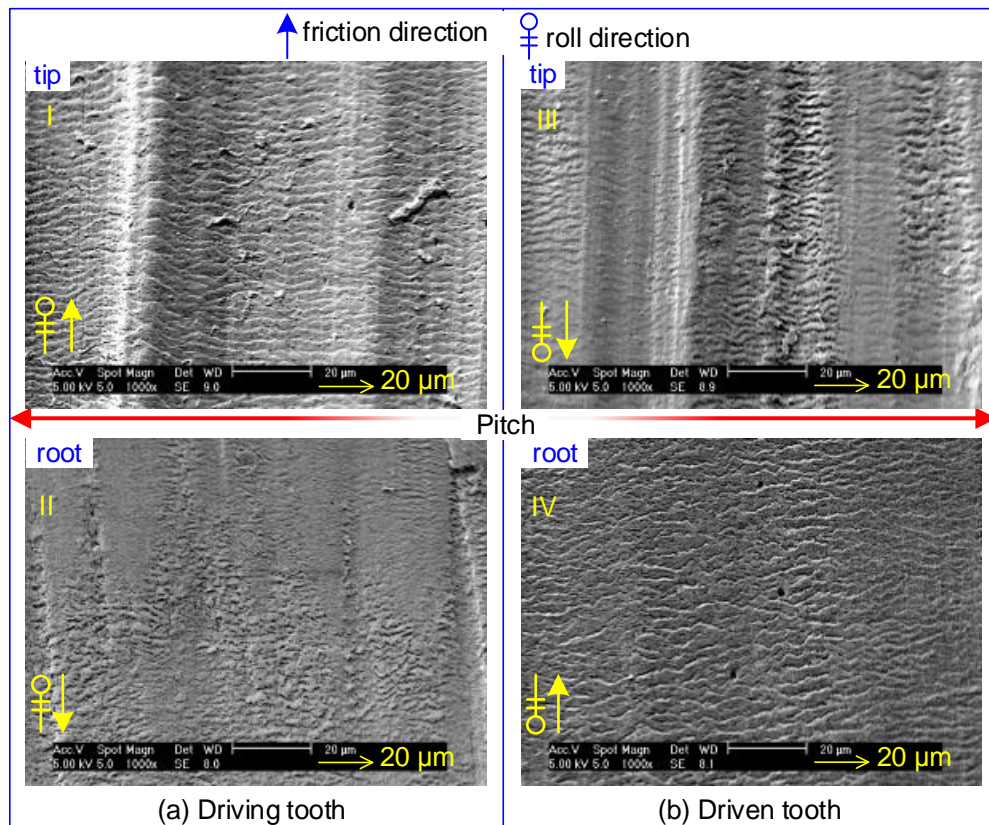


Figure 5.21 SEM micrograph comparisons of tooth tips and roots (radial deviation -0.25 mm)

An instance of the effects of various wear processes due to radial deviation on gears is shown in Figure 5.21, where II and III exhibit topologies

of worn tooth surfaces experiencing gears' approaching action, while I and IV show the pair undergoing recessing action. Effects of tension and compression stresses (contact fatigue) and abrasive wear (perhaps scratched particles) and seem to occur on the former (surfaces partly polished out) and surface contact fatigue (presence of 'sand wave' wear marks and pits) on the latter.

- **Pitting and adhesive wear**

The amount of pitting is significantly more than that on corresponding worn teeth subjected to nominally align and axially misaligned conditions. An increasing number of pits is present when getting closer to the vicinity of pitch point. The number and size of pits on the driving roots and driven tips are respectively more than those on the driving tips and driven roots.

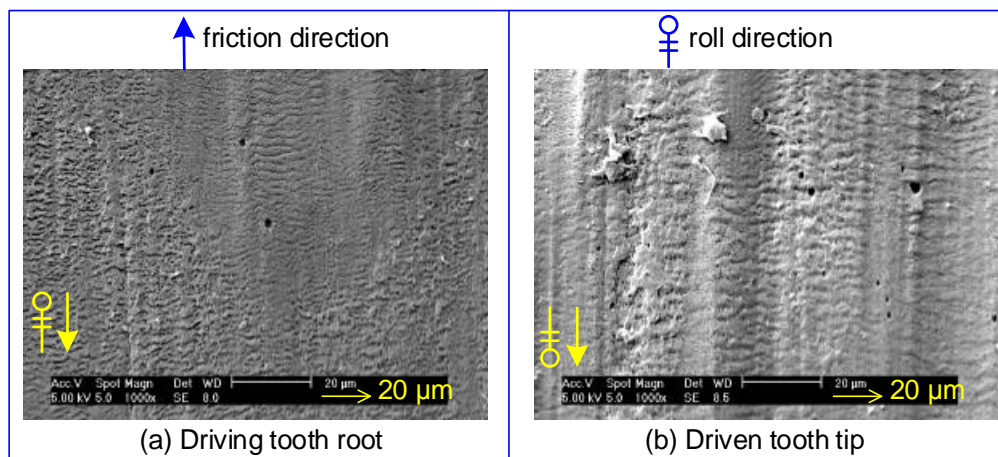


Figure 5.22 SEM micrographs of adhesive wear and pitting on polyacetal gear surfaces (radial deviation  $d$  (-0.3 mm), 7.2 N·m, 1000 rpm)

When a mating gear pair comes into mesh, in particular in the initial wear-in phase, a degree of local overheating may happen. As polyacetal (or other polymers) is sensitive to temperature, somewhere on the contact surfaces may almost instantly get soft or even melt and subsequently

adhesive wear occurs at the moment teeth are engaging. This event correlates with the flash temperature. Adhesive wear and contact surface fatigue (pitting) are indicated in Figure 5.22, which may be two important wear failure modes of polyacetal gears as stated in [52].

- **Distribution of wear debris and ‘sand wave’ wear marks**

In contrast to the axially misaligned conditions, not considerable wear debris was observed on the worn tooth surfaces and its size was significantly smaller. No clearly visible wear debris distribution patterns were noted. However, evident patterns were present under aligned and axial misaligned conditions. For aligned conditions, heavy wear debris distributed in the vicinity of pitch point of gear teeth. For the axially misaligned conditions, copious wear debris uniformly scattered over the dedendum of driver and addendum of driven teeth.

Clear ‘sand wave’ wear marks were present on relative smooth worn tooth surfaces, namely over the tips of driving gears and roots of driven gears. Taking close-up views of ‘sand wave’ wear marks shown in Figure 5.23, note again that there is always presence of wear debris surrounding or on the sliding path of ‘sand wave’. Hence apart from contact surface interaction (sliding/rolling contact actions), the wear debris may be one significant component which contributes to the generation and development of ‘sand wave’ wear marks.

Figure 5.24 shows many fringe on the edge of large ‘plate’ wear debris, which is similar to the ‘roll/string’ wear debris mentioned in Section 5.2.2. It indicates that the ‘roll/string’ wear debris is likely to be compacted

into large 'plate' wear debris after recirculation through many mesh cycles.

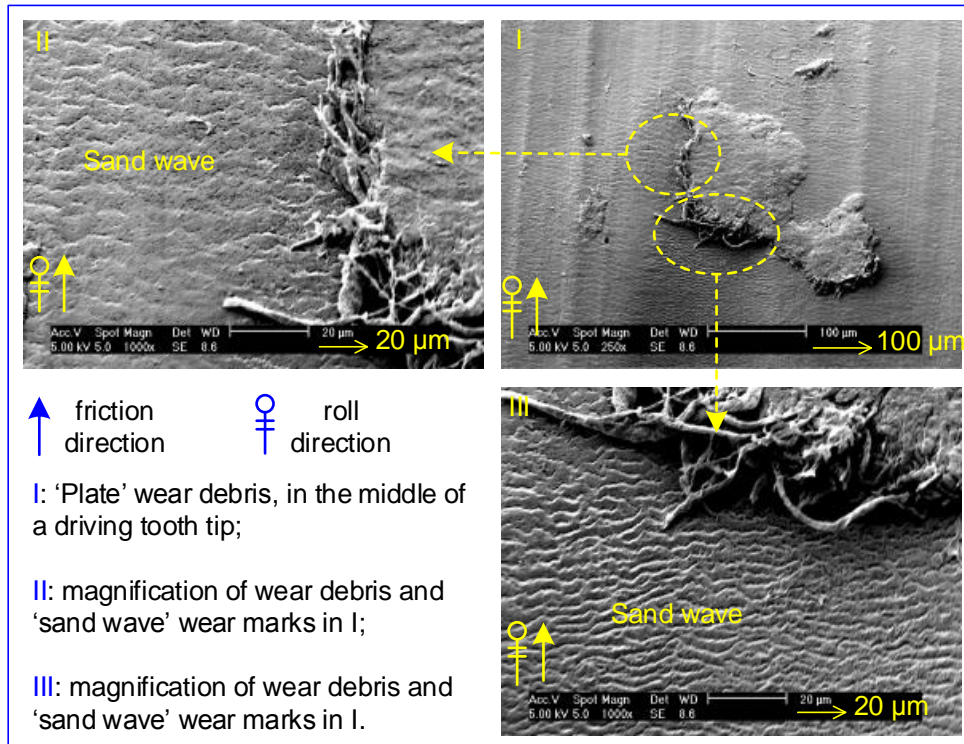


Figure 5.23 SEM micrographs of 'sand wave' wear marks and 'plate' wear debris

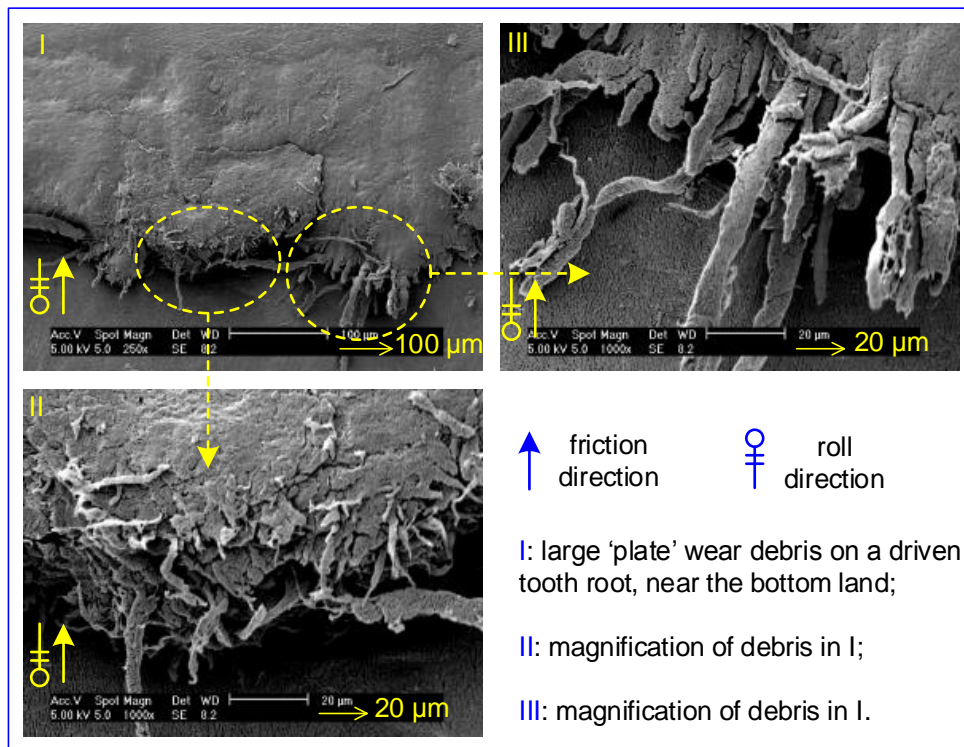


Figure 5.24 SEM micrographs of 'plate' and 'roll/string' wear debris

Figure 5.25 shows 'belt' like wear debris on a driven tooth root near



the bottom land which may originate from contact surface material cutting (shearing) off straight away due to the interference fit of mating teeth mentioned above. Further detail of wear debris will be described in Section 5.3.3.

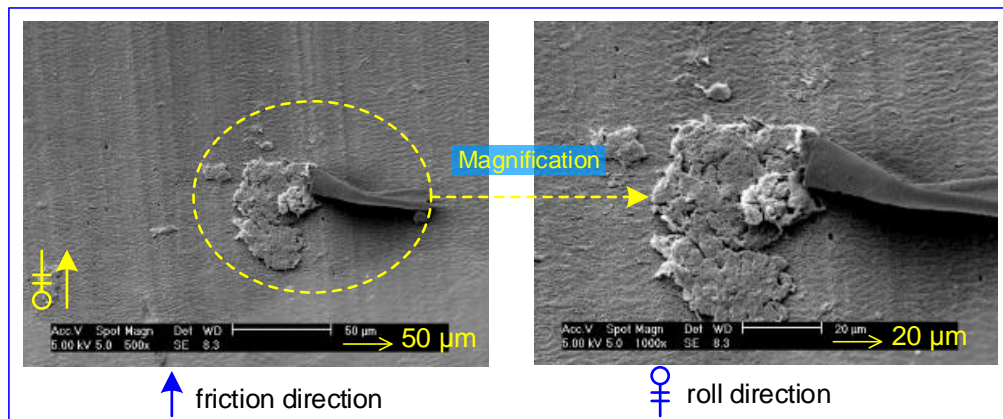


Figure 5.25 'Belt' wear debris close to the bottom of driven tooth root

### 5.3.3 Regime of wear debris

In radially misaligned tests, the wear debris generated during initial wear-in phase and the steady wear phase exhibit strikingly different characteristics.

- **Wear debris of the (-0.25 mm) radial misalignment test**

As with aligned and axially misaligned cases, translucent slice wear debris presented in initial wear-in phase and for the majority of cases its size was within 0.5 mm x 0.5 mm. A typical instance is shown in Figure 5.26. The amount and the dimensions of translucent slice wear debris are slightly larger than those in cases under axial misalignment.

Large and thick piece of wear debris were produced in the steady wear phase, as shown in Figure 5.27 (a-b). The size is over 1 mm x 1 mm. In

an close-up view, it is principally compsoed of copious ‘elongated roll/needle’ like wear debris (as in Figure 5.27(a)). The needle-like wear debris seen here correspond well with the the ‘roll/string’ like wear debris depicted in Figure 5.23 and Figure 5.24. Similar ‘cotton-wool’ wear debris was hardly observed in aligned and axial misaligned tests.

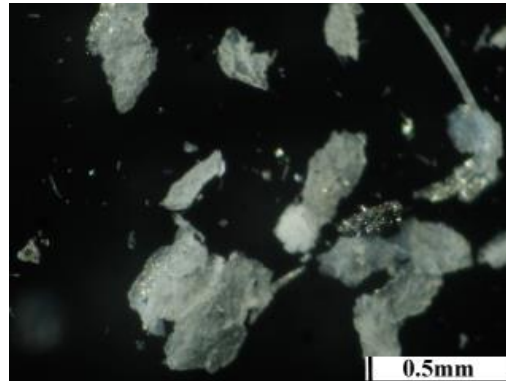


Figure 5.26 OM micrographs of translucent slice wear debris (radial deviation of -0.25 mm)

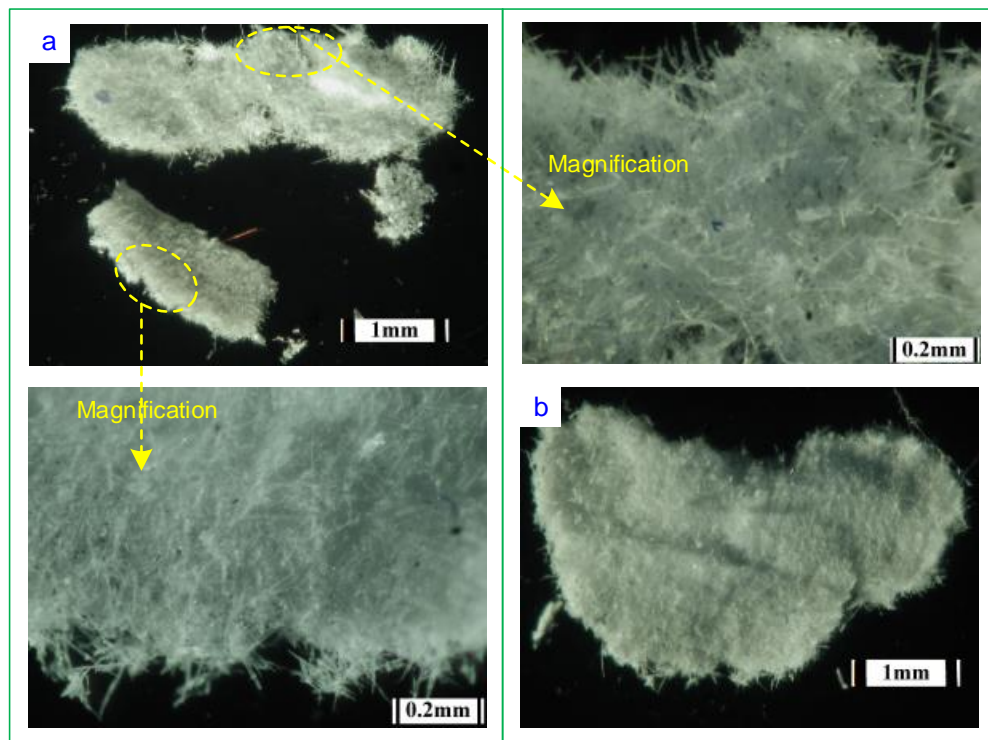


Figure 5.27 OM micrographs of ‘cotton-wool’ wear debris (radial deviation of -0.25 mm)

- **Wear debris of the (-0.3 mm) radial misalignment tests**

A striking shape of wear debris prior to steady-state wear phase was observed comprised of long strip transparent wear debris as shown in Figure 5.28(a), which seems to arise from material being torn off straight away contact surfaces. In most cases, the length is greater than 1 mm, and the width is approximately 0.5 mm.

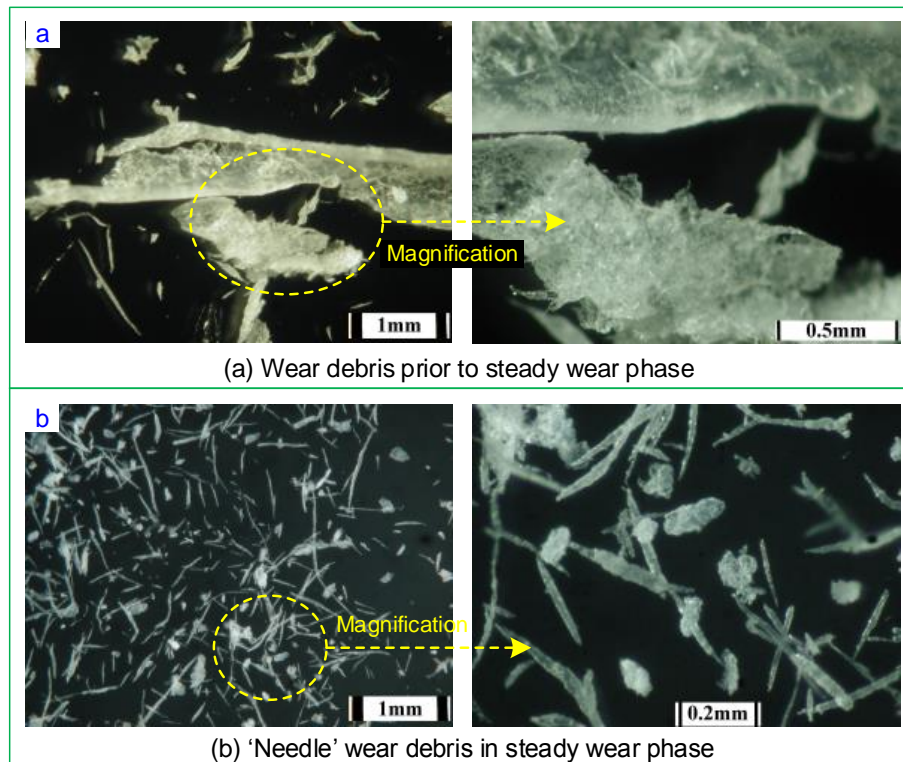


Figure 5.28 OM micrographs of wear debris (radial deviation of -0.3 mm)

Copious needle/roll-like wear debris was generated in the steady wear phase, which conspicuously differed from other tests where powdery wear debris was dominant.

The long strip and 'needle' wear types of debris reveal that the material is possibly torn immediately from the contact surfaces. This may happen because of the interference fit of matching teeth, similar to the cases

of thermal expansion occurring in the moment following the gears' engagement which will greatly degrade the wear of gears, such as was seen in the test of radial deviation of -0.3 mm.

### 5.3.4 Conclusions

The test results reveal the influences of radial misalignment on wear life of polyacetal gears. A slight increase in centre distance does not impact gear wear significantly. However a slight decrease in centre distance results in a significant increase in wear rate once the test is initiated, which increase the gear wear. Polyacetal gears may fail prematurely.

The topography of worn tooth surfaces and the shape of wear debris imply that local excessive heat occurs mainly to engaging teeth in the process of approaching, where adhesive wear and pitting (surface contact fatigue) may be two major wear modes. A decrease in centre distance highlights the contribution of the roughness of gear tooth contact surfaces: surface asperities are shearing off once relative motions initiated, with consequent amount of various translucent wear debris (i.e. slice, strip and needle/roll types of wear debris) generating. Densely deep superimposed 'ploughing' wear marks spreading over the contact surface regions which act 'entering mesh' actions.

The cases of reducing centre distance arose interference fit between matching teeth. This is speculated to be a main causal factor for forming densely deep superimposed 'ploughing' wear marks and copious translucent 'strip' and 'needle/roll' wear debris.



## 5.4 Test results and discussions for yaw misaligned gears

The introduction of yaw misalignment tends to change the shape of contact zone into skewed shape and reduces the contact area. The reduction in contact area results in a reduction of contact ratio totally. If the level of yaw misalignment is high enough, the effective contact line will be similar to that between two cylinders with skewed area, where the contact area becomes elliptical as shown in Figure 5.29 [15]. However, it is hard to obtain quantitative values of contact and bending stresses because there is no published mathematic model for polymer gears under such conditions. Nevertheless, it is predicted that yaw misalignment may result in a slight increase in wear rate. Peak stress are likely to increase with the modified contact geometry.

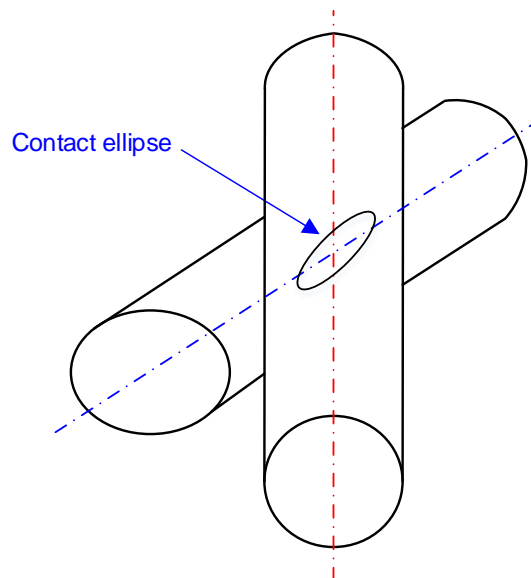


Figure 5.29 Schematic diagram of ellipse contact area

Two different sets of tests on polyacetal gears subjected to yaw misalignments were conducted at yaw angles of  $0.35^\circ$  and  $0.45^\circ$  respectively.

Detailed test results and discussions of the topographies of worn tooth surfaces and regimes of wear debris are presented in Sections 5.4.1, 5.4.2 and 5.4.3 respectively. General conclusions concerning the effects of yaw misalignment are outlined in Section 5.4.4.

### 5.4.1 Wear curve and wear rate

The yaw misalignment test results are shown in Figure 5.30, which depicts the wear curves against test duration. Note that the environment temperature of the test L3 was approximately 5°C lower than other tests, because the heating system failed during test. Did not get opportunity to repeat that test. Compared to the wear L1 (gears in aligned contact), it is evident that the introduction of yaw misalignment mainly results in a heavy wear during initial wear-in period. Maybe the low environment temperature make the wear of L3 in initial wear phase is lower than that of L2. The initial wear of L3 (yaw angle of 0.45°) is less than that of L2.

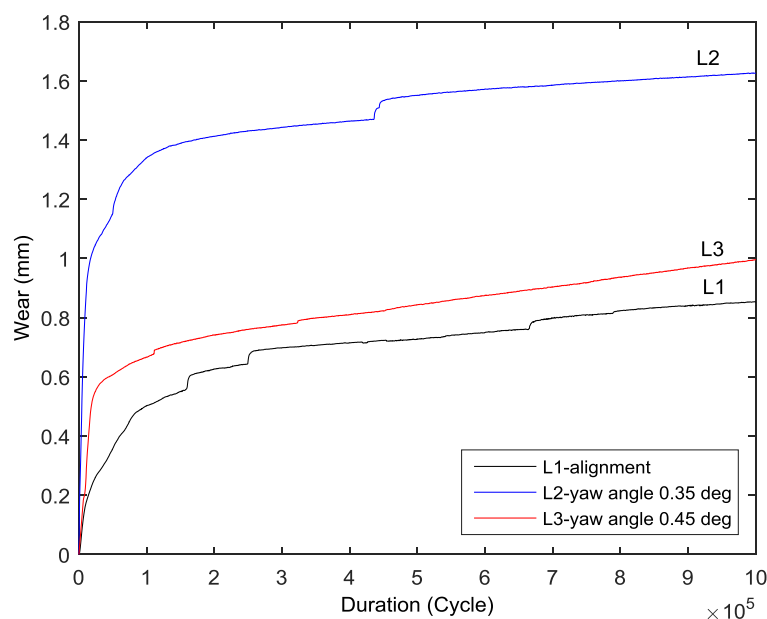


Figure 5.30 Wear versus duration of yaw misalignment tests

The wear rates before and within steady-state were calculated respectively by using the method stated in Section 5.2.1. The wear rates within these two phases subject to different yaw angles were calculated and shown in Figure 5.31, while the corresponding incremental or reduced percentages compared to the values in aligned case are shown in Figure 5.32. On the whole, wear rate before steady wear phase increases due to the degree of yaw misalignment. It is worth noting that L2 at yaw angle of  $0.35^\circ$ , the initial wear rate increases by more than 250% while the steady wear rate decreases by around 14% with respect to the aligned condition separately. One possible reason is that corner contact takes place when there is yaw misalignment which leads to high contact stress levels and heavy wear within initial wear phase. Consequently the contact surfaces get polished within initial wear-in phase which in turn cause the average wear rate in steady wear phase get slightly lower compared to the aligned case.

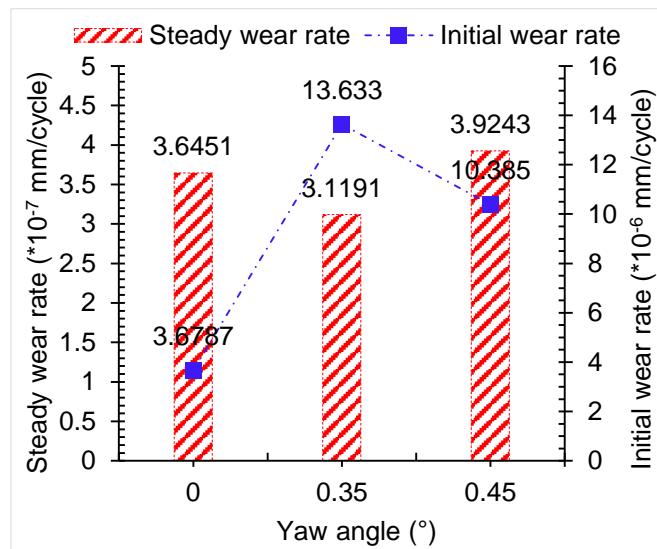


Figure 5.31 Wear rates versus yaw angles

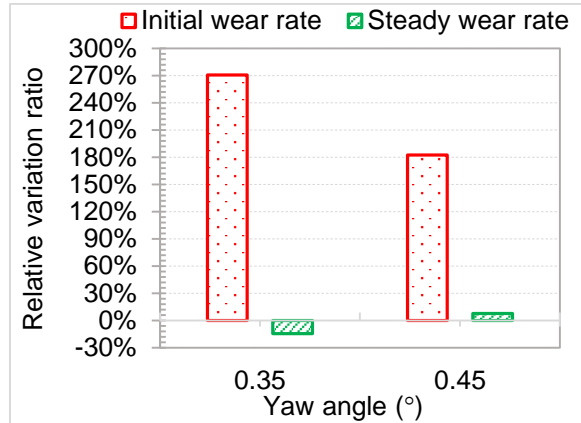
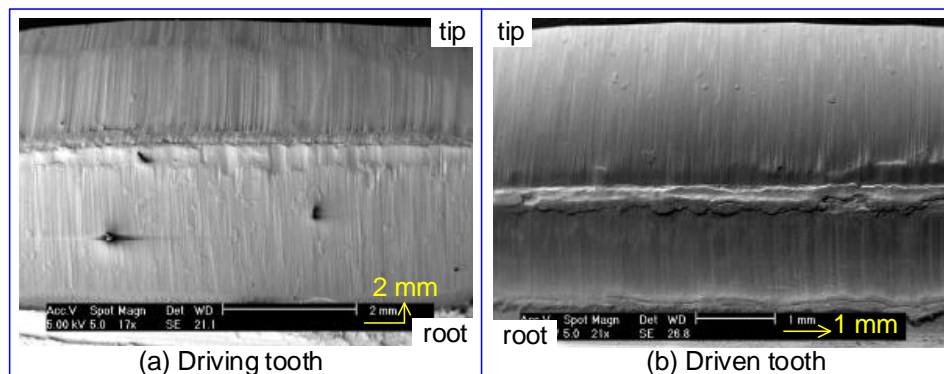


Figure 5.32 Relative variation ratio in actual wear rate versus yaw angles

### 5.4.2 Topography of worn tooth surfaces

Figure 5.33 shows SEM examinations of full views of worn tooth contact surfaces subjected to yaw angle  $0.35^\circ$ . The striking wear characterise is the clearly seen 'scoops' wear marks formed closely along the bottom of the driver's pitch point and the top of the driven gears. Perfect gear involute conjugated profiles cannot exist under yaw misalignment, which is a possible reason for scoops of material being removed from the surfaces near the pitch point. Coarse wear 'ploughing' pattern can be seen and much wear occurs over the addendum of the driving gear, as in radial misalignment tests. Copious debris scatters over driving tooth roots and driven tooth tips, although, not much as axial misalignment tests (Figure 5.6).

Figure 5.33 SEM micrographs of worn tooth surfaces (yaw angle of  $0.35^\circ$ )

Close-up views shown in Figure 5.34 reveal striking differences from the aligned ones. The wear marks resemble a ‘palm leaf vein distribution’ and ‘bamboo’ in the tip vicinity of pitch point for driving and driven gear respectively. The surface structures were not observed under other test conditions and so almost certainly arise from processes specifically caused by yaw misalignment.

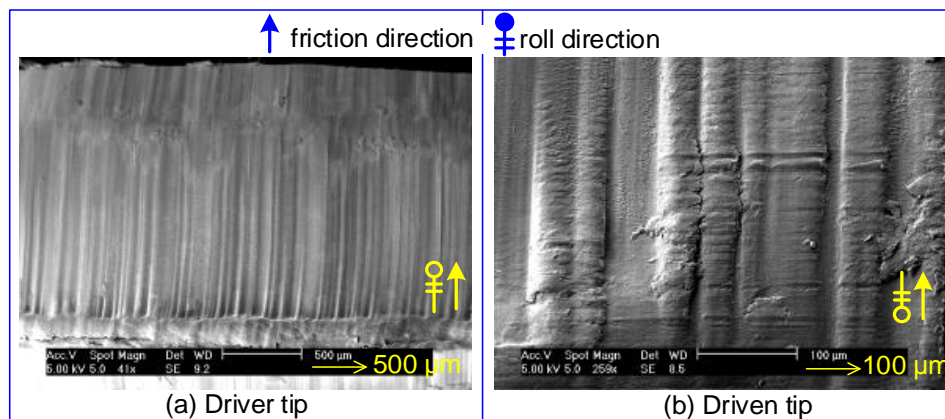


Figure 5.34 SEM micrographs of wear marks near pitch point (yaw angle of  $0.35^\circ$ )

Figure 5.35(a) presents wear marks in the root vicinity of pitch point of driver gear is similar to Figure 5.8 and there are rough surfaces near the root in Figure 5.35(b). Figure 5.36 depicts a few instances of ‘scratch’ wear marks on the driven tip and deep ‘hole’ on driven root. It seems these were caused by hard particles, abrasive wear.

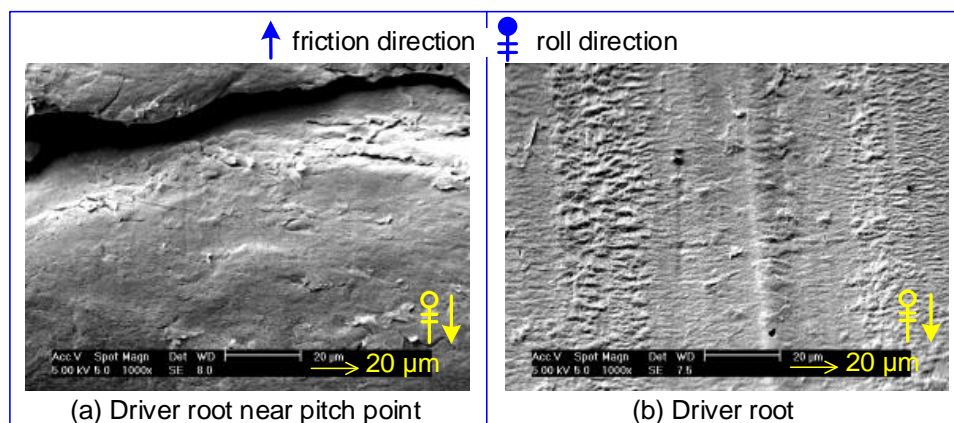


Figure 5.35 SEM micrographs of worn driver root surfaces

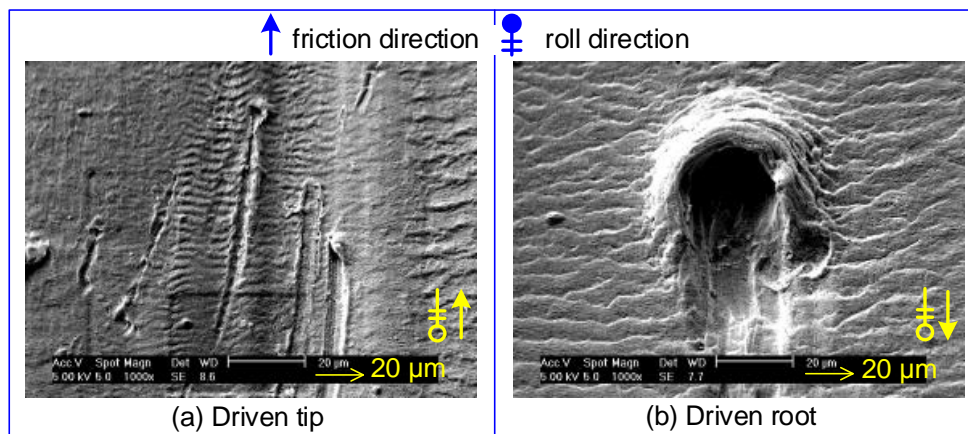


Figure 5.36 Abrasive wear and 'hole' on worn driven tooth

### 5.4.3 Regime of wear debris

The wear debris from the  $0.35^\circ$  yaw angle test generated prior to the steady wear phase is similar to that occurring in the radial misalignment tests. Translucent 'roll/needle' and 'lamellate' wear debris shown in Figure 5.37 dropped from the gears almost instantly once the test was initiated. Powdery debris dominated in the steady wear phase. The involute conjugate contacting shape of gears subject to slight yaw misalignment becomes imperfect. The contact shape shifts slightly skewed contact area. The 'roll/needle' and lamellate debris is very likely to be caused by shearing or scratches due to sliding-rolling contact and imperfect conjugate contact action as the test proceeds.

The 'needle' wear debris was examined by using SEM as shown in Figure 5.38. It resembles the top bud of asparagus and the thickness is approximate  $50\text{ }\mu\text{m}$ . The feature of its shape indicates that the 'roll/needle' wear debris also experiences cyclic many sliding and rolling actions.



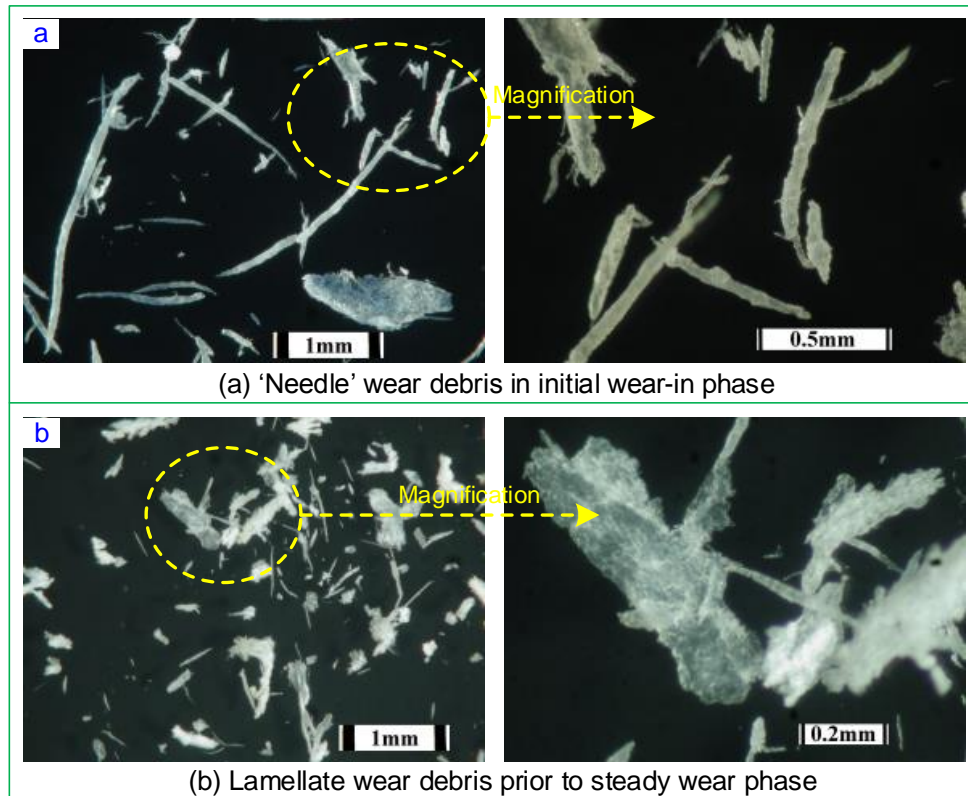


Figure 5.37 OM micrograph of wear debris (yaw angle of  $0.35^\circ$ )

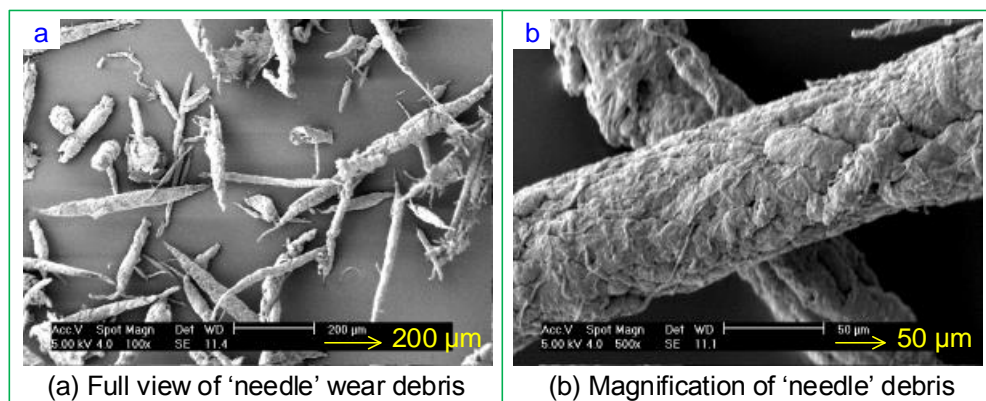


Figure 5.38 SEM micrographs of 'needle/roll' wear debris (yaw angle of  $0.35^\circ$ )

#### 5.4.4 Conclusions

Overall, polyacetal gears are not very susceptible to slight yaw misalignment in terms of relative variation ratio in steady-state wear rate, although initial wear rate is considerably greater than that under aligned conditions.

The high initial wear rate may result from an increase in contact stress because of contact area (skewed shape) reduced slightly and degree of corner contact which may no longer be present in the steady wear phase as wear proceeds. Therefore slight yaw misalignment mainly affects the wear in the initial wear phase. The presence of needle/roll-like wear debris tends to this point.

### **5.5 Test results and discussions for pitch misaligned gears**

Pitch misalignment tends to shift load towards the edge of tooth faces which results in an increase in the separation at one side of the tooth and a reduction in the separation at the other side of the tooth. It can subsequently pose a significant impact on the contact shape and stresses generated. A description of load distribution under aligned and pitch misaligned conditions is shown in Figure 5.39, which exhibit that the load is moved sharply to the left side of the tooth face. The non-conformal contact is predicted to be varied due to pitch misalignment. Therefore, the calculation of the Hertzian contact stress and the bending stress becomes complex. In theory, the position of pitch point remains the same as in the aligned condition, but, in fact contact deformation may occur due to the introduction of pitch misalignment, which results in an increase in the off line of action moments.

Three different sets of tests subjected to pitch misalignment were carried out respectively at angles of  $0.42^\circ$ ,  $0.60^\circ$  and  $0.86^\circ$ . Test results and



discussions are presented in Section 5.5.1 and the topography of worn tooth contact surfaces and wear debris are outlined in Sections 5.5.2 and 5.5.3 respectively. General conclusions in response to the effects of pitch misalignment are drawn in Section 5.5.4.

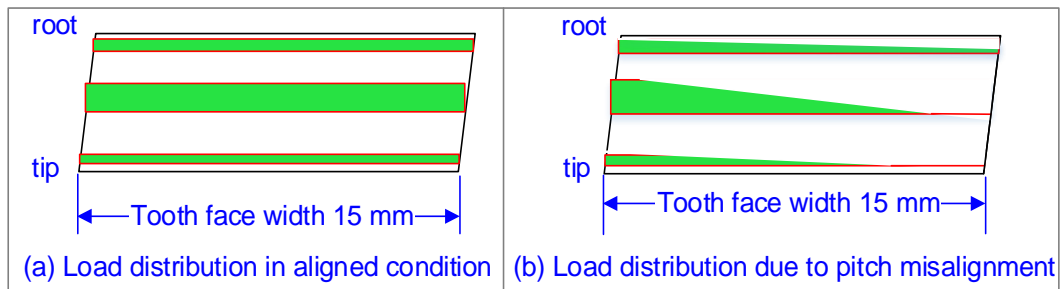


Figure 5.39 Schematic diagram of load distribution change due to pitch misalignment

### 5.5.1 Wear curve and wear rate

Figure 5.40 shows the wear subjected to pitch misalignment against operation cycles. It illustrates that there are three wear phases broadly similar to those of the aligned gears. The marked difference is that the initial wear level is high. When the pitch angle is  $0.86^\circ$ , wear prior to steady wear phase has exceeded 3 mm which is almost allowable wear limit of a gear pair. It reduces the tooth strength, resulting in gears failing prematurely.

Average wear rates (calculated as in Section 5.2.1) before and within steady-state wear phases are shown in Figure 5.41, which implies that an increase in pitch angle results in an increase in wear rate. If  $k_i$  and  $k_s$  are designated as initial and steady wear rates of the aligned tests at a load of 7.2 N·m and a speed of 1000 rpm, then those from pitch misaligned conditions can be expressed in coefficients of  $k_i$  and  $k_s$  listed in Table 5.3. Figure 5.42 clearly shows that the significant relative change ratios in wear

rates due to pitch angle in contrast to the aligned condition. Positive and negative values indicate respectively a relative increase and reduction compared to those in the aligned condition. The high differential value between initial wear rate and steady wear rate at a pitch angle of  $0.86^\circ$  may result from corner contact as mentioned in Sections 5.3.1 and 5.4.1.

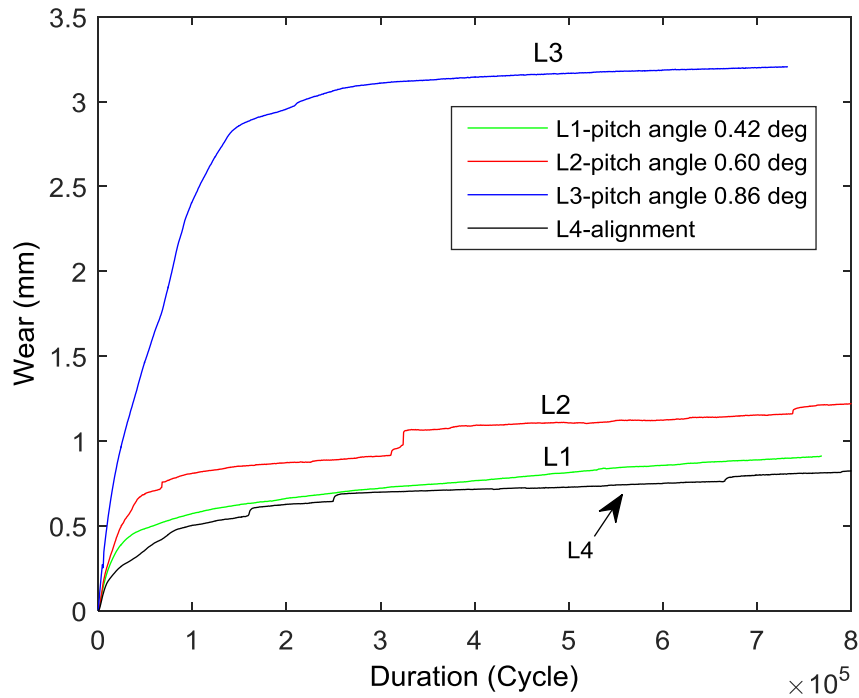


Figure 5.40 Wear versus duration in pitch misalignment tests

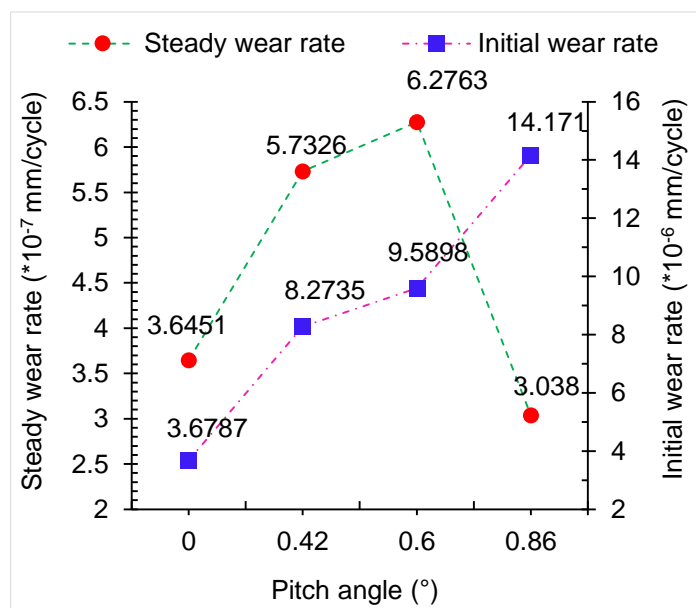


Figure 5.41 Wear rates versus pitch angles

Table 5.3 Variation in actual wear rates due to pitch misalignment

Pitch angle (°)	Initial wear rate	Steady wear rate
0	$1.0^* k_i$	$1.0^* k_s$
0.42	$2.249^* k_i$	$1.573^* k_s$
0.60	$2.607^* k_i$	$1.722^* k_s$
0.86	$3.852^* k_i$	$0.833^* k_s$

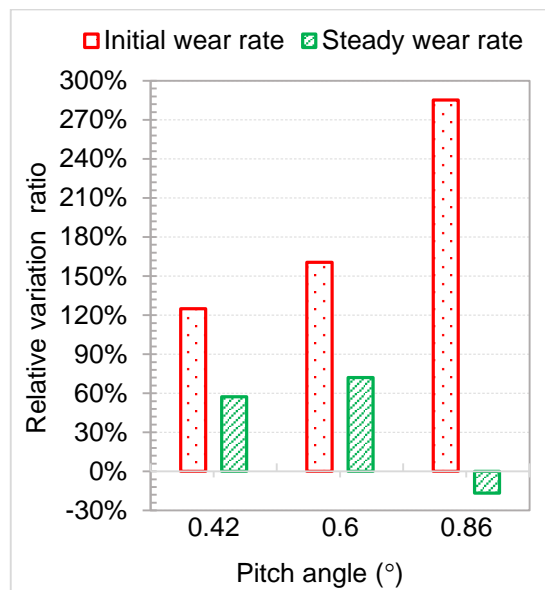


Figure 5.42 Relative variation ratios in actual wear rate versus pitch angles

### 5.5.2 Topography of worn tooth surfaces

- **Superimposed ‘palisade’ wear marks**

Coarse ‘ploughing’ wear patterns can be seen in Figure 5.43, where there is a series of ‘palisade’ wear patterns across the dedendum of the driver and addendum of the driven. A visible difference is that a ‘groove’ forms along the pitch line on the driven tooth and a ‘ridge’ on the driving tooth. Its origin may be linked closely to the tooth contact shape which is a short contact line (narrow area) or even almost a point.

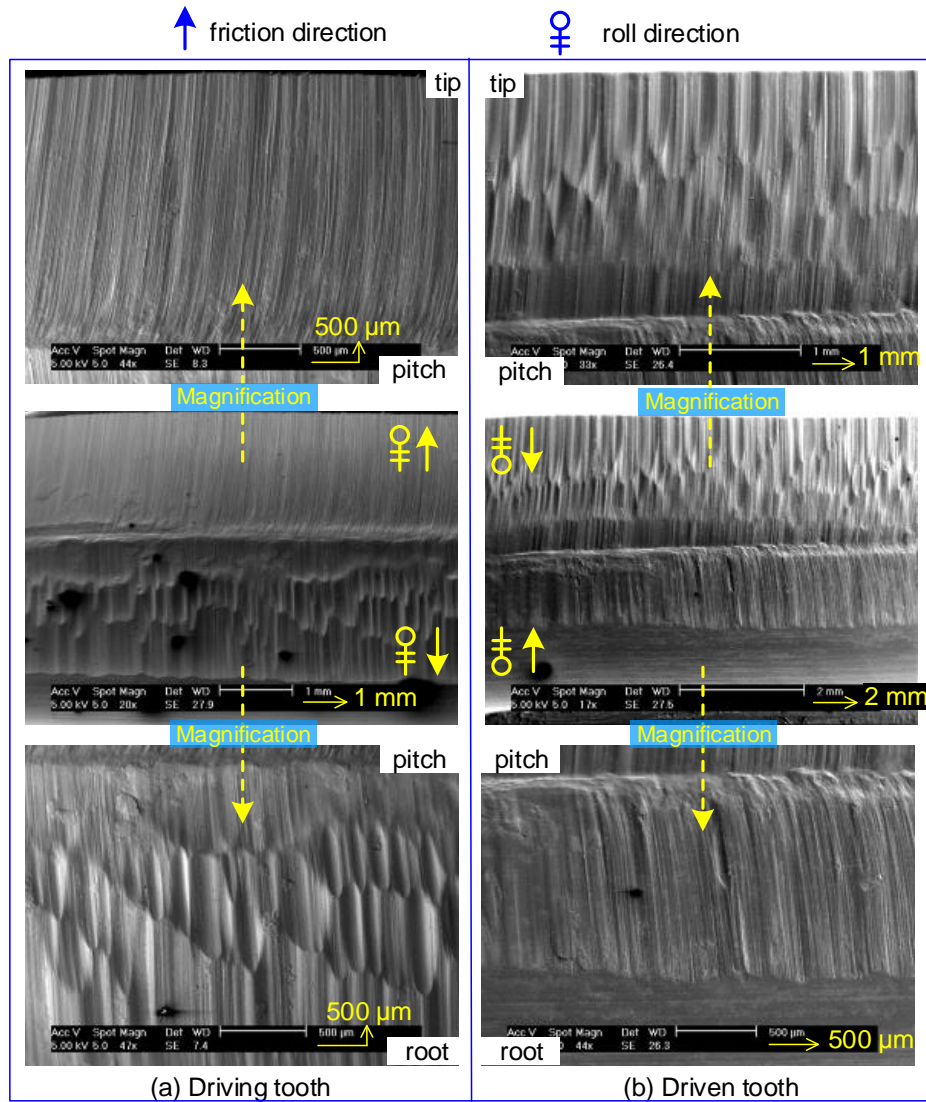


Figure 5.43 SEM micrograph of wear patterns over worn tooth surfaces (pitch angle of  $0.42^\circ$ )

- **‘Pip’ and polishing out**

In addition to pitting, ‘pip’ were observed in the vicinity of the pitch points but on the side of them towards the tip of the driving gears and towards the root of the driven gear as shown in Figure 5.44(a) and Figure 5.45(b) respectively. Both Figure 5.44(b) and Figure 5.45(a) show pits in the ‘superimposed palisade’ wear marks regions, and surfaces that seem to be polished out with some surface material left attached.

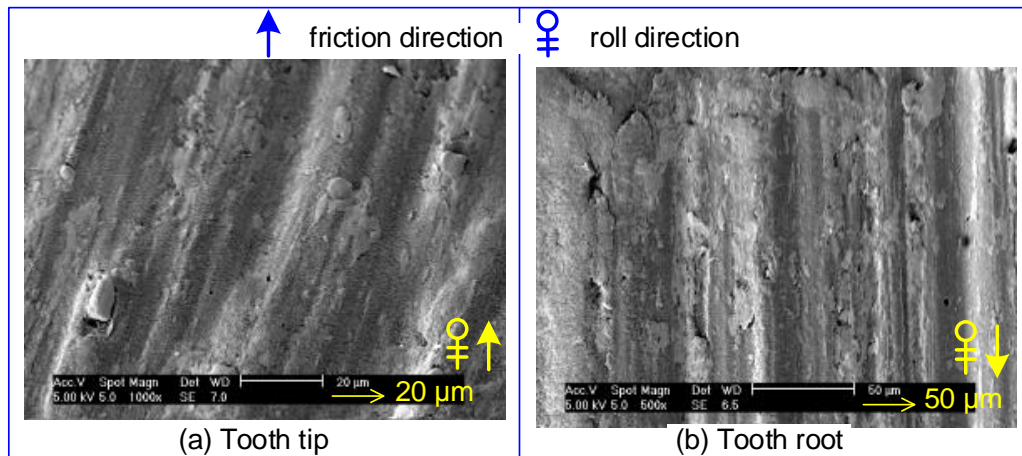


Figure 5.44 SEM micrographs of 'pip' and pitting on a worn driver tooth

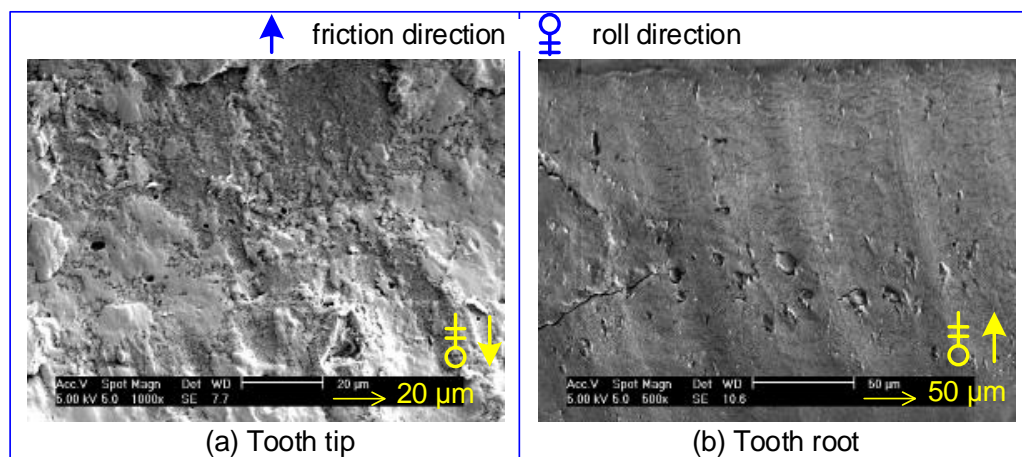


Figure 5.45 SEM micrographs of 'pitting' and 'pip' on a worn driven tooth

- **Micro-cracks near pitch points and roots**

Figure 5.46 exhibits visible micro-cracks near the pitch points of the driver and driven gears. It is interesting to note that there are also micro-cracks near tooth root, close to the bottom land, presented in Figure 5.47. These may result from an increase in bending stress which is induced by pitch misalignment. However a detailed causal mechanism has not yet been determined.

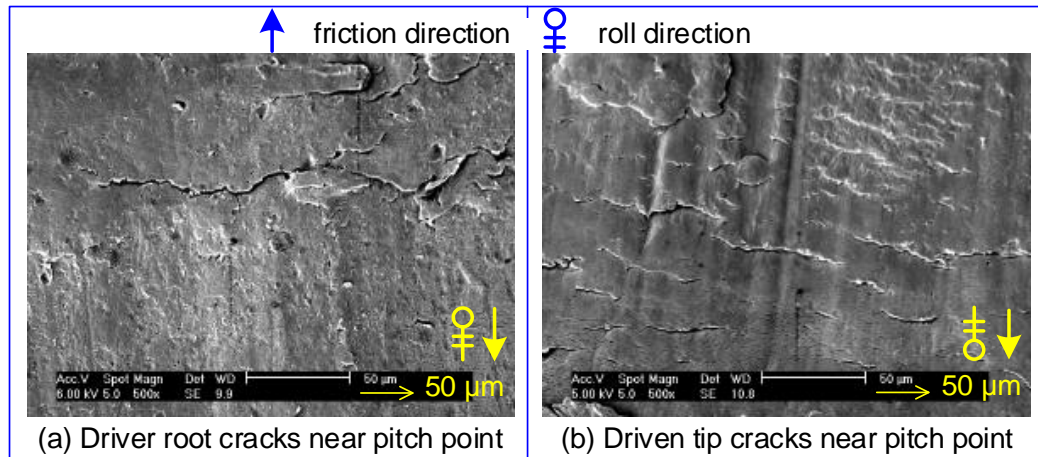


Figure 5.46 SEM micrographs of micro-cracks near pitch points

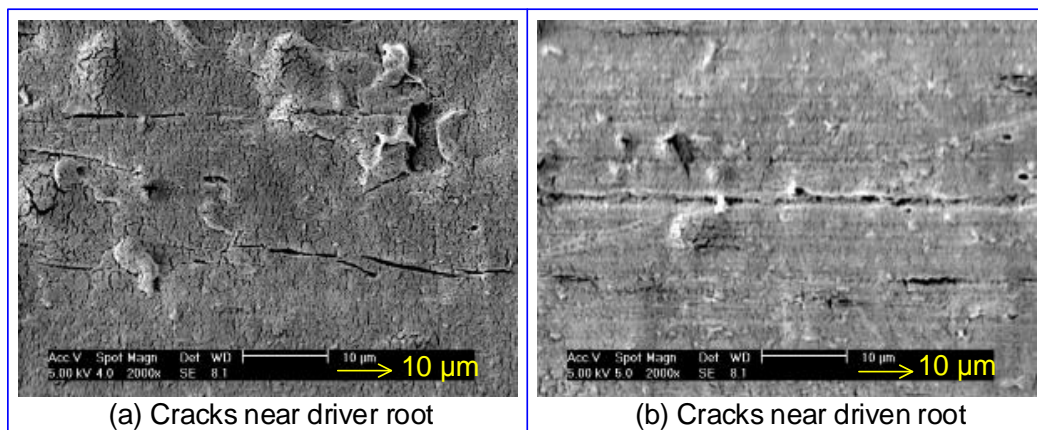


Figure 5.47 SEM micrographs of micro-cracks near tooth roots

### 5.5.3 Regime of wear debris

As in other tests, translucent lamellate wear debris were produced in the initial wear-in phase as shown in Figure 5.48 and Figure 5.49(a). It is speculated that the origin of the translucent lamellate is mainly the surface asperity of new gears shearing off during motion. There may be slight axial deviation induced by pitch misalignment. Therefore it is not surprised that the some wood-shavings-like wear debris as shown in Figure 5.49(b), was present in the  $0.6^\circ$  pitch angle tests, similar to that in the axial misalignment tests, but its size was smaller.



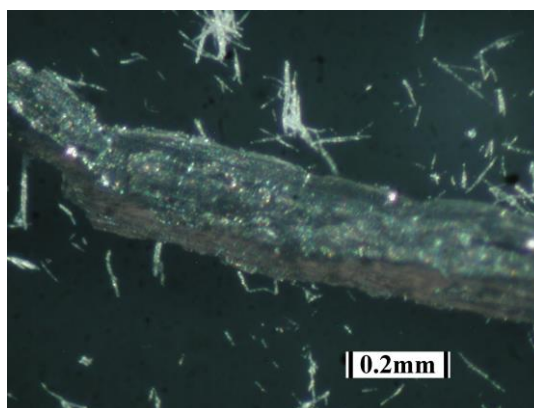
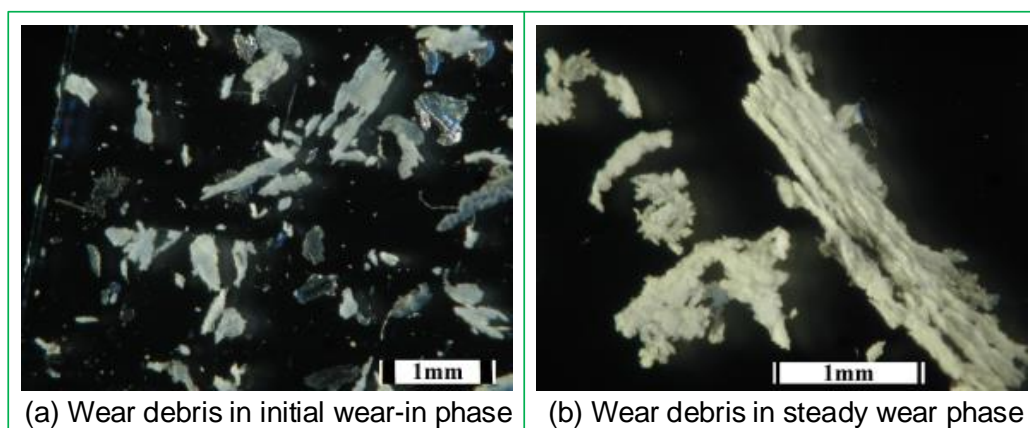


Figure 5.48 OM micrograph of transparent lamellate wear debris (pitch angle of  $0.42^\circ$ )



(a) Wear debris in initial wear-in phase

(b) Wear debris in steady wear phase

Figure 5.49 OM micrographs of wear debris (pitch angle of  $0.60^\circ$ )

However a high volume of cotton-wool-like wear debris as shown in Figure 5.50 and Figure 5.51 was generated prior to the steady wear phase and got reduced during steady wear phase. The size of cotton-wool-like wear debris increased as pitch angle increased. The superimposed layers of 'palisade' wear striations may contribute to the formation of the cotton-wool-like wear debris. First, the powdery debris was trapped in the low-lying of the superimposed layers of 'palisade' wear structures, then it was accumulated and recirculated numerous revolutions, consequently amount of powdery wear debris was compacted into large cotton-wool-like wear debris.

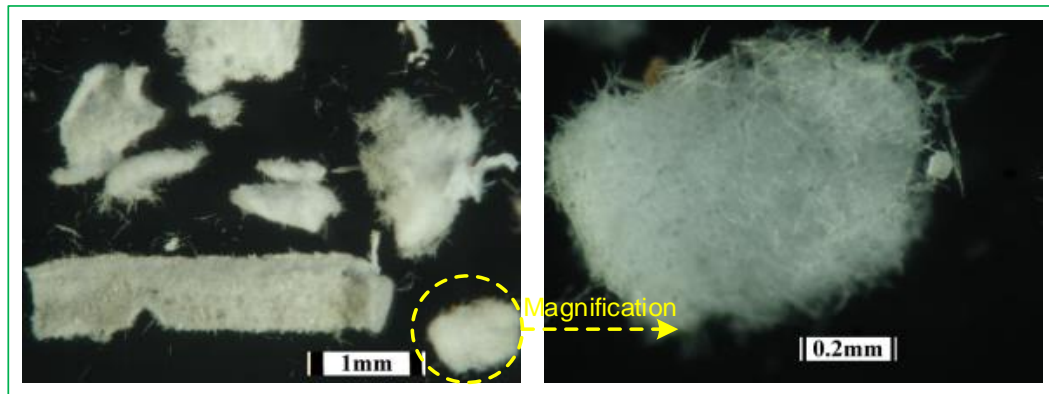


Figure 5.50 OM micrograph of 'cotton-wool-like' wear debris (pitch angle of  $0.42^\circ$ )

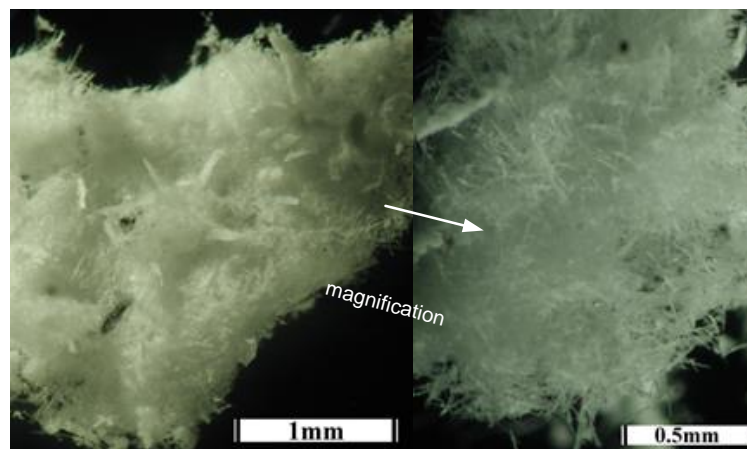


Figure 5.51 OM micrograph of 'cotton-wool-like' wear debris (pitch angle of  $0.86^\circ$ )

#### 5.5.4 Conclusions

Pitch misalignment seems to be detrimental to the wear of polyacetal gears because it results in a considerable increase in wear rate, superimposed layers 'palisade' wear structures over roots of driver gears and tips of driven gears (leading to high roughness of contact surfaces), visible micro-cracks near pitch lines and tooth root and 'pip' (like a ball) on worn tooth surfaces.

Similar to other types of tests there was translucent lamella wear debris in initial fast wear-in phase. However, amount of large cotton-wool-like wear debris, strikingly different from other tests, was present during the



whole wear processes. The presence of cotton-wool-like wear debris may be resulting from the powdery wear debris accumulated in the low-lying of the superimposed layers of 'palisade' wear structure and compacted together after many circulations.

# Chapter 6

## Thermal Tests

### 6.1 Introduction

Since polymers are temperature-sensitive materials, many of their mechanical properties are greatly dependent of temperature, for example, viscosity, modulus of elasticity, bending strength, stiffness and so on [11]. Therefore with polymer gears, it is important to accurately predict operating/contacting temperatures before design and engineering application. However the predictions of contacting temperature or net balance between the thermal generation and thermal dissipation require large amount of thermal experimental data to verify their reliabilities.

Hence this chapter concentrates on the dynamic relation between load, wear/wear rate and airflow and bulk temperatures of polyacetal gears under gears aligned condition. A wide range of temperature measurement tests were carried out. The airflow temperature surrounding testing gears and their surface temperature were measured synchronously under known loads, a speed and environment temperature conditions.

Also an approach of investigating on aerodynamic characteristics encircling operating gears was proposed, which together with airflow temperature measurement contributes towards establishing a preliminary air convective study for thermal dissipation model. The investigation of forced

air convection is of benefit to future studies to predict the bulk temperature of operating gears.

Finally based on numerous test results and intensive observations, prospective heat dissipation methods were proposed in the hope of improving the load capacity or lengthening service life of polyacetal gears.

### **6.2 Airflow temperature measurement**

An airflow temperature here is taken to be the temperature of air surrounding running gears which was within a distance of 4 mm adjacent to the ends of tooth tips. To acquire temperature distribution features around gears, an airflow temperature measurement device was designed which consists of thermocouples, a physical bracket, conditioning electronics plus A/D convertor and data logging software. Detailed design is described in Chapter 3.3.

When running a test in the light load range, firstly airflow temperature increases quickly as the test initiates; in fact it is directly in response to the initial fast wear-in phase of wear. Then the rate of increase in airflow temperature slows down progressively, which corresponds with the transitional wear phase. Finally the gears' operating conditions reach equilibrium where the airflow temperature remains level. This exactly matches the steady wear phase, implying that the operating gears have reached thermal dynamic equilibrium between the thermal generation and dissipation (transfer). An example of airflow temperature measurement at a

load of 6 N·m and a speed of 1000 rpm is shown in Figure 6.1, where ‘TC’ denotes thermocouple and the number shows its position surrounding the gears. The distribution of potential measuring points (thermocouples) is sketched in Figure 6.2.

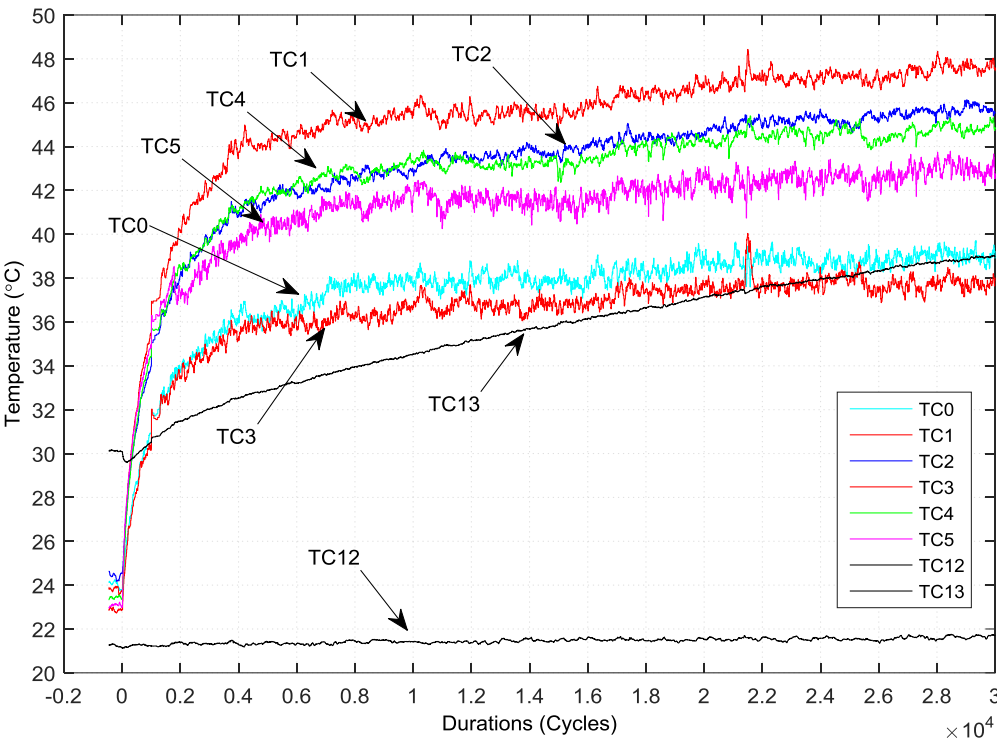


Figure 6.1 Plots of airflow temperature surrounding gears at a load of 6 N·m

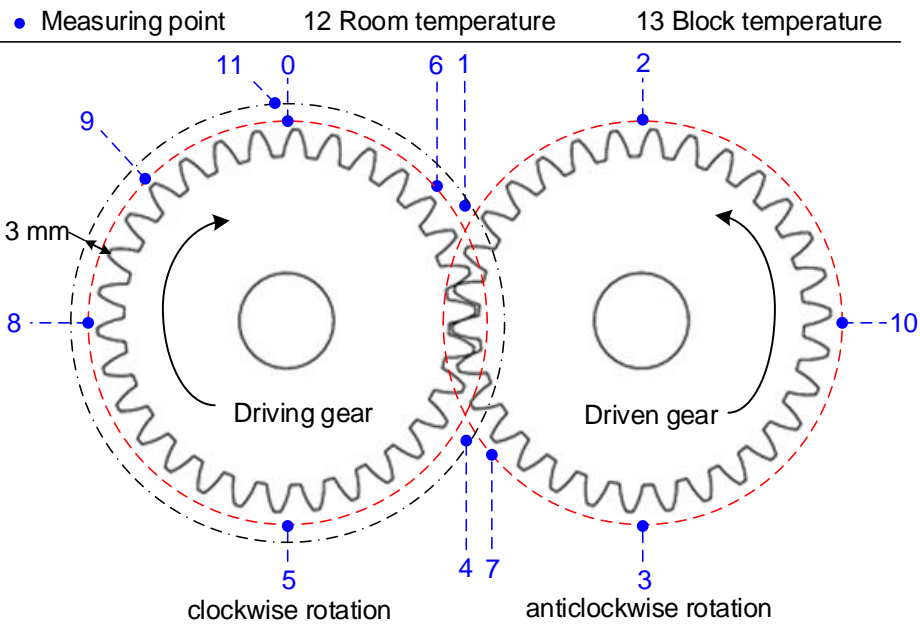


Figure 6.2 Measuring points' distribution of airflow temperature

The thermocouples sited at the locations of 0, 2, 3, 5, 6, 7, 8, 9 and 10 are to measure the airflow temperature encompassing a rotating gear pair. The points 0 and 11 are used to quantify any temperature difference in a vortex envelope (a layer of steady air turbulence surrounding running gears) which is bordered from the tooth tip, in a distance range of 0 mm to 3 mm, as shown in Figure 6.2. Measuring points 1 and 4 are to measure the temperature gain of hot air ejected by the entering mesh process of the gears and by the vortex resulting from hot air carried in gear pockets and cold air entrained by the exiting mesh process of the gears. These values are prospectively valuable to explore the forced air convection and develop aerodynamic models of flow encircling gears, which are clarified in Chapter 6.5. The room temperature (12) was measured approximately 0.70 m away from testing gears, while the block temperature (13) was measured to roughly estimate the role of thermal conduction from gears.

The airflow temperature patterns at moderate load conditions were similar except that there was an occurrence of temperature rise following the steady state, which related to fast wear phase. With respect to the cases at high loads, the temperature trend lines were similar to their wear curves, increasing quickly until the moment gears failed or the tests stopped.

More than thirty sets of experimental data were collected and their patterns are similar within a given load range apart from expected local fluctuations of data values. Therefore, one or two representative sets of test results in each load range are discussed in this chapter. Step-load test results are listed in table in Section 6.4.4.

### 6.3 Bulk temperature measurement

The most important surface temperature effects of gears are the flash temperature, body temperature and ambient temperature [7, 49]. Blok [69] explains the concept of flash temperature as being generated in a very thin surface layer during the meshing of gear teeth. Substantial temperatures grow instantaneously at the sliding contact as the contact spot moves along the tooth flank. This friction-generated heat penetrates into the solid body immediately below the contact surfaces. The body (bulk) temperature is the material temperature underlying the contacting surfaces. The ambient temperature was the environment temperature. However the airflow temperature enveloping operating gears is also important, which acts as an agent sustaining the equilibrium between environment temperature and running gear body temperature.

Temperatures of the gears were measured by an infrared video camera (FLIR SC660). Due to the arrangement of the test rig and rotating direction of gears, the temperature measurement positions are restricted by the need for clear lines of sight. The prospective measurement locations are sketched in Figure 6.3. Images of surface temperature measurement during running at loads of 7 N·m and 12.1 N·m respectively are shown in Figure 6.4, which is a good example to explain why the positions shown in Figure 6.3 are selected for measuring surface temperature. Clearly, the temperature shown in gear regions with white colour are the highest and closest to the contact temperature of running gears.

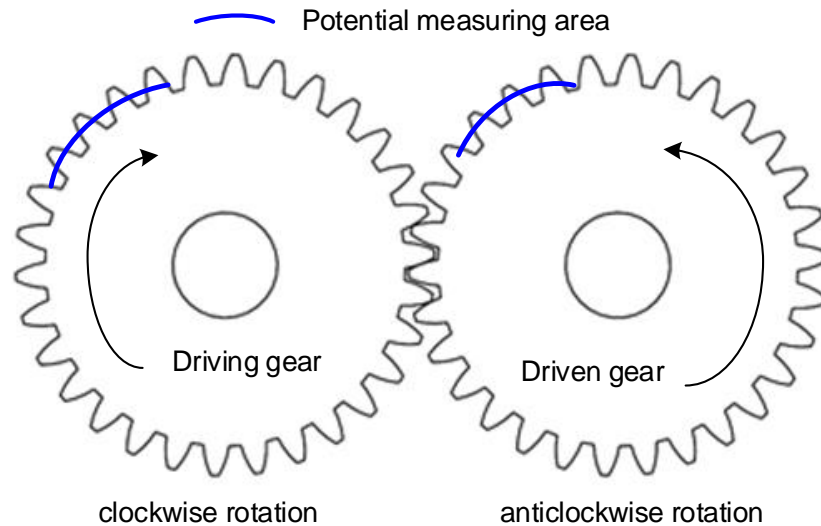


Figure 6.3 Measuring locations of bulk temperature on a gear pair

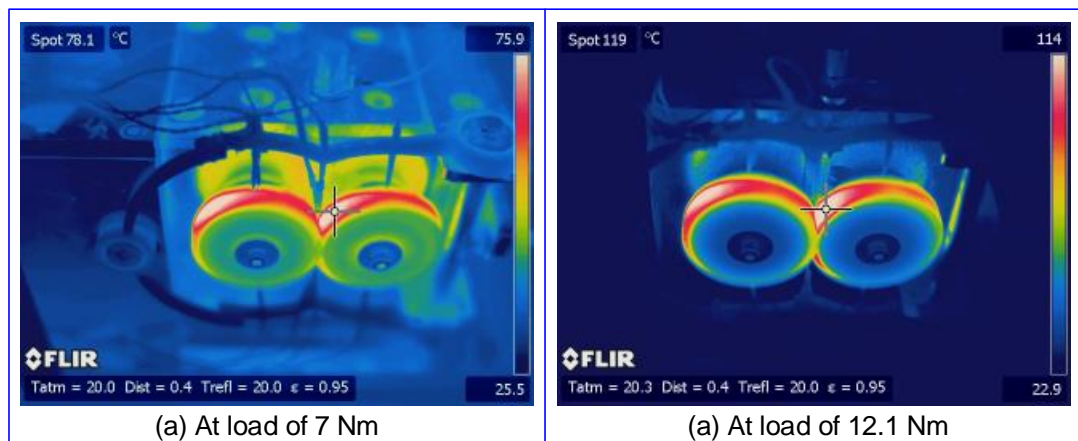


Figure 6.4 Infrared images of operating gears at speed of 1000 rpm

On account of the flash temperature degenerating almost immediately when gears come out of mesh, the surface temperature measured during running here is close to gear tooth body temperature (in particular when gears are running in a steady state).

The mean bulk temperature measurement results are presented in Section 6.4, but temperature images at a load of 14.1 N·m shown in Figure 6.5(a-b) were taken after the test stopped. From it the deformed tooth shapes (see the photograph of this deformed gear pair in Section 4.3.10) and the highest temperature region over tooth flanks can be noted. Infrared

images at loads of 8.0 and 9.0 N·m are added for comparison. The tooth shapes shown in Figure 6.5(c-d) were only slightly deformed. Note that the centre of the tooth flanks (white colour) were hotter than other areas.

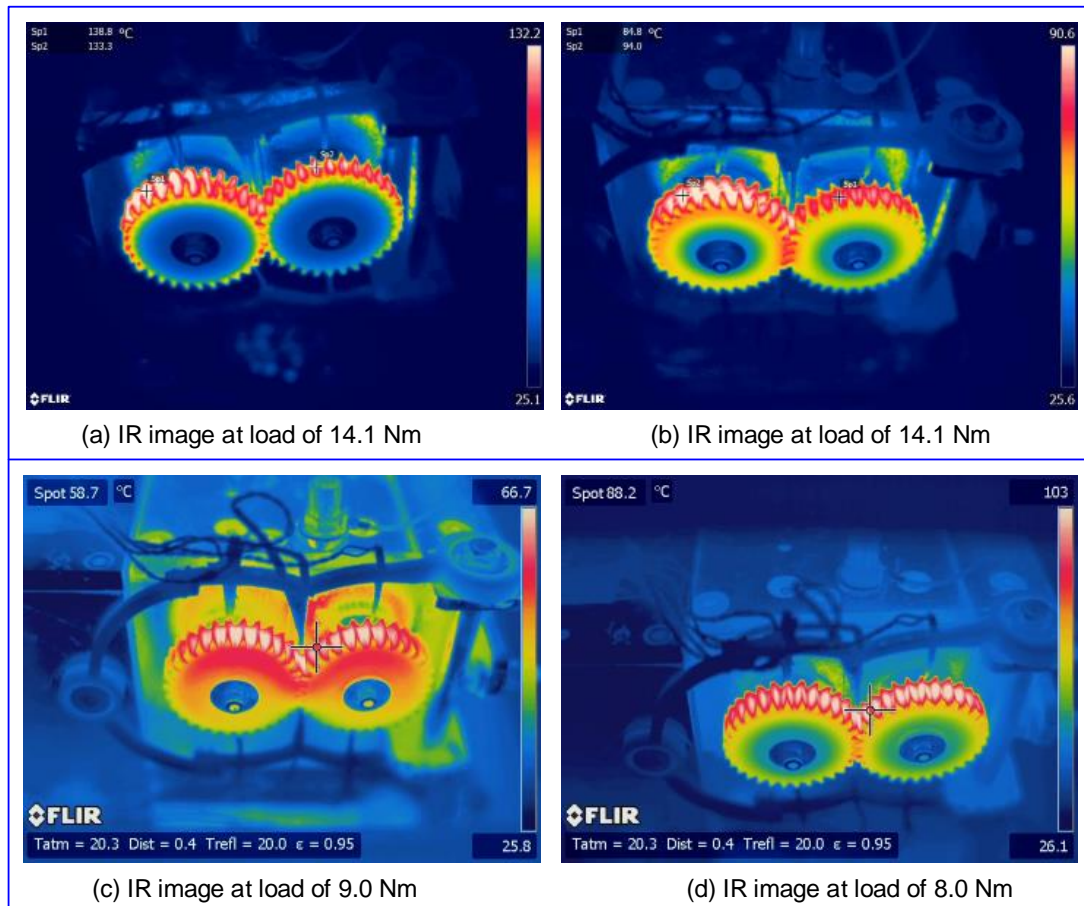


Figure 6.5 Infrared images taken after stop running gears (1000 rpm)

## 6.4 Thermal test results and discussions

The test results in which wear, bulk temperature and airflow temperature were measured simultaneously are given in detail in terms of load range in the following sections. Typical plots of wear and temperature instances are presented below, while numerical data for step-load tests are given in Section 6.4.4.



### 6.4.1 Typical test results at low loads

Test results at loads of 4.9 N·m and 7.0 N·m are presented and analysed in this section. There may exist a certain temperature span between which the wear rate holds stable. The varying temperature during periods when wear debris was ejected indicates for this that wear debris on contact tooth surfaces may affect the wear of polymer gears

Figure 6.6 shows the wear, bulk and airflow temperatures at load of 7 N·m. All the labels of the airflow temperature measurement results in Chapter 6, such as the labels in Figure 6.6(c), refer to the positions of thermocouples encircling the testing gear pair, as defined in Figure 6.2.

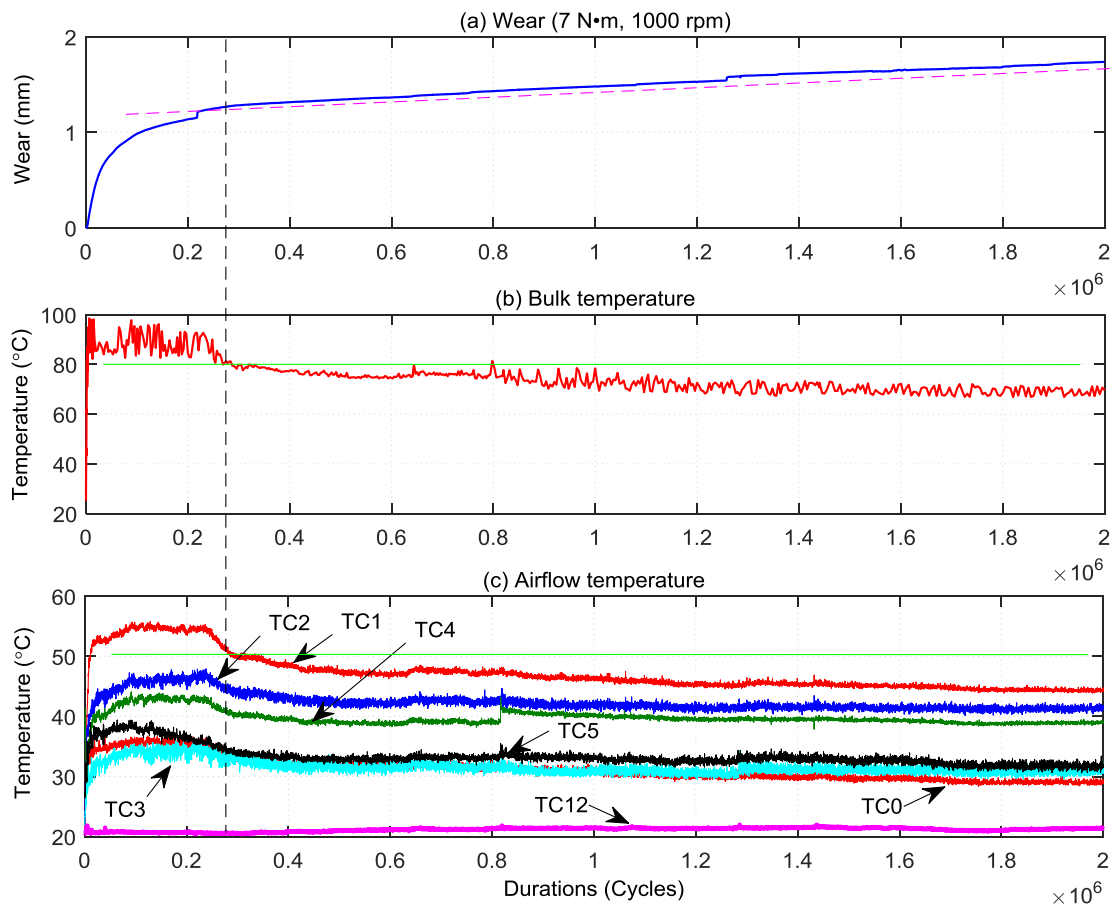


Figure 6.6 Test results of wear, bulk and airflow temperature (7 N·m, 1000 rpm)

Figure 6.6 illustrates that the air and bulk temperatures in the initial fast wear-in phase are significantly higher (20°C more for bulk temperature and 6°C more for air temperature) than those in the steady wear phase. Note that temperature in the steady wear phase decreases progressively as the number of operating revolution increases, which agrees well with the trends of wear rate such as in Figure 4.41. The airflow temperature around the top half of the gears is always slightly higher than that around the bottom half of the gears (mainly due to the forced air convection that the hot air is ejected when gears come into mesh). The temperature of the air expelled (TC2) (as gears enter into mesh) is highest while the air near the region where gears are exiting mesh (T4) is as low as the ones near the bottom half.

Since the mechanical properties of polymer depends greatly on temperature, it is essential to relate wear behaviour of polymer gears at a given load with corresponding operating temperatures in the steady wear phase. However, the real operating/contacting temperature is hard to determine through tests because flash temperature, one of its major components fades in an extremely short period. Its measurement is also restricted by many factors, such as the arrangement of the test rig and the plausible positions for measurement devices. As mentioned previously, the bulk temperature will get close to the surface temperature if operating gear system approaches thermodynamic equilibrium. Therefore it is reasonable to exploit bulk temperature as an alternative measure because it is available throughout the experimental measurement.

Figure 6.7 demonstrates the dynamic relations of the wear, wear rate

and bulk temperature in the steady wear phase. The wear rate spikes occur owing to jumps in the positions of the continuous wear sensing probe which are mainly caused by a large quantity of wear debris coming off contact tooth surfaces. It is interesting to note that the bulk temperature tends to decrease slightly when wear debris sprinkles away from the gears and it is more evident when larger wear jumps take place. This phenomenon may be explained by wear debris affecting (bringing away slight heat or marginally accelerating the wear) the wear behaviour of polymer gears which is in a good agreement with the relationship of topography of worn tooth surfaces and wear debris proposed in Chapter 4.

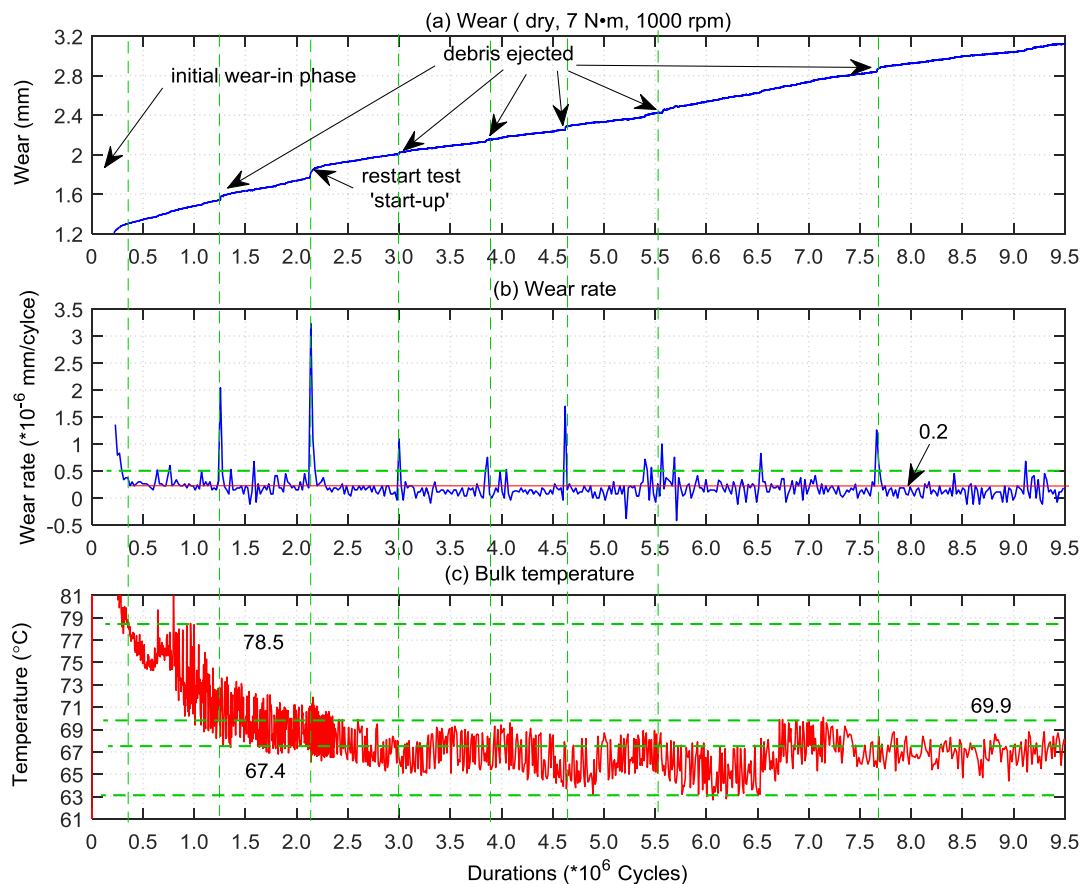


Figure 6.7 Wear, wear rate and bulk temperature in steady state (7 N·m, 1000 rpm)

The bulk temperature shown in Figure 6.7(c) fluctuates widely, where

the peak is closer to the bulk temperature of contact tooth surfaces ( $67.4^{\circ}\text{C}$  to  $78.5^{\circ}\text{C}$ ) while the low value is the temperature of non-contact tooth surfaces. The average wear rate is approximately  $0.2 \times 10^{-6}$  mm/cycle in steady wear state and the relating bulk temperature lies between  $67.4^{\circ}\text{C}$  and  $78.5^{\circ}\text{C}$ . The mean bulk temperature is approximately  $69.9^{\circ}\text{C}$ .

Figure 6.8 shows the test results at a load of 4.9 N·m and speed of 1000 rpm which was conducted with a test rig window being shielded near the driving gear side so that reduced room air came in from that side as shown in Figure 6.9. In such condition, the convective environmental air mainly comes through the existing open window in front and top of the gears.

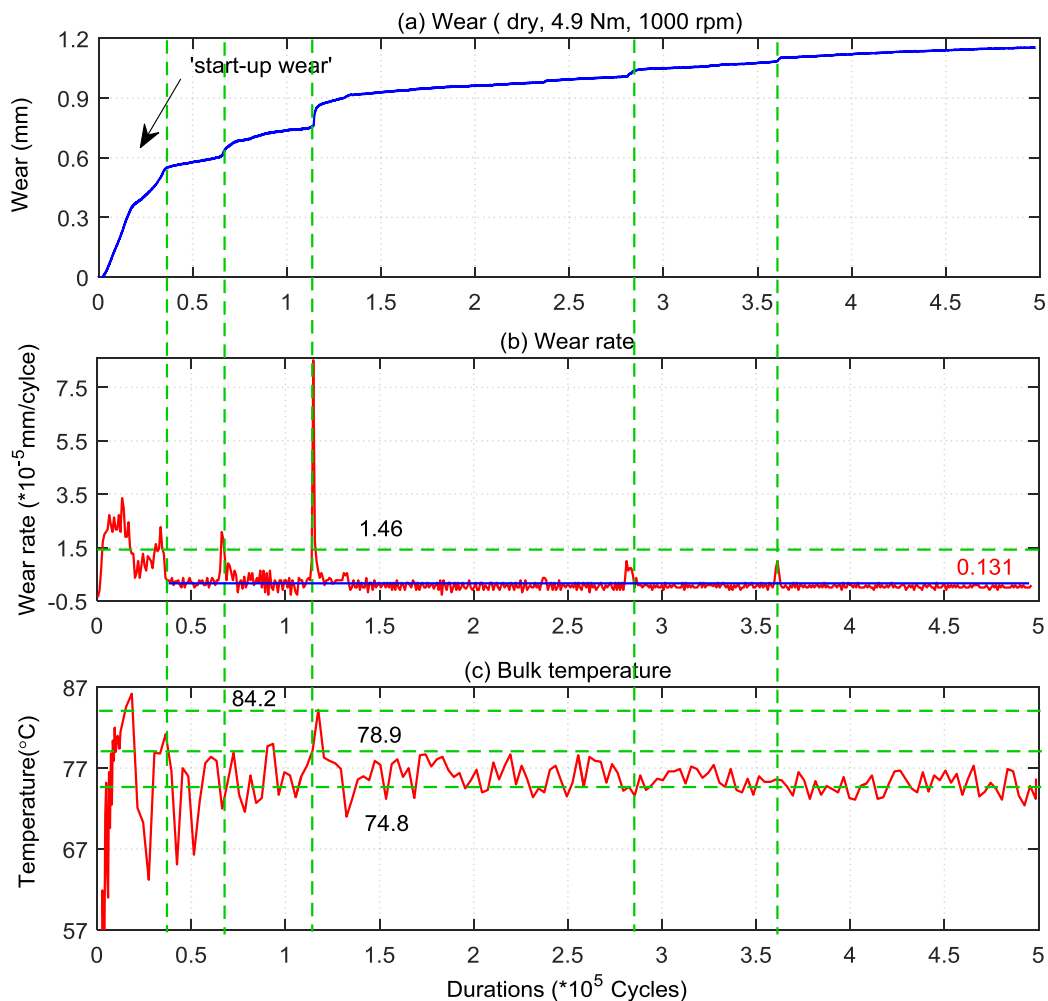


Figure 6.8 Wear, wear rate and bulk temperature versus duration (4.9 N·m, 1000 rpm)

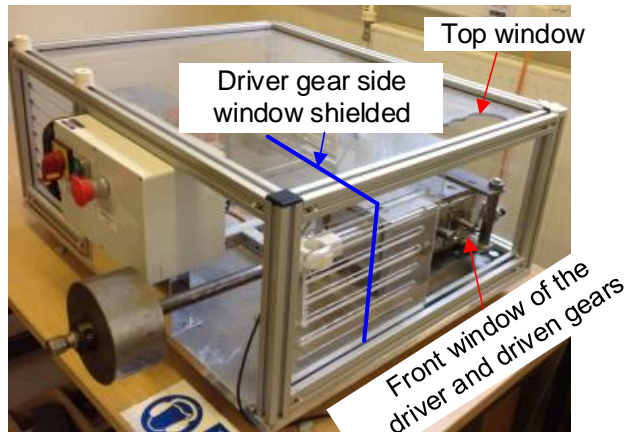


Figure 6.9 Three open windows around test gears

The average wear rate and bulk temperature at a load of 4.9 N·m are expected to be no greater than those at 7 N·m. However visible discrepancy exists between the test results at a load of 4.9 N·m and at a load of 7 N·m. The average wear rate of the former,  $1.31 \times 10^{-6}$  mm/cycle for all the steady state region, is effectively  $\sim 6.5$  times the latter ( $0.2 \times 10^{-6}$  mm/cycle). The temperature fluctuation span gets narrower but is approximately  $7^\circ\text{C}$  higher than that at a load of 7 N·m. The elevated wear rate and bulk temperature may be the consequence of the reduced air convection. Overall with the exception of just a few very local peaks (jumps), the wear rate remains less than  $1.46 \times 10^{-5}$  mm/cycle and the bulk temperature is between  $74.8^\circ\text{C}$  and  $84.2^\circ\text{C}$  and only rarely does it exceed  $78.9^\circ\text{C}$ .

#### 6.4.2 Typical test results at moderate loads

Figure 6.10 exhibits test results at a load of 8 N·m and there is a transition point (onset of a final fast wear phase) where wear and temperature increases substantially (by  $15^\circ\text{C}$  in short period. From the onset of the stable wear period, the bulk temperature rise steadily but slowly to the

transition point where it jumps  $13^{\circ}\text{C}$  (from  $110^{\circ}\text{C}$  to  $123^{\circ}\text{C}$ ) and then holds almost constant. In contrast, most of the sensors in the airflow circulating the gears show almost constant temperature throughout the steady wear period and only a small increase at the transition, although some of the airflow temperature show a slow rise followed by a distinct fairly rapid transition to a steady value of no more than  $76^{\circ}\text{C}$ . This process indicates that the bulk temperature particularly governs the wear performance of polyacetal gears. The turbulence in the aerodynamic envelop around operating gears also plays an important role in sustaining the thermodynamic balance between environment air and gears. It will be here called the 'air convection agent'.

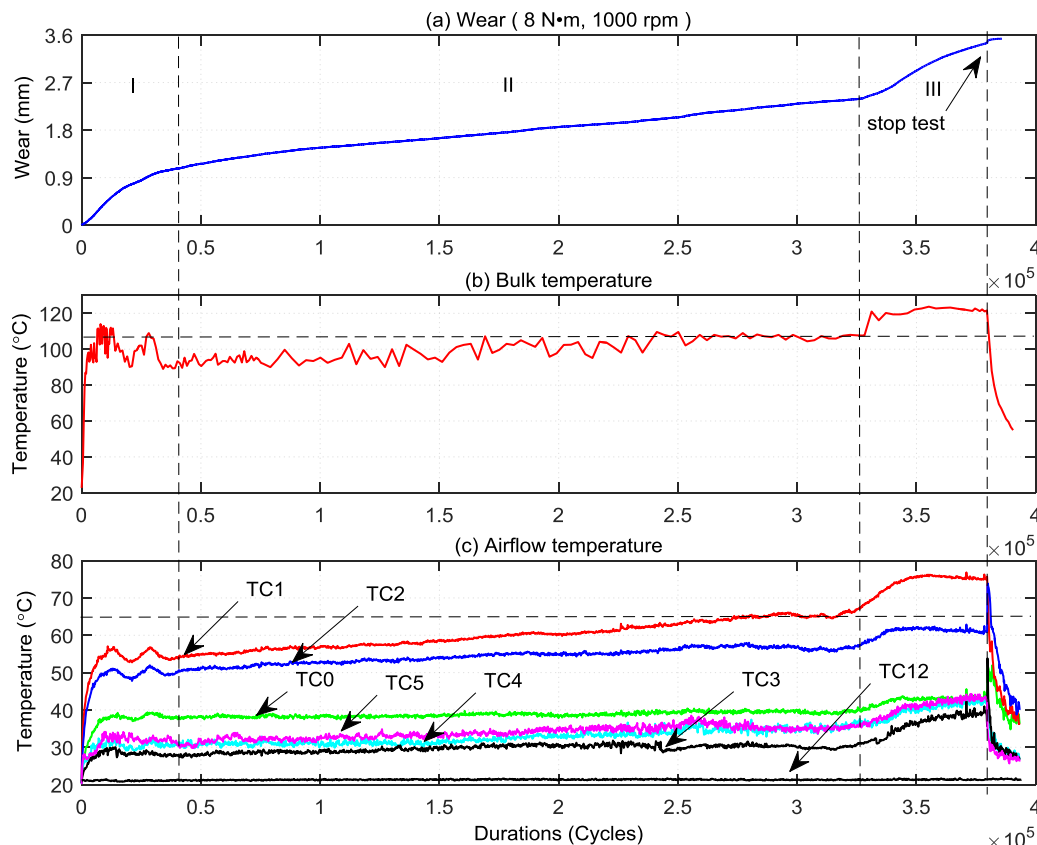


Figure 6.10 Test results of wear, bulk and airflow temperature versus duration (8 N·m)

The (average) wear rate and bulk temperature in II (stable wear) and III region (final fast wear) shown in Figure 6.10(a) are taken as key indicative

parameters and presented in in Figure 6.11. There is a critical temperature boundary at 110°C (CTB) where a striking wear rate transition occurs. If temperature is lower than CTB, the wear rate is no greater than  $1.0 \times 10^{-5}$  mm/cycle with an average value  $4.8 \times 10^{-6}$  mm/cycle in the whole of region II. When the bulk temperature is greater than CTB, the wear rate is up to  $3.74 \times 10^{-5}$  mm/cycle with an average value  $1.61 \times 10^{-5}$  mm/cycle. The average wear rate in region III is over three times that in II. It is interesting to note that a sudden increase in wear rate is almost always accompanied by an elevated bulk temperature (virtually the surface temperature).

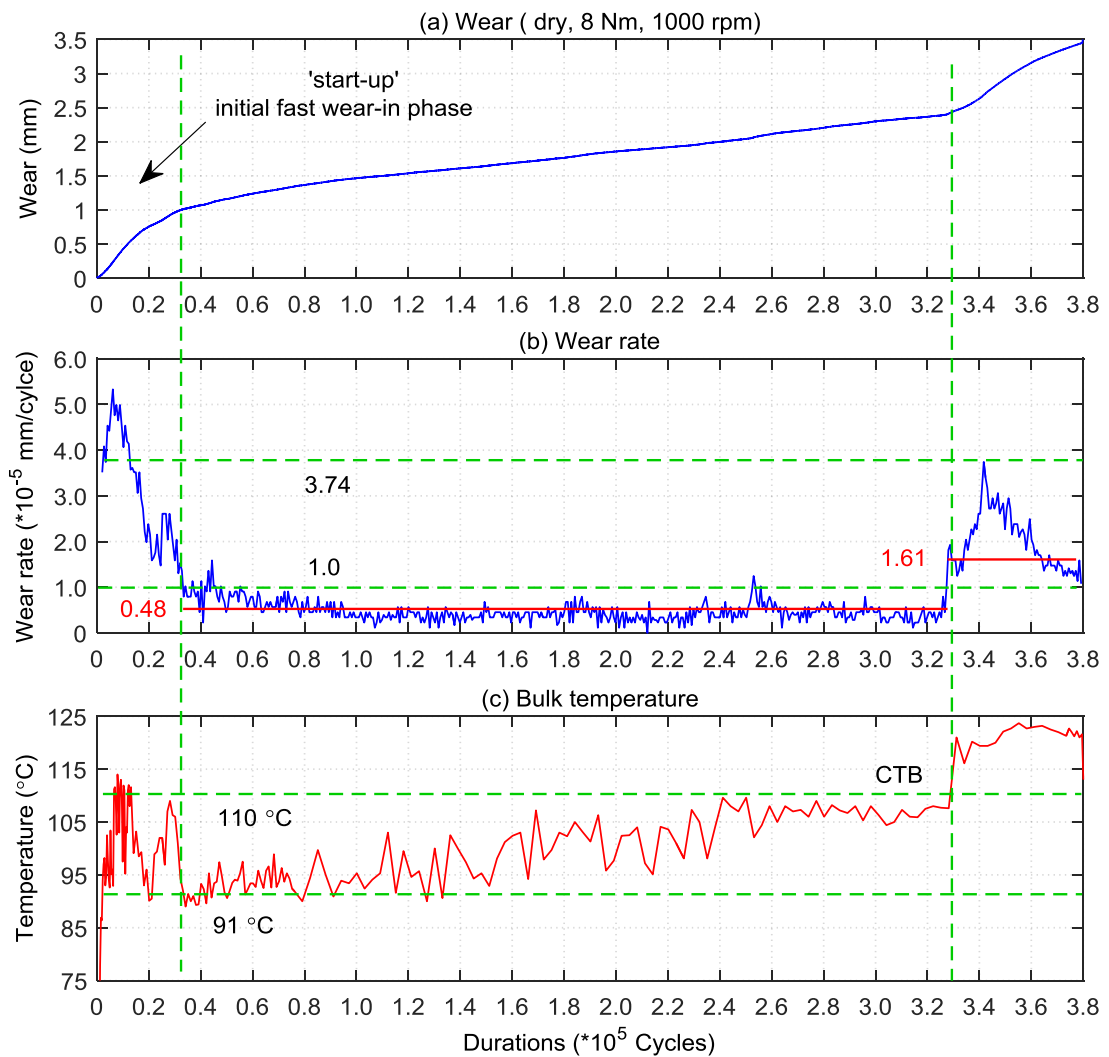


Figure 6.11 Wear, wear rate and bulk temperature versus duration (8.0 N-m, 1000 rpm)

The test result at a load of 8.5 N·m shown in Figure 6.12, exhibits similar variations in wear and temperature as those at a load of 8 N·m. Again the airflow around gears closely follows the varying bulk temperature. In the last stage where wear has exceeded 4 mm, teeth have been bent and subsequently the temperatures of the teeth and airflow get reduced.

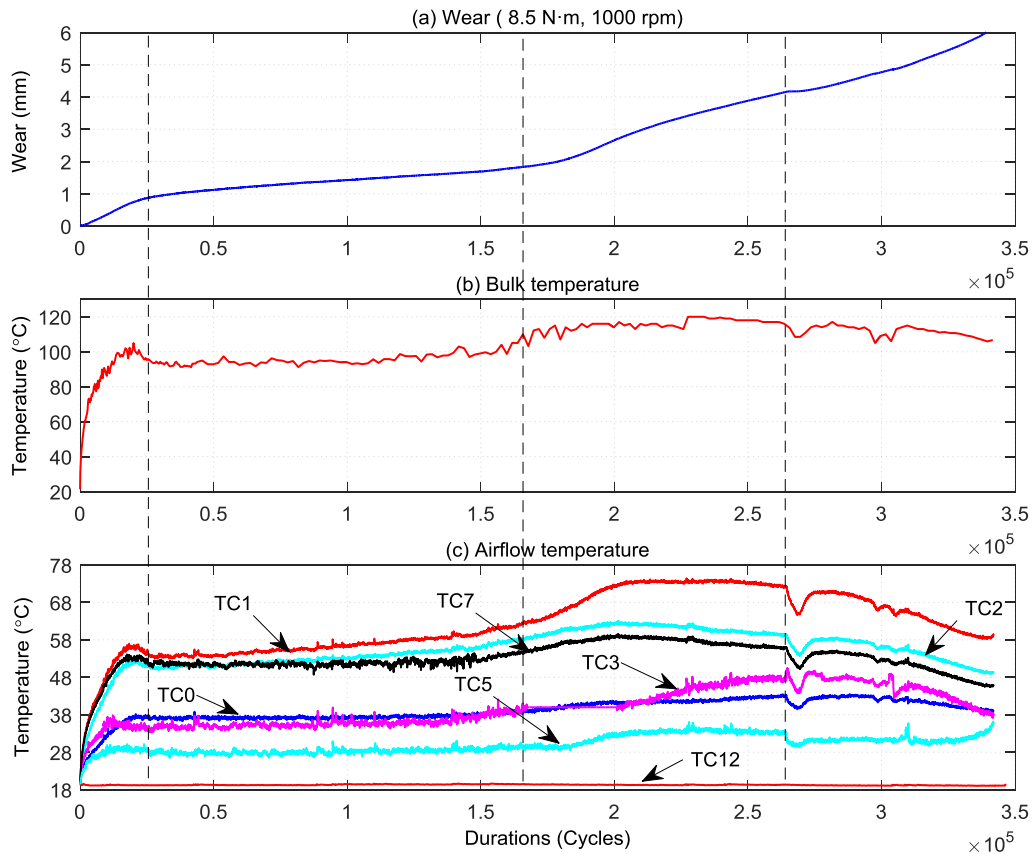


Figure 6.12 Test results of wear, bulk and airflow temperature versus duration (8.5 N·m)

Figure 6.13 shows the relationship of wear rate and bulk temperature (as proxy for surface temperature) of the operating gears at a load of 8.5 N·m. The same as at a load of 8.0 N·m, there is a critical bulk temperature (approximately 110 °C) where the wear rate increases greatly, from no higher than  $1.0 \times 10^{-5}$  mm/cycle to around  $4.0 \times 10^{-5}$  mm/cycle. A bulk temperature rises from 94 °C to 110 °C, the wear rate is almost never greater than  $1.0 \times 10^{-5}$  mm/cycle with a mean value  $0.635 \times 10^{-5}$  mm/cycle. At



temperatures between 110 °C to 120 °C, the wear rate is between  $1.0 \times 10^{-5}$  mm/cycle and  $4.0 \times 10^{-5}$  mm/cycle and the mean value is about  $2.4 \times 10^{-5}$  mm/cycle.

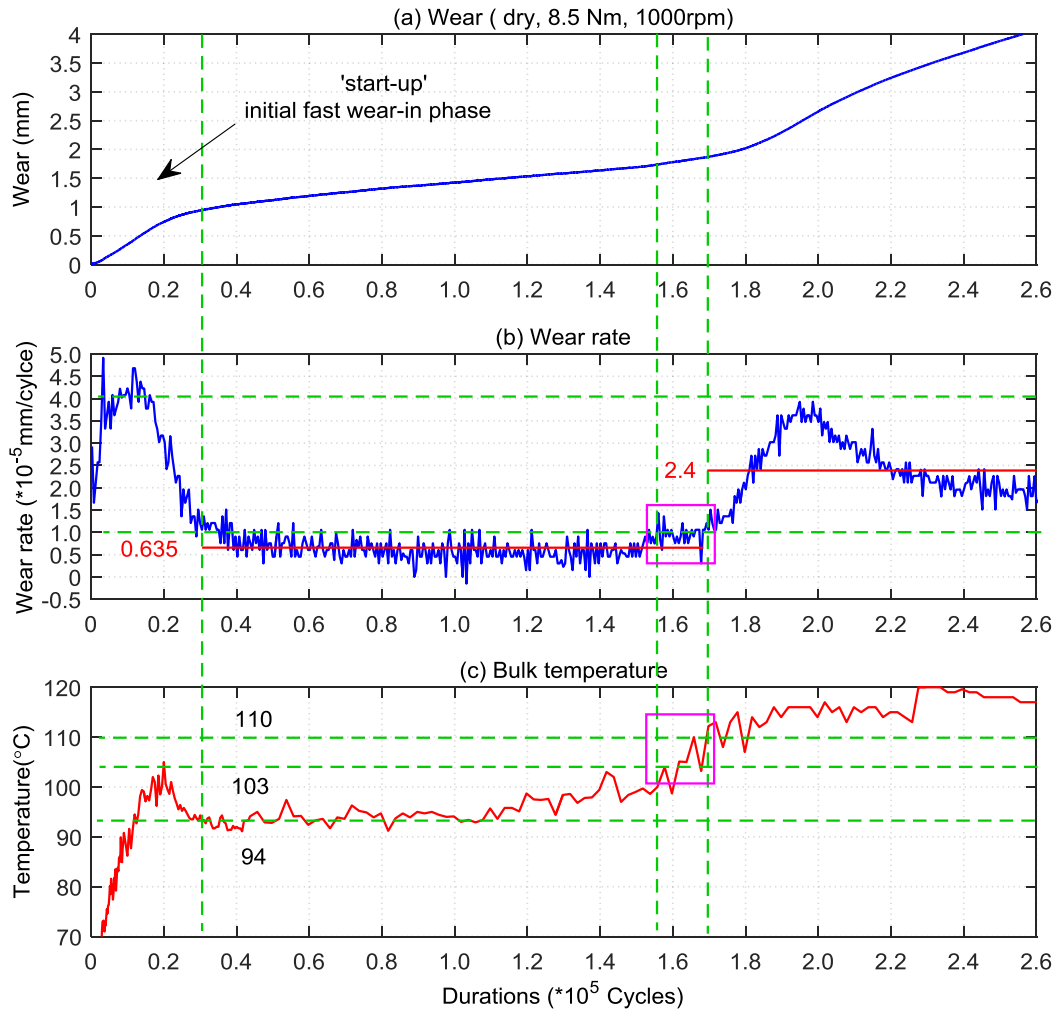


Figure 6.13 Wear, wear rate and bulk temperature versus duration (8.5 N-m, 1000 rpm)

The wear rate in the steady stage remains almost level. However, the bulk temperature increases progressively as the number of cycles increases until it reaches a transition temperature, where the wear rate suddenly accelerates. This phenomenon reveals that the wear of polyacetal gears may sustain uniform wear over a certain temperature span rather than wear rate increasing steadily as temperature rises.

Test results at a load of 9 N·m are shown in Figure 6.14, which reveals a similar wear curve to that at 8.5 N·m load, but a significantly different pattern for the bulk temperature (which can be roughly divided into three stages). The bulk and airflow temperature plots present quite similar patterns of variation. The bulk temperature increases rapidly to 100°C in short period from the start of the test (within  $2 \times 10^4$  revolutions), then continues rise gently to roughly 117°C and subsequently holds nearly constant for around  $4.6 \times 10^4$  revolutions. Finally the temperature reduces slightly.

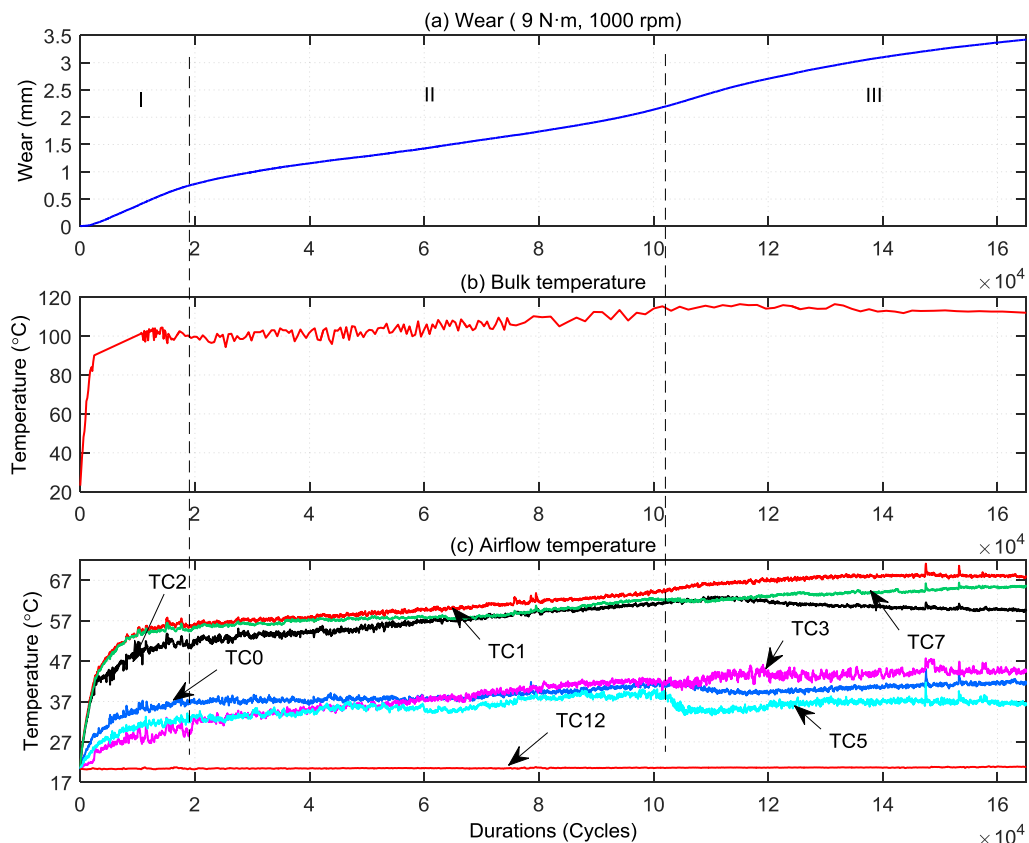


Figure 6.14 Test results of wear, bulk and airflow temperature versus duration (9 N·m)

The wear rate and bulk temperature are shown together in Figure 6.15. It reveals that the wear rate is primarily between  $1.0$  and  $2.0 \times 10^{-5}$  mm/cycle while the bulk temperature increases from 102°C to

110°C. In the subsequent  $4.6 \times 10^4$  revolutions the wear rate exhibits a parabola-like trend that first goes up to a peak of roughly  $3.54 \times 10^{-5}$  mm/cycle and then goes down to  $2 \times 10^{-5}$  mm/cycle. However, the bulk temperature almost remains level (117°C) during this period. In the last stage, the bulk temperature reduces slightly to 113.8°C and then keeps stable, while the corresponding wear rate continues to decline. The teeth may have been bent slightly in this stage which could reduce wear rate. The peak recorded temperature is around 117°C, but the worn tooth surfaces described in Chapter 4.3.6 show slight local melt or softening wear marks. Hence, the surface temperature in contact is likely to be higher than 117°C.

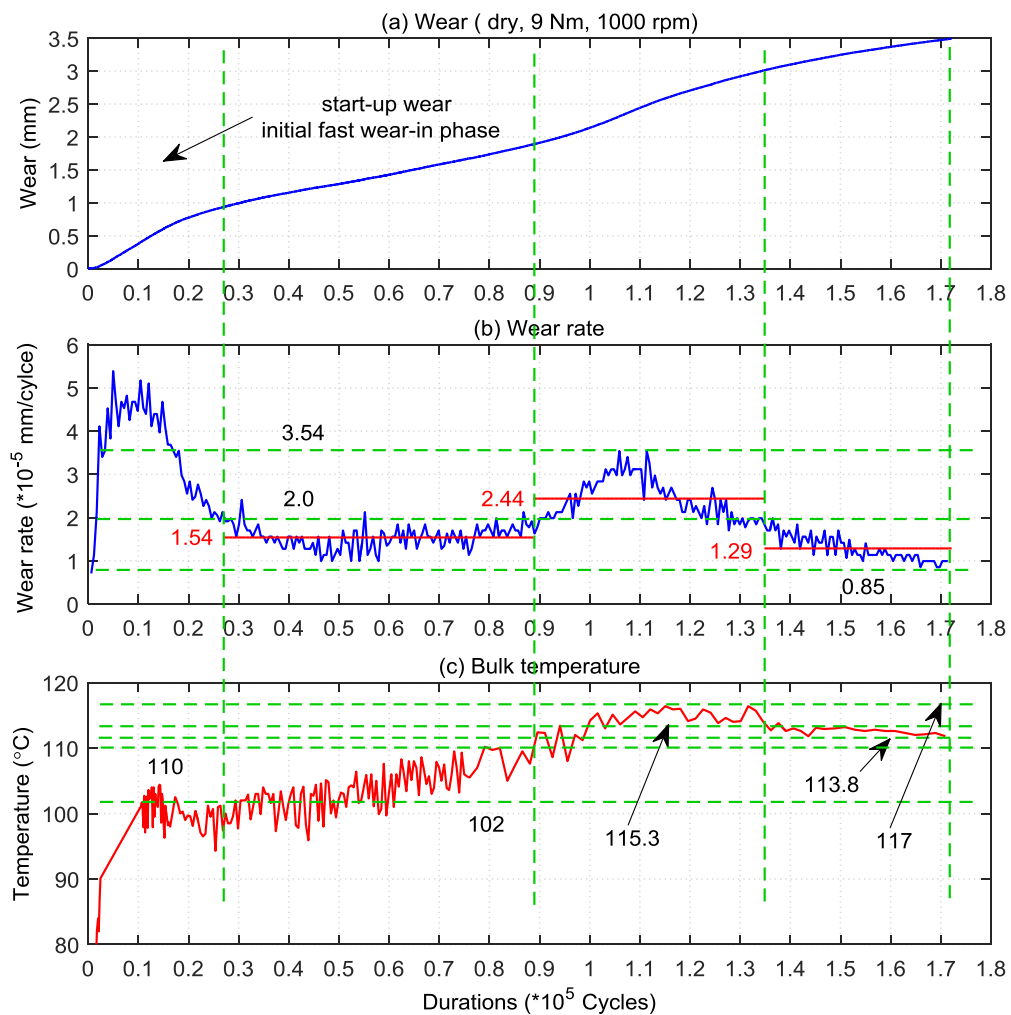


Figure 6.15 Wear, wear rate and bulk temperature versus duration (9.0 N-m, 1000 rpm)

By contrast with dry wear, the gears lubricated by graphite paste present notably different wear and temperature profiles as shown in Figure 6.16, which are significantly lower than those under dry running conditions. As wear proceeded, the operating gears became starved of lubricant and then the bulk temperature rose quite rapidly from roughly 80°C to over 110°C. The corresponding wear rate and bulk temperature are plotted in Figure 6.17. There is a uniform wear rate stage ( $<1.0 \times 10^{-5}$  mm/cycle and mean value  $2.79 \times 10^{-6}$  mm/cycle) where the bulk temperature is generally below 70°C and no greater than 79°C. The wear rate varies greatly in the unsteady wear phase.

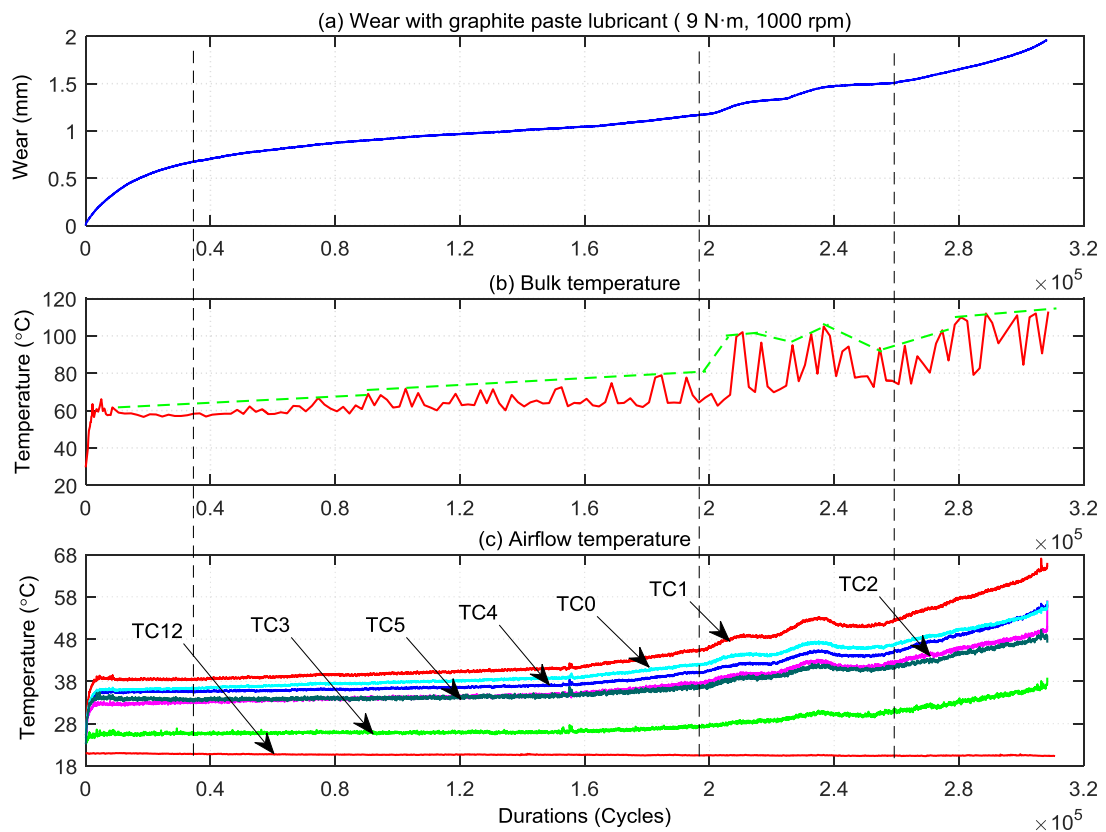


Figure 6.16 Test results of wear, bulk and airflow temperature (9 N·m, lubricated)

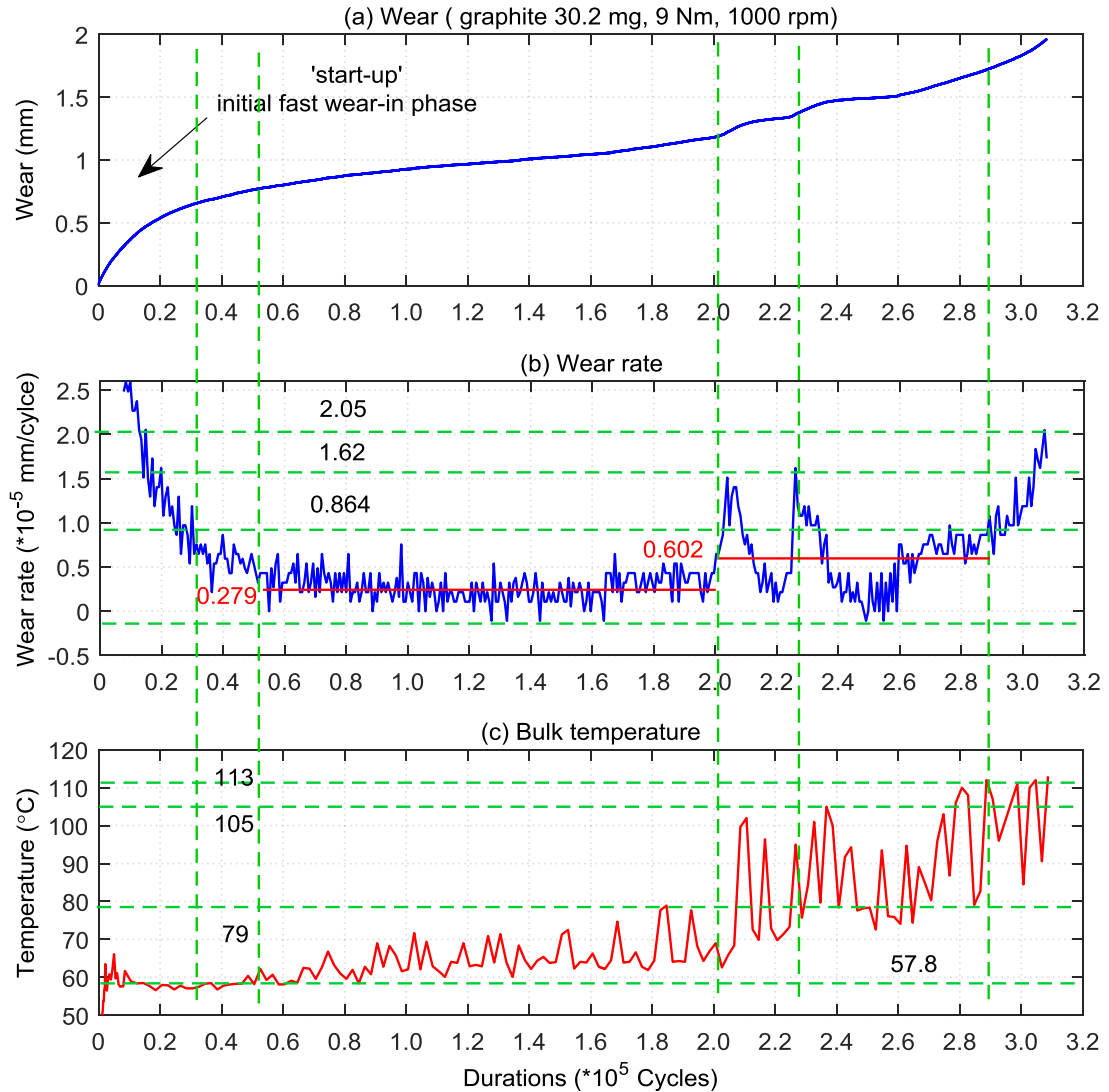


Figure 6.17 Wear, wear rate and bulk temperature versus duration (9.0 N-m, lubricated)

### 6.4.3 Typical test results at high loads

Respective airflow and bulk temperatures, wear and wear rate at a load of 10.1 N-m (including both: dry and lubricated cases), 12.1 N-m and 14.1 N-m are presented and discussed in detail in this section.

The test results at a load of 10.1 N-m (dry) are shown in Figure 6.18 and Figure 6.19. This result is included for competences, but there is a serious suspicious that the recorded bulk temperature is lower than the real

value, perhaps because of a focus issue on the I.R. camera. For example, the airflow temperatures at a load of 10.1 N·m are higher than those at 9 N·m. Hence it could be inferred that the bulk temperature should also be higher than is shown in Figure 6.18.

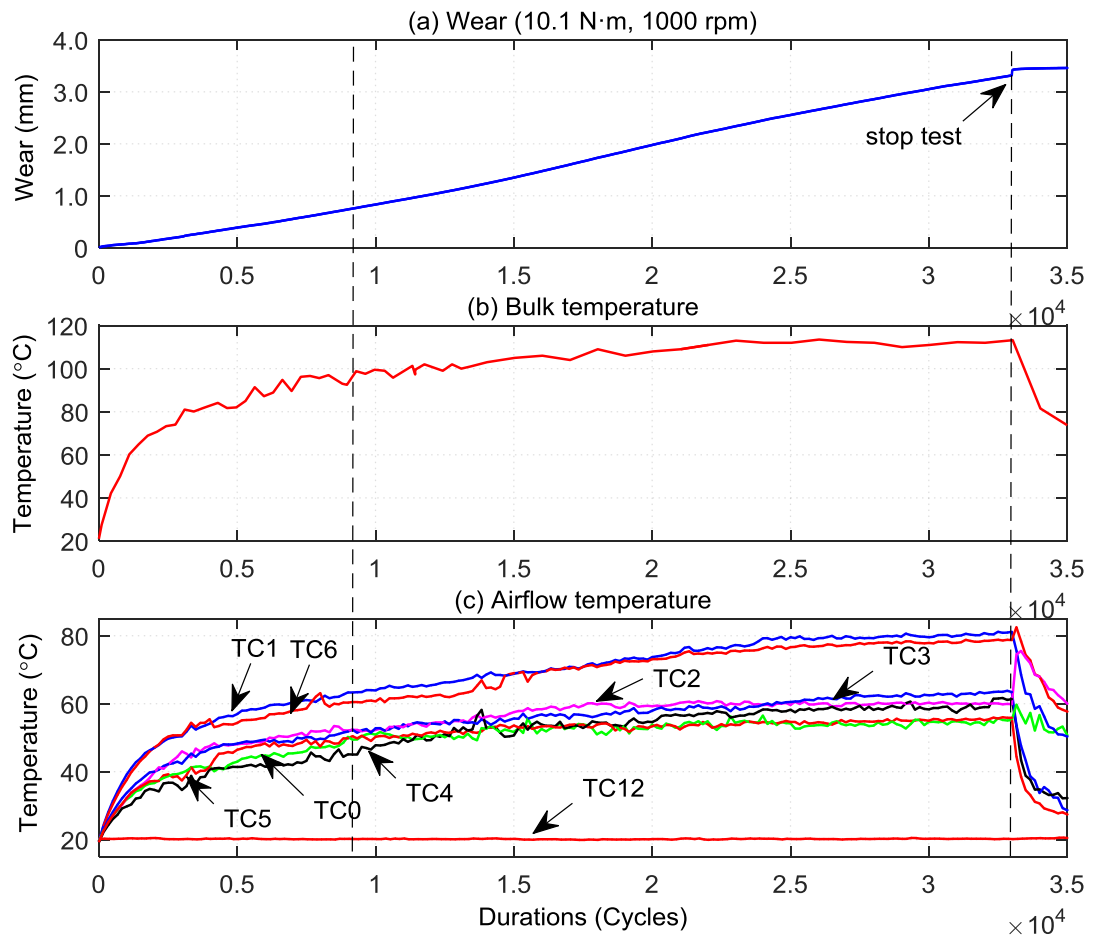


Figure 6.18 Test results of wear, bulk and airflow temperature (10.1 N·m, 1000 rpm)

Figure 6.19 illustrates that the wear rate increases progressively as the temperature increases, but tends to decrease when the bulk temperature holds stable for a period. The wear rate curve exhibits parabola-like trend which is similar to that seen at the moderate load conditions. Globally, the wear rate is high (average values are greater than  $9 \times 10^{-5}$  mm/cycle) but no significant change in wear rate occurs over the entire wear period.

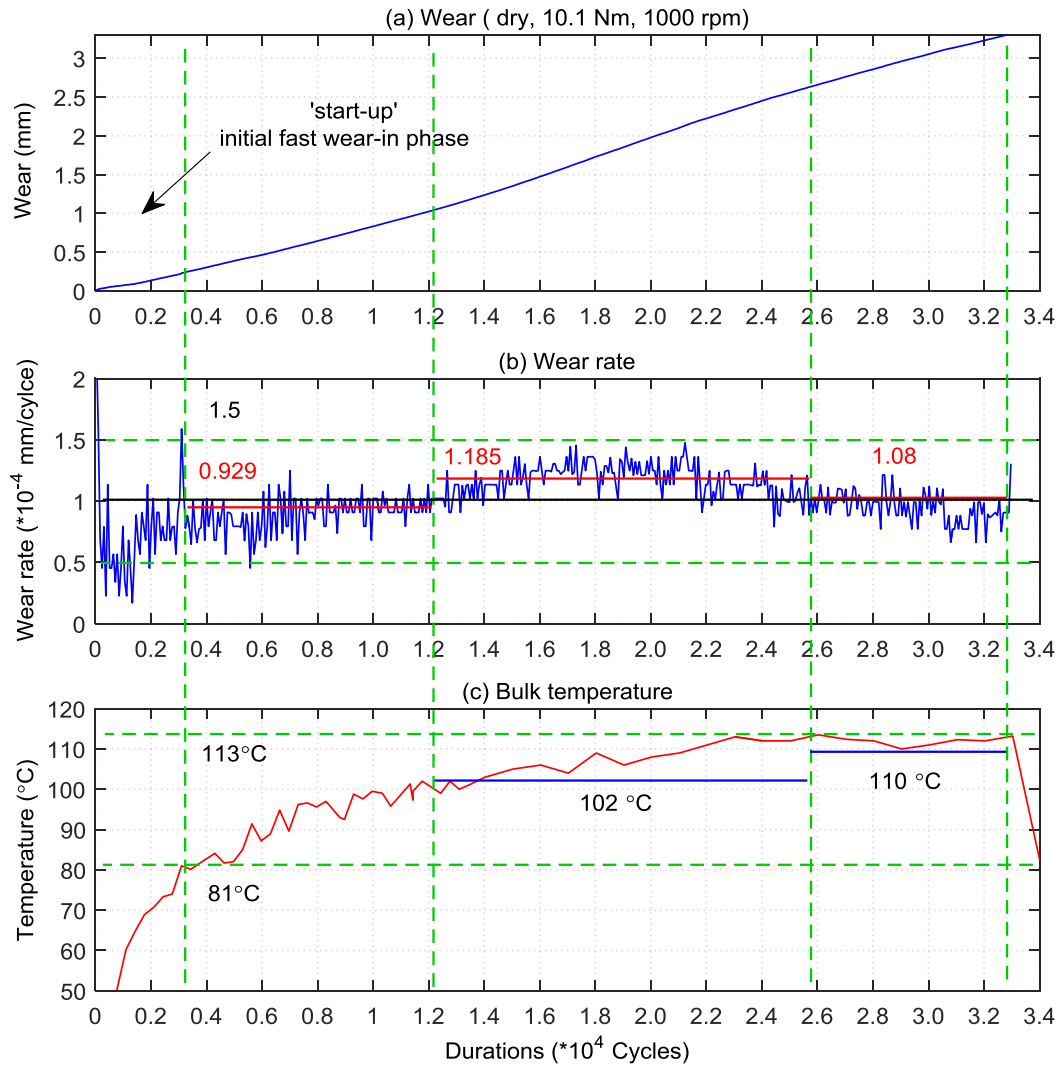


Figure 6.19 Wear, wear rate and bulk temperature versus duration (10.1 N·m)

Although substantial wear takes place when dry running at a load of 10.1 N·m, the lubricated wear shown in Figure 6.20 remains low, with marginal fluctuations, for a long period of  $3.5 \times 10^5$  cycles prior to the gears getting starved of lubricant. The corresponding body temperature rises slowly but is always lower than 97°C during this period. The wear rate and bulk temperature are presented in Figure 6.21. The stable wear rate does not exceed  $0.5 \times 10^{-5}$  mm/cycles with an average value of  $0.275 \times 10^{-5}$  mm/cycle. The bulk temperature starts to rise more steeply towards 120°C when lubricant is lost and the wear rate also increases quite sharply.

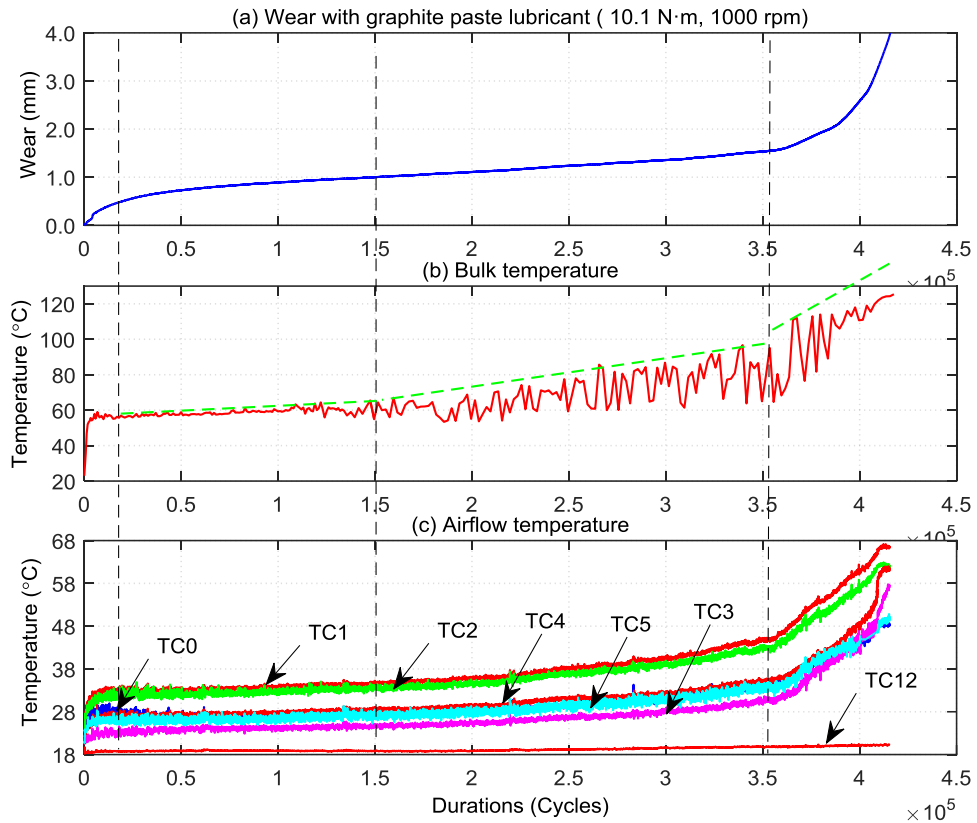


Figure 6.20 Test results of wear, bulk and airflow temperature (10.1 N-m, lubricated)

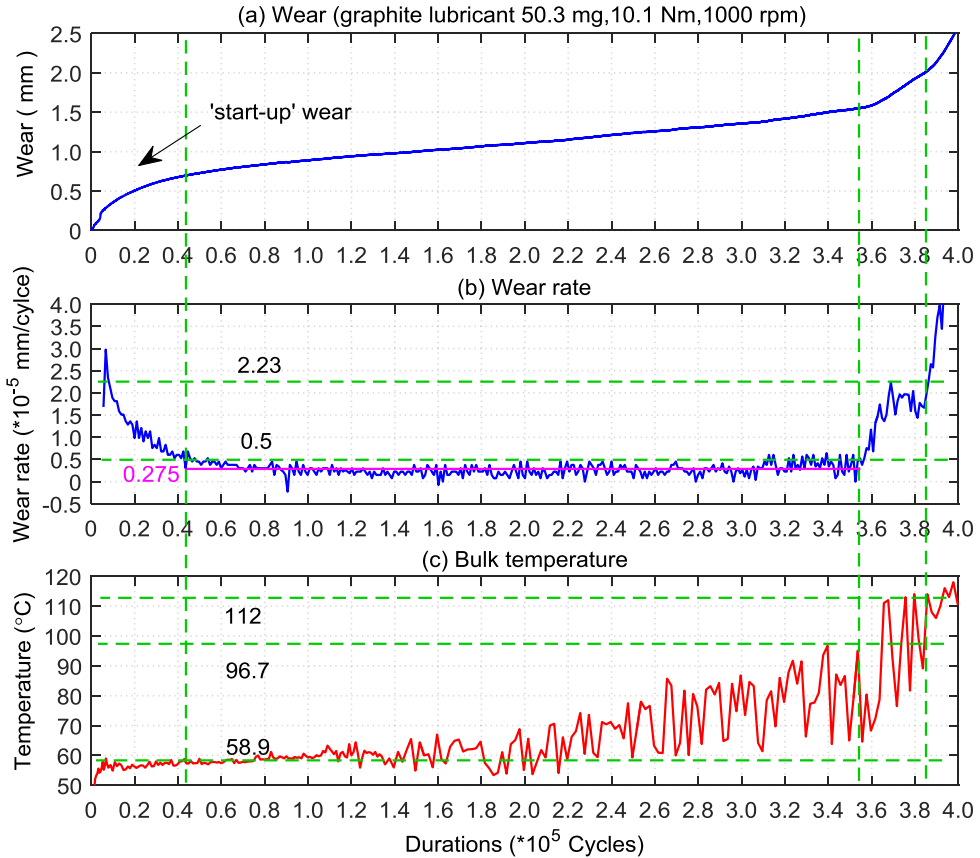


Figure 6.21 Wear, wear rate and bulk temperature versus duration (10.1 N-m, lubricated)



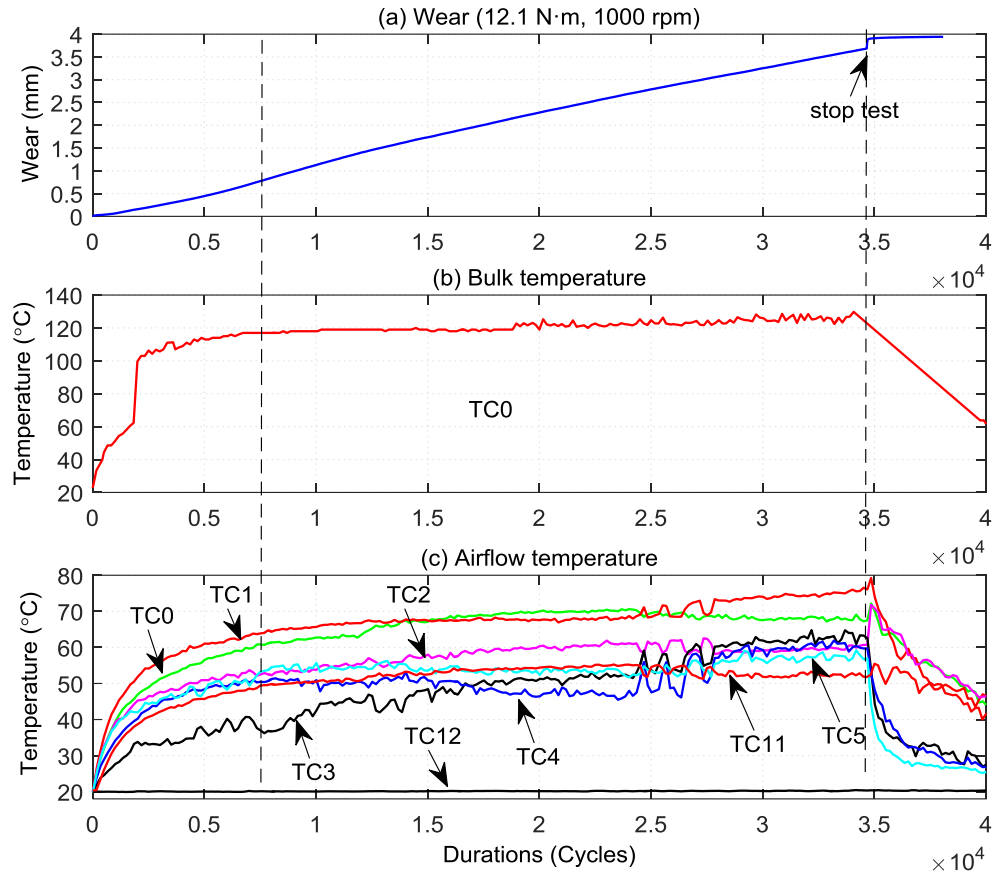


Figure 6.22 Test results of wear, bulk and airflow temperature (12.1 N·m, 1000 rpm)

Corresponding wear, airflow and body temperature at loads of 12.1 N·m and 14.1 N·m are plotted in Figure 6.22 and Figure 6.23. The bulk temperature rose more quickly than in previous tests and exceeded 128°C at 12.1 N·m and 144°C at 14.1 N·m. The airflow temperature continued to grow (to over 70°C) but it had not reached aerodynamic thermal balance when the tests were stopped. From the melt wear marks on worn tooth surfaces discussed in Sections of 4.3.9 and 4.3.10, it is estimated that the real maximum operating surface temperature had reached the melting point (165°C) or more. Hence a large deviation may exist between the measurement of bulk temperature and the real governing one when the bearing load is extremely high and operating period is short. If the airflow temperature field has not established a stable envelop, a strong forced air

convection may result in the majority of heat on tooth surfaces dissipating almost instantly when the teeth come out of mesh and only a marginal fraction penetrating into the tooth body which is measured by the infrared camera. Of course, it may also be associated with the heat absorption rate and heat capacity. Therefore it is essential to develop a new arrangement of the polymer gear test rig to collect operating temperature data for studying high-load behaviour.

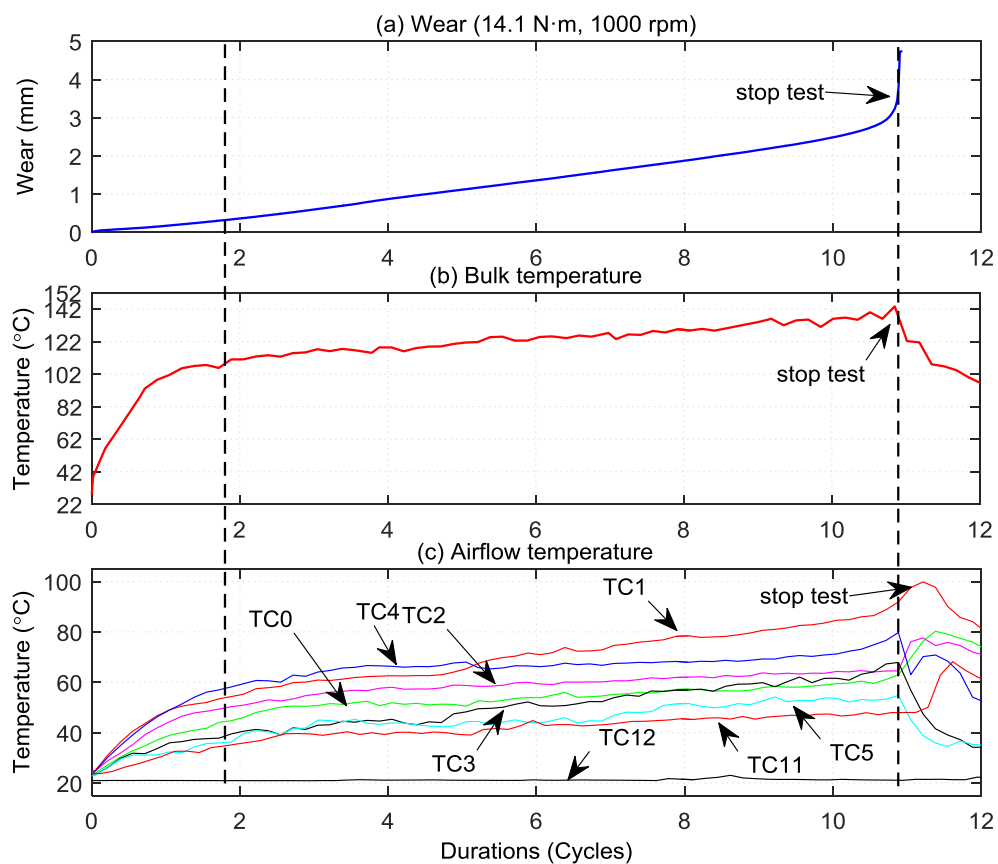


Figure 6.23 Test results of wear, bulk and airflow temperature (14.1 N·m, 1000 rpm)

The wear rates and bulk temperature in above two cases are shown in Figure 6.24 and Figure 6.25 respectively. Compared with the case at a load of 12.1 N·m, the wear rate at 14.1 N·m is relatively constant, but the average value ( $2.532 \times 10^{-4}$  mm/cycle) is at least twice as high. Note that although the wear rate was relatively stable over the period from 1000 to

about 9700 revolutions, the bulk temperature continued rising (to 136°C). When the bulk temperature exceeded 136°C, the wear rate increased rapidly until the moment of the gears failing. As with the test at a load of 12.1 N·m, there are two primary temperature ranges: 110°C to 120°C and 120°C to 130°C. In the former range, the wear rate increases a little and then decreases in a parabola-like curve while the majority of corresponding bulk temperature profile is approximately 120°C. However when temperature further increased, fluctuating between 120°C and 130°C, the wear rate tended to reduce and then keep level with a mean value about  $9.87 \times 10^{-5}$  mm/cycle for the 12.1 N·m load. However, at 14.1 N·m, the wear rate dropped much less before increasing very slowly until a rapid increase shortly before failure.

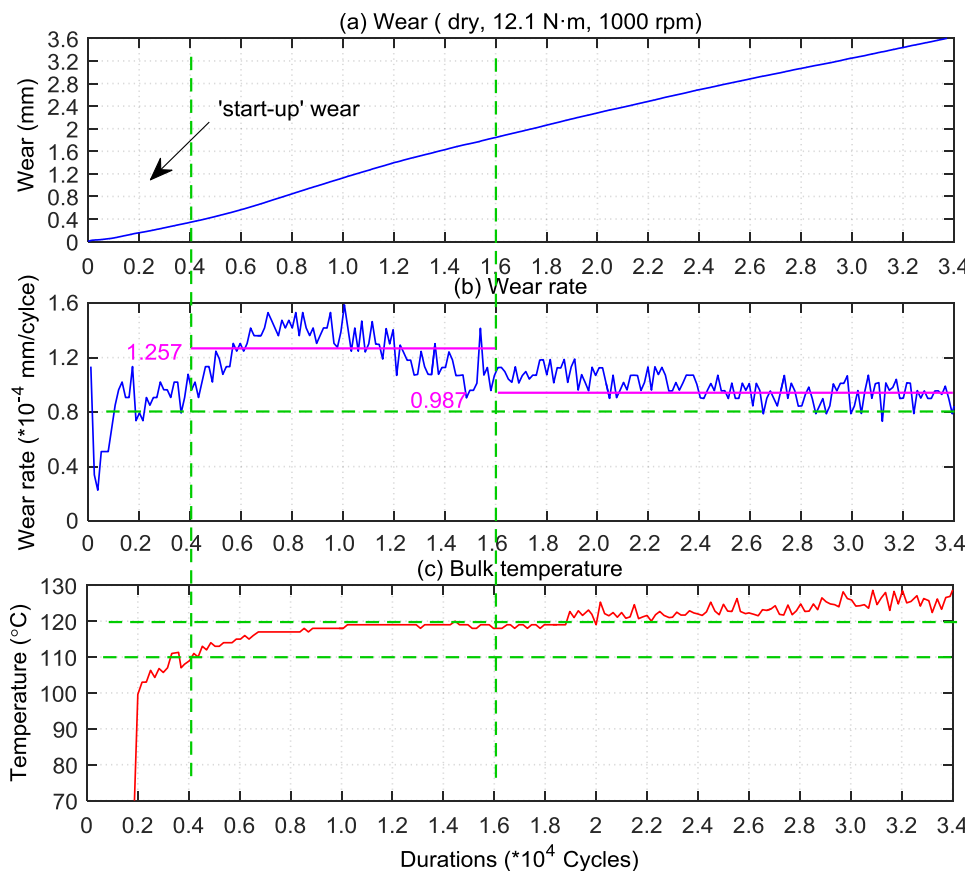


Figure 6.24 Wear, wear rate and bulk temperature (12.1 N·m)

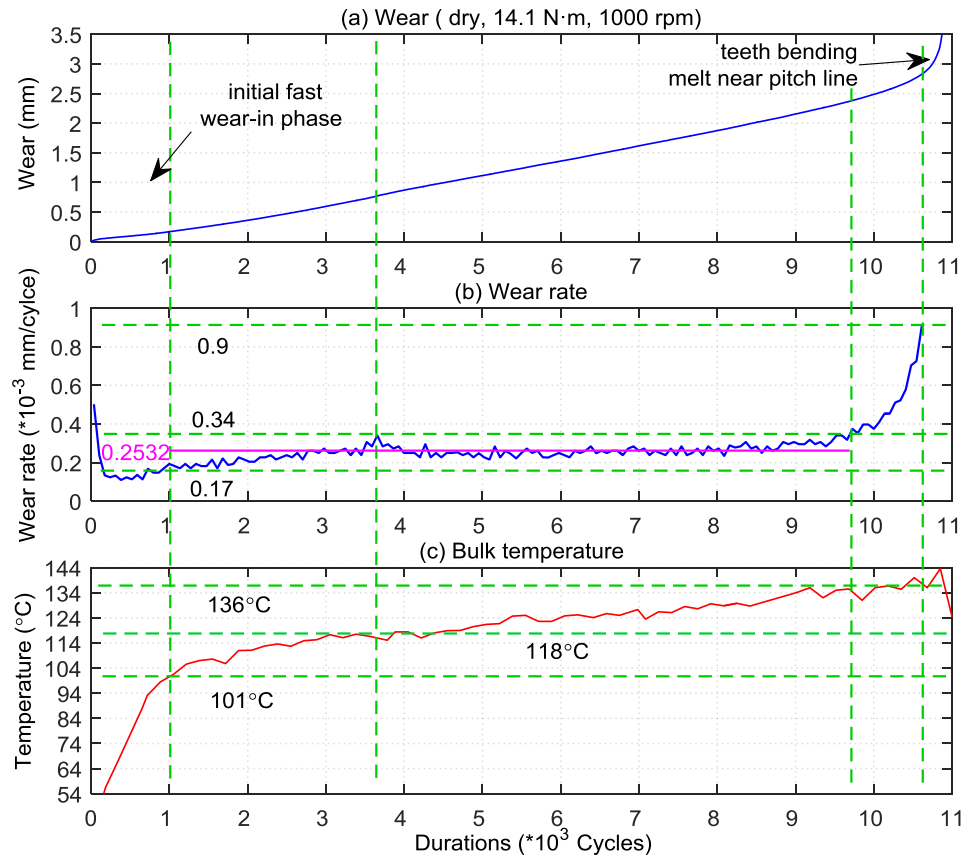


Figure 6.25 Wear, wear rate and bulk temperature (14.1 N·m)

The variation in wear rate, bulk temperature and airflow temperature in all the tests at medium and high loads indicate that there are transition temperatures (i.e.  $110^{\circ}\text{C}$ ,  $130^{\circ}\text{C}$ ) associated with different regimes of polymer behaviour. They may be linked to specific initial conditions of the material (polyacetal) such as the orientation and degree of crystallinity and affect properties such as heat absorption rate, coefficient of friction, strength and stiffness. A speculation is that the 'up and down' wear rate is a classic process linking closely to the coefficient of friction for reaching a certain material regime and thermal balance.

For all the test results, the statistics of the bulk temperature and wear rate (ranges and trends) are given in detail in Section 6.4.5 for the purpose of future investigations and as a design reference. Detailed variations in

wear rate and (prospective) coefficient of friction against the bulk temperature will also be discussed in Section 6.4.5.

#### 6.4.4 Temperature results of step-load tests

Temperature measurements were also conducted during step-load tests. The average wear rate, bulk temperature and airflow temperature in the steady-state phase or a mean value if the temperature had not reached balance are listed in Tables 6.1-6.3.

Table 6.1 Step load tests: wear rate, bulk and airflow temperature at speed of 500 rpm

Load ( N·m )	Wear rate (*10 <sup>-5</sup> mm/cycle)	Bulk temperature ( °C )	Airflow temperature ( °C )				Room temperature
			TC1	TC4	TC0	TC3	TC12
5	0.729	66	38.5	32.5	33	23.5	21
6	0.909	76	43.9	35	37	24	21.6
7	1.121	87	46	40.5	43.5	25	21.7
8	1.779	98	56	42.5	48.5	26	20.9
9	2.142	110	63	53	53	29	18.3

Table 6.2 Step load tests: wear rate, bulk and airflow temperature at speed of 1000 rpm

Load ( N·m )	Wear rate (*10 <sup>-5</sup> mm/cycle)	Bulk temperature ( °C )	Airflow temperature ( °C )				Room temperature
			TC1	TC4	TC0	TC3	TC12
5	0.6438	72	41.8	38.6	32.8	33	21
6	0.805	83	42.5	42	35	35	21
7	1.436	92	49	45.2	37.5	37.9	20
8	2.915	116	60	53	44.5	58	20.5
9	10.258	120	70	65	49	68	20.6

Table 6.3 Step load tests: wear rate, bulk and airflow temperature at speed of 1500 rpm

Load ( N·m )	Wear rate ( *10 <sup>-5</sup> mm/cycle )	Bulk temperature ( °C )	Airflow temperature ( °C )				Room temperature
			TC1	TC4	TC0	TC3	TC12
5	0.657	77	37.5	33.5	29.5	31	21.7
6	0.585	76	38.8	35	30	31	22
7	1.554	97	45.5	38	39.5	40	22.3
8	6.628	125	59	53	50	48	21.6
9	6.892	123	53	50	43	39	19.9

Table 6.4 Step load tests: wear rate, bulk and airflow temperature at speed of 2000 rpm

Load ( N·m )	Wear rate ( *10 <sup>-5</sup> mm/cycle )	Bulk temperature ( °C )	Airflow temperature ( °C )				Room temperature
			TC1	TC4	TC0	TC3	TC12
5	0.576	86	40.5	35	31	30	22
6	1.229	95	46	42	34	33	22.5
7	2.073	100	46.5	43.5	32.5	34	20.8
8	4.436	120	46	43.5	33	38	20.7

As the operational duration of the incremental step-load tests is relatively short, the majority of them had not reached the stable wear phase. Therefore, these data are provided simply for completeness and general guidance, not for formal thermal and wear evaluation.

#### 6.4.5 General discussions and conclusions

Extensive thermal tests were conducted and bulk and airflow temperatures relating to wear and wear rate throughout the entire duration were recorded. Following detailed discussions of these results, a wear rate estimation approach is proposed.

In the tests of airflow surrounding the gears, significant difference in airflow temperature can be noted between on the top half and bottom half of

gears. There appear to be three major causes: first, hot air rises (air convection); second, the majority of colder air sucked in by the gears is through the bottom half of gears, in particular the region where they are just come out of mesh and some cold air can be mixed into the air turbulence circling around the operating gears in the remaining fraction of a revolution prior to re-mesh; third, the entrained air that remains trapped in gear pockets is heated by the gear teeth. Extensive test results indicate that the hot air (at TC1) ejected by the process of the gears coming into meshing is the highest ( $45^{\circ}\text{C}$  -  $80^{\circ}\text{C}$ ), approximately 40 K lower than the bulk temperature. The air temperature around the bottom of the gears is about  $40^{\circ}\text{C}$  or less.

The temperature of airflow adjacent to the operating gears varies in terms of its distribution around the gears, and a significant difference exists between ambient and airflow temperature as discussed previously. However such a finding does not agree with previous studies [7, 49] that described no temperature rise at any point around the operating gears in addition to the immediate meshing line region. The airflow temperature data collected in this thesis are thought to be more reliable, because an extensive set of tests was conducted and at least 8 thermocouples were employed to measure the airflow temperature at various positions surrounding the gears throughout the whole wear process rather than relying solely on one thermocouple measuring for short periods. Also, these measurements synchronized with those for bulk temperature, wear progress and wear rate. Good coherence is exhibited between these four elements.

Under dry running conditions, it was found that an increase in load

results in an increase in bulk temperature, which gets close to the melting point at high load level. Also, there may be multiple temperature levels (with 'jumps') in tests with bearing loads beyond the low level. In low load tests, a single bulk temperature level was observed and it tended to decline slightly as the number of cycles increased, with a similar patterns for the wear rate.

The varying amplitude of wear rate is divided into regions of stable wear rate (with some fluctuations centring on a noticeable mean value) and unstable wear rate (conspicuous increase, decrease or a combination of both). Using these wear rate categories, the thermal test results presented in this chapter are simplified and tabulated in Table 6.5 and Table 6.6.

Table 6.5 Stable wear rate and corresponding bulk and airflow temperatures

Load (N·m)	Bulk temperature (°C)		Stable wear rate (oscillation) (*10 <sup>-5</sup> mm/cycle)		Airflow temperature (°C)
	range	trend	range	average	
4.9 covered partly	74.8-78.9	oscillation	≤1.46	0.131	oscillation
7.0	67.4-78.5 (67.4-69.9)	↓→oscillation	≤ 0.10	0.02	↓(slight)
8.0	91-110	↑→stable	≤1.0	0.48	↑ →stable
8.5	94-103	stable→↑	≤1.0	0.635	↑
9.0	102-110	↑	0.9-2.0	1.54	↑
10.1	110-113	oscillation	7-12	10.8	stable
12.1	120-129	↑→stable (129)	8-12	9.87	↑
14.1	118-136	↑	20-34	25.32	↑
9.0 (lubricated)	57.8-79	↑	<0.864	0.279	stable→↑
10.1(lubricated)	58.9-96.7	stable→↑	≤0.5	0.275	↑

Note: in tables 6.5 and 6.6, ↑ denotes increase; ↓ denotes decrease, → depicts changing process (from...to...); detailed description is added in bracket, oscillation means wear rate or temperature is stable but having slightly visible fluctuation; stable is used when comparing with clear increment and reduction. Take '↑→stable (129)' as an example, first increase and then gets stable centring on 129 °C. ↑→ ↓ (parabola), first rises and then drops



which forms a parabola-like curve.

Table 6.6 Unstable wear rate and corresponding bulk and airflow temperatures

Load (N·m)	Bulk temperature (°C)		Unstable wear rate (*10 <sup>-5</sup> mm/cycle)		Airflow temperature (°C)
	range	trend	range	trend	
8.0	115-125	oscillation	1.0-3.74	↑→↓ (parabola)	↑→stable
8.5	110-120	stable→↑→↓	1.0-4.0	↑→↓ (parabola)	↑→↓ (slight)
9.0	113.8-117	↑→stable	2.0-3.54	↑→↓ (parabola)	oscillation
	113.8-115.3	oscillation	2.0-1.0	↓	oscillation
10.1	81-102	↑	5-12.5	↑→stable(120)	↑
	102-113	↑	8-15	↑→↓ (parabola)	↑
12.1	110-120	↑→stable(120)	8.0-16	↑→↓ (parabola)	↑
14.1	101-118	↑	14.0-34.0	101-118	↑
10.1(lubricated)	112	oscillation	0.5-1.5	↑→↓ (parabola)	↑

Table 6.5 and Table 6.6 imply that a transition bulk temperature may exist, close to which the wear rate tends to get reduced or increased greatly. However the wear rate may remain nearly level over a range of temperature or vary resembling a parabola by rising and falling with a region of approximately stable or rising temperature. The traces of wear rate forming a parabola shape may link closely with the coefficient of friction and surface (or bulk) temperature (and maybe with the material regime).

At light loads (probably less than 8 N·m), it is safe to estimate roughly the average wear rate and service life according to the operating temperature (or maybe bulk temperature), such as in Figure 6.26. If more accurate domain of wear rate and operating temperature is require, more extensive experiments will be required.

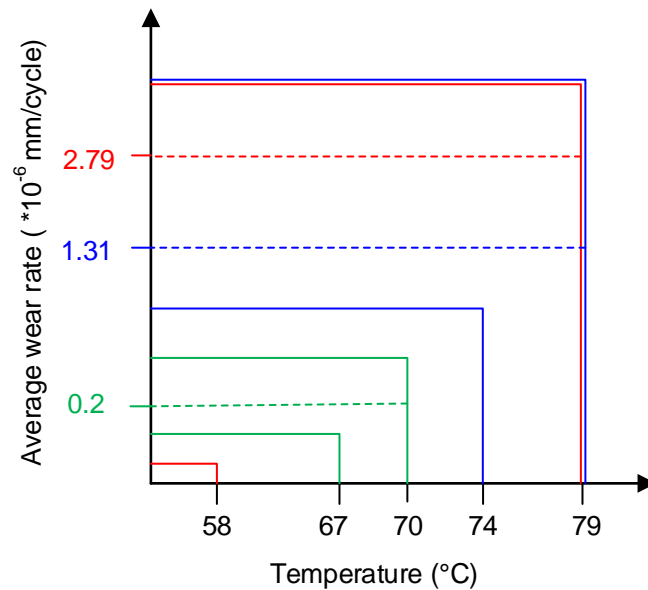


Figure 6.26 Schematic of range of wear rate and bulk temperature (broadly representative of polyacetal gears running at 1000 rpm with loads below 8 N·m).

For moderate and high load cases, there may be complicated and multiple levels of wear rate during the wear of the gears. For instance, there are primarily two levels of wear rate: less than  $1.0 \times 10^{-5}$  mm/cycle and between 1.0 and  $4.0 \times 10^{-5}$  mm/cycle at a load of 8 N·m and a speed of 1000 rpm. For the latter (varying wear rate), the curve of wear rate against bulk temperature appears to be a parabola, which is similar to the variation in coefficient of friction relating to the temperature, as shown in Figure 6.27 (given by Steijin [98]). Therefore the wear rate of polyacetal gears at high temperature (high loads/ speeds) may be linked closely to the coefficient of friction. However, for material of polyacetal, it is to hardly find relevant information on this. Hence, it is necessary to study polyacetal's coefficient of friction of polyacetal at various conditions (i.e. temperature, sliding and rolling) in future.

Base on above investigations and existing literature on coefficient of friction for polymers, two possible methods to predict wear rate are proposed:

first, If the wear rate and friction coefficient against temperature exhibiting similar curve patterns, it is reasonable to link them together to predict the wear rate/ wear/service life of polyacetal gears; second, but if their curve patterns are different, it is rational to estimate wear rate through using the transition temperature and temperature range than simply exploiting the transition torque. By observation of the variation in temperature and wear rate, there are prospects for introducing probabilistic approaches, concerning high operating temperatures to the estimation of multiple wear rates as shown in Figure 6.28. Adopting such methods, also could get the prediction of polyacetal gears' wear/wear rate closer to practical application. However the statistics of wear rate at a wide range of operating temperatures under various loads must inevitably be based on a very large amount of test data, which is well beyond the scope of this study.

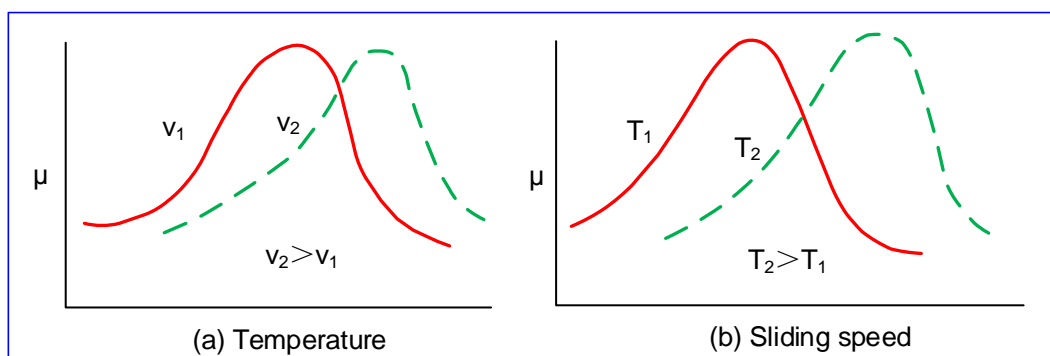


Figure 6.27 Coefficient of friction against temperature and sliding speed (after [98])

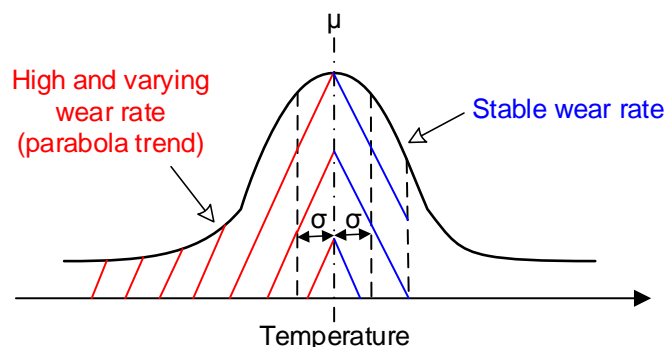


Figure 6.28 Schematic probability density function of operating temperature and wear rate

Besides, as discussed in Section 6.4.3, under high load conditions, comparing the results of measured bulk temperature with the wear marks (melting wear) on worn tooth surfaces described in Chapter 4, implies that they underestimate the real surface temperatures of operating gears. In order to probe temperatures in more representative positions and to gain data relevant to more operational situations, it will be better to reset the orientation of motor of the non-metallic gear test rig.

Typical thermal and mechanical properties of polyacetal vary with temperature and key ones have been listed in Table 6.7 and Table 6.8. Note that the temperature of tooth contact surfaces (at medium and high loads) has exceeded the heat deflection temperature ( $110^{\circ}\text{C}$ ), the Young's modulus has more than halved and the thermal expansion ratio has increased by over five times. The information given by tables illustrates that thermal and mechanical properties have degraded significantly that they can work solely in the short term.

Temperatures and heat flows associated with melting and freezing of polyacetal are illustrated in Figure 6.29 as measured by Differential Scanning Calorimetry (DSC) (using a PL-STA 1500 instrument in the Microscope and Analysis lab, University of Warwick). Between  $25^{\circ}\text{C}$  and  $235^{\circ}\text{C}$ , the only peaks visible by DSC are those for melting and freezing. No other transition appears, which contributes to polyacetal gears being suitable for short term exposure to high loads or temperatures close to the melting point. The temperature affects the orientation and degree of crystallinity, the strength, stiffness, and wear resistance.

Table 6.7 Variations of mechanical properties of acetal due to temperature rise (BS 6168 [13])

Temperature (°C)	Young's Modulus (GPa)	Thermal expansion rate $\Delta th$
20	2.93	-0.0004
40	2.58	0.0014
50	2.34	0.0023
60	2.05	0.0032
70	1.82	0.0042
80	1.58	0.0052
90	1.35	0.0063
100	1.2	0.0071

Table 6.8 Thermal properties of test polyacetal gears [9]

Parameters	Value
Heat deflection temperature (°C)	110
Melting temperature (°C)	165
Service temperature (°C), long term (min.)	-50
Service temperature (°C), long term (max.)	100
Service temperature (°C) short term	140
Coefficient of linear thermal expansion ( $10^{-6}K^{-1}$ )	110
Thermal conductivity (W/(m·K))	0.31

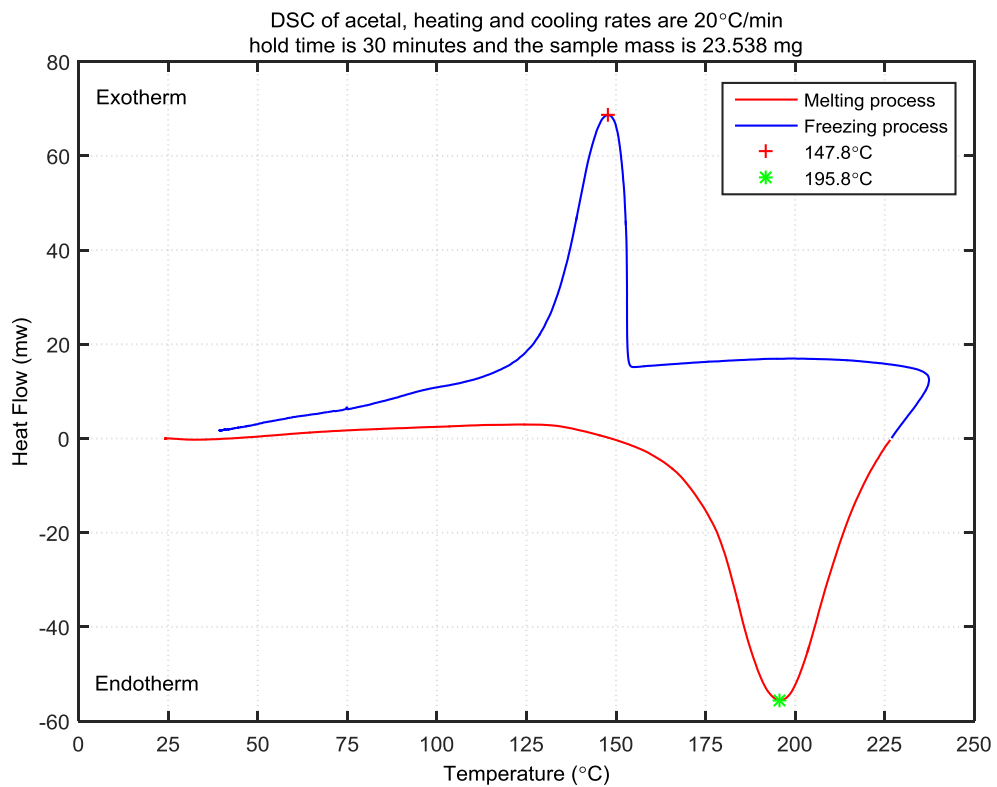


Figure 6.29 Typical DSC of test polyacetal

Typical test results and material properties demonstrate that, for both bulk and airflow temperatures, heating rates are closely associated with the wear rate. In other words, heat energy generated and wear interact strongly with each other.

The thermal test results provide encouragement to explore and establish heat transfer models, in particular a forced air convection model, to predict the performance of polyacetal gears in terms of surface temperature, wear mechanism, wear rate, service life and applicative engineering practise.

The velocity and temperature measurement of air flow distributions around rotating gears is expected to lead to improved forced air convection models. Hence, some preliminary investigations of the aerodynamic characteristics in the region encircling polyacetal gears in operation were performed and introduced in the following section.

### **6.5 Aerodynamic characteristics surrounding gears**

There are three mechanisms of heat transfer in polymer gears during operation, thermal conduction, radiation and convection. However, of them, thermal convection is thought to take the predominant role in heat dissipation due to the low thermal conductivity and low allowable operating temperature of polymer gears.

A few authors such as Hooke and Mao [7, 49, 122] have proposed over simple heat dissipation models to predict gear body temperature. They assumed that the gears were operating in the same manner as a gear pump

and that the air in each gear tooth pocket got close to the temperature of gear surface and none of the air would be lost by convection through the open end before next mesh. Then, the prediction of the body temperature attained is proportional to the load and independent of running speed. However, the test results here presented in Chapter 6.4 demonstrate a marked temperature discrepancy between hot air ejected (TC1) during meshing and bulk temperature prior to re-mesh. The temperature measurement TC1 in this thesis should approximately match the hot air temperature expelled by the instantaneous engagement of the gear teeth. Therefore the earlier heat dissipation model (air convection) is over simple and not so accurate.

In fact the thermal and aerodynamic airflows around polymer gears are very complex. They involve transient variations in air pressure, air velocity and heat flux, tooth tip ends' circumferential turbulence (envelop) and so on. It is essential to develop improved air convection models of polymer spur gears and wise to introduce the existing and advanced studies on flow/fluid in an external spur gear pump such as Diab [65], Erturk [61], Miad [63] and so on, although additional factors requires to take into account. Such models can explore improved bulk (body) temperature prediction. Typical thermal aerodynamic characteristics of Derin® gears at various loads and a speed were performed in this work. Representative advection features are discussed in the following paragraphs.

Figure 6.30 depicts the airflow temperature evolution surrounding gears during operation and after they have stopped. It shows that the air

temperature (TC1) adjacent to the region where gears come into mesh is highest. The air temperature near the top of gears is higher than that close to the bottom. In addition, the position of TC0 is close to an open window in the gear test rig cover. Hence significant forced air convection occurs to that region. The temperature of the airflow circling the gears is high and stable during the steady wear phase, which illustrates that there is temperature field that forms a stable temperature envelope as the running gear system reaches dynamic thermal equilibrium (namely net balance of heat generation and heat dissipation).

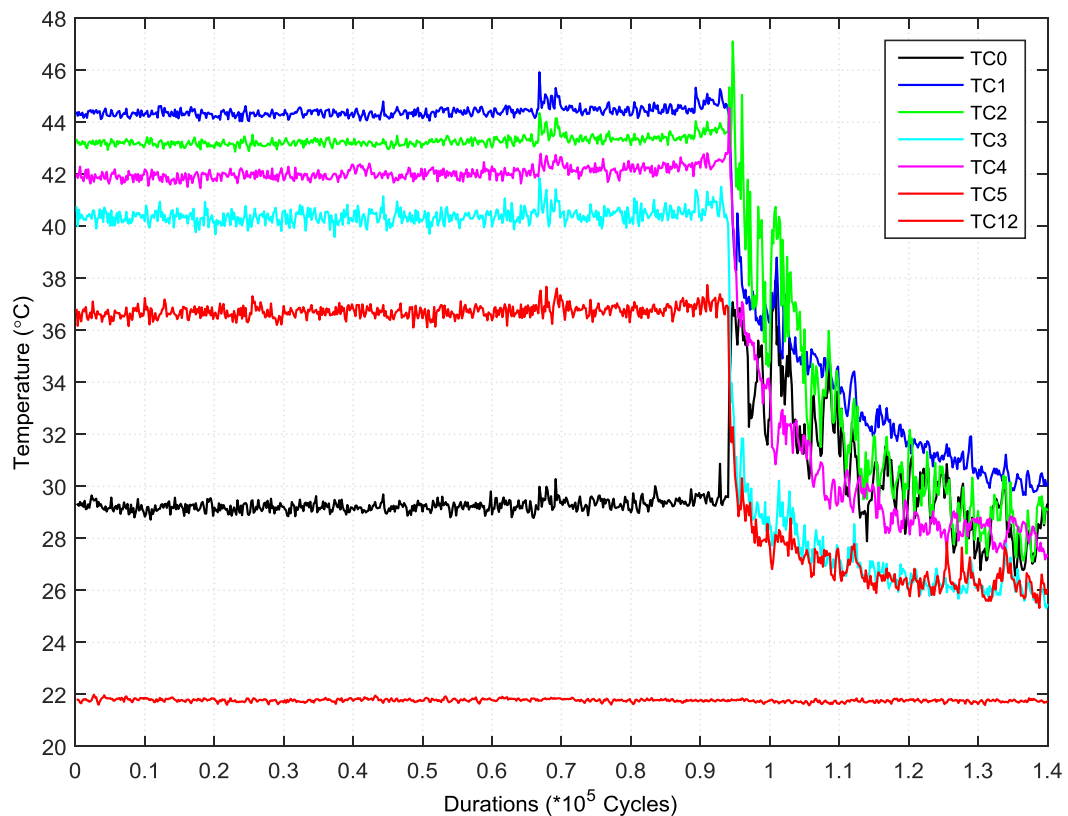


Figure 6.30 Airflow temperature changes during operation and after stopping (7 N·m, 1000 rpm)

To view the aerodynamic features clearly, pairs of temperature measurement are compared directly in Figure 6.31. The airflow temperatures along the meshing line are shown in Figure 6.31 (a), where TC1 drops as



soon as the test stops while TC4 rises immediately and briefly as the test stops. However, TC3 and TC5 drop almost instantly while TC0 and TC2 increase (a spike appears) promptly. When the test stops, free/natural air convection takes place between hot air in gear tooth pockets and environmental (cold) air as shown in Figure 6.32. That is why there are spikes at TC0, TC2 (at the top of gears) and TC 4 instantaneously as the test stops. Nevertheless, TC3 and TC5 (at the bottom of gears) drop almost directly because hot air is tending to rise up and slight natural air convection takes place. The varying instant temperature transformations before and after the test stops reveal that forced air convection plays a significant role in the heat transfer of running polymer gears. Hot air is expelled when gears come into mesh while environmental air is sucked (pumped) towards gear tooth pockets (mainly because the air pressure in tooth pockets is lower than the environment). The behaviour is acts extremely similar to a spur gear pump.

The airflow tangential velocity and temperature around the circumference of running gears were measured by using two miniature hot-wire anemometers. The measurement positions and directions are shown in detail in Figure 6.33. Figure 6.33 also shows the airflow temperature measurement points (using thermocouples), where points 6 and 7 are to measure the temperature of air expelled and sucked respectively in the axial direction of gears. Also, thermocouples 4 and 8 were now much closer to the gear tooth tips than those in Section 6.4.

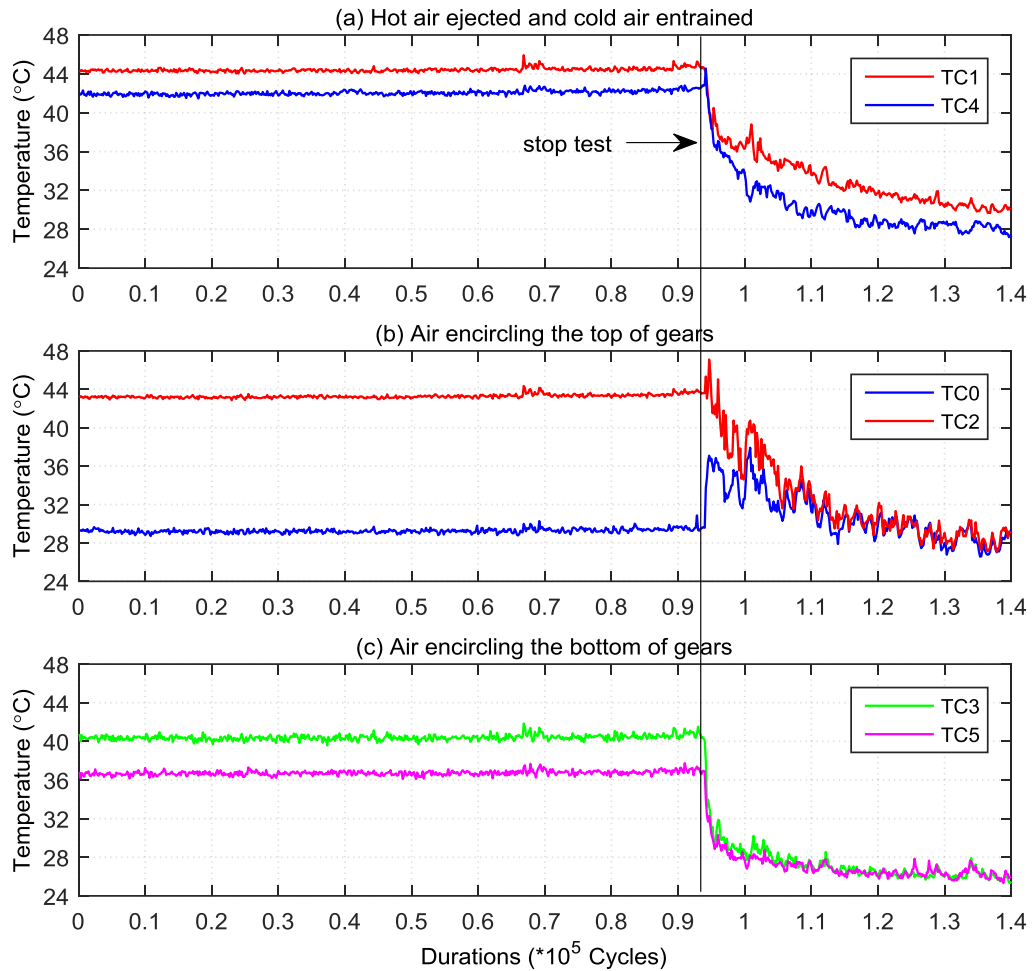


Figure 6.31 Airflow temperature comparisons between measurement positions

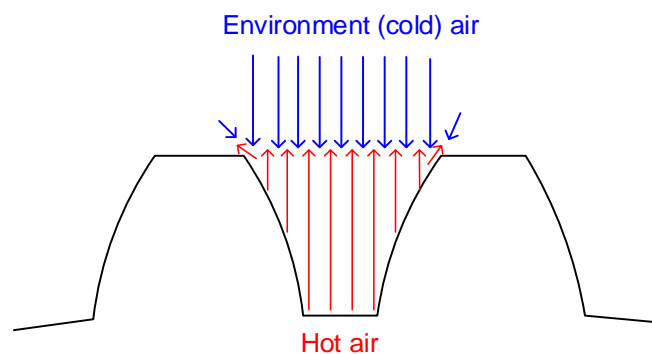


Figure 6.32 Natural air convection after test stopped

The temperature and velocity measurement results at a load of 4.2 N·m and speed of 1000 rpm are listed in Table 6.9 to Table 6.13. Of them, the data in Table 6.10 to Table 6.12 were obtained tangentially, parallel to the direction of the gears' rotation, while the data in Table 6.9 were taken

close to the meshed region of gears and in a perpendicular direction to the gear blanks, the data in Table 6.13 were attained close to the rotating gears and in a perpendicular direction of the gear blanks The corresponding airflow and bulk temperatures are presented in Figure 6.34.

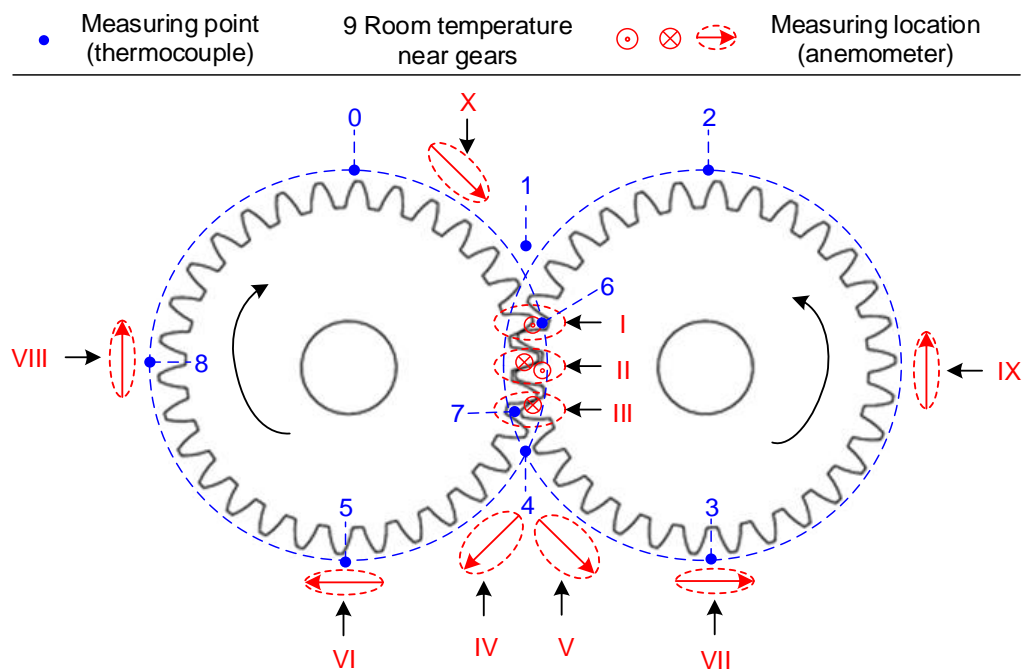


Figure 6.33 The airflow measurement at measurement positions of operating gears

Table 6.9 Air flow temperature and velocity measurements at locations close and vertical to the meshed tooth of gears as in Figure 6.33

Region I		Region II		Region III	
Velocity (m/s)	Temperature (°C)	Velocity (m/s)	Temperature (°C)	Velocity (m/s)	Temperature (°C)
3.12	36.2	2.35	37.2	1.52	25.7
3.6	36	2.21	35.2	1.65	25.5
3.27	36.1	2.17	35.7	1.58	25.4
3.06	36.7	2.26	36.1	1.47	25.3
3.87	36	2.32	36.5	1.77	26
3.48	36.1	2.29	36.6	1.58	26.1
3.58	36.2	2.28	36.7	1.70	26.1
3.72	36.6	2.3	36.9	1.78	26.3
3.83	35.9	2.38	37	1.56	26.4
3.79	35.8	2.42	37	1.59	26.6
3.26	36.7	2.4	37.1	1.51	24.4
3.39	37.1	2.41	37.1	1.47	25.9
3.47	36.8	2.41	37.2	1.49	26.1

Table 6.10 Air flow temperature and velocity measurements at locations close and parallel to the tangential velocity of rotating gears as in Figure 6.33

Region IV		Region V		Region VI	
Velocity (m/s)	Temperature (°C)	Velocity (m/s)	Temperature (°C)	Velocity (m/s)	Temperature (°C)
1.16	27	1.84	27	1.31	26.9
1.1	26.8	1.6	27.1	1.33	26.9
1.35	26.5	1.47	27	1.31	26.9
1.14	26.9	1.99	27.1	1.27	26.9
1.31	27	1.99	27	1.21	26.9

Table 6.11 Air flow temperature and velocity measurements at locations close and parallel to the tangential velocity of rotating gears as in Figure 6.33

Region VII		Region VIII		Region IX	
Velocity (m/s)	Temperature (°C)	Velocity (m/s)	Temperature (°C)	Velocity (m/s)	Temperature (°C)
1.94	27	1.69	25.8	1.73	26.3
1.99	27	1.66	25.8	1.72	26.2
2.16	27	1.69	25.8	1.74	26.2
1.09	27.2	1.7	25.8	1.72	26.1

Table 6.12 Air flow temperature and velocity measurements at locations close and parallel to the tangential velocity of rotating gears as in Figure 6.33

Region X					
Velocity (m/s)	Temperature (°C)	Velocity (m/s)	Temperature (°C)	Velocity (m/s)	Temperature (°C)
1.66	27.1	1.67	27.1	1.47	27
1.86	27.1	1.84	27	1.99	27.1
1.69	27	1.6	27.1	1.57	27.2

Table 6.13 Air flow temperature and velocity measurements locations close and vertical to the gear blank (same direction as those in Table 6.9 ) as in Figure 6.33

Region VI'		Region VII'		Region IX'	
Velocity (m/s)	Temperature (°C)	Velocity (m/s)	Temperature (°C)	Velocity (m/s)	Temperature (°C)
0.54	26.1	0.53	26.3	0.48	26.2
0.63	26.1	0.57	26.2	0.51	26.3
0.58	26.2	0.47	26.2	0.55	26.3
0.56	26.2	0.52	26.1	0.55	26.3

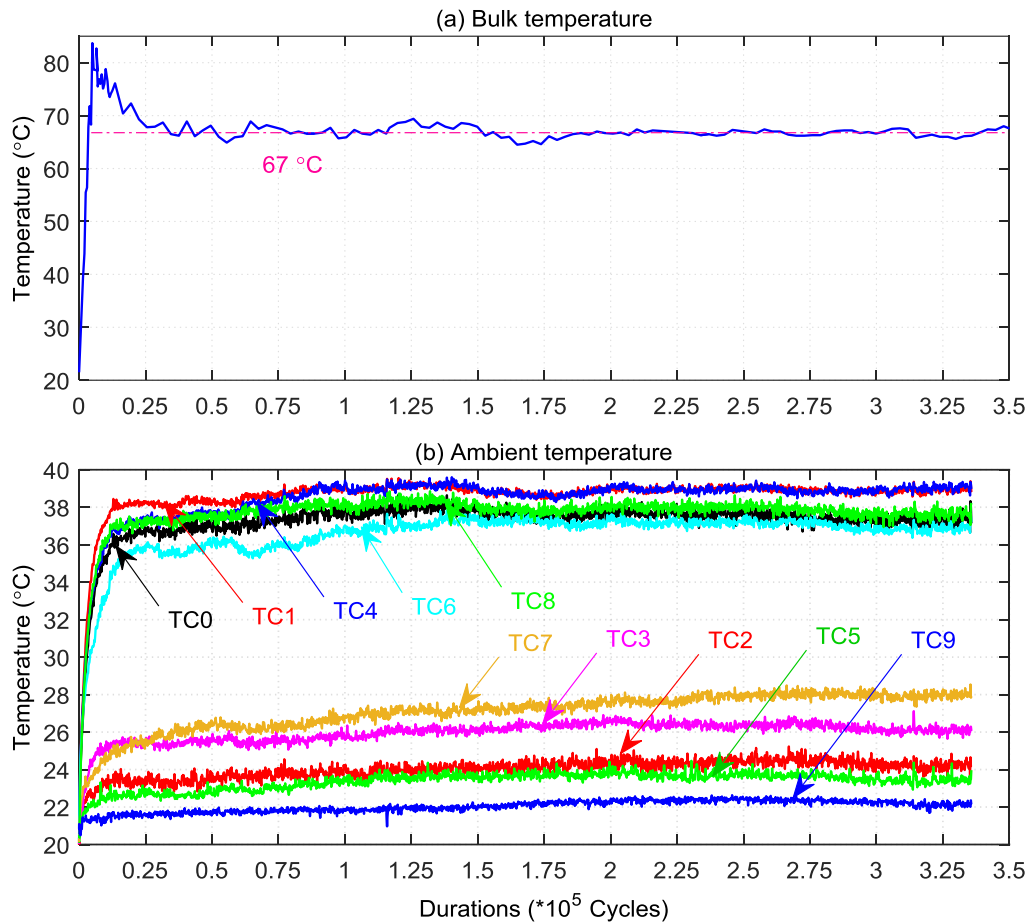


Figure 6.34 Bulk and airflow temperatures (4.2 N·m, 1000 rpm)

Although the measurement positions of anemometers were slightly further from gears than those of the corresponding thermocouples, the patterns of results are in reasonably agreement.

The data presented in Figure 6.34 and Table 6.9 to Table 6.13 again demonstrate that the temperature of hot air erupting by the gears' approach action is significantly lower ( $\sim 28^{\circ}\text{C}$ ) than the bulk temperatures of the contact tooth surfaces. This discrepancy is thought to become greater with the increase of contact load and rotation speed. The temperature of TC4 ( $39^{\circ}\text{C}$ ) here is much higher than that at slightly lower position given in Section 6.4 and is as high as TC1 here. The temperature in Region III is (at about  $25.4^{\circ}\text{C}$  to  $26.4^{\circ}\text{C}$ ) much lower than that of TC4. This phenomenon indicates

that the temperature of residual hot air trapped between the teeth, which expands out immediately during the recess action, is not lower than the hot air (TC1) ejected.

For gear having an addendum radius and rotating at a speed of 1000 rpm, the tangential velocity at their circumference is 3.351 m/s. This is compared with the average values of velocity and temperature from Table 6.9 to Table 6.13 in Figure 6.35, where GV indicates the tangential velocity of the rotating gears and the mean value measured by thermocouple TC1.

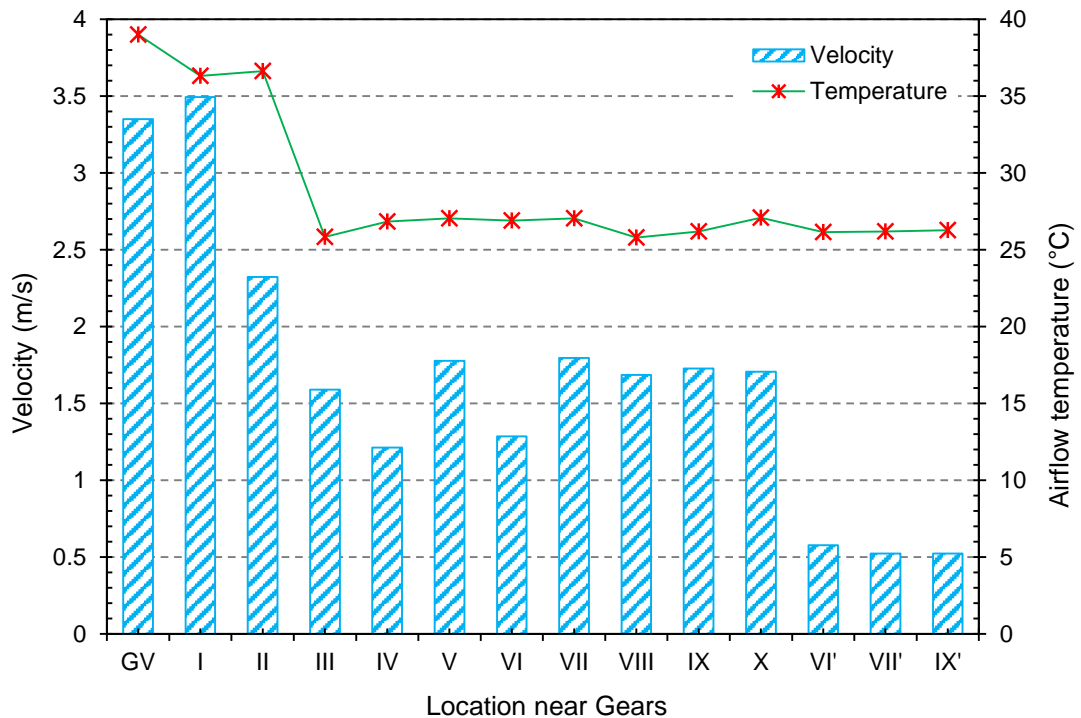


Figure 6.35 Airflow velocity and temperature surrounding and against gears

The temperature of hot air ejected in the axial direction (I and II) by the engagement of the gears is marginally lower than that in the radial direction, while the ejecting airflow axial velocity is even higher than the tangential velocity of the rotating gears. This implies that the approach action of the gears may result in a transient elevation in the pressure of the air

which is trapped between contacting teeth. The velocity and temperature in Region III imply that the recess action of the gears tends to suck cold (surrounding) air into the gap between the contacting teeth. The temperatures and velocities near regions IV to X are relatively stable and low compared with those of GV, I and II. Therefore the rotating polymer gears can form a stable velocity and temperature field (envelop) which can act as the agent for sustaining thermodynamic equilibrium between meshing gears and the environment.

Note that the heat energy of gears exchanges with the environment mainly in the radial and axial directions around the mesh zone. It is also worth mentioning that the entering and leaving mesh processes are similar to the working principle of an air piston, where compression and expansion occur. This process results in the temperature of air trapped between teeth being elevated, air pressure increased, and then, when the teeth separate, the volume between the teeth increasing almost instantly which leads to the air pressure between the teeth being reduced significantly. At that moment, cold air is rapidly entrained into the gear tooth pockets in the axial and radial directions. Hence, one conclusion to be drawn is that the trapping between the teeth causes power loss, while the trapped air is heated by this process. It would then follow that increasing the rotating speed tends to increase the power loss. These findings agree well with other studies on airflow and pumping around gears [62-65].

There may be stable aerodynamic features surrounding the gears, and also internal vortices vortex in the air in gear pockets, which is heated

during a fraction of a revolution prior to re-mesh, see Figure 6.36. This observation is in accordance with the investigations of Erturk [61], Marchesse [62] and so on.

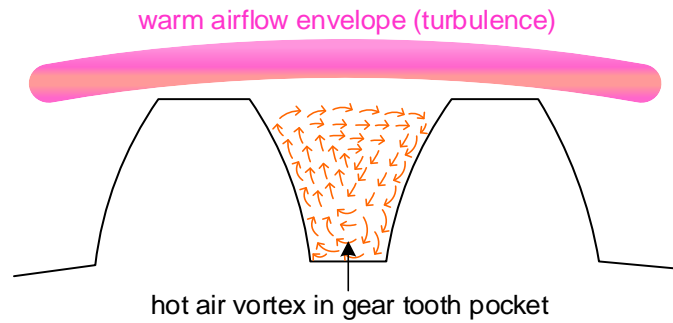


Figure 6.36 Air vortex within gear tooth pockets

In light of the typical test results and analysis in this work and prior investigations of gears' fluid dynamics, the aerodynamic characteristics of polymer gears can be summarised as in Figure 6.37.

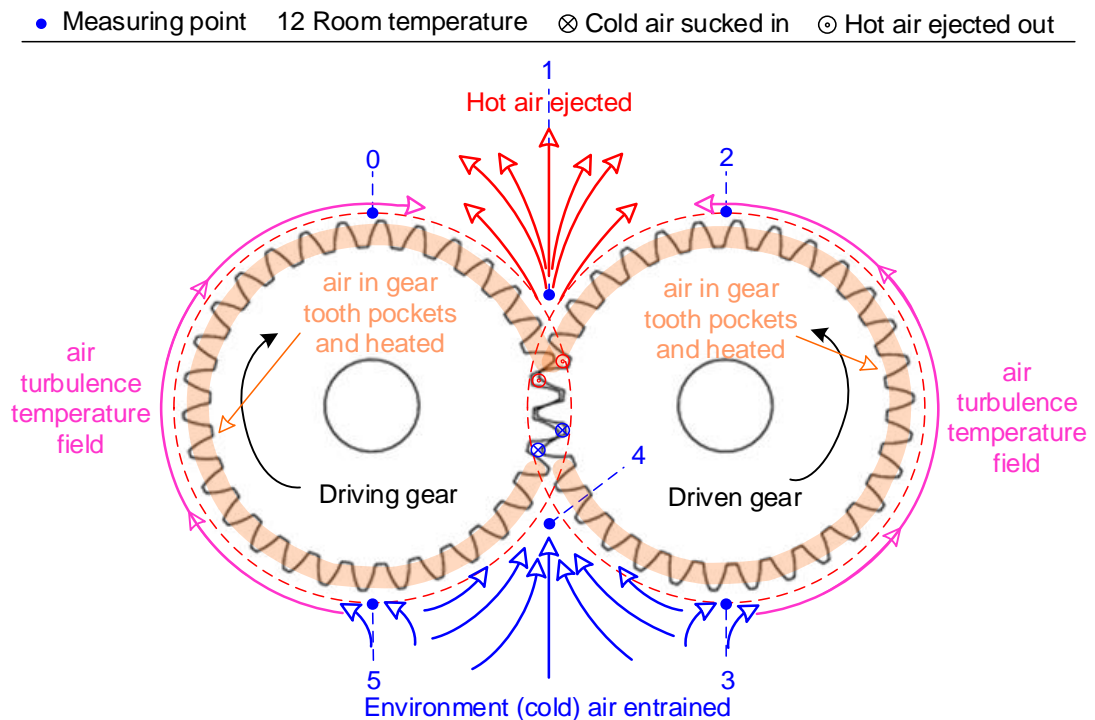


Figure 6.37 Aerodynamic features of a meshing gear pair



- **General Conclusions**

The short-period approaching and recessing processes of polymer gears worked very like an air piston, where air compression and expansion occur cyclically. Consequently, the pressure and temperature of air trapped between teeth first increases rapidly and then decreases almost instantly. The airflow velocity amplitude and direction vary significantly. It is thought that these behaviours will get more severe with increases in load, speed or both.

Thermal test results and aerodynamic measurements around polymer gears reveal that the heat generation mainly originates from the sliding friction, trapping air between teeth (air compression and pump action), with, perhaps, also some thermal conduction through the bearings and shafts. Other, marginal heating may be contributed by viscoelastic hysteresis, as in the previous studies of Terashima [29], Koffi [59], Gauvin [12] and so on.

The forced air convection heat dissipation (or heat energy exchange) of polymer gears principally takes place in the radial and axial directions during gears' engaging process. It results in rises in temperature and pressure of air trapping between teeth, and pulsating air flow (high ejecting velocity).

The air pulsating due to the gears' expulsion and pump effects can introduce extra vibration and noise in addition to that from the cyclic mechanical contact.

Therefore, one way to reduce the heat generation is to increase the residual volume of trapped in the teeth, such as a slight centre distance

extension or tip relief. This is also one reason why negative radial misalignment can cause substantial wear.

Stable temperature and velocity fields may form to envelop gears during engagement and may benefit to the maintenance of thermodynamic balance of operating gears. Also, internal air vortex generates in gear pockets and heated during a revolution.

Last but not least, it is wise to introduce ideas from existing fluid studies for operating gears to improve the predictive model of heat dissipation or bulk temperature. However, to do so is well beyond the remit of this thesis requirement for the cooperation of a large group of multiple discipline professional researchers, across the fields of mechanics, fluid, thermodynamics, polymer materials and so on.

Understanding the aerodynamic characteristics of operating gears inspires approaches for improving heat dissipation or load durability of polymer gears.

### **6.6 Durability improvement**

Based on these extensive experimental investigations, several prospective approaches to improve the load carrying capacity of polymer gears are proposed.

The first is to ensure timely removal of wear particles from contact surfaces. In this thesis, graphite paste lubricant was introduced to sweep debris to tooth tip ends, giving the significant described in Section 4.5. Of

course, lubricant also reduces the coefficient of friction.

Second, it would be beneficial to consider self-lubricated, polyblends with HDPE, PTFE, silicone, graphite and so on [123]. Or composite, with reinforced carbon fibre, glass fibre and so on.

Third, the design geometry of polymer gears should be optimized to allow more residual volume between the trapping teeth, which is expected to reduce the gear pump effects. A suitable increase the centre distance of gears might achieve this.

Fourth, seek methods to increase the heat dissipation /air convection: blowing cold air into gear boxes; adding openings on the gear box near the major heat energy exchange regions (axial and radial regions) of meshing gears; adding fins to geared system. There will need to be compromises with the potential disadvantages such as dirt ingress and extra power requirement.

Last but not least, incorporate features aimed at reducing the recirculation of hot airflow that has been expelled axially by causing this air to be pumped axially so that it rises further owing from the gears as sketched in Figure 6.38. One simple way to do this is exhibited in Figure 6.39(a), where a flat plate is added (roughly along the line P-P) to isolate the approach and recess actions into separate spaces. It is also plausible to disturb the thermodynamic equilibrium of operating gears by adding cooling fins to gears, or introducing inclined holes through gear tooth flanks ( if allowable) rather than the holes parallel to tooth flanks [87-89]. The inclined holes along tooth flanks actually act as cooling fins to pump more air through

tooth flanks and so cool the tooth bodies. Attaching fins to gear teeth provides a similar function to the holes in tooth flanks and also it tends to blow the wear debris away from the tooth contact surfaces.

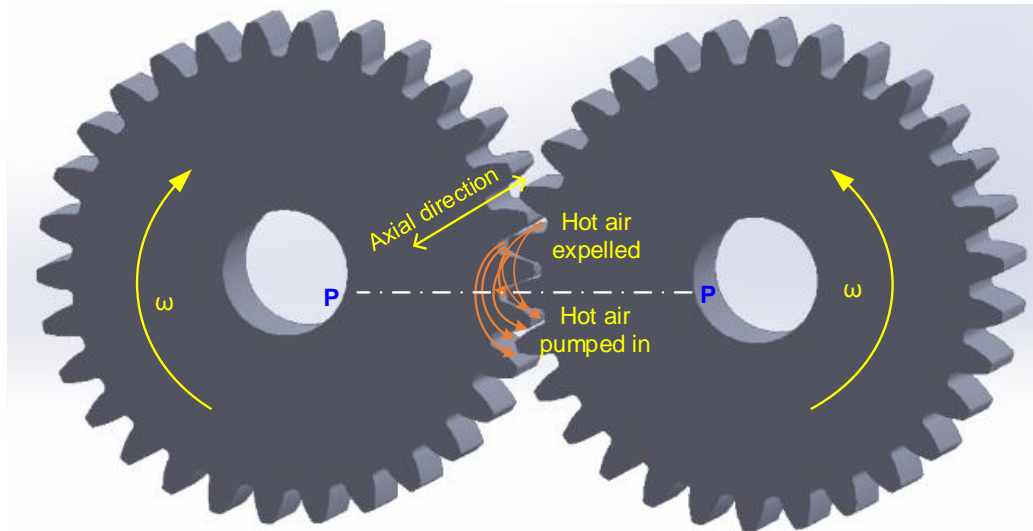


Figure 6.38 Schematic diagram of hot air recycling between the trapping of gear teeth

Given these observations, a set of experiments was conducted on a group of test gears to which a thermal isolating plate or attaching cooling fins were attached, as follows:

- I: A set of tests with an isolation plate as shown in Figure 6.39(a);
- II: A set of tests with straight fins and an eye plate as shown in Figure 6.39(b);
- III: A set of tests with straight fins without an eye plate
- IV: A set of tests with a twist fin on the driving gear as shown in Figure 6.39(c);
- V: A set of tests with twist fin to blow cold air through the gear tooth flanks as shown in Figure 6.39(d);
- VI: A set of tests with twist fin to extract cold air through the gear tooth

flanks as shown in Figure 6.39(e).

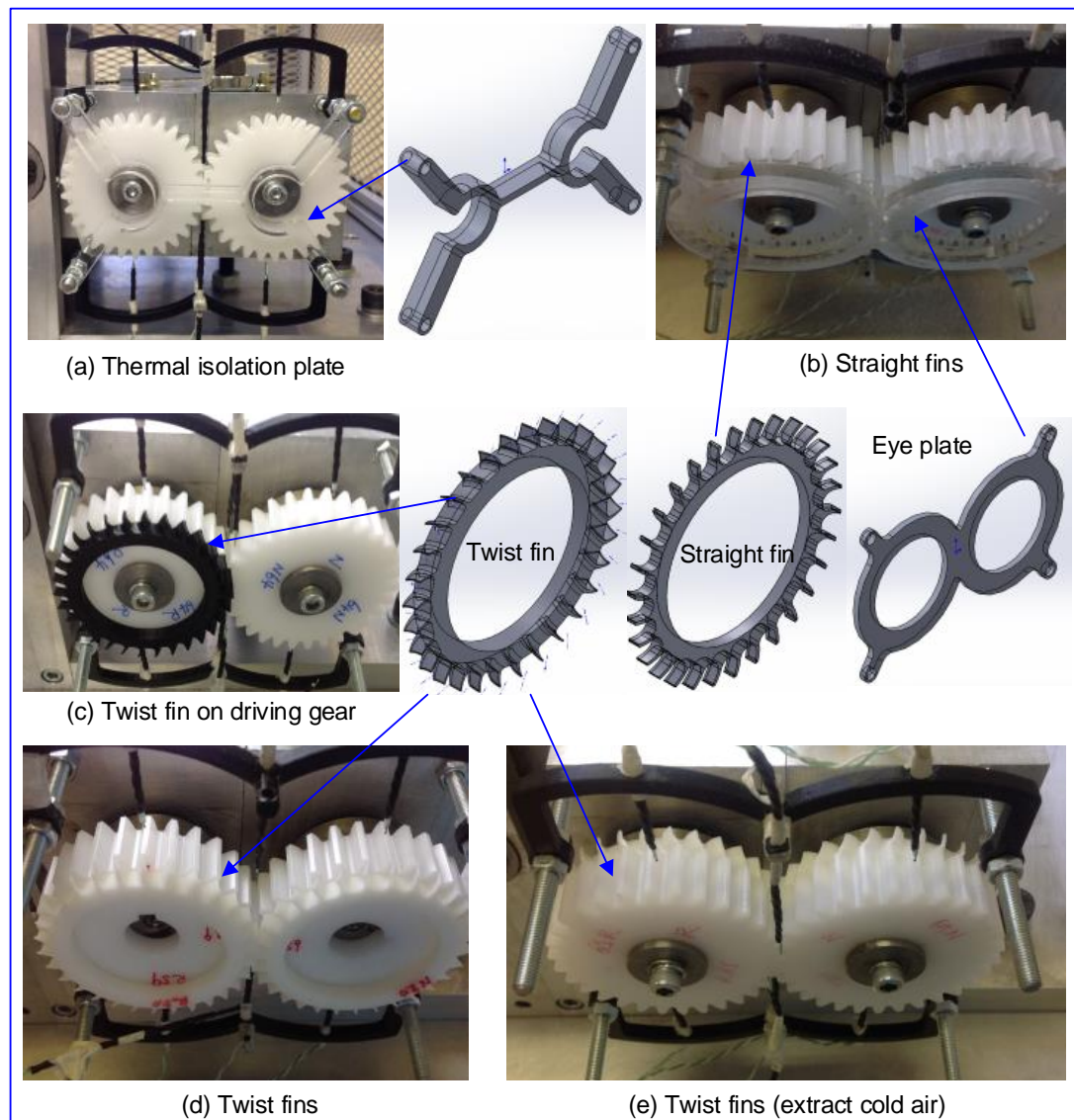


Figure 6.39 Testing gears with thermal dissipation structures

All the above six cases of polyacetal gear tests plus case VII without any structure were at the same load (5.8 N·m), speed (1000 rpm) and experienced the same duration ( $5.0 \times 10^5$  cycles). The average weight losses for each cases were obtained and are shown in Figure 6.40, which reveals that the best one is Case V and the second best is Case I. Considering the fins induce at least some extra power loss, of the six cases, Case I (introducing a isolating plate between the entering and leaving mesh actions)

may be judged the most beneficial proposal or option to improve polymer gears' power transmission or length polymer gears' service life.

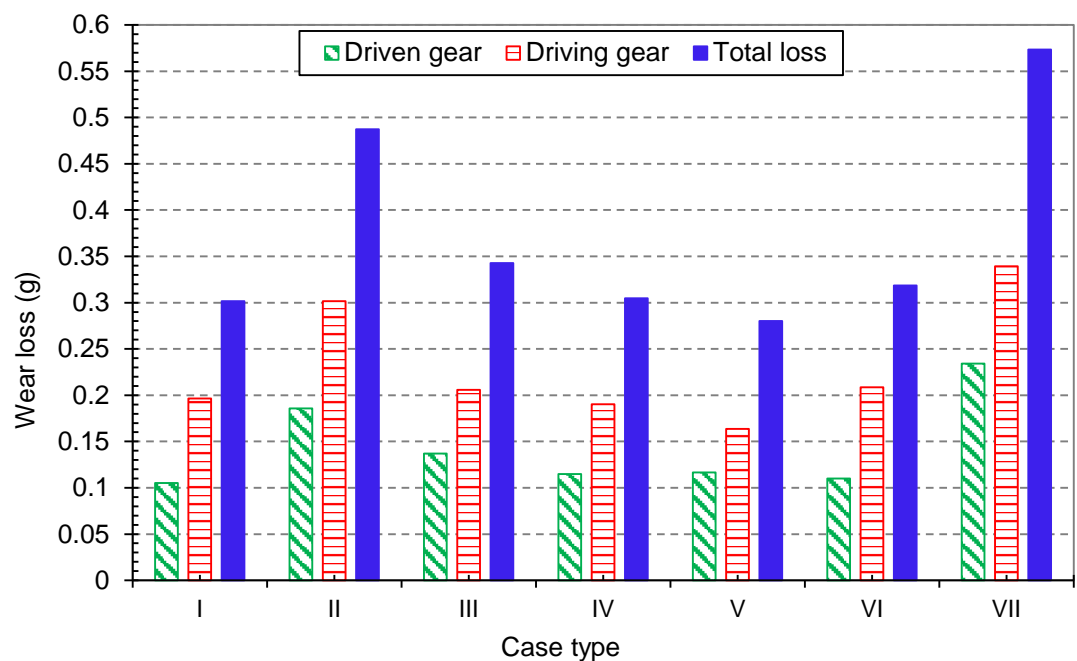


Figure 6.40 The weight loss of testing gears with various thermal dissipation structures

## **Chapter 7**

# **Conclusions and Further Work**

### **7.1 Conclusions**

Modifications were made to an existing bespoke non-metallic gear test rig, whereby nominally aligned tests and known deliberately misaligned tests could be carried out. Novel experimental measurement systems (i.e. velocity and temperature measurement of the air surrounding operating gears) were designed to serve extensive experimental investigations on thermal-wear behaviour of polyacetal gears. It is original to exploit segmented tests to assess the lifetime/durability of polymeric gears, which is conducted traditionally by continuous tests. New finding that the shapes/forms of wear debris (i.e. wood shavings-like) were closely associated with the category of gear mesh misalignment (i.e. axial misalignment). Dynamic relationship between gear body temperature, wear and wear rate was proposed and studied newly. Preliminary test results were used to consider how models and designs could be improved. Descriptions of the above research work are as follows:

#### **7.1.1 Design of additional measurement systems**

A wear measurement system was designed to measure the wear of gears. It consists of a non-contact (Hall-Effect) displacement transducer, NI-

DAQ and data logging software.

An airflow temperature measurement system was designed to obtain the temperature of airflow circling rotating gears and inspect the aerodynamic characteristics of operating polymer spur gears. To study the aerodynamic characteristics of meshing gears, two miniature anemometers was employed to measure the velocity of airflow surrounding or close to gears.

Vibration measurement system was introduced to explore the relationship of wear/ surface temperature and vibration patterns. It is likely to be one quick auxiliary way to monitor and judge the wear progress, or to detect gears' misaligned operating conditions.

### **7.1.2 Experimental investigations**

#### **7.1.2.1 Aligned configuration tests**

Numerous tests were conducted at various loads within each of three ranges (in terms of wear rate). An increase in load results in an increase in wear and wear rate. It was noted that wear debris stays on tooth contact surfaces and slightly affect the gear wear. Therefore, graphite paste lubricant was introduced to bring away the wear debris from the meshing tooth surfaces. Results confirmed that the wear debris tends to accelerate the wear rate slightly. Incremental step-load tests were carried out at various loads and speeds of 500, 1000, 1500 and 2000 rpm. An increase in speed tends to increase wear/wear rate of gears, but their effects are less than those of load imposed. The wear or failure modes of polyacetal gears were



investigated and allocated to different cases as follows.

- Low load cases ( perhaps below 8 N·m)

Within the low load range, tests continued until the allowable maximum wear limit of gear teeth (3.14 mm) were reached. However, the wear presents three wear phases: initial fast wear-in, transitional wear (these two together covering less than 5% the whole cycles, a very short period, can also be termed as a 'start-up' wear phase) and steady wear phases. No final faster wear occurs during the whole wear process. The average wear rate within the steady wear phase is less than  $10^{-6}$  mm/cycle. Worn tooth surface topographies and particle shapes were, for convenience, given names by analogy with other widely-known forms.

A quantity of pitting was observed on the worn tooth surfaces. The size and amount of pits became greater close to the pitch line regions and as the bearing load increased. There were distinct wear patterns between mating teeth regions having 'approaching' and 'recessing' contacts. 'Sand wave' wear marks were present over the fragments of tooth surfaces which act in 'recess action'. Visible 'ploughing' wear marks (deep and rough) spread over their counterparts (namely the segments acting 'approach action'). The zones where wear debris was found almost always accompany 'sand wave' wear marks. The generation and development of the 'sand wave' wear patterns are closely associated with the wear debris and, in turn, the 'sand wave' profiles may provide the circumstances for forming the roll/rod/needle/plate-like wear debris under a rolling action. 'Fish scale' like wear structures noted in the vicinity of pitch line may be caused by material

shearing off and accumulating nearby, or result from the propagation of micro-cracks.

In brief, the wear rate is stable and approximately constant, with heavier wear on the gear tooth regions that act in approach processes. Formation and growth of the 'sand wave' wear marks and debris appear to interact with each other. The roll/rod-like wear debris may also form under the roll contact (shear force). The origin of the 'fish scale' wear structure needs further research. Wear debris tends to accelerate slightly the wear of gears. Wear, pitting (fatigue) and adhesive wear are likely to be the main wear mechanism under low load circumstances (load less than 8 N·m).

- Moderate load cases (probably between 8 and 9.5 N·m)

In these situations, in addition to the three wear phases mentioned above, there was a final rapid wear phase, where the wear/wear rate accelerated significantly compared with that in the steady wear phase. Test results clearly demonstrate that an increase in load brings an earlier occurrence of the accelerated wear/wear rate. Taken over all the phases of this complex wear progression (mix of steady and final rapid wear) the average wear rate rose to being beyond  $10^5$  mm/cycle.

SEM micrographs indicated that adhesive wear occurred between rubbing teeth. The wear debris found on worn tooth surfaces varies significantly, with curved thin worm-like, bulk plate-like and thick rod/roll-like wear debris. It is speculated that the rod debris might develop from the worm-like or lamella (shearing/tearing off) debris under a roll action. Gear failure was likely to result from viscoelastic deformation (tooth bending, local

melting in the 'approach contact' regions and tensile stretching near the pitch line). Optical micrographs show that the scale of wear debris that dropped on to the bench increase significantly compared to that at low loads. A large amount of roll-like debris was observed and it seemed that it was the main element of large pieces of 'snowflake' wear debris. This may partly be caused by thermal expansion. Its presence subsequently results in a reduction in the backlash and clearance. Consequently, interference and then shearing is likely to happen. Particular worth mentioning is that some translucent lamellate debris is present in both light and medium load cases. Its presence may be due to the removal of asperities on the new tooth surfaces.

Overall, the wear or failure mechanisms at medium load is mainly by scuffing wear, viscoelastic deformation (tooth bending and elongation) or maybe softening in addition to the fundamental wear processes of pitting and micro cracks. Of course, local melting (due to excessive heat, with material properties degraded) was observed as well. These moderate load conditions are not recommended for engineering applications due to shortened endurance/service life.

- High load cases (probably beyond 9.5 N·m)

Under high load conditions, the wear accelerates significantly more rapidly once a test initiates than in the cases discussed previously. The average wear rate for the whole wear duration is in excess of  $10^{-4}$  (sometimes more than  $10^{-3}$ ) mm/cycle. Gears fail suddenly and early (wear does not reach the maximum wear limit, and gears often jump out of mesh

due to tooth melting , bending or elongation).

Copious transparent wear debris sprinkled onto the base once tests were initiated, evolving from transparent rolls to large transparent slices material as load increased. Optical micrographs reveal that the latter are cut or torn off from the tooth body directly. Clearly, the thermal expansion of teeth plays a major role within which backlash and probably clearance between mating teeth are removed. Welding is very likely to happen between engaging teeth.

SEM micrographs show that melting flow with the presence of macro open cracks takes place over the pitch line region. The worn tooth flanks show that the teeth have local melted and elongated (consequently thin and bent) near the pitch line (see Figure 4.61)

In short, plastic flow (plus welding) and viscoelastic deformation are the major wear/failure mechanisms in high load situations. It is not practical to use these higher loads for engineering applications.

Overall, polyacetal gears are mainly applicable for low power transmission, and especially those where the primary purpose is (kinematic) motion transmission.

### **7.1.2.2 Misaligned configuration tests**

Preliminary test results under known deliberately misaligned conditions (radial, axial, yaw and pitch misalignments) have been conducted. The polyacetal gears subjected to these four individual misalignments exhibit different wear characteristics. The experimental results show that the wear of

polyacetal gears is quite insensitive to radial, axial and yaw misalignments but very susceptible to pitch misalignments, which degrade the conjugate contact action. The degree of wear is conspicuous when pitch misalignments exceed a particular value, beyond which variations in the tooth non-conformal contact change from full line (narrow area) active contact into a short active contact line. This may lead a running gear pair to fail prematurely or cause uneven wear and thus degrade the designed power transmission capability. It is interesting to note that the influence of small pitch misalignments on polyacetal gears are relatively insignificant. This may be linked closely to the polymer's low elastic modulus.

In addition to wear rate, the wear mechanism of the misaligned gears was also examined by means of optical and scanning electron microscopes (OM and SEM). Strikingly different patterns of wear topographies and debris shapes were observed, indicating varying wear behaviour. Axial misalignment tends to trap more wear debris between teeth, and produce 'wood shavings' like wear debris. Slightly increase in centre distance impact slightly, but reduction in centre distance tends to accelerate wear and may cause interference fit between mating teeth. Yaw misalignment increase the wear rate slightly in initial wear-in phase with amount of roll/needle-like and lamella wear debris. However, almost no effects were noted within steady wear phase. Pitch misalignment leads to 'superimposed palisade' wear patterns over the teeth 'approaching action' regions (namely, roots of driving gears and tips of driven gears) and micro cracks near pitch points and tooth roots. Cotton-wool-like wear debris were noted all the wear processes. Wear debris regime may be helpful for diagnosis or to indicate operating

conditions, but further study is needed.

### **7.1.2.3 Thermal tests**

Test results comparing wear, wear rate, temperature of airflow surrounding gears and bulk temperature at various loads and a speed of 1000 rpm were obtained using synchronised measurement as a function of revolutions. They showed that there were transition temperatures, where wear and wear rate changed significantly. For instance, when gears' bulk temperature below 110°C, the wear was stable and wear rate was almost constant, but, when it rose beyond 110°C, the wear tended to become unstable and the wear rate increased greatly. There were temperature ranges over which the wear rate might remain nearly constant or might vary in a rising then falling parabola-like pattern. The parabola-like wear rate curve may link closely with the body and flash temperature and coefficient of friction.

For low load cases, it is safe to estimate roughly the average wear rate and service life according to the operating temperature. However, in the cases of moderate and high loads, the complicated and multiple levels of wear rate were present during the whole wear processes. It is therefore proposed that wear rate be estimated in terms of transition temperatures and temperature ranges. Coefficient of friction or probability-based statistics regarding operating temperature are proposed for use in estimating the average wear rates. However, the coefficient of friction under various conditions and the statistics of wear rates must be based on a large amount of test data and thus this work is still underway.

The airflow surrounding running gears may form stable velocity and temperature fields which act as agents for exchanging heat between the environment and gears. The bulk temperature balance is closely associated with this agency.

The 'approach and recess actions' of engaging gears work rather like a piston, with the volume of air trapped between teeth first compressed and then expanded almost instantaneously. Therefore, it may be one of the contribution heat sources (alongside: sliding friction, thermal conduction, and hysteresis). Test results indicate that the heat energy exchanges in both axial and radial directions of meshing gears. Brief data on the aerodynamic characteristics were presented. Guided by this data, several mechanical methods to improve the gears' durability were explored. Of them, a plate attachment for cutting off the hot air recycling path may be a good choice.

### 7.2 Further work

Despite the range of tests described above, it is inevitable that certain highly relevant aspects of investigations were treated very briefly or omitted. In light of the analysis of test results, some recommendations for the next phases work are:

- The orientation of the non-metallic gear test rig should be changed to facilitate more accurate measurement of body and surface temperatures;

- Coefficient of friction under various conditions, such as various temperatures, loads and speeds, is important to investigate. This should be helpful to predict wear/wear rate of polymer gears.
- A vibration monitoring system has been incorporated, and it should be studied in future work for use as a quick gear wear or operating temperature warning;
- A large series of thermal tests should be executed with a small load incremental interval (i.e. 0.1 N·m increment) and at various rotating speeds. It is expected to reveal the complex thermal-mechanical behaviour in more detail and so help deduce more reliable model relationships between wear and surface temperature;
- The airflow temperature measurement transducer assembly could be modified, replacing the small temperature sensors (K-type thermocouple) with miniature hot-wire anemometers, so that evolutions of velocity and temperature of the airflow could be obtained. A more advanced infrared camera would improve bulk temperature measurement. Together, these will benefit study of the aerodynamic characteristics of operating gears and establishing forced air convection models;
- Introduce miniature air pressure gauge to measure the air pressure in gear tooth pocket which is benefit to the study of forced air convection as stated in Section 3.5.



- Monitoring the gear teeth wear depth and wear teeth flank profiles by using a vertical profile optical projector. Coupling wear and temperature measurements, it is expected to reveal more thermal dynamic wear processes of polymer/composite gears.
- It will be benefit to take advantage of the existing investigations on power loss or vortex characteristics of external gear pump to establish forced air convection model;
- A detailed critical study of existing investigations into power loss and vortex characteristics of external gear pumps would be beneficial work to establish an air convection model;
- In addition to the visual observation of wear debris (shape and size), the morphology of wear debris (chemistry analysis such as the orientation and crystallinity) is suggested to examine.
- A much large number of tests with known deliberate misalignment is needed to establish statistically significant data on this important topic;
- Wear performance needs to be studied under a much wide range of gear configurations and materials, such as large modules, injection mould versus machine cut gears, various gear ratios and (especially) the use of PEEK and composite;
- For load capacity improvement, there should be full testing of prototypes of complex structures, such as plastic gears with cooling holes briefly discussed in this thesis.

## References

- [1] R. G. Budynas and J. K. Nisbett, *Shigley's mechanical engineering design*, Tenth ed. MC Graw Hill Education, p. 1082, 2015.
- [2] S. P. S. P. Radzevich, *Handbook of practical gear design and manufacture*, 2nd ed. Boca Raton, Fla.:CRC Press, 2012, pp. 529-699.
- [3] Ronsongears, *A brief history of gears*. Available: <http://www.ronsongears.com.au/a-brief-history-of-gears.php> (accessed 05/05/2017)
- [4] Gearsolution, *A plastic gears design update*. Available: <http://www.gearsolutions.com/article/detail/6366/a-plastic-gear-design-update> Aug. 2014 (accessed 06/08/2016)
- [5] J. Grasmeder. *High performance polymers*. Available: <https://www.victrex.com/en/blog/2017/high-performance-polymers> Feb. 2017 (accessed 06/05/2017)
- [6] Victrex, *it's time to scrap metal gears*. Available: [https://www.victrex.com/~media/literature/en/victrex\\_time-to-scrap-metal\\_gears-flyer.pdf](https://www.victrex.com/~media/literature/en/victrex_time-to-scrap-metal_gears-flyer.pdf) May 2014 (accessed 06/06/2015)
- [7] K. Mao, "The performance of dry running non-metallic gears," Ph.D thesis, The University of Birmingham, 1993.
- [8] S. Kono, "Increase in power density of plastic gears for automotive applications," Ph.D thesis, University of Birmingham, 2002.
- [9] Ondrives, *Precision gears: Materials*. Available: [https://www.ondrives.com/data/pdf/gears/precision/precision\\_gears\\_t ech.pdf](https://www.ondrives.com/data/pdf/gears/precision/precision_gears_t ech.pdf) Mar. 2017 (accessed 01/05/2017)
- [10] M. Biron, *Material selection for thermoplastic parts: practical and advanced information for plastics engineers*. Amsterdam: Elsevier, 2016.
- [11] H. Domininghaus, *Plastics for engineers: materials, properties, applications*. Munich; New York: Hanser, 1993.
- [12] R. Gauvin, G. Patrick, and Y. Henry, "Maximum surface temperature of the thermoplastic gear in a non-lubricated plastic/steel gear pair," *Ecole Polytechnique de Montreal*, pp. 20-27, August-September 1984.
- [13] B.S. 6168, "Specification for non-metallic spur gears," London: British Standards Institution, 1987.
- [14] Standard: DIN - VDI 2736 BLATT 2, "Thermoplastic gear wheels, cylindrical gears-calculation of the load-carrying capacity", 2014.

- [15] D. Houser, J. Harianto, and D. Talbot, "Gear mesh misalignment," *Gear Solutions*, no. 6, pp. 34-43, 2006.
- [16] M. H. Tsai and Y. C. Tsai, "A method for calculating static transmission errors of plastic spur gears using FEM evaluation," *Finite Elements in Analysis and Design*, vol. 27, no. 4, pp. 345-357, 1997.
- [17] P. K. Meuleman, D. Walton, K. D. Dearn, D. J. Weale, and I. Driessen, "Minimization of transmission errors in highly loaded plastic gear trains," *Proceedings of the Institution of Mechanical Engineers, Part C: Journal of Mechanical Engineering Science*, vol. 221, no. 9, pp. 1117-1129, 2007.
- [18] A. B. Cropper, "The failure mode analysis of plastic gears," Ph.D thesis, University of Birmingham, 2003.
- [19] C. J. Hooke, S. N. Kukureka, P. Liao, M. Rao, and Y. K. Chen, "The friction and wear of polymers in non-conformal contacts," *Wear*, vol. 200, no. 1-2, pp. 83-94, 1996.
- [20] C. J. Hooke, S. N. Kukureka, P. Liao, M. Rao, and Y. K. Chen, "Wear and friction of nylon-glass fibre composites in non-conformal contact under combined rolling and sliding," *Wear*, vol. 197, no. 1-2, pp. 115-122, 1996.
- [21] K. Mao, W. Li, C. Hooke, and D. Walton, "Friction and wear behaviour of acetal and nylon gears," *Wear*, vol. 267, no. 1, pp. 639-645, 2009.
- [22] Polypenco, "Polypenco Gears Design," ed. USA: Polypenco Coporation, 1985.
- [23] G. Straffelini, "Friction and wear methodologies for design and control," Springer, 2015, pp. 85-187.
- [24] K. Mao, "A new approach for polymer composite gear design," *Wear*, vol. 262, no. 3, pp. 432-441, 2007.
- [25] P. Fernandes and C. McDuling, "Surface contact fatigue failures in gears," *Engineering Failure Analysis*, vol. 4, no. 2, pp. 99-107, 1997.
- [26] D. Walton and Y. Shi, "A comparison of ratings for plastic gears," *Proceedings of the Institution of Mechanical Engineers, Part C: Mechanical Engineering Science*, vol. 203, no. 1, pp. 31-38, 1989.
- [27] M. Alanou, "Study of parameters influencing surface distress of gears," *Ann Arbor*, vol. 1050, pp. 48106-1346, 2006.
- [28] K. Marshek and P. Chan, "Wear damage to plastic worms and gears," *Wear*, vol. 44, no. 2, pp. 405-409, 1977.
- [29] K. Terashima, N. Tsukamoto, N. Nishida, and J. Shi, "Development of plastic gear for power transmission: abnormal wear on the tooth root and tooth fracture near pitch point," *Bulletin of JSME*, vol. 29, no. 251, pp. 1598-1604, 1986.
- [30] S. Senthilvelan and R. Gnanamoorthy, "Damage mechanisms in injection molded unreinforced, glass and carbon reinforced nylon 66

- spur gears," *Applied Composite Materials*, vol. 11, no. 6, pp. 377-397, 2004.
- [31] ANSI/AGMA 1010-F14, "Appearance of gear teeth-terminology of wear and failure", 2014.
  - [32] A. Pogačnik and J. Tavčar, "An accelerated multilevel test and design procedure for polymer gears," *Materials & Design*, vol. 65, pp. 961-973, 2015.
  - [33] K. Mao, "Gear tooth contact analysis and its application in the reduction of fatigue wear," *Wear*, vol. 262, no. 11, pp. 1281-1288, 2007.
  - [34] D. P. Townsend and L. S. Akin, "Analytical and experimental spur gear tooth temperature as affected by operating variables," *Journal of Mechanical Design*, vol. 103, no. 1, pp. 219-226, 1981.
  - [35] J. Yi and P. Quinonez, "Gear surface temperature monitoring," *Proceedings of the Institution of Mechanical Engineers, Part J: Journal of Engineering Tribology*, vol. 219, no. 2, pp. 99-105, 2005.
  - [36] B.-R. Höhn, K. Michaelis, and H.-P. Otto, "Influence of immersion depth of dip lubricated gears on power loss, bulk temperature and scuffing load carrying capacity," *International Journal of Mechanics and Materials in Design*, vol. 4, no. 2, pp. 145-156, 2008.
  - [37] B.-R. Höhn and K. Michaelis, "Influence of oil temperature on gear failures," *Tribology International*, vol. 37, no. 2, pp. 103-109, 2004.
  - [38] D. Wymer and P. Macpherson, "An infra-red technique for the measurement of gear tooth surface temperature," *Asle Transactions*, vol. 18, no. 4, pp. 229-238, 1975.
  - [39] L. H. Z. G. LuoWenjun, "Modelling and analysis of transient contact stress and temperature of involute gears," *Chinese Journal of Mechanical Engineering*, vol. 8, p. 004, 2004.
  - [40] T. T. Lin and A. Seireg, "An optimum design algorithm for gear systems incorporating surface temperature," *Journal Of Mechanisms, Transmissions and Automation in Design*, vol. 107, no. 4, pp. 549-555, 1985.
  - [41] K. Kurek and M. Niklewicz, "Parameters influence evaluation on gear surface temperature distribution during hardening process," *Przegł Elektrotechniczny*, vol. 84, pp. 86-94, 2008.
  - [42] N. Patir and H. Cheng, "Prediction of the bulk temperature in spur gears based on finite element temperature analysis," *Asle Transactions*, vol. 22, no. 1, pp. 25-36, 1979.
  - [43] J. Castro and J. Seabra, "Scuffing and lubricant film breakdown in FZG gears, Part II. New PV scuffing criteria, lubricant and temperature dependent," *Wear*, vol. 215, no. 1-2, pp. 114-122, 1998.
  - [44] C. Li, X. Liu, and G. Wang, "Simulation on temperature field of 50CrV4 automobile gear bar steel in continuous rolling by FEM,"

- Journal of Materials Processing Technology*, vol. 120, no. 1, pp. 26-29, 2002.
- [45] E. Atan, "On the prediction of the design criteria for modification of contact stresses due to thermal stresses in the gear mesh," *Tribology International*, vol. 38, no. 3, pp. 227-233, 2005.
  - [46] A. Seireg, "Thermal effects on the surface durability of gear teeth," vol. 215, no. 8, pp. 973-979: *Proceedings of the Institution of Mechanical Engineers: Journal of Mechanical Engineering Science, Part C*:. London, 2001
  - [47] S. Yousef, D. Burns, and W. Mckinlay, "Techniques for assessing the running temperature and fatigue strength of thermoplastic gears," *Mechanism and Machine Theory*, vol. 8, no. 2, pp. 175-185, 1973.
  - [48] R. Gauvin, P. Girard, and H. Yelle, *Prediction of the peak temperature on the surface of thermoplastic gear teeth: Pres. at the Fall Technical Meeting; Montreal, Canada, October 17-19, 1983*. AGMA, 1983.
  - [49] C. J. Hooke, K. Mao, D. Walton, A. R. Breeds, and S. N. Kukureka, "Measurement and prediction of the surface temperature in polymer gears and its relationship to gear wear," *Journal of tribology*, vol. 115, no. 1, pp. 119-124, 1993.
  - [50] K. Mao, W. Li, C. Hooke, and D. Walton, "Polymer gear surface thermal wear and its performance prediction," *Tribology International*, vol. 43, no. 1, pp. 433-439, 2010.
  - [51] K. Mao, "A numerical method for polymer composite gear flash temperature prediction," (in English), *Wear*, Article vol. 262, no. 11-12, pp. 1321-1329, May 2007.
  - [52] K. Mao, P. Langlois, Z. Hu, K. Alharbi, X. Xu, M. Milson, W. Li, C. J. Hooke and D. Chetwynd, "The wear and thermal mechanical contact behaviour of machine cut polymer gears," (in English), *Wear*, Article|Proceedings Paper vol. 332, pp. 822-826, May-June 2015.
  - [53] W. Li, A. Wood, R. Weidig, and K. Mao, "An investigation on the wear behaviour of dissimilar polymer gear engagements," *Wear*, vol. 271, no. 9, pp. 2176-2183, 2011.
  - [54] I. H. V. Melick and H. V. Dijk, "High-temperature testing of Stanyl plastic gears: A comparison with tensile fatigue data," ed: Geartechnology, 2010.
  - [55] M. Karimpour, K. Dearn, and D. Walton, "A kinematic analysis of meshing polymer gear teeth," *Proceedings of the Institution of Mechanical Engineers, Part L: Journal of Materials: Design and Applications*, vol. 224, no. 3, pp. 101-115, 2010.
  - [56] T. J. Hoskins, K. D. Dearn, Y. K. Chen, and S. N. Kukureka, "The wear of PEEK in rolling-sliding contact-Simulation of polymer gear applications," *Wear*, vol. 309, no. 1, pp. 35-42, 2014.

- [57] P. K. Singh and A. K. Singh, "An investigation on the thermal and wear behavior of polymer based spur gears," *Tribology International*, vol. 118, pp. 264-272, 2018.
- [58] J. E. Shigley, *Shigley's mechanical engineering design*. Tata McGraw-Hill Education, 2011.
- [59] D. Koffi, R. Gauvin, and H. Yelle, "Heat generation in thermoplastic spur gears," *Journal of Mechanisms, Transmissions, and automation in Design*, vol. 107, no. 1, pp. 31-36, 1985.
- [60] E. Letzelter, M. Guingand, J.-P. De Vaujany, and P. Schlosser, "A new experimental approach for measuring thermal behaviour in the case of nylon 6/6 cylindrical gears," *Polymer Testing*, vol. 29, no. 8, pp. 1041-1051, 2010.
- [61] N. Ertürk, A. Vernet, J. Pallares, R. Castilla, and G. Raush, "Small-scale characteristics and turbulent statistics of the flow in an external gear pump by time-resolved PIV," *Flow Measurement and Instrumentation*, vol. 29, pp. 52-60, 2013.
- [62] Y. Marchesse, C. Changenet, F. Ville, and P. Velez, "Investigations on CFD simulations for predicting windage power losses in spur gears," *Journal of Mechanical Design*, vol. 133, no. 2, p.024501, 2011.
- [63] M. Yazdani and M. C. Soteriou, "A novel approach for modeling the multiscale thermo-fluids of geared systems," *International Journal of Heat and Mass Transfer*, vol. 72, pp. 517-530, 2014.
- [64] K. Al-Shibl, K. Simmons, and C. Eastwick, "Modelling windage power loss from an enclosed spur gear," *Proceedings of the Institution of Mechanical Engineers, Part A: Journal of Power and Energy*, vol. 221, no. 3, pp. 331-341, 2007.
- [65] Y. Diab, F. Ville, H. Houjoh, P. Sainsot, and P. Velez, "Experimental and numerical investigations on the air-pumping phenomenon in high-speed spur and helical gears," *Proceedings of the Institution of Mechanical Engineers, Part C: Journal of Mechanical Engineering Science*, vol. 219, no. 8, pp. 785-800, 2005.
- [66] H. Houjoh, S.-I. Ohshima, S. Miyata, T. Takimoto, and K. Maenami, "Dynamic behavior of atmosphere in a tooth space of a spur gear during mesh process from the viewpoint of efficient lubrication," in *Proceedings of the ASME, Design Engineering Technical Conference, Baltimore, MD, Paper No. PTG-14372*, 2000.
- [67] T. L. Bergman and F. P. Incropera, *Fundamentals of heat and mass transfer*. John Wiley & Sons, 2011.
- [68] F. W. Schmidt, R. E. Henderson, and C. H. Wolgemuth, *Introduction to thermal sciences: thermodynamics, fluid dynamics, heat transfer*, 2nd ed. Wiley, 1993.
- [69] H. Blok, "The flash temperature concept," *Wear*, vol. 6, no. 6, pp. 483-494, 1963.

- [70] A. I. Housz, "Scuffing as a factor in the design of nylon gears," *Wear*, vol. 10, no. 2, pp. 118-126, 1967.
- [71] S. Takanashi and A. Shoji, "On the temperature rise in the teeth of plastic gears," in *International Power Transmission & Gearing Conference, San Francisco*, 1980.
- [72] H. Blok, "Measurement of temperature flashes on gear teeth under extreme pressure conditions," *Proc. Inst. Mech. Engrs.*, vol. 2, pp. 14-20, 1937.
- [73] H. Blok, "Theoretical study of temperature rise at surfaces of actual contact under oiliness lubricating conditions," *Proc. Instn. Mech. Engrs.(General discussion on lubrication and lubricants)*, vol. 2, p. 222, 1937.
- [74] J. C. Jaeger, "Moving sources of heat and temperature at sliding contacts," in *Proc. Royal Society of New South Wales*, 1942, vol. 76, p. 222.
- [75] R. Holm, "Calculation of the temperature development in a contact heated in the contact surface, and application to the problem of the temperature rise in a sliding contact," *Journal of Applied Physics*, vol. 19, no. 4, pp. 361-366, 1948.
- [76] F. P. Bowden, D. Tabor, and F. Palmer, "The friction and lubrication of solids," *American Journal of Physics*, vol. 19, no. 7, pp. 428-429, 1951.
- [77] J. Archard, "The temperature of rubbing surfaces," *Wear*, vol. 2, no. 6, pp. 438-455, 1959.
- [78] T. Nakada and S. Hashimoto, "Heat conduction in a semi-infinite solid heated by a moving heat source along the boundary," *Bulletin of JSME*, vol. 6, no. 21, pp. 59-69, 1963.
- [79] G. T. Symm, "Surface temperatures of two rubbing bodies," *The Quarterly Journal of Mechanics and Applied Mathematics*, vol. 20, no. 3, pp. 381-391, 1967.
- [80] T. Toshimi and K. Masana "A study on flash temperatures on the spur gear teeth," *Journal of Engineering for Industry*, p. 78, 1974.
- [81] J. Lancaster, "Estimation of the limiting PV relationships for thermoplastic bearing materials," *Tribology*, vol. 4, no. 2, pp. 82-86, 1971.
- [82] J. Halling, "Principles of tribology," *McaMillian, New York*, 1975.
- [83] K. Terashima, N. Tsukamoto, and N. Nishida, "Development of plastic gear for power transmission: economical methods for increasing load-carrying capacity," *Bulletin of JSME*, vol. 29, no. 247, pp. 256-259, 1986.
- [84] K. Terashima, N. Tsukamoto, and N. Nishida, "Development of plastic gear for power transmission: design on load-carrying capacity," *Bulletin of JSME*, vol. 29, no. 250, pp. 1326-1329, 1986.

- [85] H. Imrek, "Performance improvement method for Nylon 6 spur gears," *Tribology International*, vol. 42, no. 3, pp. 503-510, 2009.
- [86] H. Imrek and H. Düzcükoğlu, "Relation between wear and tooth width modification in spur gears," *Wear*, vol. 262, no. 3, pp. 390-394, 2007.
- [87] N. Tsukamoto and K. Terashima, "Development of plastic gears for power transmission: various methods of lengthening the life of plastic gears and their effect," *Bulletin of JSME*, vol. 29, no. 247, pp. 249-255, 1986.
- [88] C. H. Kim, "Durability improvement method for plastic spur gears," *Tribology International*, vol. 39, no. 11, pp. 1454-1461, 2006.
- [89] H. Düzcükoğlu, R. Yakut, and E. Uysal, "The use of cooling holes to decrease the amount of thermal damage on a plastic gear tooth," *Journal of failure analysis and prevention*, vol. 10, no. 6, pp. 545-555, 2010.
- [90] H. Düzcükoğlu, "Study on development of polyamide gears for improvement of load-carrying capacity," *Tribology International*, vol. 42, no. 8, pp. 1146-1153, 2009.
- [91] A. J. Mertens and S. Senthilvelan, "Durability enhancement of polymer gear using compressed air cooling," *Proceedings of the Institution of Mechanical Engineers, Part L: Journal of Materials: Design and Applications*, vol. 230, no. 2, pp. 515-525, 2016.
- [92] J.-I. Nozawa, T. Komoto, T. Kawai, and H. Kumehara, "Tribological properties of polymer-sheet-adhered metal hybrid gear," *Wear*, vol. 266, no. 9, pp. 893-897, 2009.
- [93] J.-I. Nozawa, "Tribology of polymer injection-molded stainless steel hybrid gear," *Wear*, vol. 266, no. 7, pp. 639-645, 2009.
- [94] S. S. Yousef, "Performance and design of thermoplastic gears," Ph.D Thesis, University of Waterloo, Canada, 1974.
- [95] N. Tsukamoto, H. Maruyama, T. Taki, and N. Nishida, "A study on strength design methods for plastic gears: estimation of operation life of plastic gears elevated-temperature environment," *JSME international journal. Ser. 3, Vibration, control engineering, engineering for industry*, vol. 34, no. 1, pp. 121-126, 1991.
- [96] A. R. Breeds, S. N. Kukureka, K. Mao, D. Walton, and C. J. Hooke, "Wear behaviour of acetal gear pairs," *Wear*, vol. 166, no. 1, pp. 85-91, 1993.
- [97] N. Wright and S. Kukureka, "Wear testing and measurement techniques for polymer composite gears," *Wear*, vol. 251, no. 1, pp. 1567-1578, 2001.
- [98] R. P. Steijin and R. D. Corneliussen, "Failure of plastics," 0-02-947510-4th ed: Society of plastic engineers and Hanser publisher, 1986.



- [99] Y. Yamaguchi, *Tribology of plastic materials: their characteristics and applications to sliding components*. Elsevier, 1990.
- [100] S. Li, "Effects of machining errors, assembly errors and tooth modifications on loading capacity, load-sharing ratio and transmission error of a pair of spur gears," *Mechanism and Machine Theory*, vol. 42, no. 6, pp. 698-726, 2007.
- [101] S. Li, "Effects of misalignment error, tooth modifications and transmitted torque on tooth engagements of a pair of spur gears," *Mechanism and Machine Theory*, vol. 83, pp. 125-136, 2015.
- [102] S. Prabhakaran, D. S. Balaji, and C. Joel, "Stress analysis and effect of misalignment in spur gear," *International Journal of Applied Engineering Research*, vol. 9, no. 22, pp. 13061-13072, 2014.
- [103] M. R. Lias, T. V. L. N. Rao, M. Awang, and M. A. Khan, "The stress distribution of gear tooth due to axial misalignment condition," *Journal of Applied Sciences*, vol. 12, no. 23, pp. 2404-2410, 2012.
- [104] H. A. Ameen, "Effect of shaft misalignment on the stress distribution of spur gears," *Journal of Engineer and Technology*, vol. 28, pp. 1321-1339, 2010.
- [105] N. Driot and J. Perret-Liaudet, "Variability of modal behavior in terms of critical speeds of a gear pair due to manufacturing errors and shaft misalignments," *Journal of Sound and Vibration*, vol. 292, no. 3, pp. 824-843, 2006.
- [106] P. Velez and M. Maatar, "A mathematical model for analyzing the influence of shape deviations and mounting errors on gear dynamic behaviour," *Journal of Sound and Vibration*, vol. 191, no. 5, pp. 629-660, 1996.
- [107] A. Saxena, A. Parey, and M. Chouksey, "Effect of shaft misalignment and friction force on time varying mesh stiffness of spur gear pair," *Engineering Failure Analysis*, vol. 49, pp. 79-91, 2015.
- [108] R. G. Jones, "The mathematical modelling of gearbox vibration under applied lateral misalignment," PhD thesis, School of Engineering, University of Warwick, UK, 2012.
- [109] V. Simon, "The influence of misalignment on mesh performance of hyoid gears," *Mechanism and Machine Theory*, vol. 33, no. 8, pp. 1277-1291, Aug. 1998.
- [110] V. Simon, "Influence of tooth errors and misalignments on tooth contact in spiral bevel gears," *Mechanism and Machine Theory*, vol. 43, no. 10, pp. 1253-1267, 2008.
- [111] V. Simon, "Influence of tooth errors and shaft misalignments on loaded tooth contact in cylindrical worm gears," *Mechanism and machine theory*, vol. 41, no. 6, pp. 707-724, 2006.

- [112] S. Raadnui, "Wear particle analysis-utilization of quantitative computer image analysis: A review," *Tribology International*, vol. 38, no. 10, pp. 871-878, Oct. 2005.
- [113] J. A. Williams, "Wear and wear particles-some fundamentals," (in English), *Tribology International*, Article vol. 38, no. 10, pp. 863-870, Oct. 2005.
- [114] P. Podsiadlo and G. W. Stachowiak, "Development of advanced quantitative analysis methods for wear particle characterization and classification to aid tribological system diagnosis," *Tribology International*, vol. 38, no. 10, pp. 887-897, 2005.
- [115] S. N. Kukureka, C. J. Hooke, M. Rao, P. Liao, and Y. K. Chen, "The effect of fibre reinforcement on the friction and wear of polyamide 66 under dry rolling-sliding contact," *Tribology International*, vol. 32, no. 2, pp. 107-116, 1999.
- [116] S. N. Kukureka, Y. K. Chen, C. J. Hooke, and P. Liao, "The wear mechanisms of acetal in unlubricated rolling-sliding contact," *Wear*, vol. 185, no. 1-2, pp. 1-8, 1995.
- [117] K. Dearn, T. Hoskins, D. Petrov, S. Reynolds, and R. Banks, "Applications of dry film lubricants for polymer gears," *Wear*, vol. 298, pp. 99-108, 2013.
- [118] Z. Hu and K. Mao, "An investigation of misalignment effects on the performance of acetal gears," *Tribology International*, vol. 116, pp. 394-402, 2017.
- [119] E. Ramsden, *Hall-effect sensors: theory and applications*, 2nd ed. Amsterdam ; Boston: Elsevier/Newnes, 2006, p. 250.
- [120] Calculate magnetic flux density with formula. Available: <https://www.supermagnete.de/eng/faq/How-do-you-calculate-the-magnetic-flux-density>, Feb. 2013 (accessed 02/11/2013)
- [121] R. C. Fernow, *Principles of magnetostatics*. Cambridge University Press, United Kingdom:, 2016.
- [122] K. Mao, W. Li, C. J. Hooke, and D. Walton, "Polymer gear surface thermal wear and its performance prediction," *Tribology International*, vol. 43, no. 1, pp. 433-439, 2010.
- [123] J.-Z. Liang and F. Wang, "Flexural and impact properties of POM/EVA/HDPE blends and POM/EVA/HDPE/nano-CaCO<sub>3</sub> composites," *Polymer Bulletin*, vol. 72, no. 4, pp. 915-929, 2015.
- [124] Ondrives. *Precision Gears: Spur gears, Backlash, Limits and fits and Modifications*. Available: [https://www.ondrives.com/data/pdf/gears/precision/precision\\_gears\\_t ech.pdf](https://www.ondrives.com/data/pdf/gears/precision/precision_gears_t ech.pdf) Mar.2017 (accessed 01/05/2017)

## Appendix A

### Data of Test Gears

The quality of polyacetal involute spur gear (module: 2) is e25 DIN 3967, Grade 8 with center distance tolerance Js7. Upper tooth thickness allowance is -0.04 mm and tooth thickness tolerance ( $T_{sn}$ ) is 0.040 mm [124]. Ondrives part: ZPG2-30 (Spur gear ISO 2M-30 Modified: dimensions are in millimetres; surface finish; tolerance: linear:  $\pm 0.1$  mm, angular:  $\pm 1$  Deg).

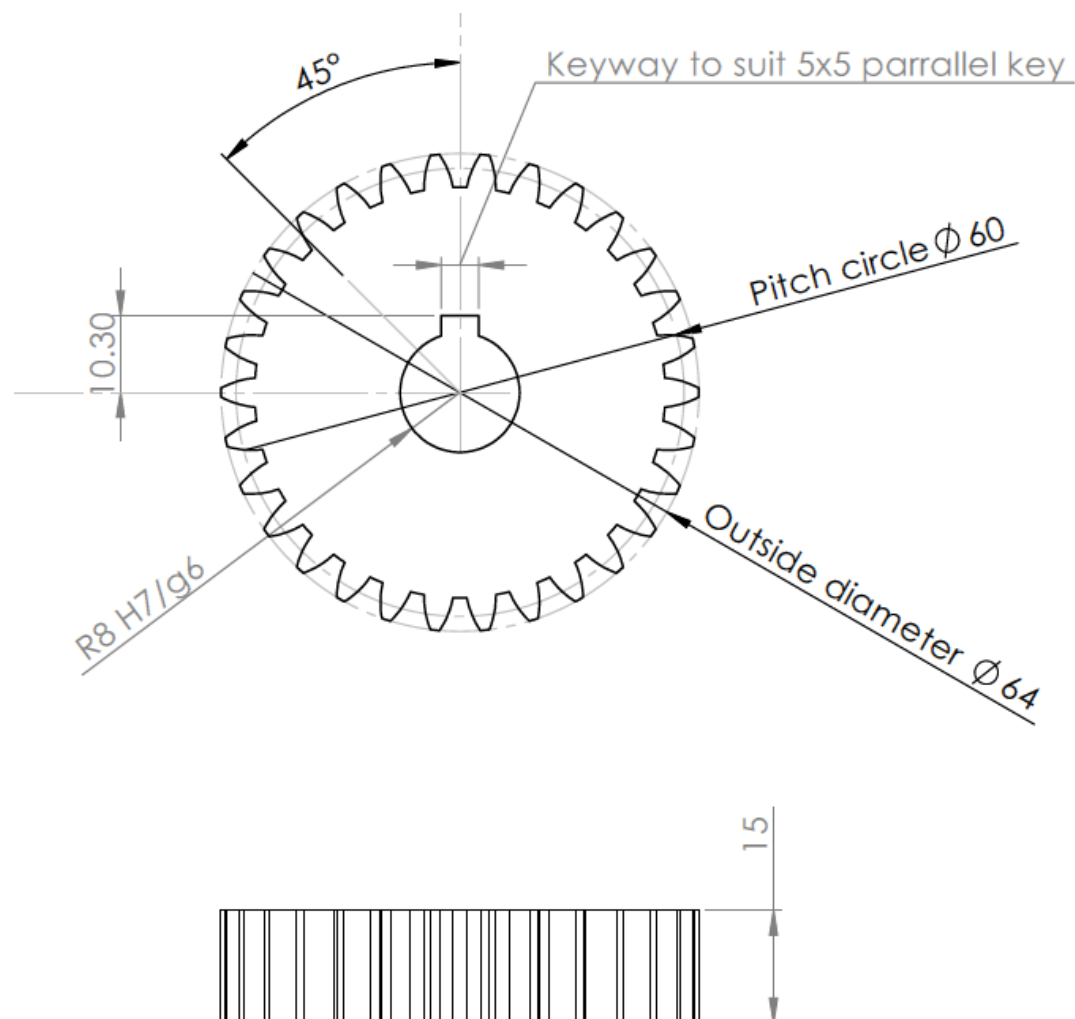


Figure A.1 Nominal dimensions of test gears

Table A.1 Material properties of test polyacetal gear samples [9]

POM	Parameters	Unit	Value
Genral properties	Density	kg m <sup>-3</sup>	1410
	Absorption of moisture		0.28%
Mechanical properties	Yield stress/Tensile strength	MPa	67
	Elongation at break	-	30%
	Poisson's ratio (@ 40°C)	-	0.35
	Tensile modulus of elasticity (@23°C)	MPa	2800
	Ball indentation hardness	MPa	150
	Shore-hardness	Skala D	81
	Coefficient of friction against dry steel		0.1-0.3
Thermal properties	Melting temperature	°C	165
	Thermal properties	W/(m·K)	0.31
	Coefficient of linear thermal expansion	10 <sup>-6</sup> K <sup>-1</sup>	110
	Service temperature, long term (min.)	°C	-50
	Service temperature, long term (max.)	°C	100
	Service temperature, short term	°C	140

## Appendix B

### Test Procedure

The test procedures are briefly summarized as follows:

- a) First weigh two new gears and scan their tooth flank profiles prior to testing;
- b) Set up the required test speed;
- c) Identify the test condition (alignment or misalignment) and configure the driving and driven bearing blocks as described in Section 3.1.4;
- d) Set the required test torque to the test gears. Choose a constant weight, adjust its position on the moment bar and then measure the equivalent load by using an electronic balance. This procedure may be repeated until the equivalent load equals the required test torque. The load bar should now be in a horizontal position;
- e) Fit the two new gears against the pivot block assembly;
- f) The moment bar should be in horizontal position after mounting gears. If necessary, adjust to horizontal level by turning the conical clutch on the driving shaft;
- g) If measuring vibration, fix the accelerometer at the position mentioned in Section 3.6.
- h) If measuring airflow temperature, mount the airflow temperature

measure device to the pivot bearing block assembly;

- i) If measuring bulk temperature measurement, focus an infrared video camera at an appropriate point on the test gears. Set related parameters, such as emissivity, room temperature and distance;
- j) Connect the displacement transducer, airflow temperature measurement device, vibration transducer to their corresponding DAQs and switch on their power supplies;
- k) Check data logging software, make sure all the sensors work properly;
- l) Start all the data-logging softwares, infrared video camera and then the motor of the test rig;
- m) After the prescribed time or wear loss, stop the motor (micro switch cuts the test at maximum wear or failure), data logging and demount systems by reversing above procedure.